

**UNIVERSITY OF NAPLES FEDERICO II**  
*Faculty of Engineering*

PH.D. PROGRAMME in MATERIALS and STRUCTURES  
COORDINATOR PROF. DOMENICO ACIERNO  
*XXII CYCLE*



ROBERTO CUZZILLA

PH.D. THESIS

**Seismic Assessment and Retrofit of Historical  
Masonry Structures**

TUTOR PROF. ANDREA PROTA  
CO-TUTOR DR. GIAN PIERO LIGNOLA

<b>INTRODUCTION.....</b>	<b>7</b>
 <b>CHAPTER 1</b>	
<b>HISTORY OF THE GOTHIC PERIOD.....</b>	<b>13</b>
<b>1.2 Gothic period : three different phases .....</b>	<b>14</b>
1.2.1. Early Gothic.....	15
1.2.2. High Gothic.....	15
1.2.3. Late Gothic.....	17
<b>1.3 Gothic structures : architectural description .....</b>	<b>18</b>
<b>1.4 Catalan gothic structures : architectural description .....</b>	<b>22</b>
<b>1.5 Description of Gothic Churches object of study.....</b>	<b>23</b>
1.5.1. Santa Maria del Pi .....	23
1.5.2. Santa Maria del mar.....	25
1.5.3. Mallorca Cathedral.....	28
<b>1.6 Past study on the Churches.....</b>	<b>29</b>
 <b>CHAPTER 2</b>	
<b>EVALUATION OF SEISMIC SAFETY OF THE HISTORICAL STRUCTURES.....</b>	<b>32</b>
<b>2.1. Knowledge of the structures.....</b>	<b>32</b>
<b>2.2. Seismic behaviour in historical constructions.....</b>	<b>33</b>
<b>2.3. Seismic behaviour of churches or other large span structures.....</b>	<b>34</b>
<b>2.4. Limit analysis and Capacity Spectrum Method (CSM).....</b>	<b>34</b>
<b>2.5. Capacity Spectrum Method for evaluation the safety of the</b>	

monuments.....	36
2.6. Evaluation of the seismic demand of the structures according to the European design rule – Eurocode 8. ....	41
2.7. Evaluation of the demand of the structures under seismic actions according to the Spanish design rule – NCSE-02.....	45
2.8. Comparison between the response spectrum and ADSR graphs previously described .....	48
2.9. Fajfar method [Capacity Spectrum Method based on inelastic demand spectra, 1999] .....	51

### CHAPTER 3

CSM RESULTS OBTAINED BY USING EC8 and NCSE-02 DESIGN CODES .....	58
3.1. Santa Maria del Pi .....	59
3.2. Santa Maria del Mar.....	72
3.3. Mallorca Cathedral .....	91
3.4. Obtained results: final remarks .....	98

### CHAPTER 4

SEISMIC BEHAVIOR OF MASONRY BUILDINGS .....	100
4.1. Construction Materials .....	101
4.2. Masonry mechanical characteristic computations .....	104
4.3. The vertical bearing elements of the masonry buildings.....	105
4.4. Collapse mechanism of vertical bearing elements .....	109

## CHAPTER 5

<b>FINITE ELEMENT MODELING AND MASONRY PANELS' VALIDATIONS.....</b>	<b>112</b>
<b>5.1. Masonry panels modelling .....</b>	<b>113</b>
<b>5.2. Masonry panel descriptions .....</b>	<b>115</b>
5.2.1. Masonry panel proposed by Alcaïno et al.....	115
5.2.2. Masonry panel proposed by Pascale et al. ....	121
5.2.3. Masonry panel proposed by Manfredi et al.....	124
<b>5.3. Final Remarks about validation .....</b>	<b>128</b>

## CHAPTER 6

<b>MASONRY PANELS PERFORMANCES BY CHANGING THE FRACTURE ENERGIES OF BOTH MATERIALS.....</b>	<b>132</b>
<b>6.1. Alcaïno et al. panels .....</b>	<b>134</b>
6.1.1. Compressive Fracture Energies for both materials .....	134
6.1.2. Tensile Fracture Energies for both materials .....	138
<b>6.2. Pascale et al. panels .....</b>	<b>142</b>
6.2.1. Compressive Fracture Energies for both materials .....	142
6.2.2. Tensile Fracture Energies for both materials .....	145
<b>6.3. Manfredi et al. panels .....</b>	<b>148</b>
6.3.1. Compressive Fracture Energies for both materials .....	148
6.3.2. Tensile Fracture Energies for both materials .....	152
<b>6.4. Final Remarks.....</b>	<b>156</b>
6.4.1. Conclusion about Alcaïno et al. experimental test.....	156
6.4.2. Conclusion about Manfredi et al. experimental tests.....	157
6.4.3. Final remarks about ductility.....	159



## **CHAPTER 7**

### **MASONRY PANELS REINFORCED BY USING frp SUBJECTED TO IN PLAN ACTIONS ..... 165**

<b>7.1. Modeling .....</b>	<b>166</b>
<b>7.2. Alcaino et al Panel .....</b>	<b>168</b>
7.2.1. Diagonal reinforcement layouts.....	168
7.2.2. Horizontal reinforcement layouts.....	176
<b>7.3. Pascale et al Panel .....</b>	<b>183</b>
7.3.1. Diagonal reinforcement layouts.....	183
7.3.2. Horizontal reinforcement layouts.....	189
<b>7.4. Manfredi et al Panel .....</b>	<b>194</b>
7.4.1. Diagonal reinforcement layouts.....	194
7.4.2. Horizontal reinforcement layouts.....	201
<b>7.5. Final Remarks.....</b>	<b>205</b>

### **CONCLUSION..... 208**

#### **ANNEX A: COLLAPSE MECHANISMS OF THE CHURCHES**

#### **ANNEX B : Application of C.S.M. to mediaeval constructions**

#### **ANNEX C: Results and comparison obtained by changing the fracture energies**

#### **ANNEX D: Results and comparison obtained by changing the FRP strengthening solutions**



## INTRODUCTION

The Italian building heritage is composed mainly of masonry structures, which over the years have acquired historic significance and artistic values in the national culture.

These buildings are particularly vulnerable to the seismic actions, because they were design for gravitational loads without considering seismic actions applied on them. Thus, the constructive details are not compliant with the present design code provisions (e.g. in plan or elevation structural regularity) and to avoid collapse or wide crack patterns, different strengthening interventions should be proposed or were done during the time (orthogonal wall connections, steel ties applications).

In recent years, conservation and restoration of existing constructions assumed very important roles to reach an appropriate structural safety level, especially for artistic and monumental constructions, taking into account the benefit achieved by building restorations reducing the new constructions.

The large number of destructive earthquakes occurred in Italy during the last century and the beginning of the new century has highlighted the need to redefine the design strategies and requirements especially in high seismic risk regions.

Therefore, different seismic design provisions have occured during the time both in national and regional levels; the most recent is the Italian provisions (named, DM2008 [1]).

The fundamental innovative aspect of the aforementioned DM2008 [1] is connected to the existing constructions and in particular it takes into account strategic buildings or structures playing very important rules for civil protection, introducing the research seismic engineering results into the professional world.

The new seismic design provision introduced by the DM2008 [1] give more emphasis on the management and maintenance of structures, which are often a relevant fraction of the total cost of the rehabilitation work. The new seismic design code have been inspired by the following general principals:

- 1) avoid structural damage and minimize non-structural damages for moderate intensity seismic events and seismic action characterized by return period comparable with the building operating life. Moreover non-structural damages for seismic events characterized by return period less than the building life should be avoided. These criteria respect the damage limit state condition (*DLS*);
- 2) The construction elements must have structural characteristics such as ductility to dissipate the energy released by earthquakes during high intensity seismic events without reaching collapse mechanisms; the safety of the people is, thus, ensured in case of events characterized by a lower probability of occurrence (return period of 475 years) which, to be endured without plastic deformation, would require an uneconomical design of the structure. A structural element damage are accepted in order to make the dissipative mechanisms possible. These criteria respect the ultimate limit state condition (*ULS*).

As stated in the seismic design code, "*...the purpose is to ensure the human life protection in case of earthquakes, the damages should be limited and the important structures in terms of civil protection should be working...*".

Materials and strengthening techniques characterized by high performances and minimal impact on the structures play a crucial role on rehabilitation and restoration of existing buildings.

The masonry structures, in a lot of cases having historic and architectural values, represent an important part of the Italian structural heritage.

Many of the structural defects related to the masonry buildings are due to inadequate techniques and materials, earthquake and wind actions (horizontal loads), foundation settlements, atmospheric agents deterioration.

In addition, higher loads acting on the structure due to different structural use and more stringent standards for seismic design provision lead to have need of appropriate strengthening interventions.

The methods traditionally used for masonry structure rehabilitation are:

- ✓ Fill cracks and voids with grout injections;
- ✓ stitching large cracks or weak areas with metal parts or concrete elements;
- ✓ reinforced perforations injected with mortar, in order to increase the masonry tensile strength;
- ✓ jacketing on one or both masonry panel sides with reinforced concrete by using an electro welded steel grid.

The use of fiber-reinforced composite materials represents an alternative to traditional intervention techniques: these materials, usually made of carbon fiber (CFRP), glass (GFRP) or aramid (AFRP) held together by a polymer matrix, provide unique combination of mechanical performances, including high strength and stiffness in fiber direction, corrosion resistance, light weight. They are available in form of sheets or rolls characterized by virtually unlimited length.

All these properties allow to realize the structural seismic reinforcement without increasing the seismic mass.

These types of composites are characterized by a high compatibility with the substrate in terms of geometric, chemical and mechanical properties.

The research activities described in the following were partially carried out in Barcelona (Spain) and several ecclesiastic structures were selected in order to evaluate their seismic behavior applying European and Spanish design codes (EuroCode 8 [2] and NCSE-02 [3], respectively).

For that reason the earthquake phenomena effects were studied on three Spanish gothic structures by using limit analysis criteria in order to compute their seismic performances in terms of safety level, according to the *Italian guide line for evaluation and reduction of the seismic risk of the cultural heritage* (2006) [4].

The structures were separated into macro-elements subjected to in-plane and out-of-plane actions, applying the Capacity Spectrum Method (CSM) and the safety levels were computed by means of seismic demand and structural capacity ratio.

Then, the attention was focused on in-plane structural behavior and, using available data from experimental tests on masonry panels carried out by other authors, a numerical simulations were implemented by using the finite element software DIANA TNO rel.9.2 [5].

Three experimental program on panels made by different materials were examined in order to be sure that the results obtained using numerical simulations were not strongly connected to the relative substrate. Thus, the analyzed models were made by

hollow bricks, solid bricks and tuff bricks respectively and different mortars for each masonry panel were also used.

Two aspects, considered of primary importance for masonry structures were analyzed:

- ✓ the global performances by changing mechanical properties of structural elements;
- ✓ the global performances reached by using FRP strengthening system.

With reference to the first point, the masonry panel behaviour was analyzed by changing the compression ( $G_{fc}$ ) and tensile fracture energy ( $G_{ft}$ ) for both bricks and mortar. The knowledge of the previous mentioned physical parameters is very complex to establish with traditional laboratory tests, but it is important to have a reliable masonry panel numerical simulation. In particular a specific range of feasible values of the fracture energy was considered, calculating them by using formulas introduced in the literature. Within that range the two extreme values and the average value or, in alternative, the value calculated according to the material mechanical strength were selected; then three different analyses were performed for each masonry panel. The second point has been performed by means of two different panel strengthening systems using Carbon Fiber reinforced (CFRP): one by using diagonal stripes and the other composed by horizontal stripes (Grid layout).

These numerical simulations, the global strengthened panel response was highlighted, changing several geometric characteristic of the strengthening system; width of the strip (for both diagonal and horizontal reinforcement) and the spacing between each strip (only for horizontal reinforcement) were modeled. The scope of the present research work was to compute the panel shear capacity and the initial stiffness of cracked panels subjected to in plane compression and shear loads by changing material mechanical properties, both for tuff and mortar, and considering different arrangement and amount of FRP reinforcement. Particular attention was also paid to the comparison between the “as built” panels and the strengthened ones by means of failure modes and crack patterns. Therefore, the present work was arranged in order to specify the structural typology where the introduced strengthening system could be applied, describing the different masonry structures and their main performances under seismic actions, such as shear capacity and failure mode. The work goes on describing the characterization of materials used in the simulation phase, the model by using DIANA software [5] considering both “as built” and strengthened masonry

panels, the comparison between the numerical analyses results and experimental ones in order to validate the modelling and, at the end, to implement the parametric analysis by changing the geometrical and mechanical properties.

## References

- [1] Decreto Ministeriale 14 Gennaio 2008. “*Nuove norme tecniche per le costruzioni*”. Pubblicato sulla G.U. il 4 Febbraio 2008.
- [2] EN 1998 Eurocode 8, 1998. “*Design of structures for earthquake resistance – Part 1: general rules, seismic actions and rules for buildings*”.
- [3] NCSE-02, 2002. “*Norma de construccion sismorresistente: parte general y edificación*”, Real decreto 997/2002 del Ministerio de obra publicas, transportes y medio ambiente
- [4] OPCM 3431, 2005. “*Italian guide line for evaluation and reduction of the seismic risk of the cultural heritage* (2006).
- [5] TNO DIANA rel. 9.2. “*International Software Company for FEA applications in civil and geotechnical engineering*”.



## **1. HISTORY OF GOTHIC PERIOD**

The first Gothic cathedrals were built in France and within the individual domain of their kings. Their architectural style was a French invention. Its spread throughout Europe signifies French influence in the later Middle Ages, as the Romanesque especially signifies Germanic power and greatness in the earlier Middle Ages. As regards England, Germany, and Spain, the Gothic was a borrowed style.

In Gothic architecture it is possible to have two distinct movements. One was the evolution as accomplished in one spot. The other was the gradual displacement of Romanesque methods in countries exterior to France, where they were supplanted by a style directly introduced and, so to speak, ready made.

As the rise and spread of Gothic cathedral architecture was undoubtedly the most important feature of art history between the thirteenth and the sixteenth centuries (1200–1500 A.D.), this period is accordingly named; but most interesting developments in the art of design were made in Italy during these centuries, which were quite independent of it, as was also mainly the Italian architecture, which is notwithstanding, for the given dates, known as the "Italian Gothic."

The word "Gothic" itself is one of Italian coinage and was used by the Italians of the later Middle Ages to designate all buildings of Northern Europe without reference to any of our own distinctions of period or style. It still speaks of the "Goths and Vandals" when barbarism wants to designate, and the word "Gothic" simply meant to Italian comprehension "Germanic," in the large sense, or as we should say "medieval." Both the Visigoths and Ostrogoths had been invaders of Italy during the downfall of

the Western Roman Empire. The word Goth was thus a characteristic designation for the Germans at large, and although France in the later Middle Ages had lost all vestige of her Frankish Germanic origins, the Italians were good enough historians to remember that all the countries of the western empire had been Germanized and that Italy had suffered most from their invasions because it had the most to lose.

This historic prejudice of the Italian against Germanic and Northern Europe explains the first use of the word "Gothic," which was subsequently adopted by Northern Europe with the style and taste of the Renaissance during and after the sixteenth century. It was this Renaissance style (revival of the Greco-Roman classic style) which finally then displaced and supplanted the Gothic. This was abandoned more or less rapidly all over Europe and there is, broadly speaking, a gap of three hundred years between the modern copies of Gothic buildings and the old originals, which gap is filled by the Italian Renaissance style.

In Northern Renaissance Europe the word "Gothic" was also applied indiscriminately to medieval buildings of all dates and without reference to the peculiar style which we distinguish by it. The word was also used in the same contemptuous and prejudicial sense. It was not till the nineteenth century that a revived interest in the Middle Ages at large led to a revived interest in the latest, largest, and most numerous cathedrals, and a distinctive name was then required for their style. This was obtained by confining the word already in use to the one period and coining new ones for the earlier styles.

This history of the word is therefore a history of the causes which led to the overthrow of the style, and also of the causes which have recently led to its revival and to the modern study of its ancient monuments.

The present paragraph has taken into account the news and information from the work "Gothic period" by Andrew Henry Robert Martindale [1].

## **1.2. Gothic period : three different phases**

Three successive phases of Gothic architecture can be distinguished, respectively called Early, High, and late Gothic.

### *1.2.1. Early Gothic*

This first phase of the Gothic style's inception from 1120-50 to about 1200. The combination of all the aforementioned structural elements into a coherent style first occurred in the Île-de-France (the region around Paris), where prosperous urban populations had sufficient wealth to build the great cathedrals that epitomize the Gothic style. The earliest surviving Gothic building was the abbey of Saint-Denis in Paris, begun in about 1140. Structures with similarly precise vaulting and chains of windows along the perimeter were soon begun with Notre-Dame de Paris (begun 1163) and Laon Cathedral (begun 1165). By this time it had become fashionable to treat the interior columns and ribs as if each was composed of a bunch of more slender parallel members. A series of four discrete horizontal levels or stories in the cathedral's interior were developed, beginning with a ground-level arcade, over which ran one or two galleries (tribune, triforium), over which in turn ran an upper, windowed story called a clerestory. The columns and arches used to support these different elevations contributed to the severe and powerfully repetitive geometry of the interior. Window tracery (decorative rib-work subdividing a window opening) was also gradually developed, along with the use of stained (colored) glass in the windows. The typical French early Gothic cathedral terminated at its eastern end in a semicircular projection called an apse. The western end was much more impressive, being a wide facade articulated by numerous windows and pointed arches, having monumental doorways, and being topped by two huge towers. The long sides of the cathedral's exterior presented a baffling and tangled array of piers and flying buttresses. The basic form of Gothic architecture eventually spread throughout Europe to Germany, Italy, England, Spain, and Portugal.

### *1.2.2. High Gothic*

The second phase of Gothic architecture began with a subdivision of the style known as Rayonnant (1200-1280 AD) on the Continent and as the Decorated Gothic (1300-75 AD) style in England. This style was characterized by the application of increasingly elaborate geometrical decoration to the structural forms that had been established during the preceding century.

During the period of the Rayonnant style a significant change took place in Gothic architecture. Until about 1250, Gothic architects concentrated on the harmonious

distribution of masses of masonry and, particularly in France, on the technical problems of achieving great height; after that date, they became more concerned with the creation of rich visual effects through decoration. This decoration took such forms as pinnacles (upright members, often spired, that capped piers, buttresses, or other exterior elements), moldings, and, especially, window tracery. The most characteristic and finest achievement of the Rayonnant style is the great circular rose window adorning the west facades of large French cathedrals; the typically radial patterns of the tracery inspired the designation Rayonnant for the new style. Another typical feature of Rayonnant architecture is the thinning of vertical supporting members, the enlargement of windows, and the combination of the triforium gallery and the clerestory until walls are largely undifferentiated screens of tracery, mullions (vertical bars of tracery dividing windows into sections), and glass. Stained glass--formerly deeply colored became lighter in colour to increase the visibility of tracery silhouettes and to let more light into the interior. The most notable examples of the Rayonnant style are the cathedrals of Reims, Amiens, Bourges, Chartres, and Beauvais.

The parallel Decorated Gothic style came into being in England with the general use of elaborate stone window tracery. Supplanting the small, slender, pointed lancet windows of the early English Gothic style were windows of great width and height, divided by mullions into two to eight brightly coloured main subdivisions, each of which was further divided by tracery. At first, this tracery was based on the trefoil and quatrefoil, the arch, and the circle, all of which were combined to form netlike patterns. Later, tracery was based on the ogee, or S-shaped curve, which creates flowing, flame like forms. Some of the most outstanding monuments of the Decorated Gothic style are sections of the cloister (c. 1245-69) of Westminster Abbey; the east end, or Angel Choir, of Lincoln Cathedral (begun 1256); and the nave and west front of York Minster (c. 1260-1320). In France the Rayonnant style evolved about 1280 into an even more decorative phase called the Flamboyant style, which lasted until about 1500. In England a development known as the Perpendicular style lasted from about 1375 to 1500. The most conspicuous feature of the Flamboyant Gothic style is the dominance in stone window tracery of a flame like S-shaped curve.

### 1.2.3. *Late Gothic*

During the 15th century much of the most elaborate architectural experiment took place in southern Germany and Austria. German masons specialized in vault designs and, in order to get the largest possible expanse of ceiling space, they built mainly hall churches (a type that had been popular throughout the 14th century). Important hall churches exist at Landshut (St. Martin's and the Spitalkirche, c. 1400), and Munich (Church of Our Lady, 1468-88). The vault patterns are created out of predominantly straight lines. Toward the end of the 15th century, however, this kind of design gave way to curvilinear patterns set in two distinct layers. The new style developed particularly in the eastern areas of Europe: at Annaberg (St. Anne's, begun 1499) and Kuttendorf (St. Barbara's, 1512). Such virtuosity had no rival elsewhere in Europe. Nevertheless, other areas developed distinctive characteristics. The Perpendicular style is a phase of late Gothic unique to England. Its characteristic feature is the fan vault, which seems to have begun as an interesting extension of the Rayonnant idea in the cloisters of Gloucester cathedral (begun 1337), where tracery panels were inserted into the vault. Another major monument is the nave of Canterbury cathedral, which was begun in the late 1370s, but the style continued to evolve. Some of the best late Gothic achievements are bell towers, such as the crossing tower of Canterbury cathedral (c. 1500). In France the local style of late Gothic is usually called Flamboyant, from the flame-like shapes often assumed by the tracery. The style did not significantly increase the range of architectural opportunities. Late Gothic vaults, for instance, are not normally very elaborate, but the development of window tracery continued and, with it, the development of elaborate facades. France also produced a number of striking 16th-century towers.

The most notable feature of the great churches of Spain is the persistence of the influence of Bourges and the preference for giant interior arcades. This is still clear in one of the last of the large Gothic churches to be built, the New Cathedral of Salamanca (begun 1510). By this time, Spanish architects were already developing their own intricate forms of vaulting with curvilinear patterns. There was a final flowering of Gothic architecture in Portugal under King Manuel the Fortunate (1495-1521). The fantastic nature of much late Gothic Iberian architecture has won for it the name Plateresque, meaning that it is like silversmith's work. The decorative elements used were extremely heterogeneous, and Arabic or Mudéjar forms emanating from the south were popular. Ultimately, during the 16th century, antique elements were added,

facilitating the development of a Renaissance style. These curious hybrid effects were transplanted to the New World , where they appear in the earliest European architecture in Central America .

All the previous information about the gothic period have been taken from the work “Gothic period 2” by Andrew Henry Robert Martindale (Professor of Visual Arts, University of East Anglia, Norwich, England, 1974–95).

### **1.3. Gothic structures : architectural description**

For the Gothic period the cathedrals were almost as much civic buildings as they were churches, and in the sense that they embodied the pride, the ambition, and the rivalries of the cities, this was eminently the case. But they were also actually used for town meetings, for public festivals, and for theatrical exhibitions. In the Middle Ages the church and the cathedral were always open, like the Catholic churches of our own day. Here the poor man was the equal of the rich. The beggar and his lord met on terms of equality in the liberty of using the building and in the theory of its religious teachings. There were no pews for favored owners. The cathedral was the palace of the poor, and its entire space outside the sanctuary was open to their daily visits and sojourn at will, without disturbance.

The cathedral was the museum of art; a museum made, not to display the ostentation of the rich or the luxury of his life, but to teach by pictures and reliefs the history of the world as then known and comprehended by the traditions of the church, and the lessons of faith and of sacrifice. Here were, moreover, the actual memorials and relics of past ages ; for here was the treasury not only of the art of the present but also of the art of the past. Finally, the cathedral was the sanctuary of the famous and illustrious dead. Their tombs were its decoration and its pride.

This popular significance and these popular uses hold for the cathedrals of all periods, consequently for the Byzantine and Romanesque as well as the Gothic periods. But the Byzantine cathedrals were more largely the erections of the clergy, the Romanesque cathedrals were largely the erections of the Germanic emperors or of the great religious orders, while the Gothic cathedrals were especially the buildings of the municipalities. The union in these buildings of the arts of stained glass, of fresco ornament and sculptured stone decoration, of panel pictures, of metal work in the

altars, shrines, and chandeliers, and of wood carving in the seats of the clergy, is to be constantly kept in mind. The pulpits were also objects of special artistic splendor.

The mathematical, geometrical, and statical science requisite for their construction is the best authority for the high civilization of their time. Their architects were moreover not, like the current ones, educated apart from the artisans and masons and sculptors who were their servants.

The architect of the cathedral was the master-mason, a fact of supreme importance for the perfection of these buildings, for the understanding of their subtle art, and for the comprehension of the changed conditions in our own time which make it impossible for us to rival them.

It is possible to take into account the interior arrangement of the Gothic churches in order to describe the gothic architecture philosophy. In all of them the solid masonry of the ceiling must be especially considered. In some of them the skeleton framework of the ribbings are the main lines of support for the ceiling. A point which cannot be well illustrated in photographs, and which can with difficulty be observed in the buildings when the ceiling is viewed from the floor, is the manner in which the spaces between the ribs are slightly arched in such a way as to make the ribs the actual supports of the ceiling. These in their turn transmit the pressure to the piers.

The piers of the Gothic clerical structures have a lighter and more slender construction than those of the Romanesque. The latter were sometimes of plain square section or were square and beveled at the corners, or were sometimes massive and clumsy round supports. With other Romanesque piers are found small pilasters leading up to the ribs above and connected with them.

In the Gothic the piers are generally treated as a cluster of slender ribs, each rising to its own definite and special functions. Effects of a massive or clumsy appearance are avoided. A strictly logical and strictly economical use of materials and forces is apparent. Round piers are not unknown to the Gothic, but they are not generally found in highly developed or characteristic examples of the style. In the use of the pointed arch there is the appearance of an aspiring tendency and of a sentiment for altitude. This is enhanced by the treatment of the pier, which multiplies, both by lights and by shadows, the rising lines which tend to enhance the effect of height. The same sentiment is visible in the actually enormous altitudes of the cathedrals. These effects of altitude are also exaggerated by a relative narrowness of nave and aisles. The general result is to dwarf the spectator and his immediate surroundings.

It was not only actual dimension but the effect of dimension which was sought for and attained. Disproportionately high apartments and those which surprise the eye by an effect of height are known to have this effect of dwarfing, in appearance, the persons in them.

For the matter of the Gothic windows we should logically be speaking of the interiors for whose service they are made, but exterior views may illustrate them more visibly as being taken from the sides of the buildings rather than down the length of nave or aisles. In developed examples almost the whole wall surface, aside from the facades, is given up to the windows. The infinitely varied designs of their delicate stone ribbings are a beautiful feature of the Gothic.

The delight in the colour effects of the stained glass window pictures is undoubtedly one explanation of their dimensions and number, but it should be added that throughout the developed and later Gothic, there is an obvious effort to dispense as far as possible with blank walls, or solid masonry surfaces. It is on this account that in developed and later Gothic, as far as the masonry appears, it is treated in filigree. Broken up as regards effect of bare surface by the expansion over the wall surfaces of a tracery system borrowed originally from the designs of the windows.

So far all the main aspects of the gothic architecture have been considered, but another aspect must be discussed in order to understand better the importance of Gothic style, namely, the stability of the building. When we remember that these tremendous vaultings of the interior have been raised high in air over walls which on the sides of the building at least are conspicuous for their flimsy appearance and large window openings, it is evident that the buttress architecture of the exterior was a serious and necessary feature and not designed for ornament or to please the eye, but the absolute and sole condition of the existence of the building.

In the old cathedrals the *flying buttress* was a necessary consequence of the higher elevation of the nave as compared with the lower elevation of the side aisles. The buttress was frequently surmounted by a pinnacle, always, in fact, when the flying buttress was used, or by a statue surmounted by a canopy. The pinnacle added an additional weight to the resisting power. It also emphasized the rising lines of the building and its effects of altitude.

An ornament which is very common in the middle Gothic and later Gothic of the continent, but less common in England, is the gable-shaped skeleton masonry form which appears over portals or window.



In the Gothic cathedral we still find the plan and essential arrangements of the basilica. The choir, which frequently occupies more than a third of the church area, is the development of the apse. The arrangement of the nave and aisles was also derived from the basilica. Although there are local instances in which the aisles rise to the height of the nave, all the great cathedrals inherited the higher nave elevation.

Architecture was the most important and original art form during the Gothic period. The principal structural characteristics of Gothic architecture arose out of medieval masons' efforts to solve the problems associated with supporting heavy masonry ceiling vaults over wide spans. The problem was that the heavy stonework of the traditional arched barrel vault and the groin vault exerted a tremendous downward and outward pressure that tended to push the walls upon which the vault rested outward, thus collapsing them. A building's vertical supporting walls thus had to be made extremely thick and heavy in order to contain the barrel vault's outward thrust.

Medieval masons solved this difficult problem about 1120 with a number of brilliant innovations. First and foremost they developed a ribbed vault, in which arching and intersecting stone ribs support a vaulted ceiling surface that is composed of mere thin stone panels. This greatly reduced the weight (and thus the outward thrust) of the ceiling vault, and since the vault's weight was now carried at discrete points (the ribs) rather than along a continuous wall edge, separate widely spaced vertical piers to support the ribs could replace the continuous thick walls. The round arches of the barrel vault were replaced by pointed (Gothic) arches which distributed thrust in more directions downward from the topmost point of the arch.

Since the combination of ribs and piers relieved the intervening vertical wall spaces of their supportive function, these walls could be built thinner and could even be opened up with large windows or other glazing. A crucial point was that the outward thrust of the ribbed ceiling vaults was carried across the outside walls of the nave, first to an attached outer buttress and then to a freestanding pier by means of a half arch known as a flying buttress. The flying buttress leaned against the upper exterior of the nave (thus counteracting the vault's outward thrust), crossed over the low side aisles of the nave, and terminated in the freestanding buttress pier, which ultimately absorbed the ceiling vault's thrust.

These elements enabled Gothic masons to build much larger and taller buildings than their Romanesque predecessors and to give their structures more complicated ground plans. The skillful use of flying buttresses made it possible to build extremely

tall, thin-walled buildings whose interior structural system of columnar piers and ribs reinforced an impression of soaring verticality.

#### **1.4. Catalan gothic structures : architectural description**

Gothic architecture is not merely about ornamentation. The Gothic style brought innovative new construction techniques that allowed churches and other buildings to reach great heights. One important innovation was the use of pointed arches. Earlier Romanesque churches had pointed arches, but builders did not capitalize on the shape. During the Gothic era, builders discovered that pointed arches would give structures amazing strength and stability.

In gothic buildings, the weight of the roof was supported by the arches rather than the wall. This meant that walls could be thinner. Earlier Romanesque churches relied on barrel vaulting. Gothic builders introduced the dramatic technique of ribbed vaulting.

While barrel vaulting carried weight on continuous solid walls, ribbed vaulting used columns to support the weight. The ribs also delineated the vaults and gave a sense of unity to the structure.

In order to prevent the outward collapse of the arches, Gothic architects began using a revolutionary *flying buttress system*. Freestanding brick or stone supports were attached to the exterior walls by an arch or a half-arch.

Since the walls themselves were no longer the primary supports, Gothic buildings could include large areas of glass. Huge stained glass windows and a profusion of smaller windows created the effect of lightness and space.

Cathedrals in the High Gothic style became increasingly elaborate. Over several centuries, builders added towers, pinnacles, and hundreds of sculptures.

In addition to religious figures, many Gothic cathedrals are heavily ornamented with strange, leering creatures. These gargoyles are not merely decorative. Originally, the sculptures were waterspouts to protect the foundation from rain. In the late 1700s, architects decided that gargoyles and other lavish sculptures were tasteless.

New techniques of construction permitted buildings to soar to amazing new heights, dwarfing anyone who stepped inside. Moreover, the concept of divine light was suggested by the airy quality of Gothic buildings, which were much lighter than churches in the earlier Romanesque style.

The distinctive characteristic of Spanish Gothic cathedrals is their spacial complexity, with many areas of different shapes leading from each other. They are comparatively short and wide, and are often completely surrounded by chapels. Like English Cathedrals, Spanish Cathedrals are stylistically diverse. This expresses itself in the addition of chapels and in the application of decorative details drawn from different sources. Among the influences on both decoration and form are Islamic architecture, and towards the end of the period, Renaissance details combined with the Gothic in a distinctive manner.

The roofline often has pierced parapets with comparatively few pinnacles. There are often towers and domes of a great variety of shapes and structural invention rising above the roof.

The basic plan was realized considering a single space in which large span can be seen. In fact, an example of large span in transversal direction is Girona Cathedral, in which it can reach a value around 22 m; while in longitudinal direction, Santa Maria del Mar Church can be taken as an example considering the span around 13 m. In general the vaults have been built using square geometry as it is possible to see in Santa Maria del Mar in Barcelona. In this church, and in other ecclesiastic Gothic structures, the lateral vaults are almost as high as the central one, taking the rule of the flying arches. There is an exception in Mallorca Cathedral, in which the lateral vaults are located in a much lower position compared with the central one and for this reason, the flying arches have an important structural role.

Connected to the structural solution before mentioned it is possible to highlight other architectural solutions as slender piers and a structural lightness.

## **1.5. Description of Gothic Churches object of study**

### *1.5.1. Santa Maria del Pi*

The church of S. Maria del Pi was built between 1319-1320 and 1391. Its pure Gothic style is evident in the single nave, almost devoid of ornaments. The middle of the main façade boasts a large rose window of 10 meters in diameter, very much in keeping with the church's Gothic style. In 1940, the rose window was entirely rebuilt after being destroyed by fire in 1936.

The tympanum or the main door is divided by two small columns, making the little chapels, the one in the middle holding the statue of the Virgin. Above this statue hang the parish and city coats-of-arms. At the end of the base of the tympanum are two pinecones which, together with the pine tree on the coat-of-arms, testify the name of the church. The side façade shows the buttresses which support the arches and vaults of the nave. In the middle of this façade is the Ave Maria doorway which still conserves some elements from the Romanesque portico of the previous church. The rear façade shows the buttresses and large windows of the apse. It, too, conserves an old doorway, dating back to 1578, which permitted access to the place of worship from the rear. Over the centuries, other buildings round about have hidden part of the church's original walls. The work of the architect Bartomeu Mas, its construction was begun in 1379 and completed around 1461. It is octagonal in structure and measures 54 m. high with the walls at the base 3,55 m wide.

It contains six bells. "Antònia" is the largest, with a diameter of 1,40 m and weighing 1806 kg, and "Andreua" the oldest, dating from 1669. The high altar consists of an alabaster table, designed by the architect Joaquim de Ros i de Ramis. It was inaugurated in 1967. The cimborium has been installed at the back of the presbytery, where there was originally an entrance door to the church. The statue in the presbytery represents Santa Maria del Pi. It is 3,30 m. high and was sculpted by Enric Monjo in 1973.

The choir-stalls were designed by Josep Mas i Dordal, were replaced in 1868 by a neogothic version. When these were destroyed by fire, the Baroque-style ones were reintroduced in 1986. The original Stained Glass Windows have not been preserved. The oldest ones still remaining date back to 1718 and of these, one portraying The Adoration of the Magi (over the Avemaria doorway), was crafted by Antoni Viladomat.

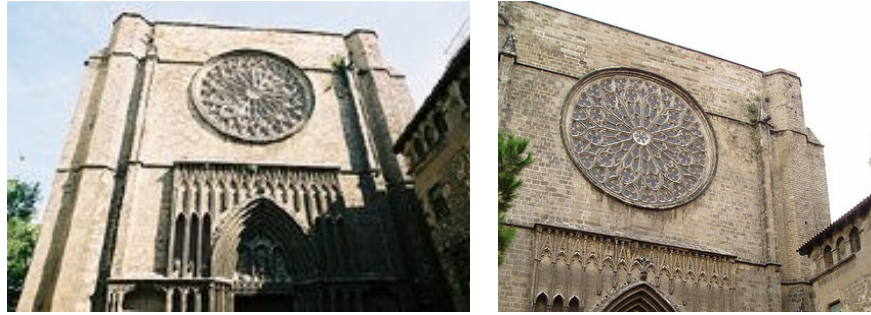


**Figure 1.5.1-A :** Principal façade of S. Maria del Pi church

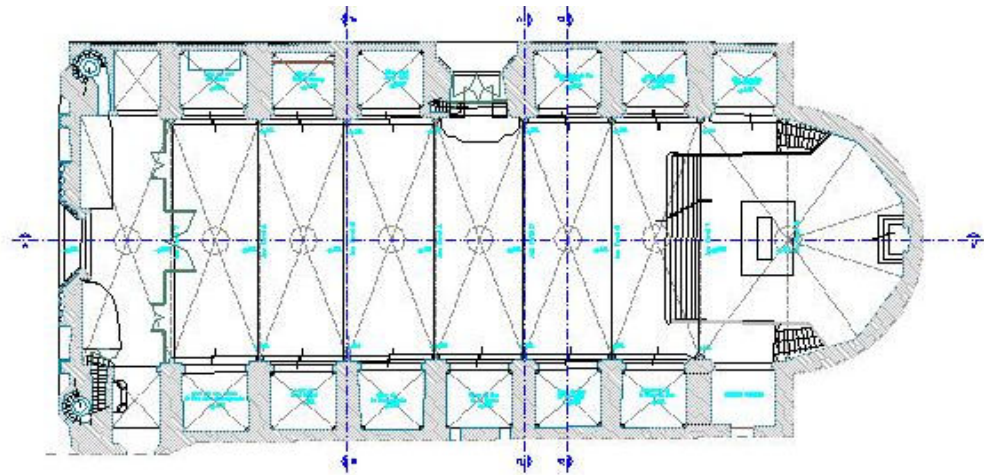


**Figure 1.5.1-B :** Plan representation of S. Maria del Pi church

### *1.5.2. Santa Maria del mar*

The most sweepingly symmetrical and classical of all Barcelona's churches, Santa Maria del Mar is a stunning contrast to the ornate and complex architecture of later Gothic and Moderniste Barcelona. Built in a record 54 years (1329-83), the church was a stonemason's bare-bones design for a classical basilica. Santa Maria del Mar was intended to bless and protect the mighty Catalan fleet at a time when Catalonia so controlled the Mediterranean. Fishermen, merchant marines, stevedores, and all other seafarers were included under the patronage of Santa Maria del Mar (St. Mary of the Sea).

The best and most beautiful existing example of early Catalan (or Mediterranean) Gothic architecture, Santa Maria del Mar is extraordinary for its unbroken lines, simplicity of form, symmetry, and elegance. The upsweeping verticality and lightness of the interior are especially surprising considering the blocky exterior surfaces. Built by a mere stonemason named Berenguer de Montagut, who chose and fitted each stone hauled down from the same Montjuïc quarry that provided the sandstone for the 4th-century Roman walls, Santa Maria del Mar is breathtakingly, nearly hypnotically, symmetrical. The 16 octagonal pillars are 1,55 meters in diameter and spread out into rib vaulting arches at a height of 16 meters. The painted keystones at the apex of the arches are 32 meters from the floor. Furthermore, the central nave is twice as wide as the lateral naves, whose width equals the difference between their height and that of the main nave. The result of all this proportional balance and harmony is a tonic sense of uplift that, especially in Modernist Barcelona, is at once exhilarating and soothing. The basilica, filled with immense and ornate side chapels and mammoth wooden choir stalls, burned for 11 days and crumbled as a result of the intense heat. Restored after the end of the Spanish civil war by a series of Bauhaus-trained architects, all of whom understood the formal purity of the original design, Santa Maria del Mar has become one of the city's most universally admired architectural gems. The 34 lateral chapels are dedicated to different saints and images. The first chapel to the left of the altar is the Capella del Santo Cristo (Chapel of the Holy Christ), its stained-glass window an allegory of Barcelona's 1992 Olympic Games, complete with names of medalists and key personalities of the day in tiny letters. An engraved stone riser to the left of the side door onto Carrer Sombrerers commemorates the spot where San Ignacio de Loyola, founder of the Jesuit Order, begged for alms in 1524 and 1525. The basilica's stark beauty is enhanced by a lovely southwest-facing rose window (built in 1425 and restored in 1485 after an earthquake) and unusually wide vaulting. Often compared to the German *Hallenkirche*, or single-naved church, the basilica is often used for choral events and early music.



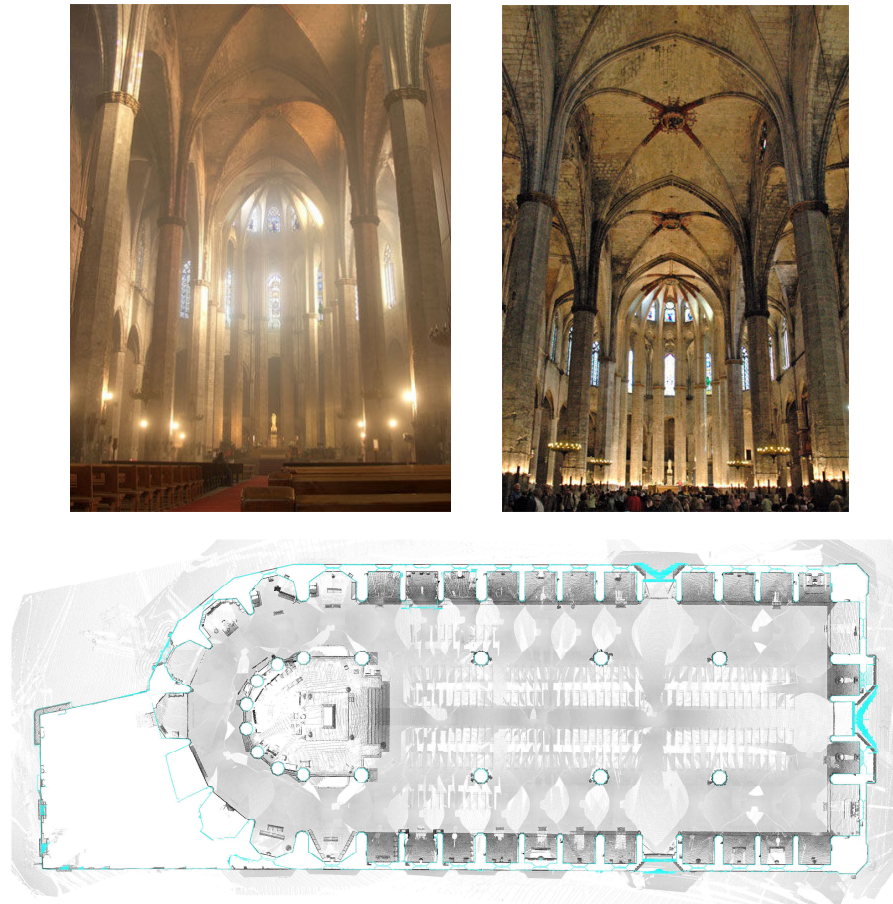


**Figure 1.5.2-A :** Interior view and plan of S. Maria del Mar Church

### *1.5.3. Mallorca Cathedral*

Made from golden limestone from the Santanyi quarries and designed in the Gothic style, the cathedral is 121 meters long and 55 meters wide. The main body of the church is set in the middle of a mass of pillars and spires, behind which lies the strong buttress reinforced with a double row of flying arches. The bell tower, still unfinished today, is 52 meters high with three ogive-arched stories. It holds nine bells, the most famous of which is the N'Eloi: 2 meters in diameter, it weighs more than 5.700 kilos. The main facade, which overlooks the Almudaina Palace, was dismantled by the 1851 earthquake and was later completely rebuilt as a new façade with the exception of the Renaissance-era door by M. Verger which miraculously emerged unscathed.

The port-side facade features another door, a true masterpiece of Spanish Gothic. It is called the "Mirador portal", or "Puerta del Mar", and is the collective work of such celebrated artists as Pedro de Moret and Juan de Valenciennes, among others. The most important of all these artists is Guillermo Sagrera, who concentrated the refined nuance of his art-work into the two statues of Saint Peter and Saint Paul that flank the portal. It features three naves resting on 44 meters tall octagonal pillars, eight chapels each side of the nave, and lacks both transept and ambulatory. The rear interior reveals the majestic "Royal Chapel", which is nearly as large as a church in its own right: 25 meters long and 16 meters wide.

Behind the main altar it is possible to see 110 breathtaking walnut choir-stalls sculpted in flaming Gothic style and, to left, a noteworthy "Renaissance pulpit". On a slightly higher level at the back of the choir-stalls, the "Chapel of the Holy Trinity" reveals the ancient tribune of the kings of Majorca and a sort of present-day pantheon for the same.



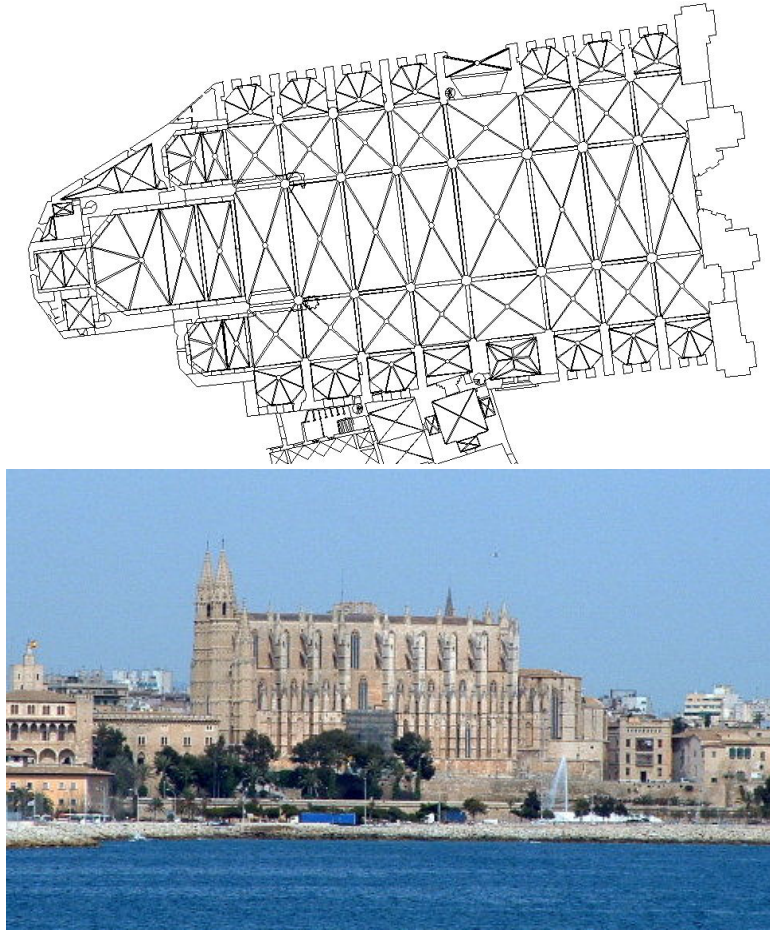


**Figure 1.5.3-A:** External and plan view of Mallorca Cathedra

## **1.6. Past study on the Churches**

A lot of information can be taken from several study realized by different authors. In fact, it is possible to find a lot of paper in which the main topic is the seismic behaviour of the churches object of the present dissertation work.

A very important help to understand the ecclesiastic structures before mentioned in terms of geometrical characteristics and structural conditions, come from the following texts:

- 1) *Curvas de capacidad para edificios monumentales: la Iglesia Santa Maria del Mar de Barcelona* by Irizarry, Podestà, Resemini, 2003 [2];
- 2) *Studies on the structure of Gothic Cathedral* by Pere Roca, 2001 [3];
- 3) *Vulnerabilidad sismica para edificios historicos de obra de fabrica de mediana y gran luz* by Guillermo Martinez Ruiz (Phd thesis, 2007) [4].

Other papers can be researched, but the previous mentioned works have given a significant contribution to develop the present study

*References*

- [1] A.H.R.Martindale, 1990 (Professor of Visual Arts, University of East Anglia, Norwich, England, 1974–95). “*Gothic Period*” .
- [2] J. Irizarry, S. Podestà, S. Resemini, 2005. “*Curvas de capacidad para edificios monumentales: la iglesias Santa Maria del Mar de Barcellona*” II Congreso Nacional de Ingeniería Sísmica, Spagna.
- [3] Pere Roca, 2003.”*Studies on the structures of gothic Cathedral*”. Historical Constructions (P.B. Lourenço, P.Roca (Eds.), Pages 71-90.
- [4] G.Martinez Ruiz, 2007. “*Vulnerabilidad sísmica para edificios historicos de obra de fabrica de mediana y gran luz*”. Phd thesis at UPC – Universitat Politecnica de Catalunya Barcelona (ES).

## 2. SAFETY EVALUATION OF THE CHURCHES

### 2.1. Knowledge of the structures

In order to have a good seismic safety evaluation of the structures and compute a better intervention to solve the construction's problem, it is necessary to know the structures themselves.

Understanding the structural schemes of the buildings is very important for the existing constructions, and it is much more interesting when the safety of the churches or monuments have to be taken into account. It is possible to have a lot of problem for a good understanding of the historical structures due to:

- Structural modifications during the time;
- Possible damage due to anthropic activities;
- Ageing of the material;

Furthermore, a complete experimental campaign cannot be carried out because it is too much invasive on the structure itself.

The correct evaluation of the structure and the interpretation of the available indications are very important in order to have qualitative and quantitative information about the construction.

## 2.2. Seismic behaviour in historical constructions

The masonry historical constructions are very different each other in terms of construction's techniques and typologies and for that reason the seismic safety evaluation is subjected to several unknown parameters and conditions.

Moreover the masonry historical constructions were built without taking into account the horizontal action due to earthquakes and, even more, the basic principal of material and structural behaviour were not applied.

The monuments were built applying experimental indications acquired from previous constructions and based on the rigid blocks equilibrium. Even though the before mentioned method is not very scientific and accurate, checking if the constructions respect the general rule of construction can be considered the main important thing and the first step to compute the seismic safety level.

Another thing to take into account is the "history testing" due to different actions acting on the structures during their life and the study of the effects produced by the natural events. But also in this case it is possible to have an important condition that can change the general interpretation of the phenomenon before said. In fact, the damages occurred on the structures due to the low intensity of past earthquakes or other natural events can lead to strength reduction of the structures.

The behavior of the structures is influenced by the seismic risk level of the zone where the construction was built. In fact, in some zone in which the seismic risk is very high, a lot of effectiveness constructive solutions have been studied by expert technicians in order to reduce the seismic vulnerability of the monuments. Thus, chains, buttresses and scaring can be used and become an important rule for well done structure especially in some regions where the earthquakes occur frequently. On the other hand, these techniques are just used to repair the existing structures damaged by significant earthquakes where these natural events are not so common.

At the end, it is possible to state that the study of all those parameters are very important and interesting in order to compute the seismic safety of the constructions, but they must be established through a deep and hard work.

Moreover the technicians cannot do a correct evaluation of the structures taking into account only the parameters and indications before said, but it is necessary a structural model using a simplify method or much more complex computations.

### 2.3. Seismic behaviour of churches or other large span structures

The damages of churches after several earthquakes occurred in Italy from 1976 to 2004 have been studied by an Italian committee (*Lagomarsino*, [1]).

These studies highlighted that the seismic behaviour of the different kinds of structures can be analyzed resolving the whole construction in smaller portions, named macro-elements, because of their autonomous seismic behaviour. All the possible macro-elements for churches and historical building have been reported in the ANNEX A of this work and are involved in the Italian design rule “*Linee guida per la valutazione e la riduzione del rischio sismico del patrimonio culturale con riferimento alle norme tecniche (in Italian)*”[2].

In this simplified model, as in the more complex models, the thrusts of arches, domes and roofing systems have to be taken into account in order to identify the capacity curve of the structures.

All the macro-elements become the references to check the structural conditions performing static analyses, linear and non linear, modelling the structures using the finite element method.

From the point of view of the structural safety evaluation, the kinematics limit analyses, linear or non linear, appears much more effective.

Moreover the assumptions, in order to have an idea about the mechanisms that may occur on the constructions, are well known because of the deep and accurate knowledge on the damages of the buildings object of the study.

### 2.4. Limit analysis and Capacity Spectrum Method (CSM)

The limit analyses can describe the ultimate condition of the structure but cannot allow to know the damage limit states. The modern formulation of limit analysis has been done by Heyman-a [3] and can be reported in the following:

- 1) Lower-bound theorem: The structure is safe, meaning that the collapse will not occur, if a statically admissible state of equilibrium can be found;

- 2) Upper-bound theorem: If a kinematically admissible mechanism can be found, for which the work developed by external forces is positive or zero, then the structure will collapse.

It is possible to consider two different kind of limit analysis studying the collapse conditions of the monuments (Heyman-b [4]):

- *Static theorem*: it is necessary to analyse the equilibrium conditions of the structures under particular load patterns, even if it does not allow to reach the exact solution;
- *Cinematic theorem*: the structure has to be divided in rigid blocks, and gives to the technicians important information about the ultimate sources of the structures.

The cinematic theorem will be used in the next chapters in order to analyse the structures object of the present work, so that it is possible to have an idea about the seismic safety of the fore mentioned constructions, using approximate procedures. The capacity curve describes the state of the structure under gradually increasing seismic actions, or under increasing displacements, until reaching the ultimate condition (collapse of the construction).

In order to check the response of the structure, the increase of the displacement can be identified as an approximation of the dynamic problem into an equivalent static problem. It is possible to obtain the capacity curve of the macro-elements of the structure considering three different analyses:

- Finite element analysis: in this case the model of the macro-element is necessary in order to apply on it a gradual increase of displacement, according to the first vibration mode.
- Limit analysis, using the static approximation and the application of uniqueness theorem: it is necessary to study the structure in order to evaluate the thrust line corresponding to the ultimate condition (formation of mechanisms). In this case, the points in which the thrust line is tangent to the boundary of the structure define the plastic hinge positions.
- Limit analysis, using the cinematic approximation: in this case it is possible to identify a decreasing curve that relates the forces with the

imposed displacement of the structure, using the principal of virtual work.

The static approximation of limit analysis could be used in order to evaluate the plastic hinge positions to take into account when the cinematic approximation of limit analysis will be applied. The limit analysis is based on three main hypotheses in the following reported:

- No-tensile strength of masonry;
- Unlimited compressive strength;
- No sliding between the rigid blocks.

Under these conditions the limit theorem of limit analysis, based on plasticity theory, is applicable on masonry structures.

## 2.5. Capacity Spectrum Method for evaluation the safety of the monuments

The capacity curve can describe the global behaviour of the structure only in case of particular monumental typology and for that reason, it is necessary to apply the method on parts of the constructions. In fact, the first step for application of capacity spectrum method on monuments consist to identify the damages and the collapses of parts of the building, namely macro-elements, and compute the capacity curves related to these structural blocks.

Thus, it is necessary to study the plastic hinges and sliding planes position in order to evaluate the collapse mechanisms of the selected macro-element of the structure. The macro-elements have to be loaded with vertical and horizontal forces. The latter are proportional to the vertical load through the coefficient  $\alpha$ . Considering the three main hypotheses for application of cinematic approximation of limit analysis and using the principal of virtual work (1), it is possible to evaluate the coefficient  $\alpha_0$  corresponding to the lose of the macro-element equilibrium.

$$\alpha_0 \left( \sum_{i=1}^n P_i \delta_{x,i} + \sum_{j=n+1}^{n+m} P_j \delta_{x,j} \right) - \sum_{i=1}^n P_i \delta_{y,i} - \sum_{h=1}^0 F_h \delta_h = L_{fi} \quad (1)$$



Where,  $n$  is the total number of the dead load applied to the different rigid blocks,  $m$  is the number of weight forces not directly acting on the blocks, but whose masses, due to the effect of the seismic action, generate horizontal forces,  $o$  is the number of external forces applied to the blocks but not related to the masses,  $P_i$  is the generic weight force,  $P_j$  is the generic weight force not directly applied on the blocks,  $\delta_{x,i}$  is the virtual horizontal displacement for  $P_i$ ,  $\delta_{x,j}$  is the virtual horizontal displacement for  $P_j$ ,  $\delta_{y,i}$  is the virtual vertical displacement for  $P_i$ ,  $F_h$  is the generic external force applied on the block,  $\delta_h$  is the virtual displacement for  $F_h$  and  $L_{fi}$  is the work done by the internal forces.

It is necessary to develop the curve until reaching the value of the coefficient  $\alpha$  equal to zero,  $d_{k0}$ , increasing the displacements up to the collapse mechanism occurs. In fact, it is possible to state that the lose of the equilibrium does not correspond to the ultimate condition of the structure, because of its capacity to support several horizontal actions even after the mechanism activation. In order to represent the capacity curve, an incremental cinematic analysis can be carried out considering different configurations and taking into account the displacement's increment of a selected control point  $k$ , named  $d_k$ . Changing the configurations, it is possible to obtain the coefficient  $\alpha_i$  using the general formulation written before obtained by the principal of virtual work.

The increment of displacement lead to a decrease of the stabilizing moment and thus, the capacity curve is represented by a gradual decrease of linear function, described through the expression (2):

$$\alpha = \alpha_o \cdot \left( 1 - \frac{d_k}{d_{k,o}} \right) \quad (2)$$

The capacity spectrum method requires the transformation to a single degree of freedom (SDOF system) of the capacity curve in order to compare it with the demand curve using the same scale. In fact, it is necessary to find a capacity curve of the equivalent oscillator by means of the relation between the spectral acceleration and the displacements, namely  $a^*$  and  $d^*$ . The participation mass of the cinematic mechanism  $M^*$ , may be defined using the formulation (3):

$$M^* = \frac{\left( \sum_{i=1}^{n+m} P_i \cdot \delta_{x,i} \right)^2}{g \cdot \sum_{i=1}^{n+m} P_i \cdot \delta_{x,i}^2} \quad (3)$$

Where  $n+m$  is the number of applied forces  $P_i$  whose masses generate horizontal forces due to the seismic action,  $\delta_{xi}$  is the virtual horizontal displacement of the point of application of  $P_i$  forces. The formulation (4) gives the seismic spectral acceleration  $\alpha_o^*$  related to the coefficient  $\alpha_o$ , the gravity acceleration  $g$  and the fraction of the participating mass of the mechanism  $e^*$ :

$$a_0^* = \frac{\alpha_0 \cdot \sum_{i=1}^{n+m} P_i}{M^*} = \frac{\alpha_0 \cdot g}{e^*} \quad (4)$$

$$e^* = \frac{g \cdot M^*}{\sum_{i=1}^{n+m} P_i} \quad (5)$$

The spectral displacement can be obtained using the formulation (6):

$$d^* = d_k \cdot \frac{\sum_{i=1}^{n+m} P_i \cdot \delta_{x,i}}{\delta_{x,k} \cdot \sum_{i=1}^{n+m} P_i} \quad (6)$$

Where  $n$ ,  $m$ ,  $P_i$ ,  $\delta_{xi}$  have been defined in the previous formulation and  $\delta_{x,k}$  is the virtual horizontal displacement of the chosen reference point  $k$ . In this case, the capacity curve has the formulation (7), similar to the formulation (2) established before:

$$a^* = a_o^* \cdot \left( 1 - d^* / d_o^* \right) \quad (7)$$

where  $d_o^*$  is the spectral displacement of the equivalent system related to the displacement  $d_{ko}$ .

Taking into account the out-of-plane collapse mechanism, especially for the upper part of the structural macro-elements, the procedures before described do not consider the influence of the whole structure because the lower parts of the elements are not involved in the mechanism. The Spanish design code allow to consider the entire structural macro-element dividing it in different masses and computing its vibration modes applying the following formulas:

$$\Phi_{ik} = \text{sen} \left[ \frac{(2i-1) \cdot \pi \cdot h_k}{2H} \right] \quad (8)$$

$$\eta_{ik} = \Phi_{ik} \frac{\sum_{k=1}^n m_k \cdot \Phi_{ik}}{\sum_{k=1}^n m_k \cdot \Phi_{ik}^2} \quad (9)$$

Where  $i$  is the masses number used to divided the whole macro-element,  $h_k$  is the floor height,  $H$  is the macro-element total height,  $m_k$  is the associated mass and  $\Phi_{ik}$  is the vibration mode associated to the selected mass.

Adopting the formula (9) the seismic reduction parameter has been obtained for each mass and it was applied in order to reduce the structural capacity curve by using the expressions reported below:

$$\eta_{tot,i} = \sqrt{\sum_{i=1}^n (\eta_{i,n})^2} \quad (10)$$

$$\alpha_\eta = \frac{\alpha_o}{\eta_{tot,i}} \quad (11)$$

The structure verification is based on two points in the following listed:

- *Damage limit state*: from the spectral acceleration  $a_o^*$  related to the activation of the mechanisms;

- *Ultimate limit state*: the collapse can be assumed equal to 40% of the displacement  $d_{k0}$ , as it is possible to state from experimental dynamic testing carried out by some authors (Doherty [4], Restrepo-Velez and Magenes [5]).

The elastic branch of the capacity curve should be taken into account in order to have all the information about the mechanism chosen for each macro-element of the structure. It is necessary to know three parameters:

- $a_y$ : acceleration corresponding to the yielding condition;
- $d_y$ : displacement corresponding to the  $a_y$  acceleration;
- $T_s^*$ : secant period, namely represent the inclination of the elastic branch of the capacity curve.

The *Annex 11.C of Ordinance PCM 3431/2005* (Italian design rules) [6] establishes that the displacement  $d_y$  can be evaluated considering it equal to 40% of the ultimate displacement  $d_u^*$ , as shown in the formulation (12):

$$d_y = 0,40 \cdot d_u^* \quad (12)$$

Using the Formulation (7), in which  $d^*$  is substituted by  $d_y$ , it is possible to obtain the acceleration  $a_y$  corresponding to the yielding condition.

The secant period will be obtained applying the formulation (13):

$$T_s = 2\pi \sqrt{\frac{d_y}{a_y}} \quad (13)$$

The Figure reported below is taken as an example in order to explain all the value obtained using the procedure listed in this paragraph:

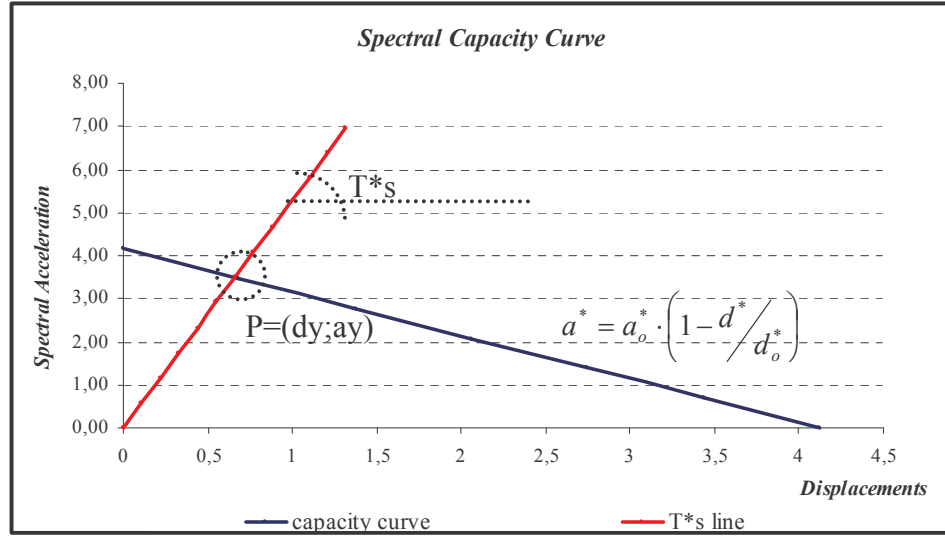


**Figure 2.5.1:** Representation of all the parameters evaluated to know the capacity curve

The T\*s line represents the elastic branch of the capacity curve (blue line). P is the elastic limit, in which the behaviour changes from elastic to inelastic and it is characterized by two values, horizontal coordinate ( $d_y$ , elastic displacement) and vertical coordinate ( $a_y$ , acceleration corresponding to the elastic limit).

## 2.6. Evaluation of the seismic demand of the structures according to the European design rule – Eurocode 8 [7].

Catalonia region is not prone to heavy earthquakes like other European sites. In fact, taking into account that the peak ground acceleration (PGA) in Barcelona is equal to 0.04 g, it is possible to state that, this value chosen to identify the seismic action on the structure, is much lower than PGA computed for other parts of the world.

The EuroCode 8 establishes all the parameters that have to be taken into account in order to evaluate the seismic action acting on the structures located in particular areas of the state. One of the most important parameters is the soil effect that can increase the ground motion acceleration based on soil mechanical properties.

The following studies have been carried out considering the worst soil mechanical properties as shown in some papers consulted in order to have a better idea about the ground. Choosing the fore mentioned value it is also possible to have maximum amplification of the seismic effect. The applied method is based on the evaluation of the elastic response spectrum for a given earthquake.

The European design rule gives three different soil typology named A, B, and C. The type B represent the soil with the worst mechanical properties that lead to a maximum amplification of the seismic actions. In the following graph is depicted the difference in terms of spectral acceleration due to the different soil typology considering the following parameters and relations:

	S	$\beta_0$	$K_1$	$K_2$	$T_B$	$T_C$	$T_D$	$a_g = a \cdot g$
A	1	2.5	1	2	0.1	0.4	3	0.3924
B	1	2.5	1	2	0.15	0.6	3	0.3924
C	0.9	2.5	1	2	0.2	0.8	3	0.3924

**Table 2.6.1:** Values adopted by the EC8 to compute the spectral acceleration

$$0 \leq T \leq T_B : S_e(T) = a_g \cdot S \cdot \left[ 1 + \frac{T}{T_B} \cdot (\eta \cdot 2.5 - 1) \right]$$

$$T_B \leq T \leq T_C : S_e(T) = a_g \cdot S \cdot \eta \cdot 2.5$$

$$T_C \leq T \leq T_D : S_e(T) = a_g \cdot S \cdot \eta \cdot 2.5 \cdot \left[ \frac{T_C}{T} \right]$$

$$T_D \leq T \leq 4s : S_e(T) = a_g \cdot S \cdot \eta \cdot 2.5 \cdot \left[ \frac{T_C \cdot T_D}{T^2} \right]$$

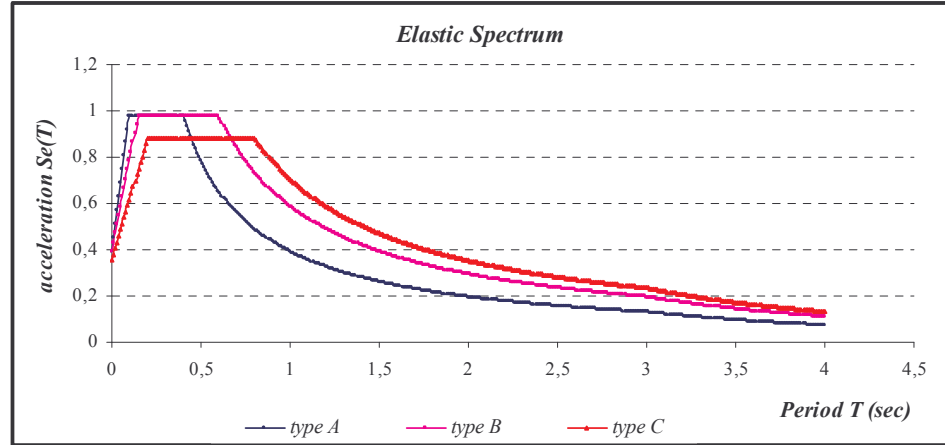


**Figure 2.6.1:** Representation of the elastic spectrum for each soil type using  $PGA=0.04g$

In order to compute the demand curve for a given structure under seismic action, the evaluation of ADSR (*Acceleration-Displacement Response Spectra*) graph is necessary.

The fore mentioned graph has the spectral acceleration on the vertical axis and the spectral displacement on the horizontal axis.

The spectral displacement can be related to the spectral acceleration using the formulation (14):

$$S_d = \frac{T^2}{4 \cdot \pi^2} \cdot S_{ae} \quad (14)$$

Considering the parameters before listed and the soil type B, the ADSR graph is modelled and assume the following shape:

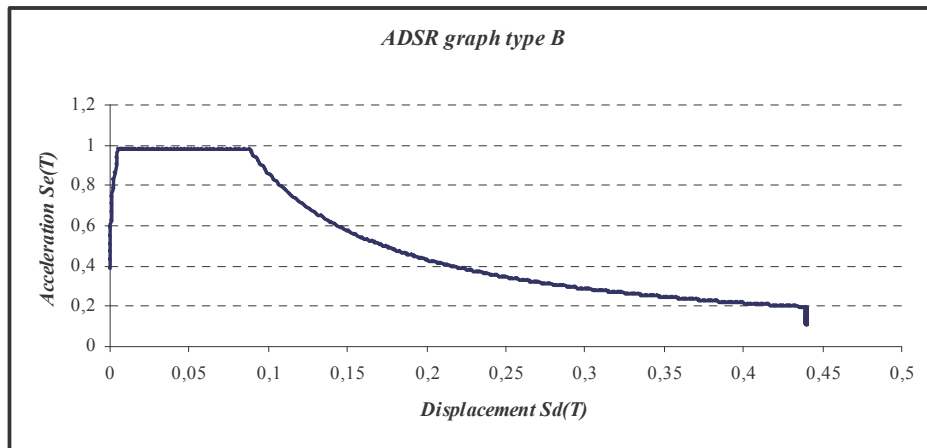


**Figure 2.6.2:** Representation of the ADNR graph considering the soil type B using  $PGA=0.04g$

The before depicted graphs, obtained using the EuroCode 8 [7], can be used for two of the three total analysed churches.

In fact, taking into account the *Martinez's phd-thesis* [8] it is possible to state that Mallorca cathedral presents a different value of PGA. Compared with Santa Maria del Mar and Santa Maria del Pi, it is slightly higher and equal to 0.06g. For that reason, using the same parameters listed in the **Table 2.6.1**, but considering a PGA value as above reported, it is possible to depict the following elastic response spectrum and ADNR graph used only for Mallorca Cathedral calculations.

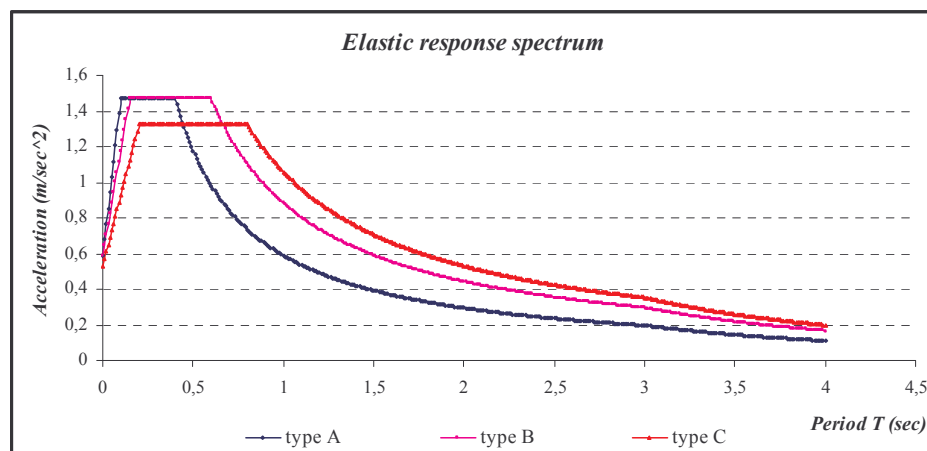


**Figure 2.6.3:** Representation of the elastic spectrum for each soil type using  $PGA=0.06g$



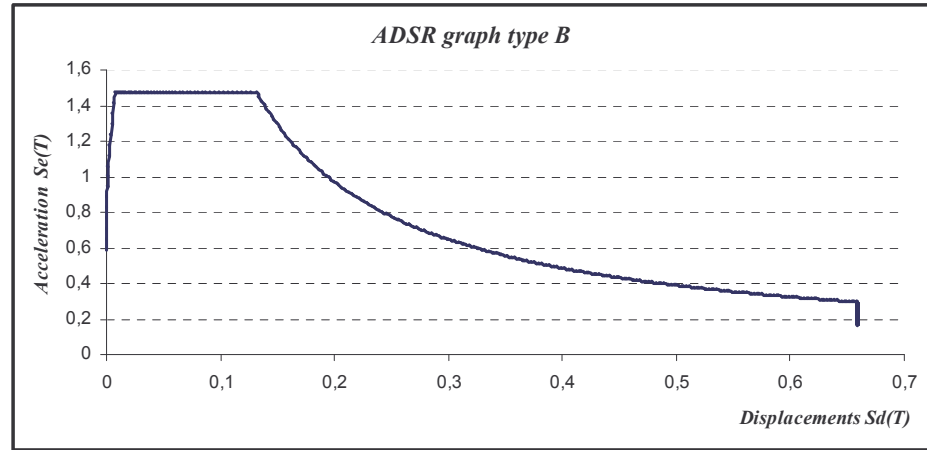


**Figure 2.6.4:** Representation of the ADSR graph considering the soil type B using  $PGA=0.06g$

## 2.7. Evaluation of the demand of the structures under seismic actions according to the Spanish design rule – NCSE-02 [9].

As it has been said in the previous paragraphs, the Fajfar method [10] will be discussed in order to compute the safety of the structure under seismic actions in according to the European and Spanish design rules.

The European design rules (EC8) have already been introduced and in the followings rows the evaluation of the demand curve according to the Spanish rule will be computed.

The formulations used in order to calculate the spectral acceleration are reported in the following:

$$\begin{aligned}
 T \leq T_A : a(T) &= 1 + 1.5 \cdot \frac{T}{T_A} \\
 T_A \leq T \leq T_B : a(T) &= 2.5 \\
 T \geq T_B : a(T) &= K \cdot \frac{C}{T}
 \end{aligned}$$

where all the values are depicted in the table below and an acceleration of  $0.04g$  has been used. The same ground mechanical properties established in the EC8 have been considered in order to have a possible comparison between the two design rules.

	$a_b = a \cdot g$	$\rho$	C	S	$a_c$	$T_A$	$T_B$
A	0.392	1.3	2	1.6	0.816	0.2	0.8

**Table 2.7.1:** Values adopted by the NCSE-02 to compute the spectral acceleration

The shape of the response spectrum is described in the next **Figure 2.7.1**:

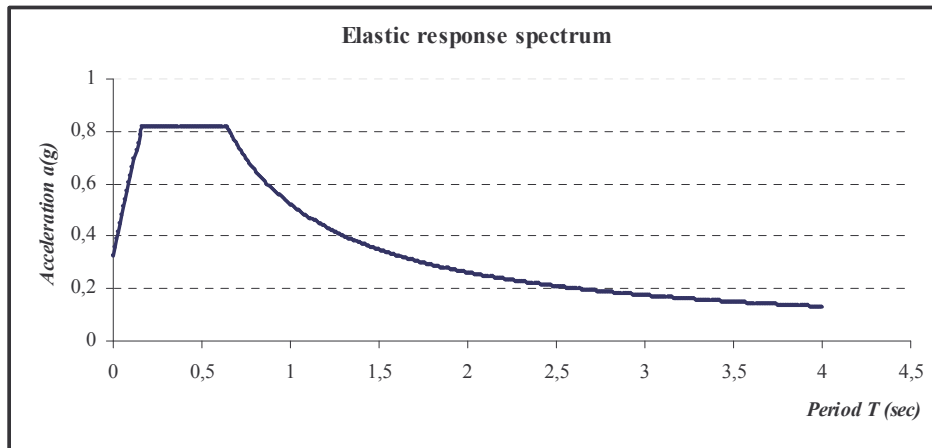


**Figure 2.7.1:** Spectral acceleration graph in according to the NCSE-02 using  $PGA=0.04g$

It is possible to relate the spectral accelerations to the spectral displacements in order to depict the ADSR graph, using the formulation introduced before.

The ADSR graph obtained is the following:

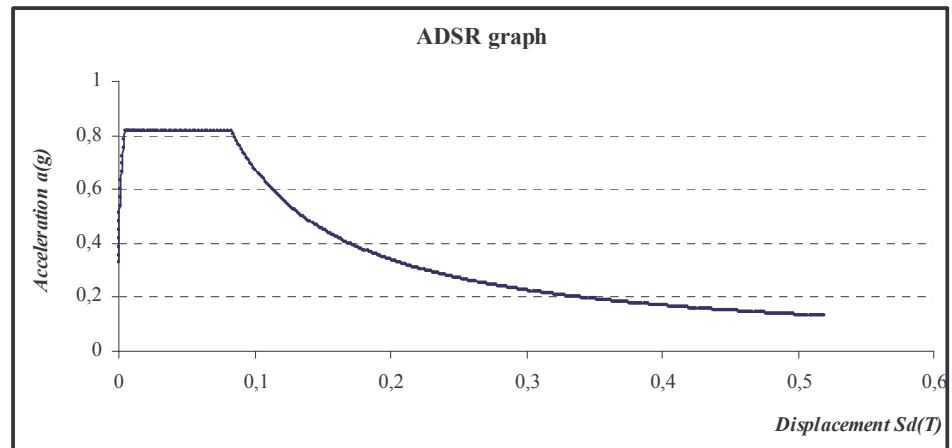


**Figure 2.7.2:** ADSR graph in according to the NCSE-02 using PGA=0.04g

Also in this case, a different PGA for Mallorca Cathedral has to be considered and, namely, taking it equal to 0.06g. For that reason, using the same parameters listed in the **Table 2.7.1**, but considering a PGA value as above reported, it is possible to depict the following elastic response spectrum and ADSR graph used only for Mallorca Cathedral calculations.

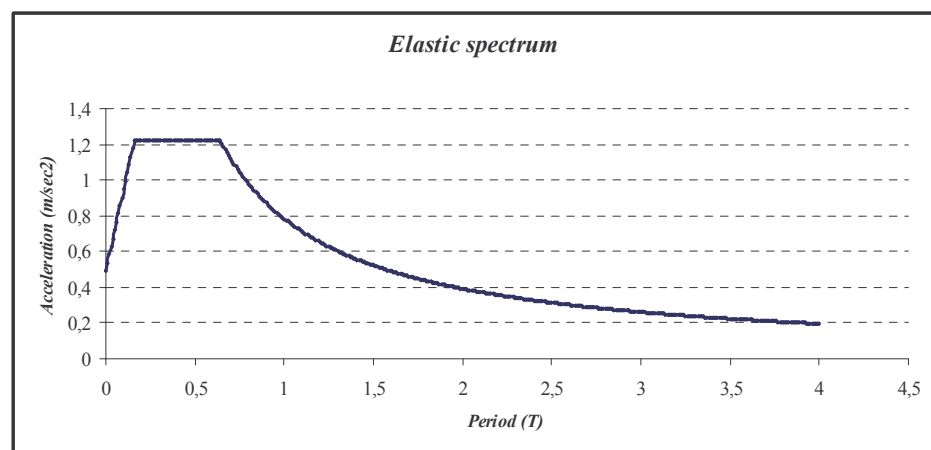


**Figure 2.7.3:** Spectral acceleration graph in according to the NCSE-02 using PGA=0.06g

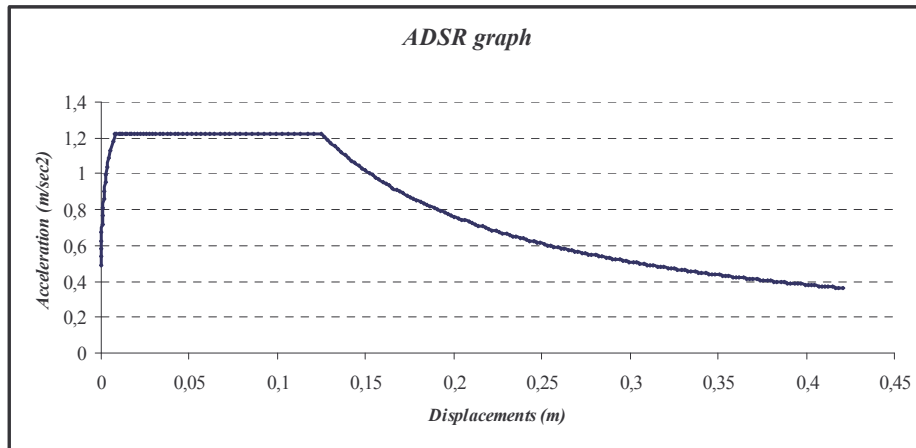


Figure 2.7.4: ADSR graph in according to the NCSE-02 using  $\text{PGA}=0.06\text{g}$

## 2.8. Comparison between the response spectrum and ADSR graphs previously described

The two graphs have been put in the same charter to get easier the comparison and highlight the differences in terms of spectral accelerations and ADSR graphs.

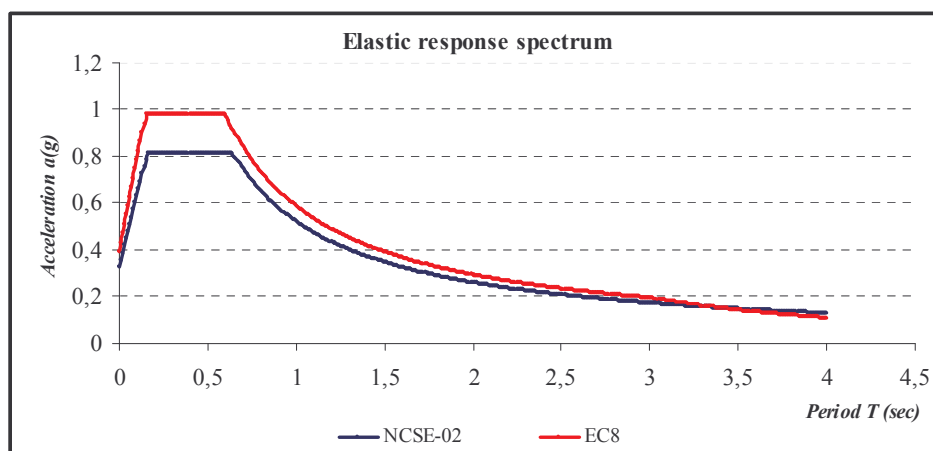
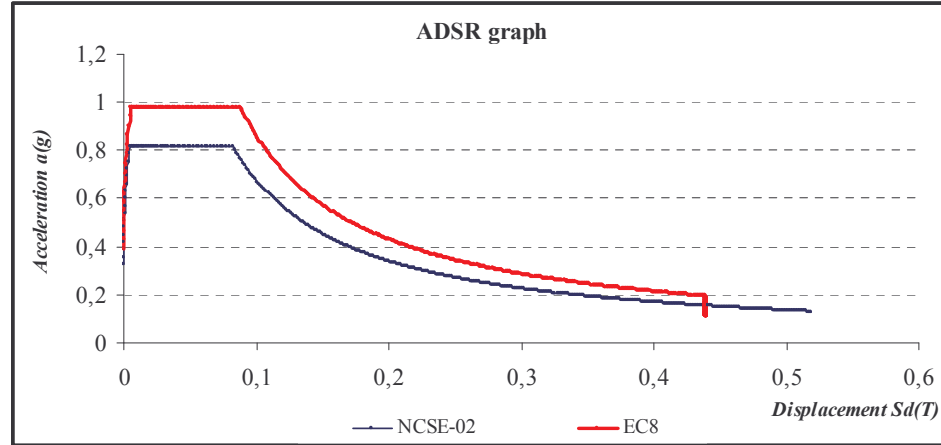


Figure 2.8.1: Comparison between the Spectral acceleration graphs using the EC8 and NCSE-02 using  $\text{PGA}=0.04\text{g}$



**Figure 2.8.2:** Comparison between the ADSR graphs using the EC8 and NCSE-02 using the PGA=0.04g

In both cases it is possible to see the higher values reached using the European code EC8 in terms of spectral acceleration.

In fact, pay attention on the first graph it is clear the following condition:

$$S_a(T) = 0.981 \frac{m}{sec^2} [EC8] \Rightarrow S_a(T) = 0.816 \frac{m}{sec^2} [NCSE - 02]$$

Taking into account the results achieve in the second graph, the lower pseudo-displacement computed using EC8 is underlined.

In the following graphs the differences between the elastic response spectrum and the ADSR graphs obtained using a PGA=0.06g are depicted.

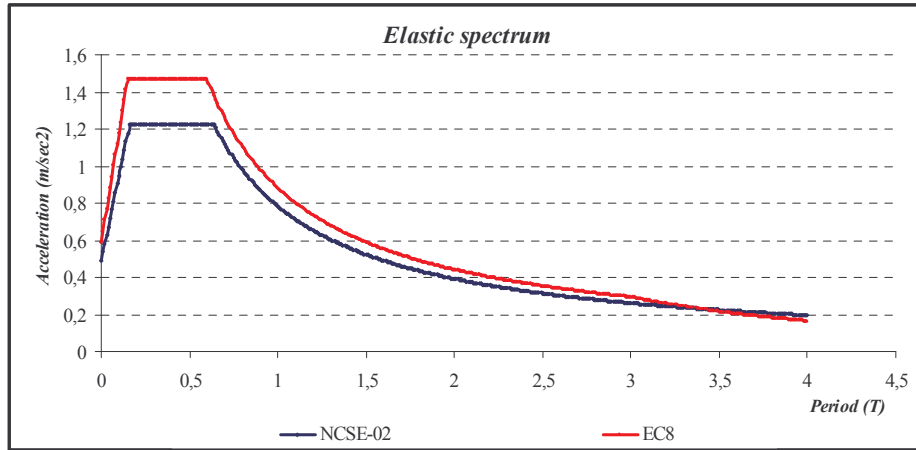


**Figure 2.8.3:** Comparison between the Spectral acceleration graphs using the EC8 and NCSE-02 using  $PGA=0.06g$

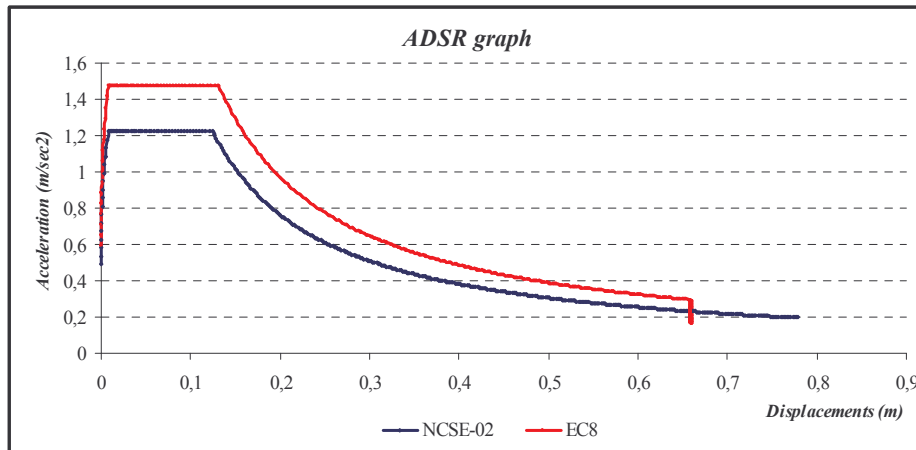


**Figure 2.8.4:** Comparison between the ADSR graphs using the EC8 and NCSE-02 using the  $PGA=0.06g$

In both cases it is possible to see the higher values reached using the European code EC8 in terms of spectral acceleration. In fact, pay attention on the first graph it is clear the following condition:

$$S_a(T) = 1.47 \frac{m}{sec^2} [EC8] \Rightarrow S_a(T) = 1.22 \frac{m}{sec^2} [NCSE - 02]$$

## 2.9. Fajfar method (Capacity Spectrum Method based on inelastic demand spectra) [10]

The dissipative capacity of a structure is represented by the global structural ductility  $\mu$ , called ductility factor.

The ductility factor is defined by the ratio between the ultimate displacement,  $u_u$ , and the limit elastic displacement  $u_y$ , as it is possible to show in the formulation (15):

$$\mu = \frac{u_u}{u_y} \quad (15)$$

The global ductility of a structure gives to the designers an important parameter to identify the capacity of dissipation of the energy due to its inelastic deformation.

The real behaviour of the structures under seismic action is inelastic because of the irreversible degradation phenomenon and the load-unload cycles on the structures due to the earthquakes.

The non linear dynamic analysis should be performed in order to take into account the non linear structural characteristics in terms of material and geometry. The global structural ductility can be evaluated knowing the capacity curve of the structure. The latter curve determines the structural response considering vertical and horizontal forces applied on the structures up to the ultimate condition (collapse). The curve is obtained considering the force-displacement evolution (taking into account one controlled point) step by step.

An example of capacity curve of a structure is reported in the picture below:

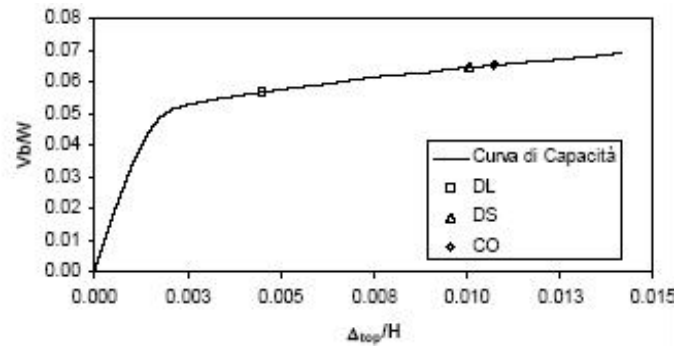


Figure 2.9.1: An example of capacity curve for a structure

The capacity curve is influenced by other parameters as vertical loads, application of the loads, external conditions, material viscosity etc, and for all the reasons said before, the collapse mechanism does not occur when the first plastic hinge appear. The real behaviour does not introduce a suddenly stiffness variation, but a gradual decrease. Apart from the behaviour factor  $q$ , that is possible to evaluated accurately for new structures, the inelastic properties of the ancient buildings can be taken into account applying the ductility factor  $\mu$ . In the previous paragraph, the ADSR graphs have been introduced taking into account two design rules, Eurocode 8 and NCSE-02 (Spanish seismic code).

In both cases only the viscous damping equal to 5% has been considered, but in order to consider the real behaviour of the structures under seismic action, another parameter have to be introduced to take into account the load-unload earthquakes cycles and to consider the hysteretic energy dissipation.

It is possible to use the formulation (16) proposed by Vidic [11] slightly modified by Miranda and Bertero [12] in their works.

$$\begin{aligned} R_\mu &= (\mu - 1) \cdot \frac{T}{T_0} + 1 & \text{if } T \leq T_0 \\ R_\mu &= \mu & \text{if } T \geq T_0 \end{aligned} \quad (16)$$

Where  $\mu$  is the ductility factor defined as the ultimate displacement and yield displacement ratio and  $R_\mu$  is the reduction factor due to the ductility.

$T_0$  has been chosen equal to  $T_c$ , where the constant acceleration of the response spectrum passes to the constant velocity of the spectrum. Moreover, when  $R_\mu$  and  $\mu$  are computed, the formulations (17) have been introduced in order to relate the acceleration spectrum  $S_a$  and displacement spectrum  $S_d$ , for the inelastic SDOF system with a bilinear force-displacement relation.

$$\begin{aligned} S_a &= \frac{S_{ae}}{R_\mu} \\ S_a &= \frac{\mu}{R_\mu} \cdot S_{de} = \frac{\mu}{R_\mu} \cdot \frac{T^2}{4 \cdot \pi^2} \cdot S_{ae} = \mu \cdot \frac{T^2}{4 \cdot \pi^2} \cdot S_a \end{aligned} \quad (17)$$

it is possible to distinguish two different structural cases :



- The procedure taking into account the hysteretic energy dissipation can be applied when the intersection point between the spectral capacity curve and ADSR graph is located on the inelastic branch of the spectral capacity curve (**Figure 2.9.2-A**);
- when the intersection point is located on the elastic branch of the spectral capacity curve, the hysteretic energy dissipation cannot be taken into account (**Figure 2.9.2-B**). The performance point is the horizontal coordinate of the intersection point before mentioned.

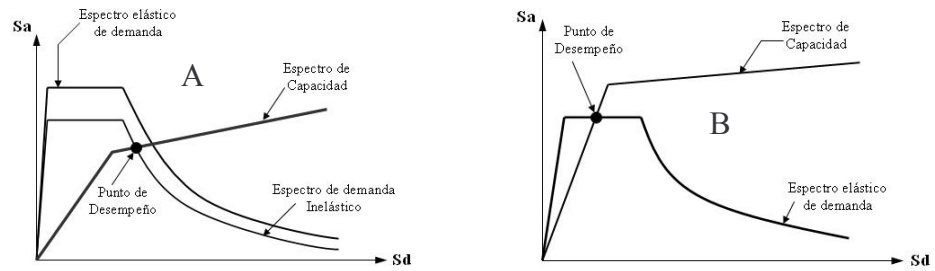


**Figure 2.9.2:** A – intersection point in the inelastic branch of spectral capacity curve; B- intersection point in the elastic branch of spectral capacity curve.

In the calculations reported in the next chapter, the hysteretic energy dissipation is always assumed. It is possible to apply the following step in order to take into account the inelatic properties of the structure:

- Evaluation of the reduction factor  $R_\mu$  as a ratio between the acceleration corresponding to the intersection point between the elastic period and the elastic response spectrum, and the yield acceleration, using the following relation:

$$R_\mu = \frac{a_s^*}{a_y}$$

- Check the value of the elastic period compared with the fundamental period  $T_c$

- i.  $T_s^* > T_c \rightarrow R_\mu = \mu$
  - ii.  $T_s^* \leq T_c \rightarrow R_\mu = (\mu - 1) \frac{T}{T_c} + 1$
- c) The value of  $R_\mu$  is known from the point a) and it is possible to know the value of the ductility factor from the point b), using the inverse formulation:
- i.  $T_s^* > T_c \rightarrow R_\mu = \mu$
  - ii.  $T_s^* \leq T_c \rightarrow R_\mu = (\mu - 1) \frac{T}{T_c} + 1 \rightarrow \mu = (R_\mu - 1) \frac{T_c}{T} + 1$
- d) Evaluation of displacement demand using all the point before listed :
- i.  $T_s^* > T_c \rightarrow R_\mu = \mu \rightarrow S_d = S_{de}$
  - ii.  $T_s^* \leq T \rightarrow R_\mu = (\mu - 1) \frac{T}{T_c} + 1 \rightarrow \mu = (R_\mu - 1) \frac{T_c}{T} + 1 \rightarrow S_d = \frac{\mu}{R_\mu} S_{de}$

The value of the spectral displacement evaluated using the previous formulation will be compared with the ultimate displacement of the structure in order to assess its safety. Moreover, the same value can be used to establish the level of the damage according to Lagomarsino's assumption. When the spectral capacity curve is known, it is possible to identify four different regions that represent the level of the damage and are evaluated using the formulation reported below.

Lagomarsino established five different levels of the damage that is possible to have on the structure and are reported in the following **Table 2.9.1** and **Table 2.9.2**.

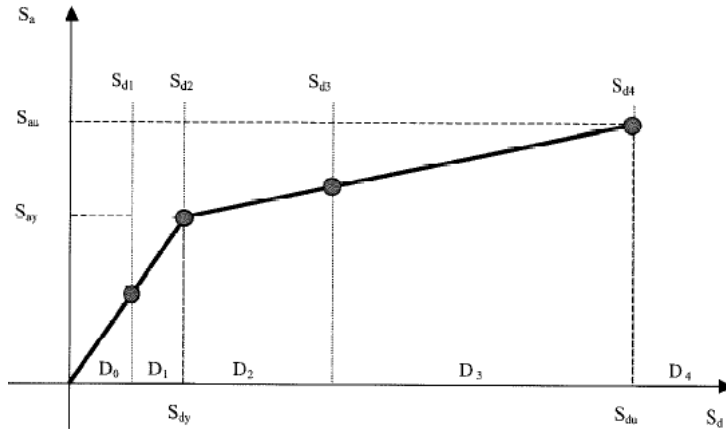


**Figure 2.9.3:** Different level of damages

<i>label of damages</i>	<i>spectral displacements</i>
D0	$S_d \leq 0.7 S_{dy}$
D1	$0.7 S_{dy} \leq S_d \leq S_{dy}$
D2	$S_{dy} \leq S_d \leq 0.25 S_{du}$
D3	$0.25 S_{du} \leq S_d \leq 0.5 S_{du}$
D4	$S_d > 0.5 S_{du}$

**Table 2.9.1:** Level of damages and its formulations

The method can be applied comparing the  $S_d$  value fore mentioned with the level  $D_i$  above defined.

<i>label of damages</i>	<i>damages description</i>
D0	no damage
D1	lightly damage
D2	moderate damage
D3	extensive and severe damage
D4	complitely damage or collapse

**Table 2.9.2:** Level of damages and its descriptions

Using this method it is possible to be aware about the damages that can occur on the selected macro-element when seismic actions are applied on the structure.

The procedure fore mentioned will be applied for both the design rule, EuroCode 8 and NCSE-02, in order to make a final comparison among the obtained results.

## References

- [1] Lagomarsino, S., Podestà, S. Resemini, S., 2004. *“Observational and mechanical models for the vulnerability assessment of monumental buildings”*, Proc. of the 13<sup>th</sup> World Conference on Earthquake Engineering, Vancouver BC, Canada.
- [2] OPCM 3431, 2005. *“Italian guide line for evaluation and reduction of the seismic risk of the cultural heritage (2006).”*
- [3] J. Heyman, 1966. *“The stone skeleton”*. International Journal Solids Structures, Vol.2, Pages 249-279.
- [4] J. Heyman, 1969. *“The safety of masonry arches”*. International Journal Mechanics Sciences, Vol.11, Pages 363-385.
- [5] K.Doherty, M.C.Griffith, N.Lam, J.Wilson, 2002. *“Displacement-based seismic analysis for out-of-plane bending of unreinforced masonry walls”*. Earthquake Engineering and Structural Dynamics, Vol.31, Pages 833-850.
- [6] L.F.Restrepo-Vélez, G.Magenes, 2004. *“A mechanics-based procedure for the seismic risk assessment of masonry buildings at urban scale”*. Proceedings of the XI Convegno Nazionale ANIDIS, Genova.
- [7] UNI EN 1998 Eurocode 8, *“Design provisions for earthquake resistance of structures - Part 1: general rules, seismic actions and rules for buildings”*.
- [8] NCSE-02, 2002. *“Norma de construccion sismorresistente: parte general y edificación”*, Real decreto 997/2002 del Ministerio de obra publicas,

transportes y medio ambiente

- [10] P.Fajfar – 1999. “*Capacity Spectrum Method based on inelastic demand spectra*”. Earthquake Engineering & Structural Dynamics, Vol. 28 – Issue 9, Pages 979-993.
  
- [11] T.Vidic, P.Fajfar, M.Fischinger, 1994. “*Consistent inelastic design spectra: strength and displacement*”. Earthquake Engineering and Structural Dynamics, Vol.23:507-21.
  
- [12] E.Miranda, VV.Bertero, 1994. “*Evaluation of strength reduction factor for earthquake-resistence design*”. Earthquake Spectra, Vol.10:357-79.

### 3. CSM RESULTS OBTAINED BY USING EC8 AND NCSE-02 DESIGN CODES

In the previous chapter, the Capacity Spectrum Method (C.S.M.) has been introduced and all the steps and formulations have been described in order to have clear the meaning of this simplify analysis of the structures.

In the present chapter the results obtained using the C.S.M. were reported for all the structures object of study taking into account the EuroCode 8 [1] and NCSE-02 [2] design codes.

The structures was divided into macro-elements and for each of them, the computation method has been applied. The steps reported in the following were used in order to obtain the results by using the CSM applied on the structures aforementioned:

- 1) Using the seismic code (Eurocode 8 and NCSE-02), it is possible to obtain the demand curve;
- 2) Select the macro-elements and obtain the capacity curve using the procedure already introduced (Chapter 2 of the present research work);
- 3) Convert the capacity curve in order to compare it with the demand curve computed at point 1);
- 4) Find the intersection point (performance point) between the functions defined by demand displacement (the horizontal coordinate) and spectral acceleration (vertical coordinate);
- 5) Compare the capacity displacement with demand displacement (safety factor);

- 6) Apply the Lagomarsino assumption (Lagomarsino [3]) in order to estimate the possible level of damage of the constructions under seismic actions.

In the following, the main results for each selected mechanisms were reported. The whole procedures and computations for the overturning of the principal façade of Santa Maria del Pi Church and for in-plane mechanism of the triumphal arch of Santa Maria del Mar Church were submitted in the ANNEX B.

Another approach was computed in order to take into account the whole principal façade that may influence the structural behaviour of the upper part of the aforementioned macro-element. This approach was based on the first three vibration mode of the studied macro-element that led to change the obtained capacity curve. In the following only the principal results were listed, while the whole procedure and calculations were reported in the ANNEX B.

### 3.1. Santa Maria del Pi

All the considered mechanisms were described in the **Table 3.1.1** in which the name of mechanism and a brief description are reported.

mechanism	typology	description of mechanisms
1	total tower	<i>out of plane rotation of the whole tower</i>
2	upper tower	<i>out of plane rotation of the upper part of the tower</i>
3	upper facade (no r.w.)	<i>out of plane rotation of the upper part of the principal façade</i>
3 mode	upper facade (no r.w.)	<i>out of plane rotation of the upper part of the principal façade</i>
4	upper facade (with r.w.)	<i>out of plane rotation of the upper part of the principal façade</i>
4 mode	upper facade (with r.w.)	<i>out of plane rotation of the upper part of the principal façade</i>
5	whole facade	<i>out of plane rotation of the whole principal façade</i>
6	transept	<i>in plane motion of the transept under trasversal horizontal load</i>
7	in-plane upper facade	<i>in plane motion of the upper part of the principal façade</i>
8	in-plane whole facade	<i>in plane motion of the whole principal façade</i>
9	apse 1	<i>out of plane rotation of one part of the apse</i>
10	apse 2	<i>out of plane rotation of one part of the apse</i>
11	apse 3	<i>out of plane rotation of one part of the apse</i>
12	apse 4	<i>out of plane rotation of one part of the apse</i>

**Table 3.1.1:** All the mechanisms studied on the S.Maria del Pi church

Mechanism 1: tower rotation

In the **Figure 3.1.1** the out-of-plane mechanism of the whole tower has been represented, taking into account a rotation point on the base of the structure.

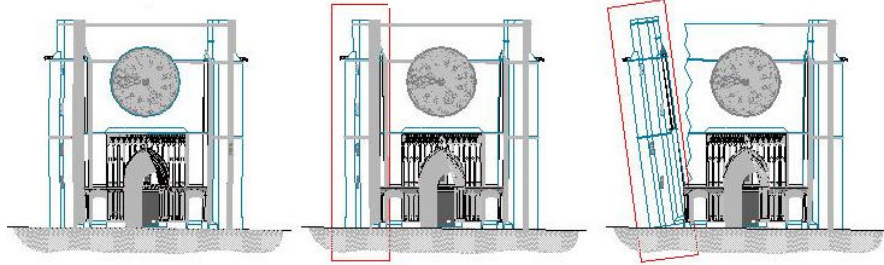


**Figure 3.1.1:** Mechanism 1 studied on the S.Maria del Pi church

$\alpha_0$	$d_u$ (m)	$d_d$ (m)	$S.F. = d_u / d_d$	$D_i$ (level of damage)
0,204	1,143	0.164	6,97	Do

**Table 3.1.2:** Main obtained results by using EC8 provisions

$\alpha_0$	$d_u$ (m)	$d_d$ (m)	$S.F. = d_u / d_d$	$D_i$ (level of damage)
0,204	1,143	0.160	7,14	Do

**Table 3.1.3:** Main obtained results by using NCSE-02 provisions

Where,  $\alpha_0$  is the seismic coefficient for the studied mechanism,  $d_u$  is the ultimate displacement of the selected mechanism of the macro-element object of the study,  $d_d$  is the demand displacement of the macro-element under seismic action considering the selected mechanism, S.F. is safety factor obtained by the ultimate displacement ( $d_u$ ) and demand displacement ( $d_d$ ) ratio and  $D_i$  is the level of damage described in Lagomarsino [3].



Mechanism 2: upper tower rotation

Comparing with the mechanism 1, the rotation point of the introduced mechanism was considered in order to involve the tower upper part only.

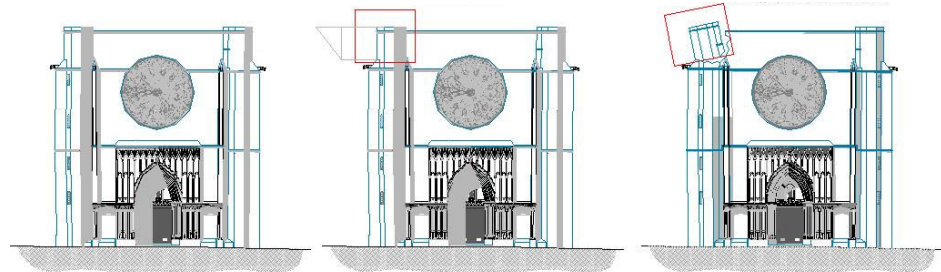


**Figure 3.1.2:** Mechanism 2 studied on the S.Maria del Pi church

$\alpha_0$	$d_u$ (m)	$d_d$ (m)	$S.F. = d_u / d_d$	$D_i$ (level of damage)
0,709	1,143	0.164	6,97	Do

**Table 3.1.3:** Main obtained results by using EC8 provisions

$\alpha_0$	$d_u$ (m)	$d_d$ (m)	$S.F. = d_u / d_d$	$D_i$ (level of damage)
0,709	0,790	0,070	11,29	Do

**Table 3.1.4:** Main obtained results by using NCSE-02 provisions

Mechanism 3: over turning upper part of façade (Out-of-plane)

The out-of-plane of the principal façade was described by a partial over turning of the structural element as reported in the following picture:

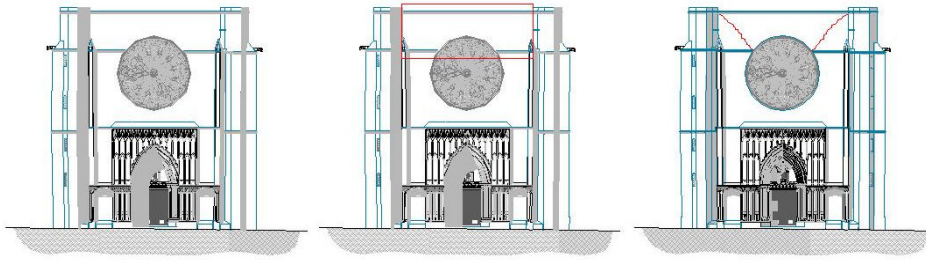


**Figure 3.1.3:** Mechanism 3 studied on the S.Maria del Pi church

$\alpha_0$	$d_u$ (m)	$d_d$ (m)	$S.F. = \frac{d_u}{d_d}$	$D_i$ (level of damage)
0,133	0.150	0.057	2.63	D1

**Table 3.1.5:** Main obtained results by using EC8 provisions

$\alpha_0$	$d_u$ (m)	$d_d$ (m)	$S.F. = \frac{d_u}{d_d}$	$D_i$ (level of damage)
0,133	0.150	0.051	2.94	D1

**Table 3.1.6:** Main obtained results by using NCSE-02 provisions

*Mechanism 3 Mode: over turning upper part of façade taking into account all the façade structure*

The mechanism 3 mode is the same of the mechanism 3, but taking into account the whole principal façade that may influence the structural behaviour of the upper part. For that reason it is possible to consider the **Figure 3.1.3** to understand the mechanism and in the following only the main results will be reported.

$\alpha_0$	$d_u$ (m)	$d_d$ (m)	$S.F. = \frac{d_u}{d_d}$	$D_i$ (level of damage)
0,084	0.150	0.089	1.69	D2

**Table 3.1.7:** Main obtained results by using EC8 provisions

$\alpha_0$	$d_u$ (m)	$d_d$ (m)	$S.F. = d_u / d_d$	$D_i$ (level of damage)
0,084	0.150	0.075	2,00	D2

**Table 3.1.8:** Main obtained results by using NCSE-02 provisions

Mechanism 4: over turning upper part of façade

In the following picture the mechanism has been represented considering the over turning of the upper part of the Principal façade, considering the rose window in the mechanism.

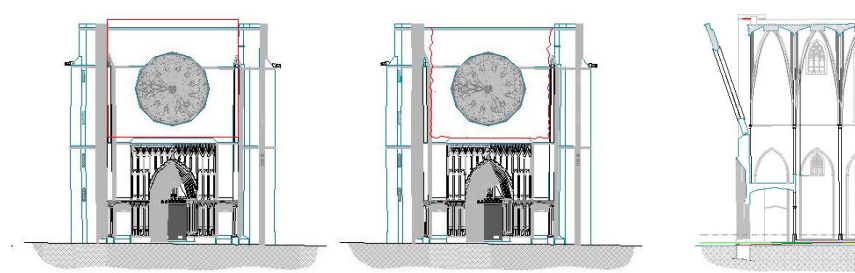


**Figure 3.1.4:** Mechanism 4 studied on the S.Maria del Pi church

$\alpha_0$	$d_u$ (m)	$d_d$ (m)	$S.F. = d_u / d_d$	$D_i$ (level of damage)
0,05	0.150	0.116	1.29	D3

**Table 3.1.9:** Main obtained results by using EC8 provisions

$\alpha_0$	$d_u$ (m)	$d_d$ (m)	$S.F. = d_u / d_d$	$D_i$ (level of damage)
0,05	0.150	0.105	1.43	D3

**Table 3.1.10:** Main obtained results by using NCSE-02 provisions

Mechanism 4 Mode: over turning upper part of façade taking into account all the façade structure

Also in this case, the whole façade has been taken into account in order to have a more realistic result as the procedure seen in the mechanism 3 mode, before introduced. For this reason, the mechanism is the same reported in the **Figure 4.1.4**.

$\alpha_0$	$d_u$ (m)	$d_d$ (m)	$S.F. = d_u / d_d$	$D_i$ (level of damage)
0,041	0.150	0.126	1.19	D3

**Table 3.1.11:** Main obtained results by using EC8 provisions

$\alpha_0$	$d_u$ (m)	$d_d$ (m)	$S.F. = d_u / d_d$	$D_i$ (level of damage)
0,041	0.150	0.115	1.30	D3

**Table 3.1.12:** Main obtained results by using NCSE-02 provisions

Mechanism 5: over turning of the central part of the façade

In the following picture the mechanism has been represented considering the over turning of the upper part of the Principal façade, considering the rose window in the mechanism.

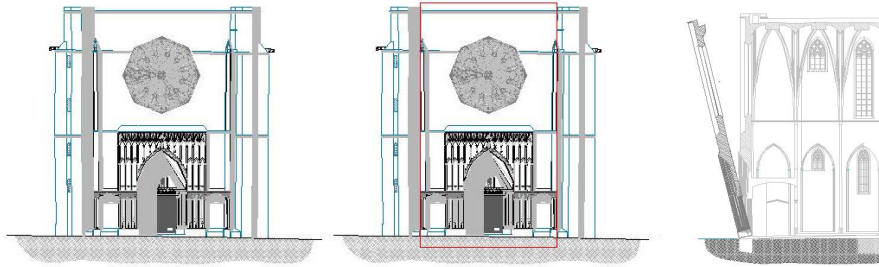


**Figure 3.1.5:** Mechanism 5 studied on the S.Maria del Pi church

$\alpha_0$	$d_u$ (m)	$d_d$ (m)	$S.F. = d_u/d_d$	$D_i$ (level of damage)
0,068	0.328	0.129	2.54	D1

**Table 3.1.13:** Main obtained results by using EC8 provisions

$\alpha_0$	$d_u$ (m)	$d_d$ (m)	$S.F. = d_u/d_d$	$D_i$ (level of damage)
0,068	0.328	0.117	2.80	D1

**Table 3.1.14:** Main obtained results by using NCSE-02 provisions

Mechanism 6: transversal seismic action

In the following picture the mechanism has been represented considering the transversal behaviour of the transept.

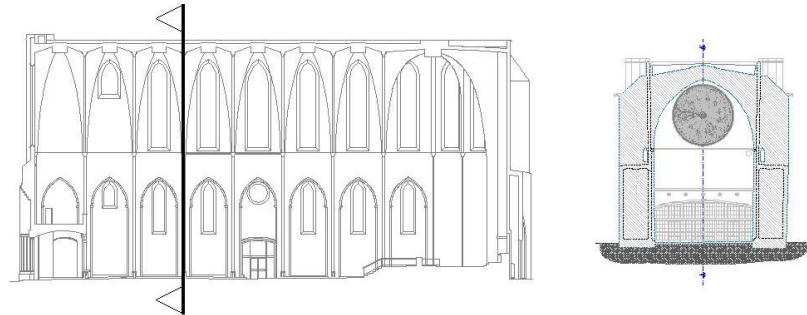


**Figure 3.1.6:** Mechanism 6 studied on the S.Maria del Pi church

$\alpha_0$	$d_u$ (m)	$d_d$ (m)	$S.F. = d_u/d_d$	$D_i$ (level of damage)
0,135	0.693	0.157	4.42	D0

**Table 3.1.15:** Main obtained results by using EC8 provisions

$\alpha_0$	$d_u$ (m)	$d_d$ (m)	$S.F. = d_u/d_d$	$D_i$ (level of damage)
0,135	0.693	0.144	4.82	D0

**Table 3.1.16:** Main obtained results by using NCSE-02 pr

Mechanism7: transversal seismic action of the principal façade

In the following picture the mechanism has been represented considering the transversal behaviour of the transept.

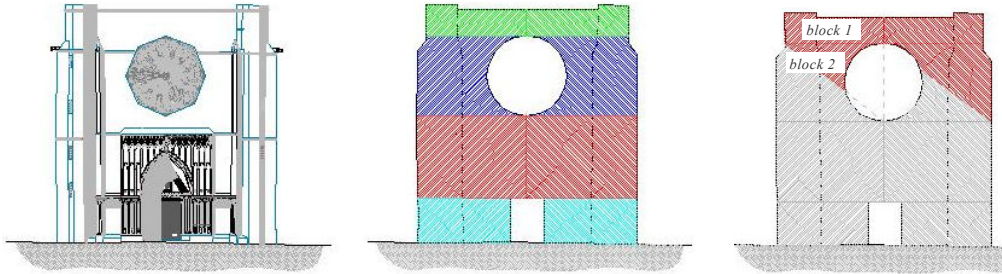


**Figure 3.1.7:** Mechanism 7 studied on the S.Maria del Pi church

$\alpha_0$	$d_u$ (m)	$d_d$ (m)	$S.F. = d_u / d_d$	$D_i$ (level of damage)
0,846	1.875	0.145	12.93	D0

**Table 3.1.17:** Main obtained results by using EC8 provisions

$\alpha_0$	$d_u$ (m)	$d_d$ (m)	$S.F. = d_u / d_d$	$D_i$ (level of damage)
0,846	1.875	0.130	14,42	D0

**Table 3.1.18:** Main obtained results by using NCSE-02 provisions

Mechanism8: transversal seismic action of the principal façade

In the following picture the mechanism has been represented considering the transversal behaviour of the transept

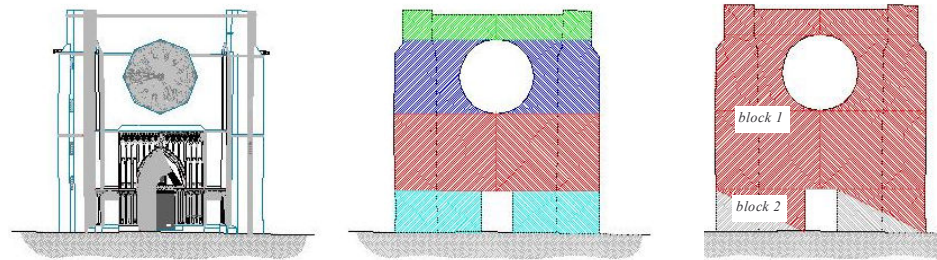


**Figure 3.1.8:** Mechanism 8 studied on the S.Maria del Pi church

$\alpha_0$	$d_u$ (m)	$d_d$ (m)	$S.F. = d_u / d_d$	$D_i$ (level of damage)
1.56	1.787	0.145	12.32	D0

**Table 3.1.19:** Main obtained results by using EC8 provisions

$\alpha_0$	$d_u$ (m)	$d_d$ (m)	$S.F. = d_u / d_d$	$D_i$ (level of damage)
1.56	1.787	0.12	14,89	D0

**Table 3.1.20:** Main obtained results by using NCSE-02 provisions

*Mechanism 9: Apse over turning*

In the following picture the mechanism has been represented considering the over turning of one part of the apse.

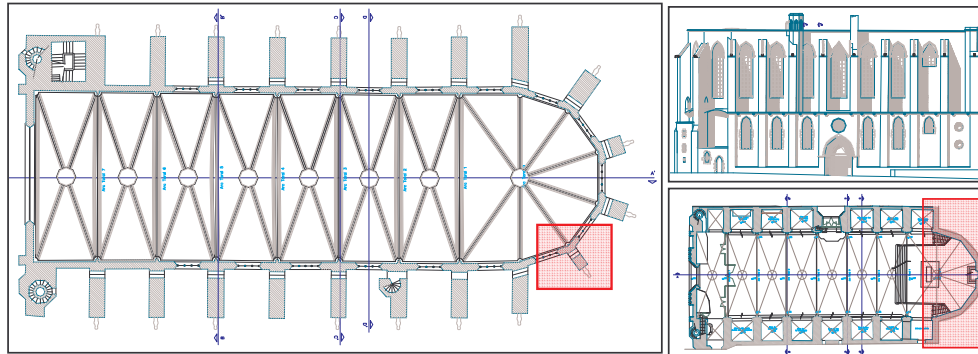


**Figure 3.1.9:** Mechanism 9 studied on the S.Maria del Pi church

$\alpha_0$	$d_u$ (m)	$d_d$ (m)	$S.F. = \frac{d_u}{d_d}$	$D_i$ (level of damage)
0.109	0.543	0.151	3.60	D0

**Table 3.1.21:** Main obtained results by using EC8 provisions

$\alpha_0$	$d_u$ (m)	$d_d$ (m)	$S.F. = \frac{d_u}{d_d}$	$D_i$ (level of damage)
0.109	0.543	0.140	3.88	D0

**Table 3.1.22:** Main obtained results by using NCSE-02 provisions



Mechanism 10: Apse over turning

In the following picture the mechanism has been represented considering the over turning of one part of the apse.

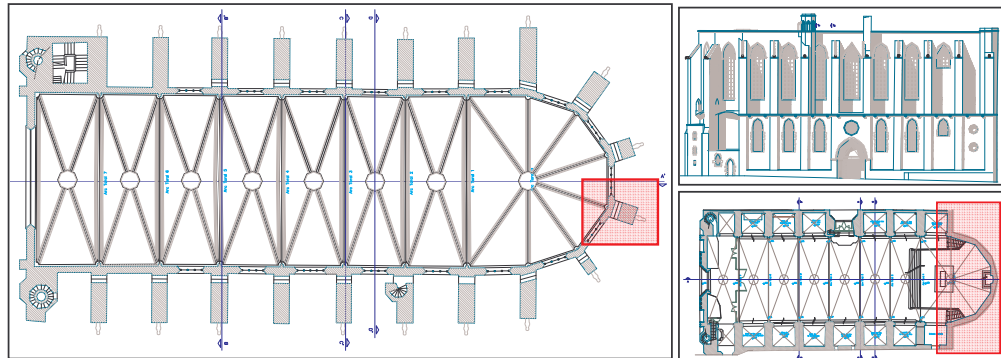


**Figure 3.1.10:** Mechanism 10 studied on the S.Maria del Pi church

$\alpha_0$	$d_u$ (m)	$d_d$ (m)	$S.F. = d_u / d_d$	$D_i$ (level of damage)
0.124	0.614	0.151	4.06	D0

**Table 3.1.23:** Main obtained results by using EC8 provisions

$\alpha_0$	$d_u$ (m)	$d_d$ (m)	$S.F. = d_u / d_d$	$D_i$ (level of damage)
0.124	0.614	0.140	4.38	D0

**Table 3.1.24:** Main obtained results by using NCSE-02 provisions

Mechanism 11: Apse over turning

In the following picture the mechanism has been represented considering the over turning of one part of the apse.

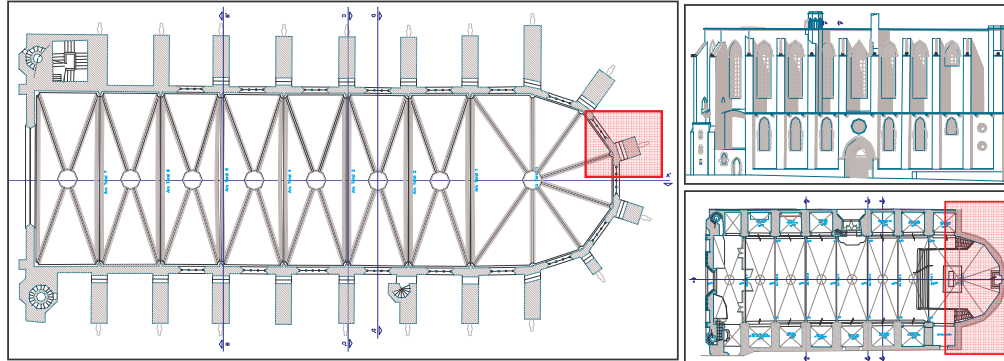


Figure 3.1.11: Mechanism 11 studied on the S.Maria del Pi church

$\alpha_0$	$d_u$ (m)	$d_d$ (m)	$S.F. = \frac{d_u}{d_d}$	$D_i$ (level of damage)
0.111	0.553	0.148	3.74	D0

Table 3.1.25: Main obtained results by using EC8 provisions

$\alpha_0$	$d_u$ (m)	$d_d$ (m)	$S.F. = \frac{d_u}{d_d}$	$D_i$ (level of damage)
0.111	0.553	0.140	3.95	D0

Table 3.1.26: Main obtained results by using NCSE-02 provisions

Mechanism 12: Apse over turning

In the following picture the mechanism has been represented considering the over turning of one part of the apse.

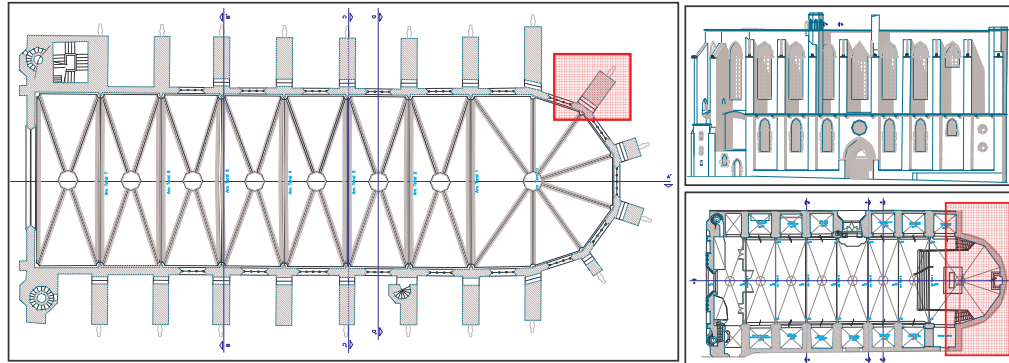


**Figure 3.1.12:** Mechanism 12 studied on the S.Maria del Pi church

$\alpha_0$	$d_u$ (m)	$d_d$ (m)	$S.F. = d_u / d_d$	$D_i$ (level of damage)
0.182	0.895	0.164	5.46	D0

**Table 3.1.27:** Main obtained results by using EC8 provisions

$\alpha_0$	$d_u$ (m)	$d_d$ (m)	$S.F. = d_u / d_d$	$D_i$ (level of damage)
0.182	0.895	0.1650	5.97	D0

**Table 3.1.28:** Main obtained results by using NCSE-02 provisions

### 3.2. Santa Maria del Mar

All the considered mechanisms are reported in the **Table 4.2.1** in which the name of mechanism and a brief description are reported.

mechanism	typology	mechanisms' description
1	total tower	<i>out of plane rotation of the whole tower</i>
2	central upper facade	<i>out of plane rotation of the upper part of the principal façade</i>
2 mode	central upper facade	<i>out of plane rotation of the upper part of the principal façade</i>
3	upper part facade	<i>out of plane rotation of the upper part of the principal façade</i>
3 mode	upper part facade	<i>out of plane rotation of the upper part of the principal façade</i>
4	total facade	<i>out of plane rotation of the whole principal façade</i>
5	in-plane upper facade	<i>in plane motion of the upper part of the principal façade</i>
6	in-plane facade-tower	<i>in plane motion of the upper part of the principal façade</i>
7	in-plane half facade	<i>in plane motion of half part of the principal façade</i>
8	transept 1st hypothesis	<i>in plane motion of the transept under trasversal horizontal load</i>
9	transept 2nd hypothesis	<i>in plane motion of the transept under trasversal horizontal load</i>
10	transept 3rd hypothesis	<i>in plane motion of the transept under trasversal horizontal load</i>
11	apse	<i>out of plane rotation of one part of the apse</i>
12	first upper tower	<i>out of plane rotation of the first upper part of the tower</i>
12 mode	first upper tower	<i>out of plane rotation of the first upper part of the tower</i>
13	first upper tower	<i>out of plane rotation of the first upper part of the tower</i>
13 mode	first upper tower	<i>out of plane rotation of the first upper part of the tower</i>
14	second upper tower	<i>out of plane rotation of the second upper part of the tower</i>
14 mode	second upper tower	<i>out of plane rotation of the second upper part of the tower</i>
15	second upper tower	<i>out of plane rotation of the second upper part of the tower</i>
15 mode	second upper tower	<i>out of plane rotation of the second upper part of the tower</i>

**Table 3.2.1:** All the mechanisms studied on the S.Maria del Mar church

As done in the previous paragraph, the mechanisms and the main results obtained using the C.S.M. are reported.

Mechanism 1: tower rotation

In the following picture the mechanism has been represented considering the rotation of the whole tower, taking into account a rotation point in the base of the structure.

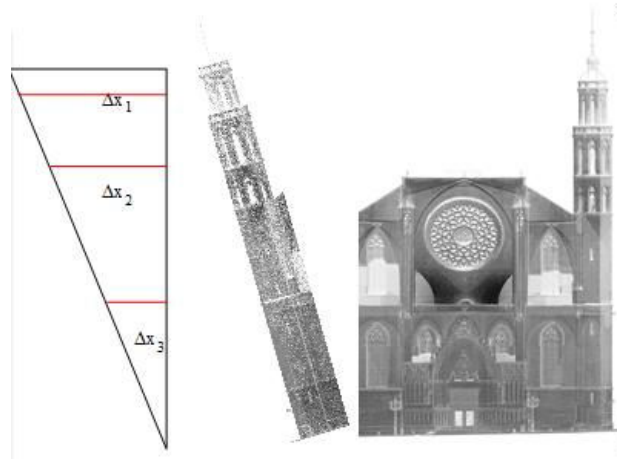


**Figure 3.2.1:** Mechanism 1 studied on the S.Maria del Pi church

$\alpha_0$	$d_u$ (m)	$d_d$ (m)	$S.F. = \frac{d_u}{d_d}$	$D_i$ (level of damage)
0,123	0,930	0.165	5.64	Do

**Table 3.2.2:** Main obtained results by using EC8 provisions

$\alpha_0$	$d_u$ (m)	$d_d$ (m)	$S.F. = \frac{d_u}{d_d}$	$D_i$ (level of damage)
0,123	0,930	0.160	5.81	Do

**Table 3.2.3:** Main obtained results by using NCSE-02 provisions

Mechanism 2: over turning of the upper part of façade

In the following picture the mechanism has been represented considering the rotation of the upper part of the façade.

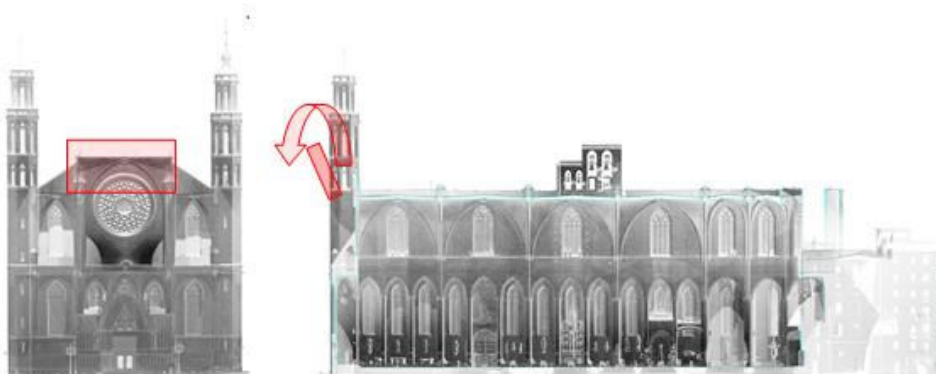


**Figure 3.2.2:** Mechanism 2 studied on the S.Maria del Pi church

$\alpha_0$	$d_u$ (m)	$d_d$ (m)	$S.F. = \frac{d_u}{d_d}$	<b>D<sub>i</sub> (level of damage)</b>
0,142	0,150	0.056	2.68	D1

**Table 3.2.4:** Main obtained results by using EC8 provisions

$\alpha_0$	$d_u$ (m)	$d_d$ (m)	$S.F. = \frac{d_u}{d_d}$	<b>D<sub>i</sub> (level of damage)</b>
0,142	0,150	0.049	3,06	D1

**Table 3.2.5:** Main obtained results by using NCSE-02 provisions

Mechanism 2 Mode: over turning upper part of façade taking into account all the façade structure

The mechanism 2 mode is the same of the mechanism 2, but taking into account the whole principal façade that may influence the structural behaviour of the upper part.

$\alpha_0$	$d_u$ (m)	$d_d$ (m)	$S.F. = d_u / d_d$	$D_i$ (level of damage)
0,142	0,150	0.08	1.88	D2

**Table 3.2.6:** Main obtained results by using EC8 provisions

$\alpha_0$	$d_u$ (m)	$d_d$ (m)	$S.F. = d_u / d_d$	$D_i$ (level of damage)
0,142	0,150	0.071	2,11	D2

**Table 3.2.7:** Main obtained results by using NCSE-02 provisions

Mechanism 3: over turning upper part of façade

In the following picture the mechanism has been represented considering the rotation of the whole tower, taking into account a rotation point in the base of the structure.

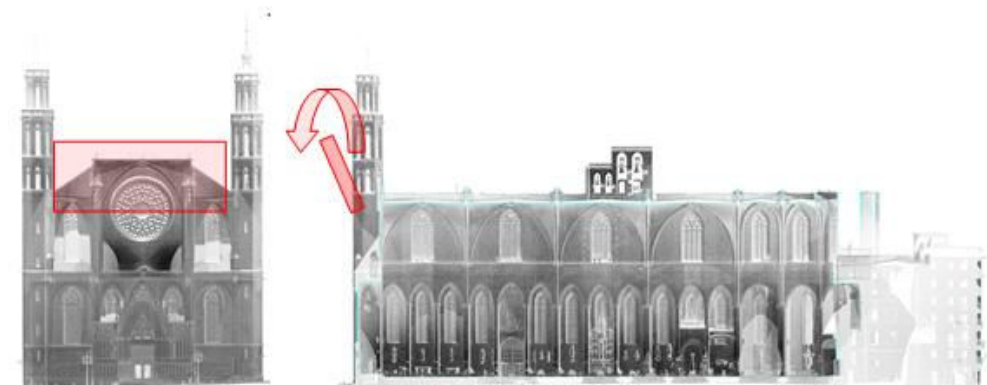


**Figure 3.2.3:** Mechanism 3 studied on the S.Maria del Pi church

$\alpha_0$	$d_u$ (m)	$d_d$ (m)	S.F. = $d_u/d_d$	<b>D<sub>i</sub> (level of damage)</b>
0,089	0,20	0,10	2,00	D2

Table 3.2.8: Main obtained results by using EC8 provisions

$\alpha_0$	$d_u$ (m)	$d_d$ (m)	S.F. = $d_u/d_d$	<b>D<sub>i</sub> (level of damage)</b>
0,089	0,20	0,092	2,17	D2

Table 3.2.9: Main obtained results by using NCSE-02 provisions

Mechanism 3 Mode: over turning upper part of façade taking into account all the façade structure

As said for the mechanism 2 mode, even in this case it is possible to state that the mechanism 3 mode is the same of the mechanism 3, but taking into account the whole façade.

$\alpha_0$	$d_u$ (m)	$d_d$ (m)	S.F. = $d_u/d_d$	<b>D<sub>i</sub> (level of damage)</b>
0,059	0,20	0,125	1,60	D2

Table 3.2.10: Main obtained results by using EC8 provisions

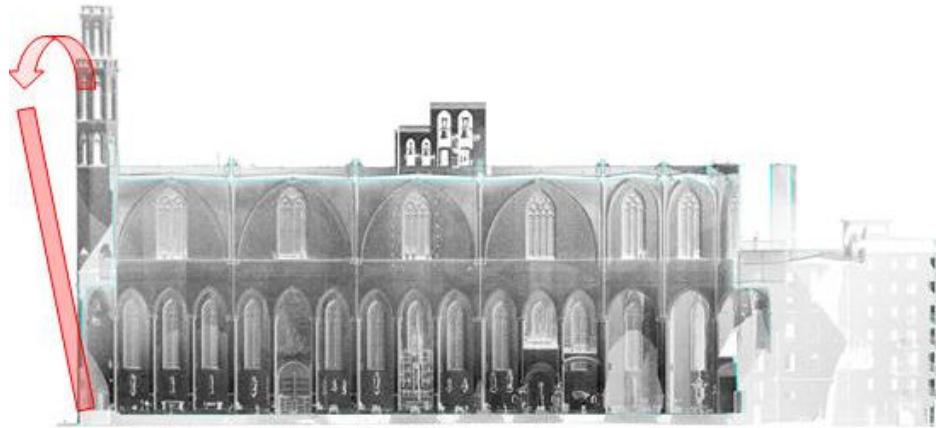
$\alpha_0$	$d_u$ (m)	$d_d$ (m)	S.F. = $d_u/d_d$	<b>D<sub>i</sub> (level of damage)</b>
0,059	0,20	0,11	1,82	D2

Table 3.2.11: Main obtained results by using NCSE-02 provisions



Mechanism 4: Over turning of façade

In the following picture the mechanism has been represented considering the rotation of the whole principal façade, taking into account a rotation point in the base of the structure.



**Figure 3.2.4:** Mechanism 4 studied on the S.Maria del Pi church

$\alpha_0$	$d_u$ (m)	$d_d$ (m)	$S.F. = d_u / d_d$	$D_i$ (level of damage)
0,0624	0,566	0,153	3,70	D0

**Table 3.2.12:** Main obtained results by using EC8 provisions

$\alpha_0$	$d_u$ (m)	$d_d$ (m)	$S.F. = d_u / d_d$	$D_i$ (level of damage)
0,0624	0,566	0,140	4,04	D0

**Table 3.2.13:** Main obtained results by using NCSE-02 provisions

Mechanism 5: upper part tower rotation

In the following picture the mechanism has been represented considering the rotation of the upper part of the tower tower.

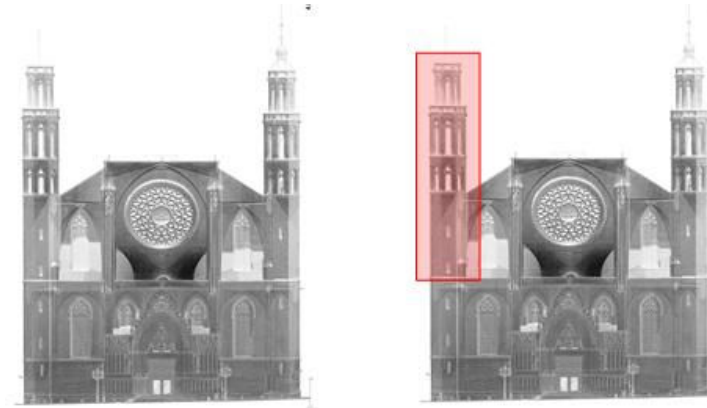


**Figure 3.2.5:** Mechanism 5 studied on the S.Maria del Pi church

$\alpha_0$	$d_u$ (m)	$d_d$ (m)	$S.F. = d_u / d_d$	$D_i$ (level of damage)
0,681	0,530	0,05	10,61	D0

**Table 3.2.14:** Main obtained results by using EC8 provisions

$\alpha_0$	$d_u$ (m)	$d_d$ (m)	$S.F. = d_u / d_d$	$D_i$ (level of damage)
0,681	0,530	0,053	10,01	D0

**Table 3.2.15:** Main obtained results by using NCSE-02 provisions

Mechanism 6: tower rotation

In the following picture the mechanism has been represented considering the rotation of the whole tower, taking into account a rotation point in the base of the structure.

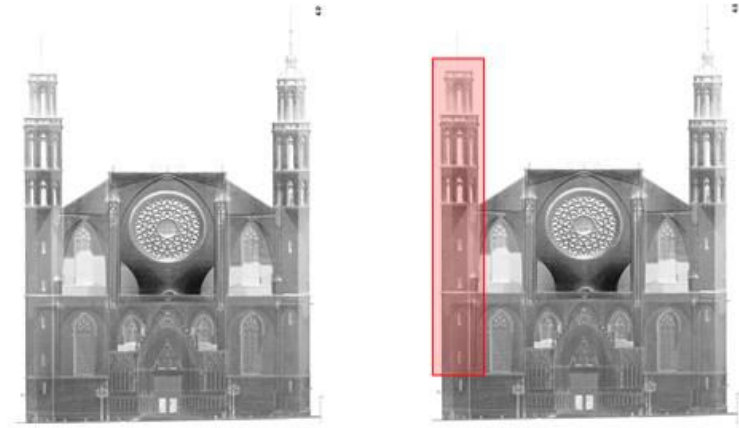


**Figure 3.2.6:** Mechanism 6 studied on the S.Maria del Pi church

$\alpha_0$	$d_u$ (m)	$d_d$ (m)	$S.F. = \frac{d_u}{d_d}$	$D_i$ (level of damage)
0,701	0,397	0,04	9,93	D0

**Table 3.2.16:** Main obtained results by using EC8 provisions

$\alpha_0$	$d_u$ (m)	$d_d$ (m)	$S.F. = \frac{d_u}{d_d}$	$D_i$ (level of damage)
0,701	0,397	0,04	9,93	D0

**Table 3.2.17:** Main obtained results by using NCSE-02 provisions

Mechanism 7: in plane mechanism of the principal façade

In the following picture the mechanism has been represented considering the rotation of the whole tower, taking into account a rotation point in the base of the structure.

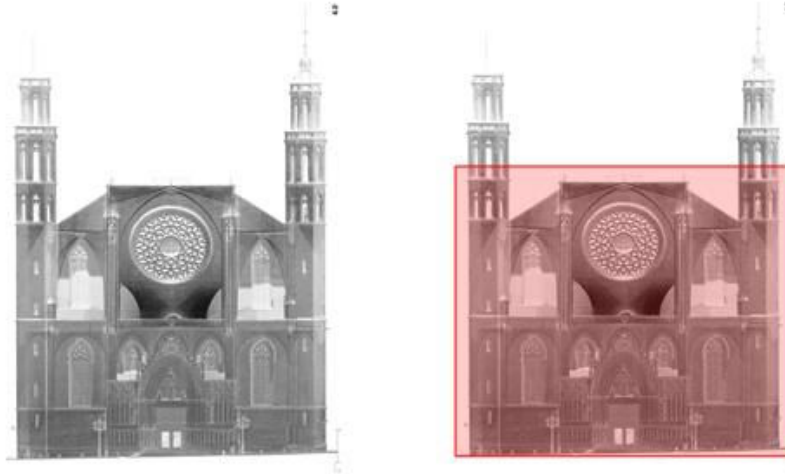


**Figure 3.2.7:** Mechanism 7 studied on the S.Maria del Pi church

$\alpha_0$	$d_u$ (m)	$d_d$ (m)	$S.F. = d_u / d_d$	$D_i$ (level of damage)
1,46	0,950	0,06	15,83	D0

**Table 3.2.18:** Main obtained results by using EC8 provisions

$\alpha_0$	$d_u$ (m)	$d_d$ (m)	$S.F. = d_u / d_d$	$D_i$ (level of damage)
1,46	0,950	0,062	15,32	D0

**Table 3.2.19:** Main obtained results by using NCSE-02 provisions

Mechanism 8: transversal seismic action

In the following picture the mechanism has been represented considering the transversal behaviour of the transept.

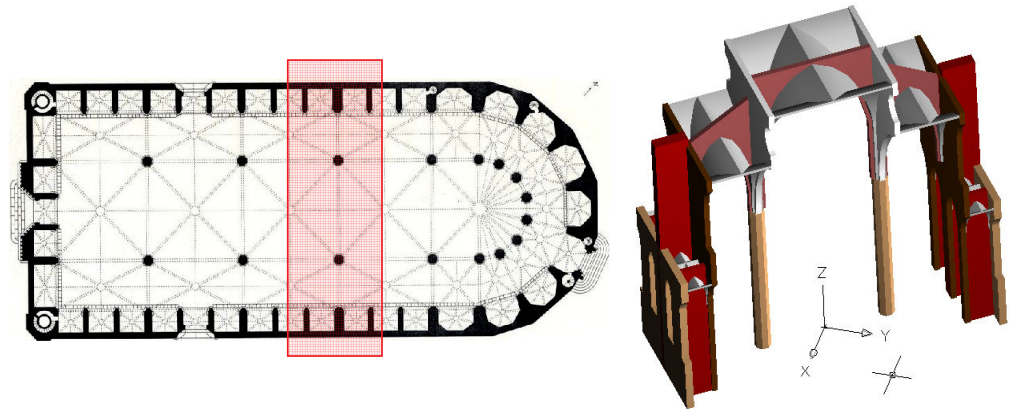


Figure 3.2.8: Mechanism 8 studied on the S.Maria del Pi church

$\alpha_0$	$d_u$ (m)	$d_d$ (m)	$S.F. = \frac{d_u}{d_d}$	$D_i$ (level of damage)
0,088	0,846	0,202	4,19	D0

Table 3.2.20: Main obtained results by using EC8 provisions

$\alpha_0$	$d_u$ (m)	$d_d$ (m)	$S.F. = \frac{d_u}{d_d}$	$D_i$ (level of damage)
0,088	0,846	0,180	4,70	D0

Table 3.2.21: Main obtained results by using NCSE-02 provisions

Mechanism 9: transversal seismic action of the transept

In the following picture the mechanism has been represented considering the transversal behaviour of the transept.

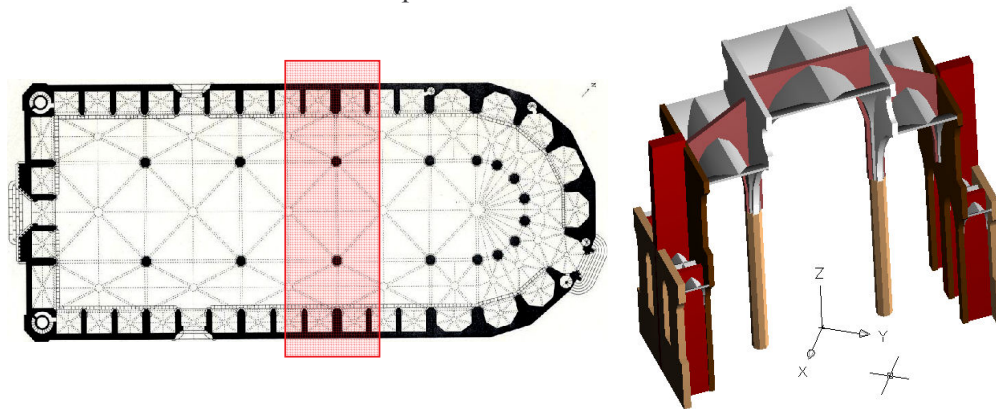


Figure 3.2.9: Mechanism 9 studied on the S.Maria del Pi church

$\alpha_0$	$d_u$ (m)	$d_d$ (m)	$S.F. = d_u / d_d$	$D_i$ (level of damage)
0,102	1,257	0,254	4,95	D0

Table 3.2.22: Main obtained results by using EC8 provisions

$\alpha_0$	$d_u$ (m)	$d_d$ (m)	$S.F. = d_u / d_d$	$D_i$ (level of damage)
0,102	1,257	0,220	5,71	D0

Table 3.2.23: Main obtained results by using NCSE-02 provisions

Mechanism 10: transversal seismic action of the transept

In the following picture the mechanism has been represented considering the transversal behaviour of the transept.

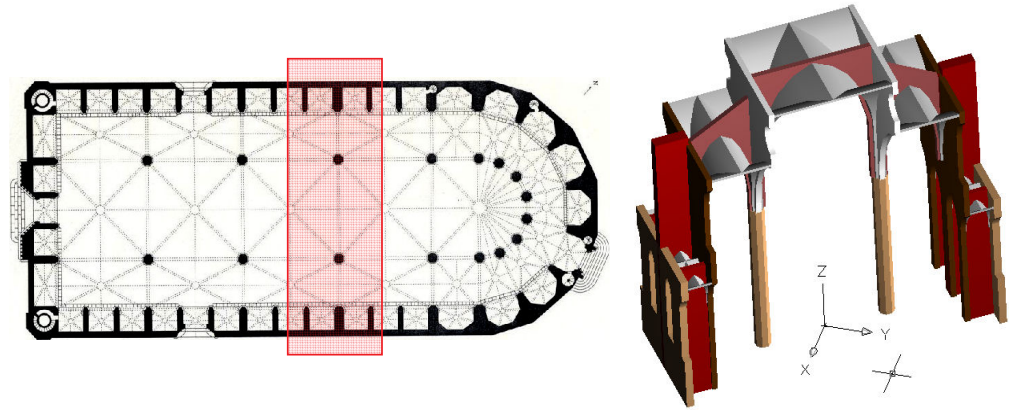


**Figure 3.2.10:** Mechanism 10 studied on the S.Maria del Pi church

$\alpha_0$	$d_u$ (m)	$d_d$ (m)	$S.F. = d_u / d_d$	$D_i$ (level of damage)
0,083	1,118	0,225	4,97	D0

**Table 3.2.24:** Main obtained results by using EC8 provisions

$\alpha_0$	$d_u$ (m)	$d_d$ (m)	$S.F. = d_u / d_d$	$D_i$ (level of damage)
0,083	1,118	0,200	5,59	D0

**Table 3.2.25:** Main obtained results by using NCSE-02 provisions

Mechanism 11: Apse over turning

In the following picture the mechanism has been represented considering the over turning of one part of the apse.

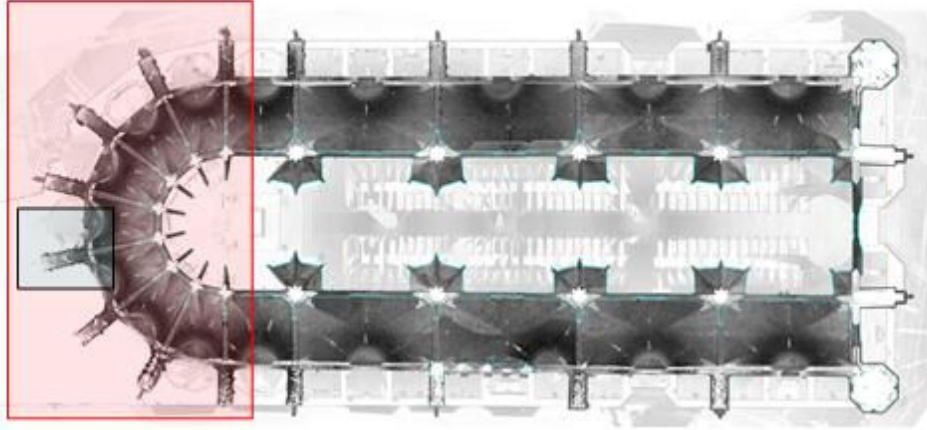


**Figure 3.2.11:** Mechanism 11 studied on the S.Maria del Mar church

$\alpha_0$	$d_u$ (m)	$d_d$ (m)	$S.F. = d_u / d_d$	$D_i$ (level of damage)
0,158	0.940	0,178	5,28	D0

**Table 3.2.26:** Main obtained results by using EC8 provisions

$\alpha_0$	$d_u$ (m)	$d_d$ (m)	$S.F. = d_u / d_d$	$D_i$ (level of damage)
0,158	0.940	0,160	5,88	D0

**Table 3.2.27:** Main obtained results by using NCSE-02 provisions



Mechanism 12: torsion on the upper part of the tower

In the following picture the mechanism has been represented considering the over turning of one part of the apse.

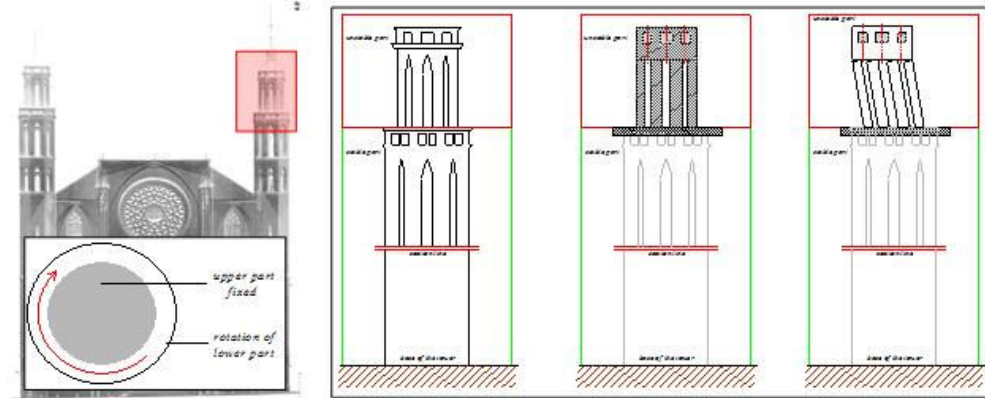


**Figure 3.2.12:** Mechanism 12 studied on the S.Maria del Mar church

$\alpha_0$	$d_u$ (m)	$d_d$ (m)	$S.F. = d_u / d_d$	$D_i$ (level of damage)
0,128	0,139	0,054	2,57	D2

**Table 3.2.28:** Main obtained results by using EC8 provisions

$\alpha_0$	$d_u$ (m)	$d_d$ (m)	$S.F. = d_u / d_d$	$D_i$ (level of damage)
0,131	0,132	0,043	3,06	D1

**Table 3.2.29:** Main obtained results by using NCSE-02 provisions

Mechanism 12 Mode: torsion on the upper part of the tower

The mechanism 12 mode is the same of the mechanism 12, but taking into account the whole principal façade that may influence the structural behaviour of the upper part.

$\alpha_0$	$d_u$ (m)	$d_d$ (m)	S.F. = $d_u/d_d$	D <sub>i</sub> (level of damage)
0,086	0,139	0,072	1,93	D2

Table 3.2.30: Main obtained results by using EC8 provisions

$\alpha_0$	$d_u$ (m)	$d_d$ (m)	S.F. = $d_u/d_d$	D <sub>i</sub> (level of damage)
0,088	0,132	0,061	2,16	D2

Table 3.2.31: Main obtained results by using NCSE-02 provisions

Mechanism 13: translation on the upper part of the tower

In the following picture the mechanism has been represented considering the over turning of one part of the apse.

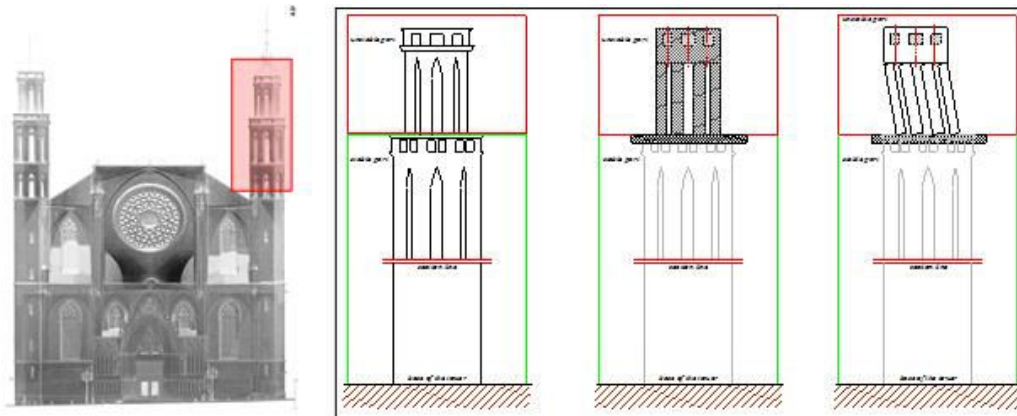


Figure 3.2.13: Mechanism 13 studied on the S.Maria del Mar church

$\alpha_0$	$d_u$ (m)	$d_d$ (m)	$S.F. = d_u/d_d$	$D_i$ (level of damage)
0,14	0,174	0,021	8,30	D0

**Table 3.2.32:** Main obtained results by using EC8 provisions

$\alpha_0$	$d_u$ (m)	$d_d$ (m)	$S.F. = d_u/d_d$	$D_i$ (level of damage)
0,14	0,174	0,021	8,30	D0

**Table 3.2.33:** Main obtained results by using NCSE-02 provisions

Mechanism 13 Mode: translation on the upper part of the tower

$\alpha_0$	$d_u$ (m)	$d_d$ (m)	$S.F. = d_u/d_d$	$D_i$ (level of damage)
0,10	0,174	0,03	5,81	D0

**Table 3.2.34:** Main obtained results by using EC8 provisions

$\alpha_0$	$d_u$ (m)	$d_d$ (m)	$S.F. = d_u/d_d$	$D_i$ (level of damage)
0,10	0,174	0,03	5,81	D0

**Table 3.2.35:** Main obtained results by using NCSE-02 provisions

Mechanism 14: torsion on the upper part of the tower

In the following picture the mechanism has been represented considering the over turning of one part of the apse.

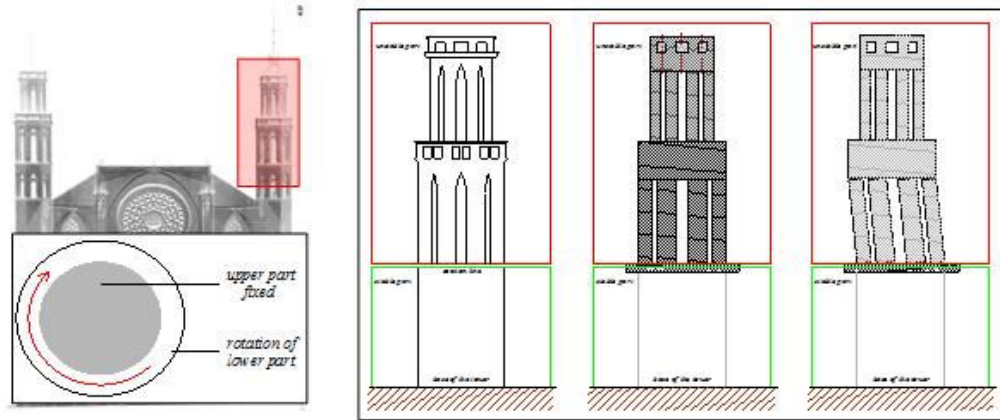


**Figure 3.2.14:** Mechanism 14 studied on the S.Maria del Mar church

$\alpha_0$	$d_u$ (m)	$d_d$ (m)	$S.F. = d_u / d_d$	$D_i$ (level of damage)
0,115	0,148	0,061	2,42	D2

**Table 3.2.36:** Main obtained results by using EC8 provisions

$\alpha_0$	$d_u$ (m)	$d_d$ (m)	$S.F. = d_u / d_d$	$D_i$ (level of damage)
0,115	0,148	0,053	2,78	D1

**Table 3.2.37:** Main obtained results by using NCSE-02 provisions

Mechanism 14 Mode: torsion on the upper part of the tower

$\alpha_0$	$d_u$ (m)	$d_d$ (m)	$S.F. = d_u / d_d$	$D_i$ (level of damage)
0,084	0,148	0,082	1,80	D2

**Table 3.2.38:** Main obtained results by using EC8 provisions

$\alpha_0$	$d_u$ (m)	$d_d$ (m)	$S.F. = d_u / d_d$	$D_i$ (level of damage)
0,082	0,148	0,073	2,02	D2

**Table 3.2.39:** Main obtained results by using NCSE-02 provisions

Mechanism 15: translation on the upper part of the tower

In the following picture the mechanism has been represented considering the over turning of one part of the apse.

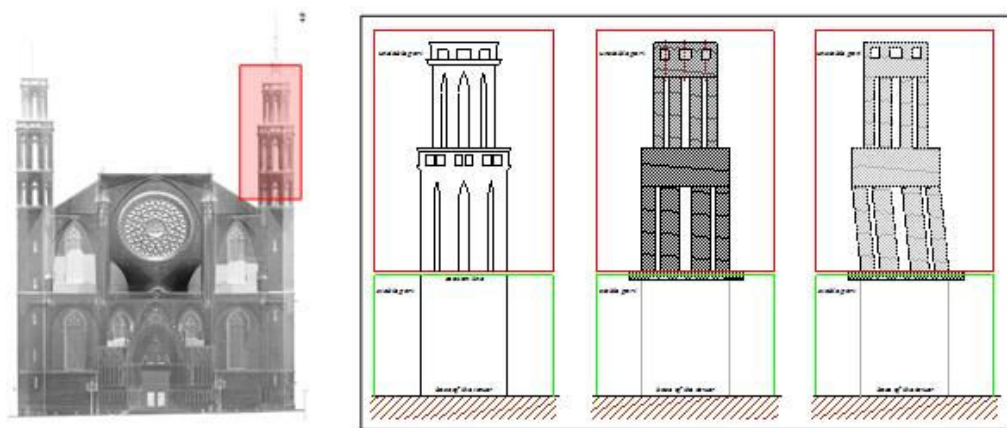


**Figure 3.2.15:** Mechanism 15 studied on the S.Maria del Mar church

$\alpha_0$	$d_u$ (m)	$d_d$ (m)	S.F. = $d_u/d_d$	<b>D<sub>i</sub> (level of damage)</b>
0,11	0,193	0,041	4,71	D0

**Table 3.2.40:** Main obtained results by using EC8 provisions

$\alpha_0$	$d_u$ (m)	$d_d$ (m)	S.F. = $d_u/d_d$	<b>D<sub>i</sub> (level of damage)</b>
0,11	0,193	0,034	5,68	D0

**Table 3.2.41:** Main obtained results by using NCSE-02 provisions

*Mechanism 15 Mode: translation on the upper part of the tower*

$\alpha_0$	$d_u$ (m)	$d_d$ (m)	S.F. = $d_u/d_d$	<b>D<sub>i</sub> (level of damage)</b>
0,08	0,193	0,056	3,45	D1

**Table 3.2.42:** Main obtained results by using EC8 provisions

$\alpha_0$	$d_u$ (m)	$d_d$ (m)	S.F. = $d_u/d_d$	<b>D<sub>i</sub> (level of damage)</b>
0,08	0,193	0,050	3,86	D0

**Table 3.2.43:** Main obtained results by using NCSE-02 provisions

### 3.3. Mallorca Cathedral

All the considered mechanisms are reported in the **Table 4.3.1** in which the name of mechanism and a brief description are reported.

mechanism	typology	mechanisms' description
1	whole facade	<i>out of plane rotation of the whole pricipal façade</i>
2	central whole facade	<i>out of plane rotation of the central part of the pricipal façade</i>
3	upper facade with r.w.	<i>out of plane rotation of the upper part of the principal façade</i>
3 mode	upper facade with r.w.	<i>out of plane rotation of the upper part of the principal façade</i>
4	upper facade (no r.w.)	<i>out of plane rotation of the upper part of the principal façade</i>
4 mode	upper facade (no r.w.)	<i>out of plane rotation of the upper part of the principal façade</i>
5	tower	<i>out of plane rotation of the whole tower</i>
6 - Martinez	typical transept	<i>in plane motion of the transept under trasversal horizontal load</i>
6 - Vaca	typical transept	<i>in plane motion of the transept under trasversal horizontal load</i>

**Table 3.3.1:** All the mechanisms studied on the Mallorca Cathedral

The same procedures of the previous paragraphs, will be followed also in the present one, taking into account for every mechanism the main results obtained by using C.S.M.

#### Mechanism 1: over turning whole principal façade

In the following picture the mechanism has been represented considering the rotation of the whole principal façade, taking into account a rotation point in the base of the structure.

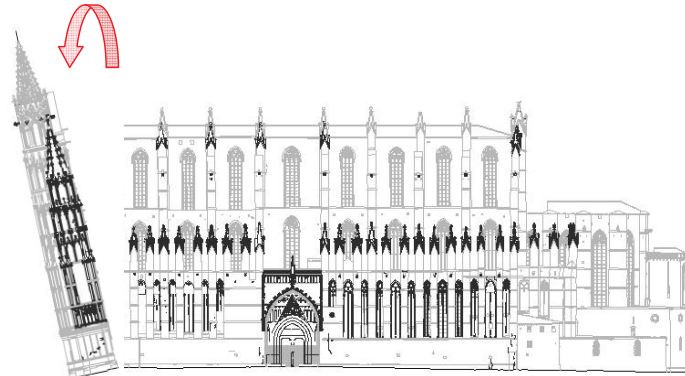


**Figure 3.3.1:** Mechanism 1 studied on the Mallorca Cathedral

$\alpha_0$	$d_u$ (m)	$d_d$ (m)	$S.F. = d_u/d_d$	$D_i$ (level of damage)
0,271	1,649	0.202	8,16	Do

Table 3.3.2: Main obtained results by using EC8 provisions

$\alpha_0$	$d_u$ (m)	$d_d$ (m)	$S.F. = d_u/d_d$	$D_i$ (level of damage)
0,271	1,649	0.190	8,68	Do

Table 3.3.3: Main obtained results by using NCSE-02 provisions

Mechanism 2: over turning of the central part of principal façade

In the following picture the mechanism has been represented considering the rotation of the cen

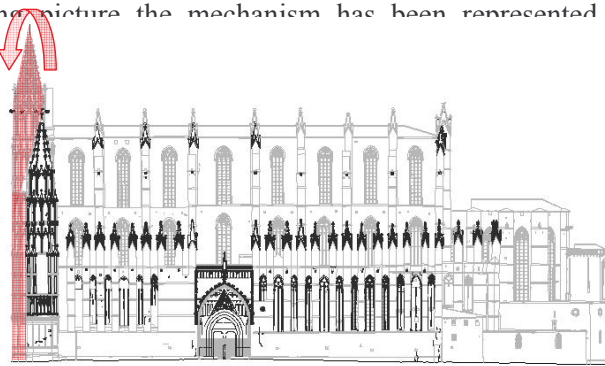


Figure 3.3.2: Mechanism 2 studied on the Mallorca Cathedral

$\alpha_0$	$d_u$ (m)	$d_d$ (m)	$S.F. = d_u/d_d$	$D_i$ (level of damage)
0,14	1,365	0,185	7,38	D0

Table 3.3.4: Main obtained results by using EC8 provisions

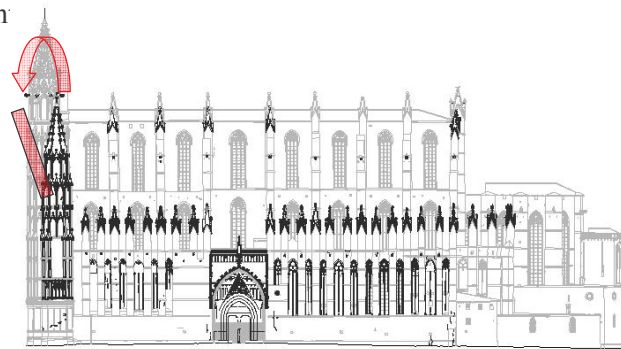
$\alpha_0$	$d_u$ (m)	$d_d$ (m)	$S.F. = d_u/d_d$	$D_i$ (level of damage)
0,138	1,365	0,180	7,58	D0

Table 3.3.5: Main obtained results by using NCSE-02 provisions



Mechanism 3: over turning of the upper part of principal façade

In the following picture the mechanism has been represented considering the rotation of the cen



**Figure 3.3.3:** Mechanism 3 studied on the Mallorca Cathedral

$\alpha_0$	$d_u$ (m)	$d_d$ (m)	$S.F. = \frac{d_u}{d_d}$	$D_i$ (level of damage)
0,14	1,365	0,185	7,38	D0

**Table 3.3.6:** Main obtained results by using EC8 provisions

$\alpha_0$	$d_u$ (m)	$d_d$ (m)	$S.F. = \frac{d_u}{d_d}$	$D_i$ (level of damage)
0,246	1,113	0,190	5,86	D0

**Table 3.3.7:** Main obtained results by using NCSE-02 provisions

Mechanism 3 Mode: over turning upper part of façade taking into account all the façade structure

The mechanism 3 mode is the same of the mechanism 3, but taking into account the whole principal façade that may influence the structural behaviour of the upper part.

$\alpha_0$	$d_u$ (m)	$d_d$ (m)	$S.F. = d_u/d_d$	$D_i$ (level of damage)
0,246	1,113	0,222	5,01	D0

Table 3.3.8: Main obtained results by using EC8 provisions

$\alpha_0$	$d_u$ (m)	$d_d$ (m)	$S.F. = d_u/d_d$	$D_i$ (level of damage)
0,246	1,113	0,190	5,86	D0

Table 3.3.9: Main obtained results by using NCSE-02 provisions

Mechanism 4: over turning of the upper part of principal façade without rose window

In the following picture the mechanism has been represented considering the rotation of the whole tower, taking into account a rotation point at the base of the structure.

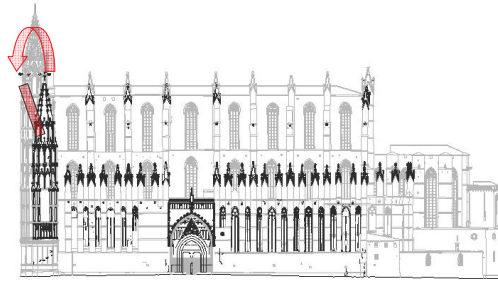


Figure 3.3.4: Mechanism 4 studied on the Mallorca cathedral

$\alpha_0$	$d_u$ (m)	$d_d$ (m)	$S.F. = d_u/d_d$	$D_i$ (level of damage)
0,336	1,058	0,145	7,30	D0

Table 3.3.10: Main obtained results by using EC8 provisions

$\alpha_0$	$d_u$ (m)	$d_d$ (m)	$S.F. = d_u/d_d$	$D_i$ (level of damage)
0,336	1,058	0,150	7,06	D0

Table 3.3.11: Main obtained results by using NCSE-02 provisions

Mechanism 4 Mode: over turning upper part of façade without rose window taking into account all the façade structure

$\alpha_0$	$d_u$ (m)	$d_d$ (m)	$S.F. = d_u / d_d$	$D_i$ (level of damage)
0,336	1,058	0,191	5,54	D0

Table 3.3.12: Main obtained results by using EC8 provisions

$\alpha_0$	$d_u$ (m)	$d_d$ (m)	$S.F. = d_u / d_d$	$D_i$ (level of damage)
0,222	1,058	0,180	5,88	D0

Table 3.3.13: Main obtained results by using NCSE-02 provisions

Mechanism 5: Over turning of whole tower

In the following picture the mechanism has been represented considering the rotation of the whole tower, taking into account a rotation point at the base of the structure

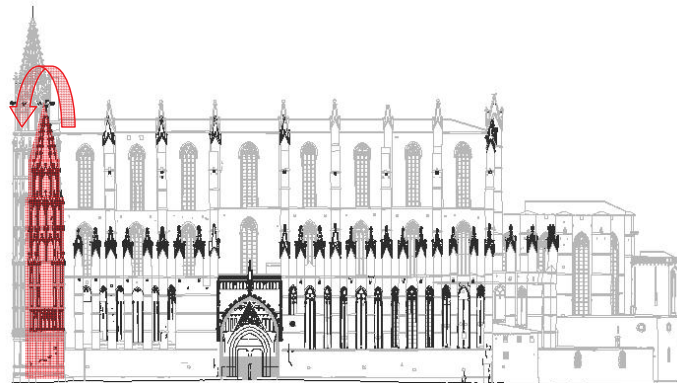


Figure 3.3.5: Mechanism 5 studied on the Mallorca Cathedral

$\alpha_0$	$d_u$ (m)	$d_d$ (m)	$S.F. = d_u/d_d$	$D_i$ (level of damage)
0,167	1,20	0,215	5,58	D0

**Table 3.3.14:** Main obtained results by using EC8 provisions

$\alpha_0$	$d_u$ (m)	$d_d$ (m)	$S.F. = d_u/d_d$	$D_i$ (level of damage)
0,167	1,20	0,200	6,00	D0

**Table 3.3.15:** Main obtained results by using NCSE-02 provisions

*Mechanism 6-1: transversal action on the transept*

In the following picture the mechanism has been represented considering the transversal action applied on the transept. The mechanism and the capacity curve have been considered from the *Phd thesis of Martinez*.

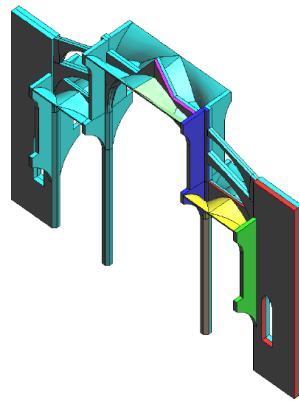


**Figure 3.3.6:** Mechanism 6-1 studied on the Mallorca Cathedral

$\alpha_0$	$d_u$ (m)	$d_d$ (m)	$S.F. = d_u/d_d$	$D_i$ (level of damage)
0,15	0,248	0,045	5,51	D1

**Table 3.3.16:** Main obtained results by using EC8 provisions

$\alpha_0$	$d_u$ (m)	$d_d$ (m)	S.F. = $d_u/d_d$	$D_i$ (level of damage)
0,15	0,248	0,042	5,90	D1

**Table 3.3.17:** Main obtained results by using NCSE-02 provisions

*Mechanism 6-2: transversal action on the transept*

The same mechanism has been studied by *Vaca* in his Phd thesis work, but considering different plastic hinges location.

*Vaca* applied the limit analysis procedure in order to obtain the capacity curve of transept; based on the *Vaca* assumptions, the following results were reached:

$\alpha_0$	$d_u$ (m)	$d_d$ (m)	S.F. = $d_u/d_d$	$D_i$ (level of damage)
0,103	0,900	0,310	2,90	D1

**Table 3.3.18:** Main obtained results by using EC8 provisions

$\alpha_0$	$d_u$ (m)	$d_d$ (m)	S.F. = $d_u/d_d$	$D_i$ (level of damage)
0,103	0,900	0,271	3,32	D1

**Table 3.3.19:** Main obtained results by using NCSE-02 provisions

As showed in the results reported in the **Table 3.3.16 - Table 3.3.19**, the second procedure (*Vaca* assumptions) lead to a lower safety factor for the macro-element object of the study and seems much more realistic in terms of obtained results compared with the first one described as *Mechanism 6-1* (*Martinez* assumption).

### 3.4. Obtained results: final remarks

The results obtained by using the C.S.M. based on the EC8 and reported in the previous paragraphs for the three Churches object of the study, show a general satisfactory seismic protection level, especially for Santa Maria del Mar and Mallorca Cathedral.

In these ecclesiastic structures, it is reached a maximum level of the damage equal to D2 corresponding to a moderate damage caused by the earthquake events.

The main seismic problem occur on Santa Maria del Pi Church in which, for the upper part of the principal façade, the level of damage D3 is reached. The D3 level corresponds to an extensive damage and it must be taken under control, to avoid possible collapse or changing of the equilibrium conditions.

According to the NCSE-02, the demand curves are quite similar to that obtained by using the aforementioned European design code.

The safety factors appear lower compared with the previous results, but it depends on the more restricted rules introduced by the EC8.

At the end, Santa Maria del Mar Church and Mallorca Cathedral have not be taken into account any strengthening intervention, while according to the obtained results, it seems necessary for Santa Maria del Pi church.

## References

- [1] UNI EN 1998 Eurocode 8, “*Design provisions for earthquake resistance of structures - Part 1: general rules, seismic actions and rules for buildings*”.
- [2] NCSE-02, 2002. “*Norma de construccion sismorresistente: parte general y edificación*”, Real decreto 997/2002 del Ministerio de obra publicas, trasportes y medio ambiente
- [3] Lagomarsino, S., Podestà, S. Resemini, S., 2004. “*Observational and mechanical models for the vulnerability assessment of monumental buildings*”, Proc. of the 13<sup>th</sup> World Conference on Earthquake Engineering, Vancouver BC, Canada.
- [4] G.Martinez Ruiz, 2007. “*Vulnerabilidad sismica para edificios historicos de obra de fabrica de mediana y gran luz*”. Phd thesis at UPC – Universitat Politecnica de Catalunya Barcelona (ES)

## 4. SEISMIC BEHAVIOR OF MASONRY BUILDINGS

In the recent years there was a renewed interest on the masonry structures due to their unique performances, in particular higher fire resistance compared with other construction materials (eg, wood and steel).

Furthermore the masonry building exhibited very good performances under cyclic loads due to earthquake events and in a lot of cases they showed signs of partial collapse while the reinforced concrete structures fell entirely down.

Moreover, the masonry buildings are comparable with RC structures in terms of costs especially for less than three floors.

Considering the construction system, the masonry buildings may exhibit different performances, according to the masonry mechanical characteristics, as reported in the following (Augenti [1]):

- *first class*: the horizontal structures have been realized by using masonry vaults, loading the masonry panels in the horizontal direction, eliminable by using appropriate steel ties. Hence, the thickness increment allow the vertical loads to be incremented, thus reducing the force eccentricity;
- *second-class*: the horizontal structures are not connected to the vertical ones. The horizontal beams are simply supported on bearing walls and moreover, there are no horizontal actions. Vertical and horizontal structures are cooperating by means of gravitational loads, behaving completely independent regarding seismic actions. The lack of horizontal structural elements connecting the different walls means



that, as a result of seismic action, the non-synchronous oscillations of different construction units may cause differential displacements close to the edges. The gravitational load eccentricity may produce out-of-plane mechanisms, avoidable by applying internal ties or external contrast elements (buttresses);

- *third class*: the horizontal and vertical structures are generally connected each other. Currently the design code provides three-dimensional structural performances for all the buildings. The floors and bearing walls connections are realized by means of RC structural element, having the same dimension of the vertical structures. Thus, the structures are less vulnerable than previous types, especially regarding to seismic actions.

#### 4.1. Construction Materials

The masonry is an anisotropic material, where the strength depends on the load application and on the direction also. The masonry structures are composed by two constituent elements (mortar and brick or stone) having very different mechanical properties. The construction method, geometric characteristics and different mechanical performances of mortar and bricks do not allow to consider the masonry as a proper construction material. The different stone arrangement or the different mortar joint thickness are just two of the total variables that lead to have different performances of masonry panels built using the same components.

Thus, it is reasonable to expect that the mechanical masonry performances are intermediate to the mechanical properties of their components.

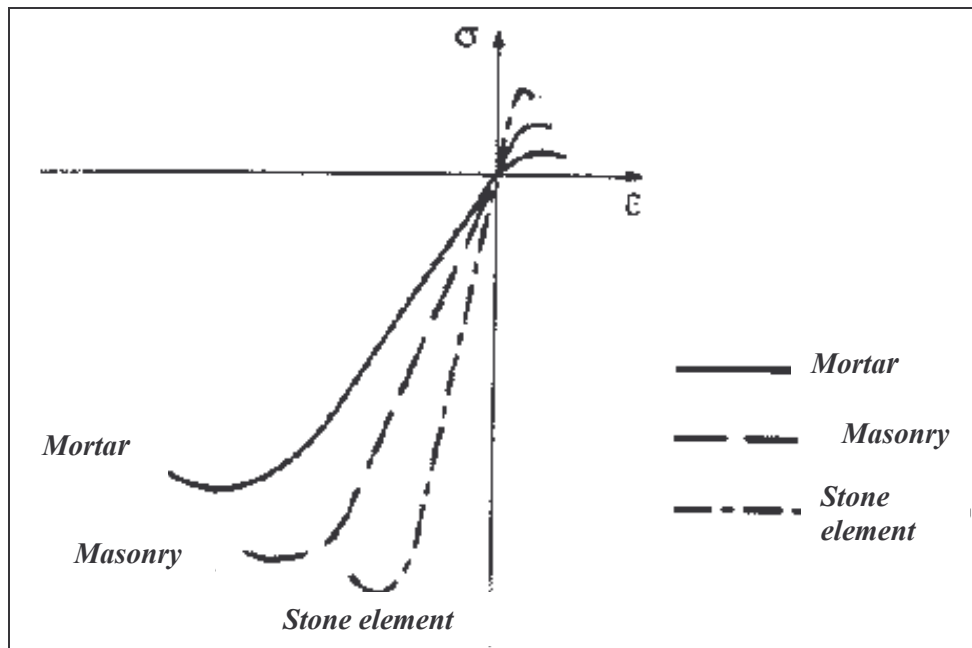


Fig. 4.1.1: Diagramma  $\sigma - \varepsilon$  della muratura

The mortar is composed by three distinct mixed components:

- Water (clear, non-aggressive, without organic material);
- Inert (sand without organic material, earthy or clay);
- binder.

Depending on the type of binder, the mortar may be defined as:

- air-setting, if the binder is hydrated lime;
- hydraulic, if the binder is hydraulic lime;
- cement, if the binder is cement;
- composed, if the cement is mixed with another binder.

The Italian design provisions ([2] and [3]) define six different mortar types, based on their composition, showing the average compression strength  $f_{mm}$ :

TYPE	COMPONENTS					CLASS	$f_{mm}$
	cement	air-setting	hydraulic	sand	pozzolana		Mpa
<i>Cementitious</i>	1	----	----	3	----	M1	12
<i>Cementitious</i>	1	----	0,5	4	----	M2	8
<i>Mixed</i>	1	----	1	5	----	M3	5
<i>Mixed</i>	1	----	2	9	----	M4	2,5
<i>Pozzolanic</i>	----	1	----	----	3	M4	2,5
<i>Hydraulic</i>	----	----	1	3	----	M4	2,5

Table 4.1.1: Classification of the different kinds of mortar

The mortar composition heavily influence the global masonry strength; in seismic regions only cement mortar should be used as reported in the design code provisions. Considering the executive point of view, the mortar horizontal layers should be around 0.5-1 cm thick in order to prevent their expansion under load combination avoiding horizontal stresses on the masonry.

Recent studies have shown that the mortar mechanical properties are characterized by significant differences according to the experimental tests performed in order to obtain the main structural capacity parameters. In fact, the values obtained by using compression tests performed on mortar samples (cubic or prismatic) and the values computed by compression tests directly on the masonry lead to results totally different. The aforementioned phenomena depend mainly on the different amount of water present in the mortar joint that in case of the joints realized *in-situ*, suffers a significant reduction due to the stone elements absorption.

Regarding to the stone element, different types are listed in the following:

- natural stone, obtained by cutting the rock, should not be brittle or flaky, have good frost resistant and have good adhesion to the mortar also. Comparing all the different natural stones, limestone and tuff have good resistance combined with an easy workability.
- artificial stones, generally formed in parallelepiped shape, obtained by using the following materials:
  - brick (e.g. clay bricks);
  - concrete.

The compressive strength is an important mechanical property of stone elements, natural or artificial, defined by the design provisions related to the characteristic compressive strength  $f_{bk}$ .

$$f_{bk} = 0.75 \cdot f_{bm}$$

where  $f_{bm}$  is the average compressive strength obtained by testing 30 specimens.

#### 4.2. Masonry mechanical characteristic computations

The evaluation of the masonry mechanical characteristics is a very complex issue and requires, as essential parameter, the knowledge of strengths and material elastic modulus. Even using reliable calculation procedures the material mechanical characteristics influence the outcomes; in fact, numerical simulation results show high variations in terms of global response of the masonry panels, slightly changing the material properties.

Therefore, the masonry is treated as an equivalent material whose characteristics are highly dependent on the following factors: stone element and mortar mechanical properties and constructive details. Thus, the masonry mechanical performances can be detected only by fixing typological parameters and constructive details. The experimental data available in literature are related to different masonry types and several testing method and, moreover, these data are derived by using formulas processed for different collapse criteria.

The masonry strength capacity computation can be analyzed by applying the following tests:

- *simple compression tests* (carried out on panels and walls): the test allows to apply the compression load by using two hydraulic jacks acting on sharing plates placed on the specimen extreme sections through a mortar layer; then the material constitutive law, the compression strength capacity and the corresponding deformation can be detected;
- *diagonal compression tests*: the test methods are codified by ASTM rules; the compression load is applied on the panels considering an inclined direction of  $45^\circ$  with respect to mortar layers; the collapse occurs in opposite direction compared to the tensile stresses.
- *Shear-compression tests*: the rectangular masonry panels are subjected to vertical load constantly applied on the top of the specimens and to horizontal load gradually increased throughout the test. The external

constraints should allow to have horizontal displacements but not rotations. These tests provide stress states very close to those found in real buildings under earthquake events. The test may be conducted by gradually increasing the horizontal load up to the masonry panels collapse in order to provide the shear capacity considering a predetermined normal stress  $N$ . The horizontal load and the corresponded displacements define the masonry panel characteristic curve, useful to evaluate the real behavior of masonry structures real behavior under seismic actions.

In general, the masonry strengths obtained by using the aforementioned tests are not comparable each other because of different stress states on the samples.

### 4.3. The vertical bearing elements of the masonry buildings

The vertical bearing structures of masonry buildings are constituted by two-dimensional elements (solid or perforated walls) bending in two orthogonal directions.

Considering the loads acting on the structures the following classification can be done. Related to the gravitational load:

- bearing masonry panels, subjected to self-weight, to the vertical elements self-weight and to horizontal structure load;
- Non-bearing walls, only affected by self-weight (e.g. partition walls);

Related to horizontal loads, however, the following grading can be done:

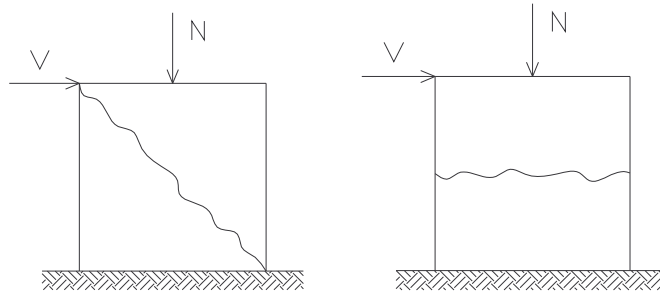
- strut masonry panels, which are opposed to horizontal forces in the longitudinal direction (parallel to them);
- connecting walls, arranged orthogonally to the horizontal force direction.

With respect to the horizontal actions the structural elements (walls and horizontal structures) may exhibit isolated or combined behavior: in the first, every structural panel, subjected to horizontal and vertical actions, behaves as an element completely independent from the others. In the second case, due to the horizontal structures, the masonry walls cooperate to absorb external stresses. The transversal and longitudinal masonry panels collaboration may be considered as a safety reserve. In fact, several

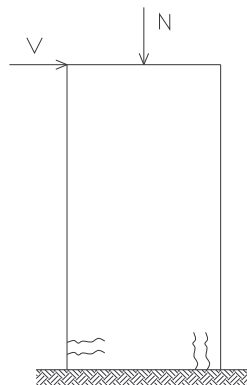
experimental programs have shown that all the masonry building walls can be assumed isolated without making great errors in terms of global strength capacity.

The walls of masonry buildings can be divided into two types: without opening or with opening. The solid masonry panels (without openings) are composed by a two dimensional structural element ( $H$  and  $B$ ) with constant or variable thickness ( $s$ ). The aforementioned masonry panel behaviour, with respect to the in plane horizontal actions, depends on the  $H/B$  ratio (as well as on the normal stress applied):

- Panels with  $H/B$  ratio close to the unity, usually have diagonal crack patterns due to the shear actions;
- Particular types of masonry panels with  $H/B$  ratio close to the unity can show horizontal cracks due to the sliding shear action.



- Panels with  $H/B$  ratio more than 1.5, usually have crack patterns characterized by short horizontal and vertical damages as reported in the following picture:



To understand the link between the collapse mechanism and H/B ratio it is necessary to observe the total displacement of a masonry panel characterized by H (height) x B (width) x s (thickness) when an horizontal force is acting on the structure; the total displacement is composed by two different terms, flexural ( $\delta_m$ ) and shear ( $\delta_v$ ) displacement and they are represented by the following formulas:

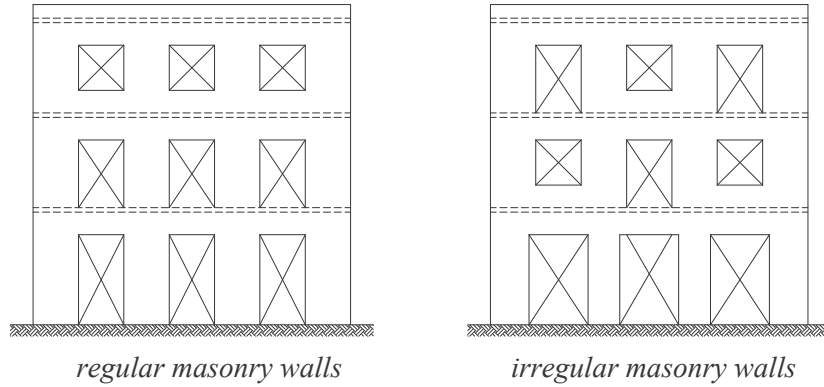
$$\delta_M = \frac{FH^3}{3EI} = \frac{F \cdot H^3}{\frac{3 \cdot E \cdot s \cdot B^3}{12}} = \frac{4 \cdot F}{E \cdot s} \cdot \left( \frac{H}{B} \right)^3$$

$$\delta_V = \frac{\chi \cdot F \cdot H}{G \cdot A} = \frac{\chi \cdot F}{G \cdot s} \cdot \left( \frac{H}{B} \right)$$

Therefore, the flexural displacement prevails with respect to the shear displacement when H/B ratio is more than the unity, while is the second term to be more important when the aforementioned ratio is less than the unity.

The masonry walls with openings are always characterized by rectangular shape and they are defined in the following:

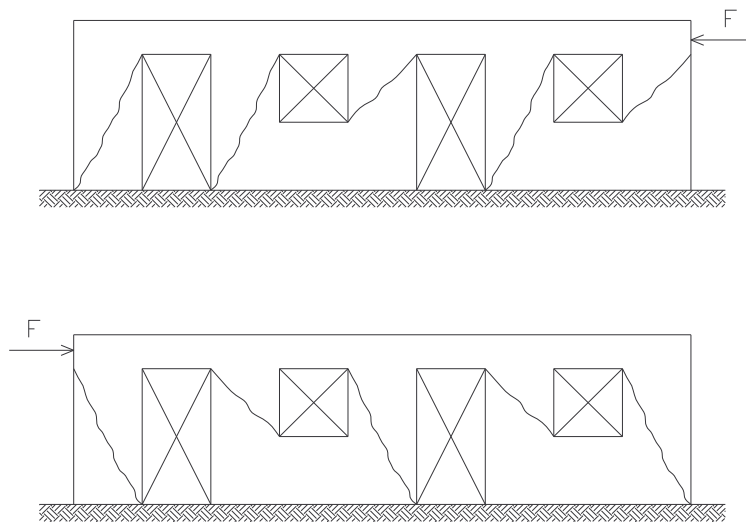
- regular, if the openings are lined and have the same height for each floor;
- irregular, if the openings have different heights or are not aligned.



If the openings border lines are ideally extended, several structural parts can be detected and reported in the following:

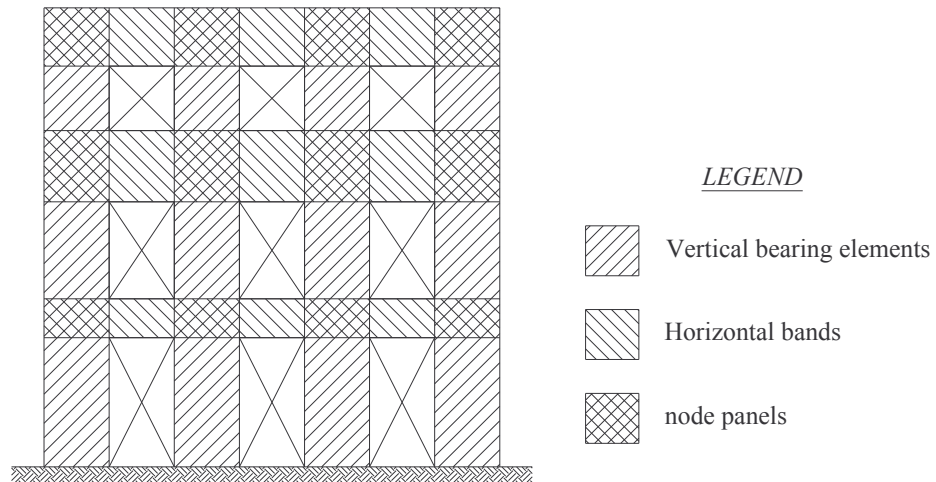
- horizontal bands of masonry lying between two openings (except for the last level); they have a constant height and represent the horizontal bearing elements of the walls (their function is to distribute and transmit the loads);
- bands between two vertical openings of the wall (except for the ends of the wall) and characterized by constant width  $B$ ;

Looking at the masonry crack patterns characterized by irregular openings subjected to intense seismic events, it is noticed that the vertical bearing structural elements with different heights have also different behaviour depending on the direction of the earthquake direction :



The walls, therefore, can be in-plane schematized by vertical bearing elements and bands. The intersection between them defines another important element, called nodal panel. The latter plays an important role in the global response of the buildings because of its bearing capacity and it allows a better transmission of the loads.





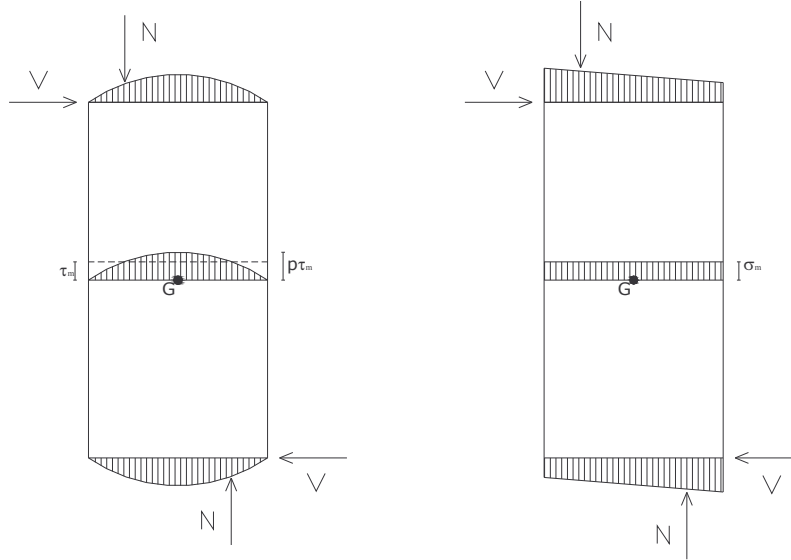
#### 4.4.Collapse mechanism of vertical bearing elements

Two possible collapse mechanism types can be detected on vertical bending elements: the first, common in slender panels, is due to stresses acting on the extreme sections when the normal stresses reach the maximum value in one or more points; the second mechanism (which is associated with panel brittle behaviour) is induced by shear stresses which exceed the ultimate tensile normal stress (almost always through the stone elements) or, sometimes, due to sliding mechanism (usually between stone elements and mortar).

With reference to the collapse mechanisms  $R_i$  and  $R_s$  are the shear and normal stress resultants acting on the bottom and on the top of the masonry panel, respectively. Such resultants should be balanced at the translation and rotation, and thus, they are characterized by the same intensity but opposite direction. Additionally, because such actions must be balanced by the stress state in the masonry panels where they act, an ideal strut can be considered inside the panel itself (identifying the material reagent part). Taking into account that, depending on whether the resulting stress is internal or external to the inertia central core, each section can be entirely or partially reagent. The diagram amplitude  $b$  and the maximum normal stress  $\sigma_{\max}$  may be different for the

sides of masonry panel, but their product has to be constant in order to verify the vertical equilibrium. In addition, the vertical bearing elements subjected to vertical and horizontal loads can also reach a tensile maximum value due to the shear actions.

This particular case can be identified on the central part of the masonry panels, where the shear stress is greater. The tensile stresses are no longer tolerated by the material leading to a diagonal cracking progressively extended from the centre to the whole panel surface involving both stone elements and mortar.



Another collapse mechanism due to the shear load is characterized by the sliding displacement.

*References*

- [1] N.Augenti, 2004. *“Il calcolo sismico degli edifici in muratura”*. UTET Università, codice EAN: 978887750942
- [2] Ministero dei Lavori Pubblici, Decreto 20 Novembre 1987. *“Norme tecniche per la progettazione, esecuzione e collaudo degli edifici in muratura e per il loro consolidamento”*. Pubblicato nel supplemento ordinario alla G.U. n. 285 del 5 Dicembre 1987.
- [3] Decreto Ministeriale 14 Gennaio 2008. *“Nuove norme tecniche per le costruzioni”*. Pubblicato sulla G.U. il 4 Febbraio 2008.

## 5. FINITE ELEMENT MODELING AND MASONRY PANELS' VALIDATIONS

In the previous chapter the different seismic damage typologies of masonry structures have been introduced. In particular, the in plane seismic behaviour of the vertical structural elements was highlighted describing the feasible collapses mechanisms. Moreover, the influence of the aforementioned construction units with respect to the global seismic response of the masonry structures was also considered.

Thus, giving to those structural elements a strength increment or improving seismic performance is considered of primary importance to preserve the masonry buildings structural integrity under seismic actions and to assure the human life preservation.

Nowadays, several design options for seismic strengthening of masonry panels have been introduced in construction field, as traditional strengthening interventions or based on the use of fiber reinforced polymers.

In recent years, the innovative solutions have been characterized by a growing interest of scientific community that have led to a legal document for design and verification of structures reinforced by using the aforementioned materials (CNR DT 200/2004 [1]).

At this point, establishing the design solution effectiveness for structural strengthening by using innovative materials assumes great interest. Furthermore, the attention has been pointed out on the reinforced masonry panels' global performances by changing the component mechanical characteristics, such as bricks and mortar, and using different geometrical solution for strengthening arrangements.

For that reason, experimental tests on masonry panels performed by several authors were selected and numerical simulations have been carried out by using finite element modeling software, DIANA TNO rel.9.2 [2].

The tests were selected considering different masonry types in order to get results that were not related to the material mechanical characteristics, such as bricks and mortar, or related to the interfaces between the masonry panels and fiber composite materials.

The three experimental programs, taken into account to model the numerical simulations, have been listed in the following:

- Alcaïno et al. [3]: experimental tests were performed on reinforced and unreinforced hollow clay brick masonry panels subjected to shear loading;
- Pascale et al. [4]: experimental tests were performed on unreinforced clay brick masonry panels in order to design a shear strengthening system by using Glass Fiber Reinforced Polymer (GFRP);
- Manfredi et al. [5]: shear-compression experimental tests were set up on unreinforced tuff masonry panels in order to perform an innovative strengthening solution by using steel frames.

### 5.1. Masonry panels modeling

The present work has focused on in plane behaviour of masonry panels subjected to horizontal actions; thus a two dimensional non linear structural analysis has been performed.

The masonry panel modelling was based on separate definition of the two components, brick and mortar, respectively, already used by Lignola et al. [6], where the global behavior of tuff masonry panels was analyzed by changing the mortar thickness in order to reproduce irregularities and defects of real installations.

Hence, plane stress elements were selected because the thickness was smaller than other element dimensions and, moreover, the loads act in the plane of the elements.

Plane stress elements are characterized by the fact that the stress component perpendicular to the face is zero ( $\sigma_{zz} = 0$ ). These elements may only be applied if there is no bending outside the plane of the structure, as in these masonry panels.

Linear and non linear elastic mechanical properties were defined for both materials. In particular, the isotropic elastic behavior was defined by the Young's modulus,  $E$ , and poisson's coefficient,  $\nu$ ; the post elastic behavior was modeled according to Rankine/Von Mises criterion to define the tensile and compression performances respectively, by means of the tensile ( $f_t$ ) and compression ( $f_c$ ) strengths and tensile ( $G_f$ ) and compression ( $G_{fc}$ ) fracture energies.

The quasi brittle behavior of both materials has been simulated by using post peak linear softening.

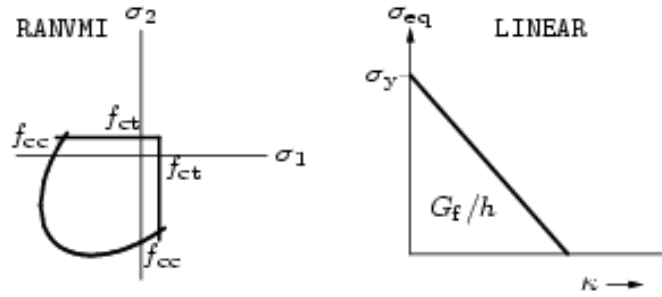


**Figure 5.1.1:** Rankine/von Mises criteria and post peak linear softening behaviour

Another important issue for non linear analyses is the mesh element choice. Linearly interpolated isoparametric elements (e.g. Q8MEM, Q8OME, etc) have intrinsic shortcomings, like parasitic shear and volumetric locking, which cannot be easily dealt with in nonlinear analyses.

Unfortunately, in nonlinear analysis the use of the aforementioned elements harm the stability of the solution procedure and may cause spurious kinematic modes. It is therefore recommended to apply higher order elements, for instance the quadratically interpolated CQ16M.

The CQ16M element is an eight-node quadrilateral isoparametric plane stress element. It is based on quadratic interpolation and Gauss integration.

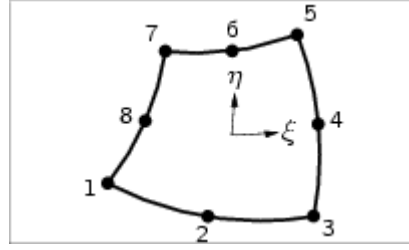


**Figure 5.1.2:** CQ16M quadrilateral isoparametric plane stress elements

The polynomial for the displacements  $u_x$  and  $u_y$  can be expressed as:

$$u_i(\xi, \eta) = a_0 + a_1 \cdot \xi + a_2 \cdot \eta + a_3 \cdot \xi \cdot \eta + a_4 \cdot \xi^2 + a_5 \cdot \eta^2 + a_6 \cdot \xi^2 \cdot \eta + a_7 \cdot \xi \cdot \eta^2$$

Typically, this polynomial yields a strain  $\epsilon_{xx}$  which varies linearly in  $x$  direction and quadratically in  $y$  direction. The strain  $\epsilon_{yy}$  varies linearly in  $y$  direction and quadratically in  $x$  direction. The shear strain  $\gamma_{xy}$  varies quadratically in both directions.

The three masonry panels were subjected to a shear-compression test. The gravitational load has been applied on the top surface of the panel, while the horizontal action has been modeled by means of gradual displacement increment due to the hydraulic jack actions.

Capacity curves have been provided by numerical simulations, focusing on the initial stiffness, peak shear capacity and the displacement corresponding to the maximum shear capacity of masonry panels.

## 5.2. Masonry panel descriptions

### 5.2.1. Masonry panel proposed by Alcaino et al.[3]

The present work is based on the experimental shear-compression tests available in literature, regarding masonry panels made by hollow clay bricks.

In the next, Alcaino et al. experimental tests have been reported and analyzed with particular attention on theoretical-experimental comparison of shear capacity and crack patterns.

The masonry panels were made by standard dimension hollow clay bricks characterized by  $112 \times 290 \times 140 \text{ mm}^3$  arranged in 16 layers and 15 mm thick of premixed cementitious mortar were interposed among the brick beds.

Two steel bars 25 mm of diameter were placed close to the panel extreme sections in order to avoid the collapse mechanism due to flexure.

Two R.C. beams have been located on the bottom and on the top of the panels to embed the panels by using fixed restrains and to allow the load application, respectively.

In particular, a distributed gravitational load equal to 98 kN was applied in order to reproduce the actions normally present in three stories masonry buildings. The horizontal actions have been modeled by using hydraulic jack to impress controlled displacements applied on a reference point placed on the top of the panels, ensuring the plan shape of the top panel sections, always parallel to the ground.

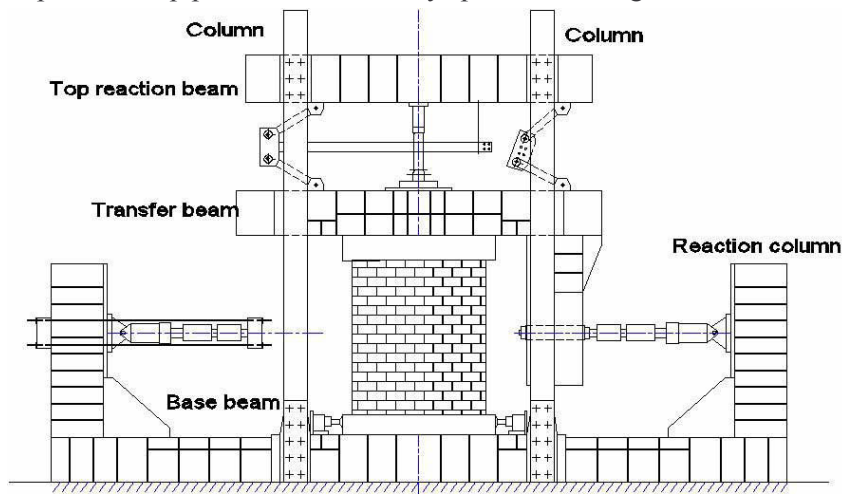


**Figure 5.2.1.A:** Set up of the Alcaïno et al. experimental tests

The numerical simulations have been modeled to have a maximum displacement of about 15 mm considered enough compared to the maximum value (14 mm) reached during the experimental tests.

Several material mechanical properties were not described in the previous reported paper selected to model the numerical simulations, and thus they were selected inside a range of experimental values, computed by Kaushik et al. [7] Mathematical equations based on experimental regressions have been proposed by the authors in order to relate the material compression strength with the Young's modulus. In this case, the material



mechanical characteristics have been deduced from the technical documentations provided by the manufacturer; the range of the Young's modulus values has been assigned based on those values. Moreover, even for the compression and tensile fracture energies of both materials a range of feasible values has been assumed in order to obtain the model validation.

In the following chapters the masonry panel global behavior has been detected by changing both compression and tensile fracture energies, justifying the chosen values in terms of mechanical performances. In the following tables the material mechanical properties used to validate and to implement the models have been reported.

	$E$	$\nu$	$f_c$	$f_t$	$G_{f,c}$	$G_{f,t}$
	$kN/mm^2$	-	$N/mm^2$	$N/mm^2$	$N/m$	$N/m$
<b>Bricks</b>	2,5	0,25	15	0,40	60	40
<b>Mortar</b>	1	0,20	10	0,30	0,03	0,045

**Table 5.2.1.A:** Material mechanical properties

<i>Experimental equations [6]</i>	<i>Reference values</i>	
$E_b = 150 \cdot f_c \div 500 \cdot f_c$	2250 ÷ 7500 N/mm <sup>2</sup>	Brick Young's modulus
$E_m = 100 \cdot f_c \div 400 \cdot f_c$	1000 ÷ 4000 N/mm <sup>2</sup>	Mortar Young's modulus

**Table 5.2.1.B:** Young's modulus reference values

The steel bars were placed on the masonry panel to have a collapse mechanism due to the shear actions. Thus, they were modeled using structural elements anchored on both top and bottom beams, avoiding bond between the masonry panels and the steel bars along its length.

The steel bar mechanical performances have been tested in the laboratory and reported in the following table, where  $d$ , is the steel bar diameter and  $f_y$  is the yielding stress.

	$d$	$E$	$f_y$
	$mm$	$kN/mm^2$	$N/mm^2$
<b>Steel bars</b>	25	210	420

Table 5.2.1.C: Steel bars mechanical properties

The experimental tests have been carried out on strengthened masonry panels by using carbon fiber reinforced polymer (CFRP), applied on the panel surfaces by means of diagonal and horizontal layouts.

Thus, the numerical analyses were also performed on reinforced masonry panels in order to validate the global response of the structural elements when an innovative strengthening system is applied.

The CFRP has been modeled according to the perfect bond criterion, without taking into account the interfacial mechanical properties. The adopted properties in terms of Young's modulus  $E$ , dry fiber ultimate stress  $f_{fu}$  and ultimate deformation  $\epsilon_{fu}$  have been provided by the manufacturer and reported in the following table:

	$E$	$f_{fu}$	$\epsilon_{fu}$
	$kN/mm^2$	$N/mm^2$	
<b>C-FRP</b>	230	4300	2.1%

Table 5.2.1.D: CFRP mechanical properties

The debonding stress  $f_{del}$  has been computed according to the CNR DT 200/2004 and reported in the next two equations are given depending on the different debonding modality; moreover,  $k_{cr}$  was computed assuming  $c_1$  equal to 0.64 in order to take into account the average material mechanical properties:

$$f_{fdd} = \frac{1}{\gamma_{fd} \cdot \sqrt{\gamma_c}} \cdot \sqrt{\frac{2 \cdot E_f \cdot \Gamma_{fk}}{t_f}} \quad \text{extreme debonding (mod.1)}$$

$$f_{fdd} = \frac{k_{cr}}{\gamma_{fd} \cdot \sqrt{\gamma_c}} \cdot \sqrt{\frac{2 \cdot E_f \cdot \Gamma_{fk}}{t_f}} \quad \text{intermediate debonding (mod.2)}$$

where  $\Gamma_{fm} = c_1 \cdot \sqrt{f_{i,a} \cdot f_{it,a}}$  is the FRP fracture energy depending on the  $c_1$  coefficient, the compression and tensile brick strengths.

The numerical simulations modeled by means of finite element produced the results listed in the next, where the comparison between the experimental and numerical outcomes have been also reported:

<i>Panels</i>	<i>Average Experimental Shear Capacity</i>	<i>FEM Shear Capacity</i>	<i><math>\Delta</math> (Exp- FEM)</i>
	<i>kN</i>	<i>kN</i>	<i>%</i>
<i>UnReinforced</i>	141	153	-9,3%
<i>H_100</i>	215	206	4,2%
<i>H_150</i>	225	223	1,1%
<i>D_200</i>	222	222	-0,1%
<i>D_300</i>	255	256	-0,3%

**Table 5.2.1.E:** Comparison between FEM and Experimental results

The theoretical and numerical shear capacity evaluation were performed after, using the two different formulas proposed by CNR design code and Prota et al. [8] for horizontal and diagonal reinforcement layouts, respectively.

$$V_{rd,f} = \varepsilon_{fd} \cdot E_f \cdot A_f \cdot \cos \alpha \quad \text{Diagonal layout FRP contribution} \quad (1)$$

$$V_{rd,f} = \frac{1}{\gamma_{rd}} \cdot 0,6 \cdot d_f \cdot f_{fd} \cdot \frac{A_f}{p_f} \quad \text{Horizontal layout FRP contribution} \quad (2)$$

where  $\varepsilon_{fd}$  is the minimum value between the design ultimate FRP deformation and the deformation produced by the intermediate debonding;  $A_f$  is the FRP cross section area,  $\alpha$  is the fiber angle in diagonal layout,  $d_f$  is the distance between the compressed panel section and the center of gravity of reinforced system,  $p_f$  is the spacing between the strips and  $f_{fd}$  depends on the FRP Young's modulus  $E_f$  and the deformation  $\varepsilon_{fd}$ .

<i>Panels</i>	<i>Average Experimental Shear Capacity</i>	<i>Theoretical shear Capacity</i>	<i><math>\Delta</math> (Exp-teor)</i>
	<i>kN</i>	<i>kN</i>	<i>%</i>
<i>UnReinforced</i>	141	135	4,3%
<i>H_100</i>	215	179	16,7%
<i>H_150</i>	225	199	11,6%
<i>D_200</i>	222	280	-26,0%
<i>D_300</i>	255	306	-19,5%

**Table 5.2.1.F:** Comparison between the experimental and theoretical results

The comparison between numerical and experimental results points out a satisfactory value of the computed shear capacity; the difference was lower than 10 %. Similar results have been obtained comparing the experimental and theoretical outcomes showing an average difference in percentage equal to 13%. Furthermore, the crack patterns obtained by the numerical simulations are almost equal to the crack propagations showed during the experimental tests where a principal diagonal crack comes before distributed micro-cracking on the panel surfaces. The experimental tests have been set up by means of cyclic loading producing two symmetric diagonal cracks, while the Finite Element numerical simulation has been performed applying a monotonic horizontal action causing one principal diagonal cracks on the compressed strut direction.

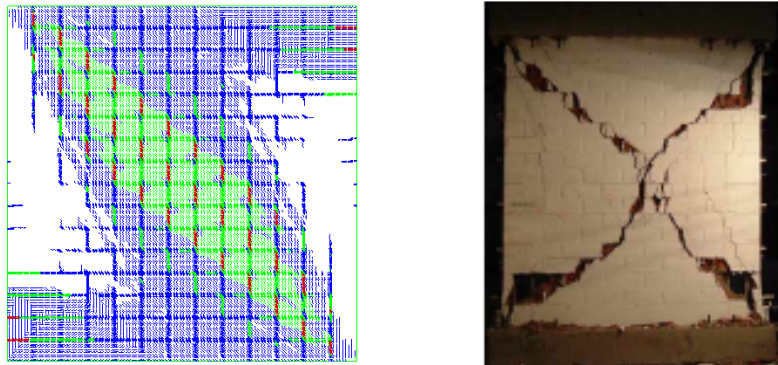


**Figure 5.2.1.B:** Numerical/Experimental comparison in terms of crack patterns of unreinforced panels

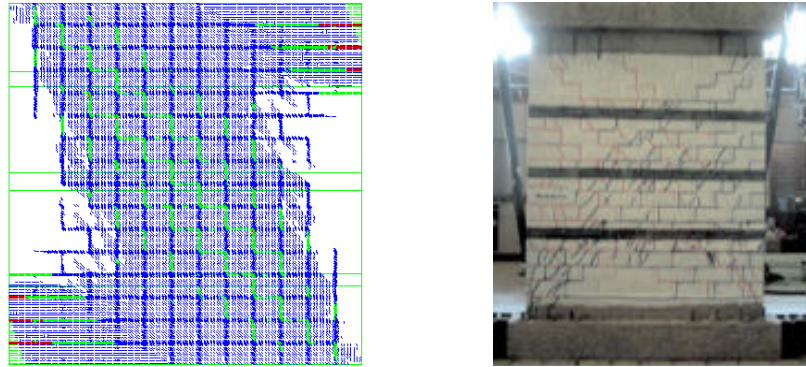


**Figure 5.2.1.C:** Numerical/Experimental comparison in terms of crack patterns of horizontal layout reinforced panels

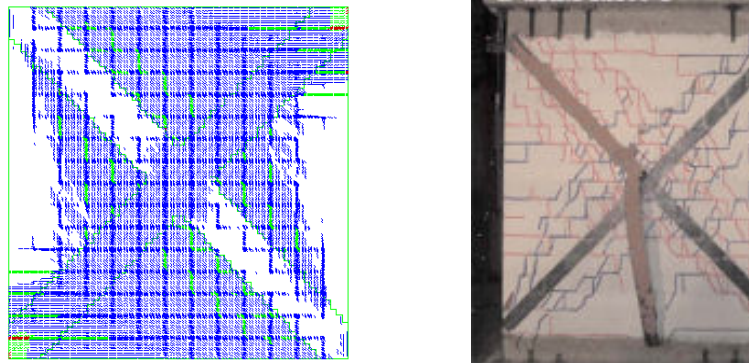


**Figure 5.2.1.D:** Numerical/Experimental comparison in terms of crack patterns of diagonal layout reinforced panels

### 5.2.2. Masonry panel proposed by Pascale et al.[4]

In the following the second experimental program performed by Pascale et al. have been described and shear capacity, displacements of a reference point and crack patterns were also highlighted.

The masonry panels were made by clay bricks characterized by standard dimensions equal to  $55 \times 120 \times 250 \text{ mm}^3$ . The bricks were arranged in 15 layers and 15 mm thick premixed cementious mortar was placed among the brick rows.

Two steel beams were placed on the bottom and on the top of the experimental structural elements in order to ensure the correct loads application and to avoid out-of-plane overturning. Moreover a particular system composed by steel inserts were designed to increase the stiffness and to avoid local deformations and collapses. The distributed gravitational load was applied on the specimen top sections by means of two forces equal to 50 kN and spacing at 600 mm each other. The horizontal actions were realized by means of controlled displacements applied on a reference point placed at 1000 mm from the panel foundation beam by using a hydraulic jack.

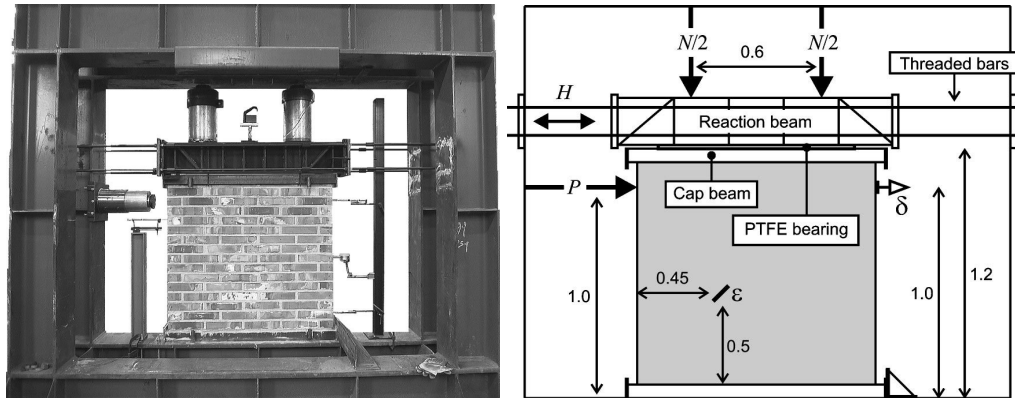


Figure 5.2.2.A: Set up of Pascale et al. Experimental tests

The numerical analyses have been modeled to a global displacement of 15 mm against the reached experimental displacements smaller than 14 mm.

As well as the experimental tests described previously, several material mechanical properties were not provided in the work made by *Pascale et al.* and thus, a range of feasible values was taken into account in order to justify the numerical simulation input data. In fact, compression and tensile fracture energies of both materials were calibrated inside a range composed by typical values for bricks and mortar used to build the specimens. Furthermore, correlation formula were also used to compute the mortar tensile strength starting from its compression strength. The material mechanical characteristics used into the finite element numerical simulations were listed in the following

	$E$	$\nu$	$f_c$	$f_t$	$G_{f,c}$	$G_{f,t}$
	$kN/mm^2$	-	$N/mm^2$	$N/mm^2$	$N/m$	$N/m$
<b>Bricks</b>	15,8	0,13	62,0	8,90	120 *	2,50 *
<b>Mortar</b>	0,32	0,20	11,0	0,30 *	190 *	2,50 *

**Table 5.2.2.A:** Bricks and mortar mechanical properties

Comparing the experimental tests and numerical simulation results satisfactory accordance between them is reached, showing a difference in percentage less than 10% in term of shear capacity and global displacements (see **Table 5.2.2.B**)

Furthermore, the crack patterns shown by numerical simulation are almost the same as those reached during the experimental tests on the specimens. In fact, a sliding shear crack on both top and bottom panel sections has been shown and a crack pattern distributed on the panel surface is also depicted (**Figure 5.2.2.B.**).

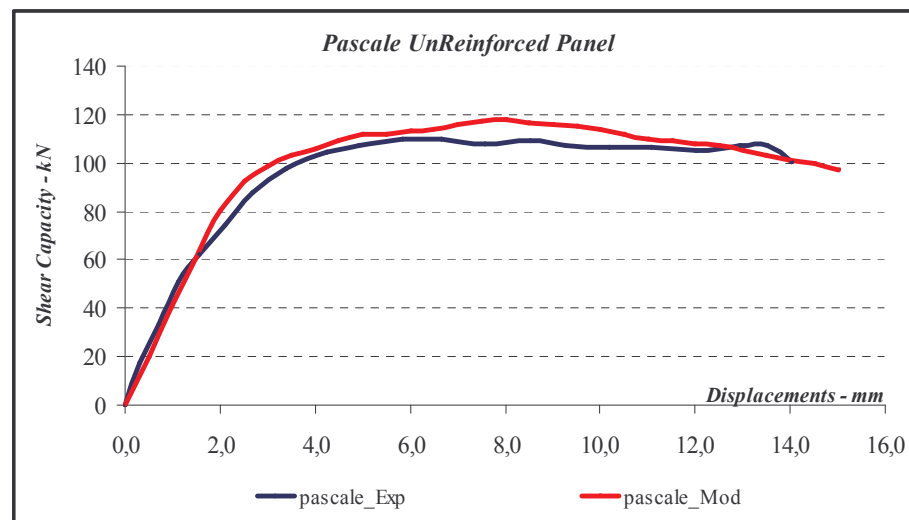


**Figure 5.2.2.A:** Experimental and numerical Shear Capacity vs Displacements graphs

<i>Panel</i>	<i>Experimental Result – Shear capacity kN</i>	<i>FEM result – Shear Capacity kN</i>	<i><math>\Delta</math> (Exp-FEM) %</i>
<i>UnReinforced Panel</i>	109,0	118,0	-8,3 %

<i>Panel</i>	<i>Experimental Result – Max Displacement mm</i>	<i>FEM result – Max Displacement mm</i>	<i><math>\Delta</math> (Exp-FEM) %</i>
<i>UnReinforced Panel</i>	6,9	7,5	+8,7 %

**Table 5.2.2.B:** Comparison between experimental and numerical results

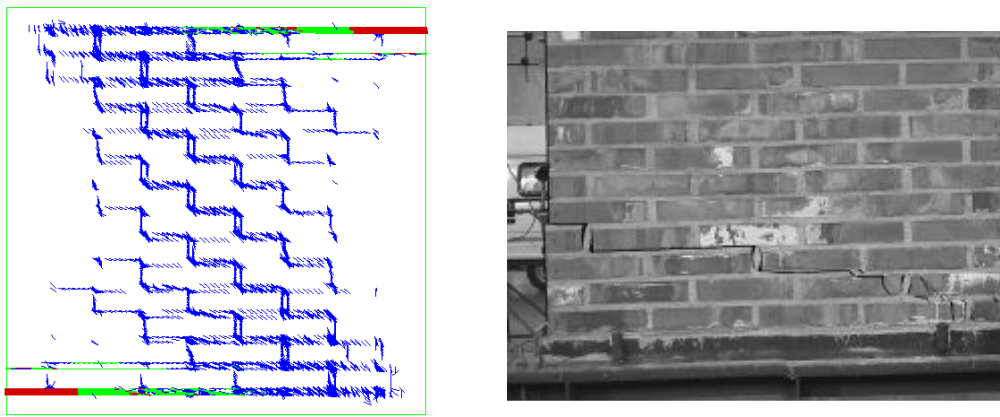


**Figure 5.2.2.B:** Experimental / numerical validation

### 5.2.3. Masonry panel tested by Manfredi et al.[5]

In the following the experimental tests performed by Manfredi et al. were described and were analyzed in numerical simulations in terms of shear capacity, global displacements and crack patterns. The masonry panels were made by tuff blocks characterized by standard dimensions equal to  $240 \times 120 \times 400 \text{ mm}^3$ , arranged in 5 rows using a premixed cementitious mortar layers 15 mm thick.



Two HE 300 steel beams were placed on both top and bottom specimen sections in order to have the in plane stresses only on the panel and to avoid out-of plane overturning or bending actions. The connection between the masonry panel and the set up foundation system was made by RC beam 250 mm high and another RC beam characterized by the same dimensions placed to apply the horizontal and vertical loads on the specimens. The experimental tests were designed applying on the masonry structural elements two different distributed gravitational loads equal to 130 kN and 325 kN respectively, to study the differences in terms of specimen global response, due to various load level. The numerical simulation was validated considering on the model both 130 kN and 325 kN gravitational loads.

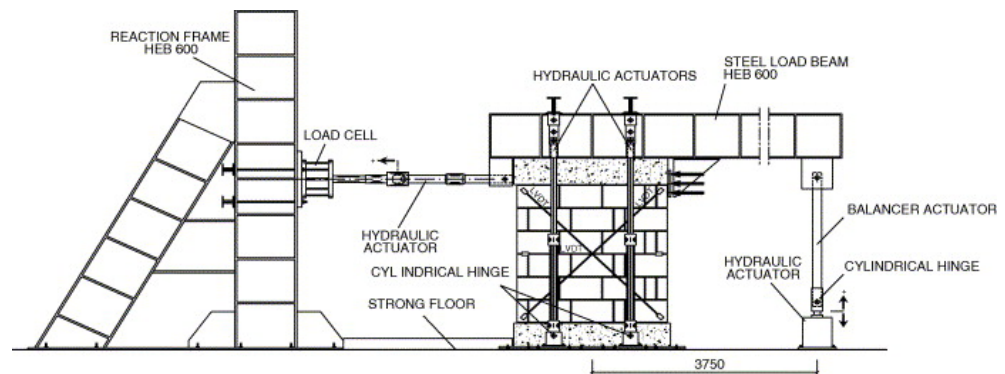


**Figure 5.2.3.A:** Set-up of Manfredi et al. Experimental tests

The first load was applied up to a global displacement of about 15 mm, while the second was realized considering a maximum global displacement equal to 5 mm as shown by the available experimental results. The horizontal actions were modeled by using hydraulic jacks in order to implement controlled displacements on the masonry specimens, applied on a reference point placed on the top RC beam.

Manfredi et al. work did not provide compressive and tensile fracture energies for both materials and the mortar tensile strength; thus, experimental formulas available in literature were selected to complete the available information and knowledge of masonry panel.

In the following table the material mechanical properties were listed:

	$E$	$\nu$	$f_c$	$f_t$	$G_{f,c}$	$G_{f,t}$
	$kN/mm^2$	-	$N/mm^2$	$N/mm^2$	$N/m$	$N/m$
<b>Bricks</b>	0,50	0,20	3,50	0,25 *	11,2 *	0,06 *
<b>Mortar</b>	0,25	0,20	2,00	0,10 *	8,00 *	0,02 *

Table 5.2.3.A: Material mechanical properties

The shear capacity computed by the numerical simulation compared to the experimental results shows a good approximation characterized by a difference in percentage less than 5 %. The masonry panel global displacements evaluated on the reference point when the maximum shear capacity is reached, are characterized by a difference in percentage almost equal to 8 %. Besides the numerical crack patterns appear to be equal to the actual crack propagation noticed during the experimental tests. In particular, the first load condition shows clearly three diagonal cracks, while the second shows only one widespread diagonal crack. For both load cases, diffused micro-cracks were noticed on the panel surface.

The parametric simulations, considering the CFRP strengthening system application studied in the following chapters, were carried out using the lower gravitational load, because of its more likely to be present in most common masonry buildings.

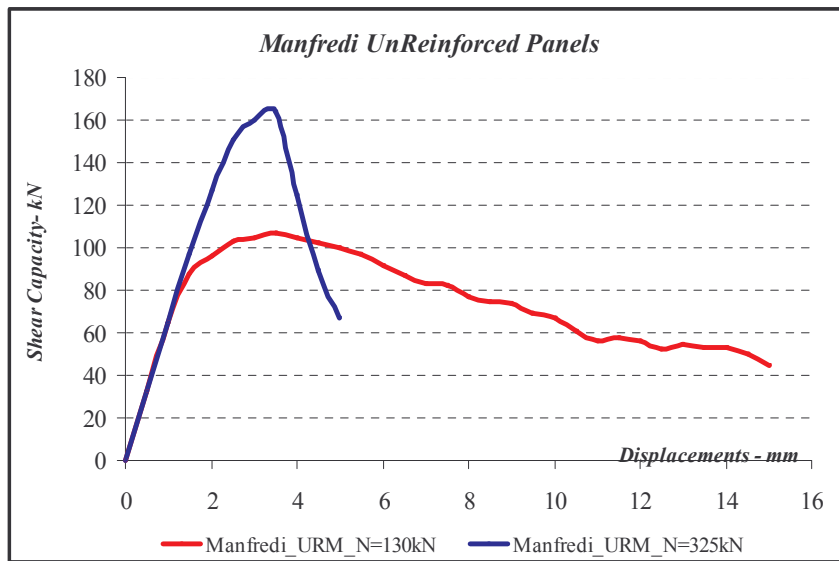


Figure 5.2.3.B: Numerical simulation curves A) Unreinforced panel loaded by N=130kN; B) Unreinforced panel loaded by N=325kN

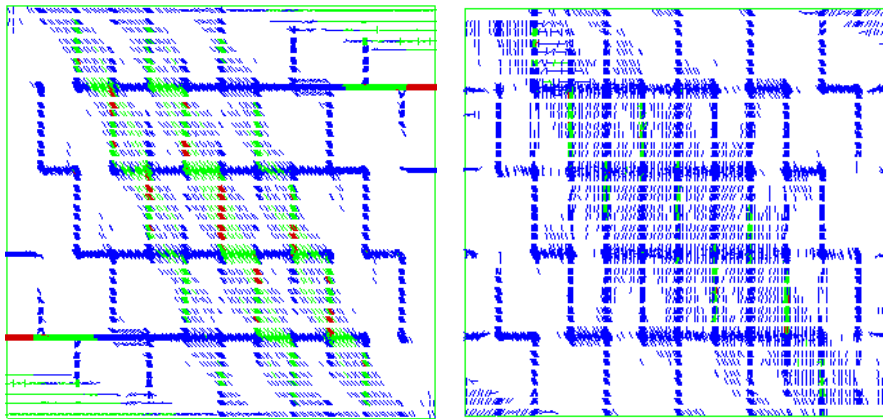
<i>Panel</i>	<i>Experimental Result – Shear capacity kN</i>	<i>FEM result – Shear Capacity kN</i>	<i><math>\Delta</math> (Exp-FEM) %</i>
<i>UnReinforced Panel N=130 kN</i>	102	107	-5,0 %

<i>Panel</i>	<i>Experimental Result – Max Displacement mm</i>	<i>FEM result – Max Displacement mm</i>	<i><math>\Delta</math> (Exp-FEM) %</i>
<i>UnReinforced Panel N=130 kN</i>	3,00	3,25	-8,3 %

<i>Panel</i>	<i>Experimental Result – Shear capacity kN</i>	<i>FEM result – Shear Capacity kN</i>	<i><math>\Delta</math> (Exp-FEM) %</i>
<i>UnReinforced Panel N=325 kN</i>	165,7	164,0	+1,0 %

<i>Panel</i>	<i>Experimental Result – Max Displacement mm</i>	<i>FEM result – Max Displacement mm</i>	<i><math>\Delta</math> (Exp-FEM) %</i>
<i>UnReinforced Panel N=325kN</i>	3,50	3,50	0,0 %

**Table 5.2.3.B:** Comparison between experimental and numerical results



A) Unreinforced masonry panel

 $N = 130 \text{ kN}$ 

B) Unreinforced masonry panel

 $N = 325 \text{ kN}$ 

**Figure 5.2.3.C:** Numerical/experimental validation A) Unreinfrcd panel loaded by  $N=130\text{kN}$ ; B) Unreinforced panel loaded by  $N=325\text{kN}$

### 5.3. Final Remarks about validation

The present chapter is based on the numerical simulation of experimental tests performed in the lab by different authors on three kind of brickwork panels made by using hollow clay bricks, clay bricks and tuff blocks. The numerical simulation was carried based on available data in Finite Element Software DIANA TNO rel.9.2.

The micro-model criterion was taken into account and thus, both bricks and mortar materials were described separately by means of linear elastic and post-elastic behaviour. The validation was based on the numerical model and experimental tests comparison in terms of shear capacity, global displacements and crack patterns. Considering the experimental and numerical simulation average results for all the panels, very good outcomes have been highlighted, reaching a difference always lower than 10 % and in particular:

- ✓ experimental and numerical shear capacity differ about 10 % each other;
- ✓ the experimental and numerical masonry panel global displacements differ about 7% each other;

- ✓ the experimental and numerical crack patterns show a very close crack spread and placing.

After validating the numerical model by comparing the available experimental and numerical results using the aforementioned software, several parametric analyses have been performed as described in the next.

In the following chapter the influence of different values for both compressive and tensile fracture energies were simulated. The fracture energies were not easily computed during the tests, but they affect the obtained numerical results when implemented in the numerical simulation.

A range of feasible values was computed and inside it most likely fracture energy values have been chosen to validate the model. At this point, analyzing the masonry panel global response assume great interest by changing the compressive and tensile fracture energy values, however selected into that range. In particular, three values have been selected for both fracture energies maintaining constant the other mechanical properties used to validate the numerical masonry panels. Another important issue is related to the CFRP strengthening system application. The structural reinforcement geometrical characteristics were changed, producing several parametric analyses to determine the influence of the CFRP mechanical properties on the masonry panel structural behaviour.

The different strengthening arrangements by means of horizontal or diagonal strips have been modeled and compared in terms of shear capacity and global displacements.

In particular, the diagonal layouts were analyzed by choosing different width strips and the horizontal layouts have been changed by means of width strips and spacing.

### References

- [1] CNR DT 200/2004, 2004. *“Guide for the design and construction of externally bonded FRP systems for strengthening existing structures”*. Rome – CNR Institute.
- [2] TNO DIANA rel. 9.2. *“International Software Company for FEA applications in civil and geotechnical engineering”*.
- [3] Alcaino P., Santa Maria H., 2008. *“Experimental response of externally retrofitted masonry walls subjected to shear loading”*. ASCE Journal of Composites for Construction, Vol. 12, issue 5, Pages 489-498.
- [4] T.Stratford, G.Pascale, O.Manfroni and B.Bonfiglioli, 2004. *“Shear strengthening masonry panels with sheet GFRP”*. ASCE Journal of Composites for Construction, Vol. 8(5).
- [5] G.Faella, G.Manfredi, R.Realfonzo, 1991. *“Comportamento sperimentale di pannelli in muratura di tufo sottoposti ad azioni orizzontali di tipo ciclico”* . V Italian Congress - L’Ingegneria Sismica in Italia 1991- Palermo.
- [6] G.P. Lignola, A. Prota and G. Manfredi,, 2009. *“Non-Linear Analyses Of Tuff Masonry Walls Strengthened With Cementitious Matrix–Grid Composites”*, ASCE Journal of Composites for Construction, In Press.
- [7] H.B. Kaushik, D.C. Rai, S.K. Jain, 2007. *“Stress-Strain Characteristics of clay brick masonry under uniaxial compression”*. ASCE Journal of Material in civil engineering, Vol. 19 n. 9, Pages 728-739.
- [8] A.Prota, G.Manfredi, F.Nardone, 2008. *“Assessment of design formulas for In-*

*plane FRP strengthening of masonry walls*". ASCE Journal of composites for construction, Vol.12 n.6, Pages 643-649.

## 6. MASONRY PANELS PERFORMANCES BY CHANGING THE FRACTURE ENERGIES OF BOTH MATERIALS

The strong variability of mechanical properties of materials in masonry structures influences the construction global behavior.

Experimental tests have been usually carried out to evaluate the compression and tensile strength for both mortar and bricks, but they do not easily provide other mechanical properties. Starting from the experimental tests, numerical simulation have been modeled and a comparison between the outcomes was done.

As reported in the previous chapter, the constitutive laws for both mortar and bricks are defined, when micro-modeling is chosen, by means of Rankine (tension) – Von Mises (compression) theory, in order to evaluate the masonry panel performances. Moreover the linear elastic and post elastic behavior of the materials assume great importance with regards to non linear analyses.

Thus the mechanical parameters related to the post elastic masonry panel performances should be known even if experimental tests did not provide them. Several common equations, generally used to relate the material mechanical strength to other material properties, can be found in literature and they can be used to have an extensive knowledge about the masonry panels.

There are several mechanical information necessary to model correctly the brickwork structural elements as, for example, the fracture energies.

In fact, compression and tensile fracture energies, strongly related to the materials strength, are characterized by a crucial role in numerical non linear simulations.



The experimental test programs, carried out on different masonry brickworks (clay bricks or tuff blocks) already validated in the previous chapter, were selected and analyzed by using parametric analyses.

Thus, the aim of these analyses is to point out how the behavior of the panel changes varying these physical quantities, unknown during the experimental tests, but playing a fundamental role to describe properly the panel performances in numerical simulations.

Post elastic non linear behaviour was assumed by means of linear softening and starting from that, both fracture energies were computed as reported in the following:

$$\frac{f_i \cdot \varepsilon_y}{2} = G_f \rightarrow \frac{f_i^2}{2 \cdot E} = 0,5 \cdot \frac{f_i^2}{E} = G_f$$

The fracture energies depend on the strength capacity and deformation; the latter can reach a value three times that reported before and thus:

$$\frac{f_i \cdot 3 \cdot \varepsilon_y}{2} = G_f \rightarrow \frac{3 \cdot f_i^2}{2 \cdot E} = 1,5 \cdot \frac{f_i^2}{E} = G_f$$

Selecting the lowest and the highest values by using the aforementioned formula. The fracture energies range, adopted in the numerical simulation is:

$$\alpha \cdot \frac{f_i^2}{E} \rightarrow \alpha = (0,5 \div 1,5)$$

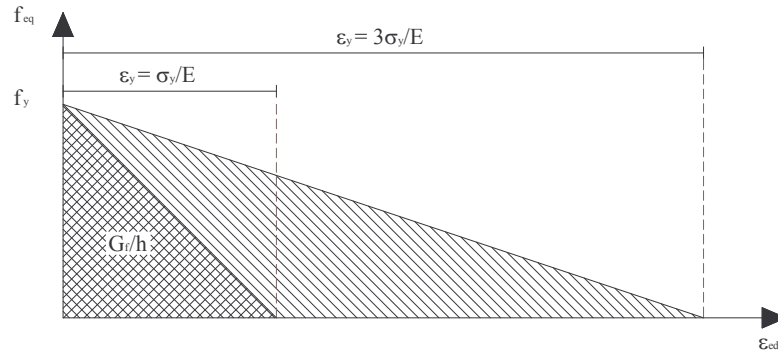


Figure 6.1: Linear softening behavior

In the following, the influence of these energies has been analyzed, highlighting both involved materials on the masonry global behavior.

A range of values for the aforementioned mechanical properties were selected and three of them were implemented into the numerical model in order to assess the panel global response.

<i>1<sup>st</sup> value</i>	$G_{fi} = 0,5 \cdot \frac{f_i^2}{E}$
<i>2<sup>nd</sup> value</i>	$G_{fi} = 1,0 \cdot \frac{f_i^2}{E}$
<i>3<sup>rd</sup> value</i>	$G_{fi} = 1,5 \cdot \frac{f_i^2}{E}$

**Table 6.1:** Fracture energies values

All the plots and summary tables of all the numerical parametric analyses are reported in Annex C.

## 6.1. Alcaïno et al. panels [1]

### 6.1.1. Compressive Fracture Energies for both materials

Alcaïno et al experimental tests were performed on masonry panels composed by hollow clay bricks and premixed cementitious mortar. The validation shown in the previous chapter was based on the mechanical properties reported in the following table. Linear elastic and post elastic behavior was analyzed with respect to Rankine – Von Mises criterion. In particular the linear elastic behavior of both bricks and mortar, have been defined in terms of Young's modulus and poisson's coefficient; post elastic non linear behavior of both materials have been described by means of compressive and tensile strength and compressive and tensile fracture energies.

		Brick	Mortar
linear elastic	$E$	2500 N/mm <sup>2</sup>	1000 N/mm <sup>2</sup>
	$\nu$	0,2	0,2
post elastic non linear	$f_c$	15 N/mm <sup>2</sup>	10 N/mm <sup>2</sup>
	$f_t$	0,4 N/mm <sup>2</sup>	0,3 N/mm <sup>2</sup>
	$G_{fc}$	0,06 N/mm	0,05 N/mm
	$G_{ft}$	0,000032 N/mm	0,000045 N/mm

**Table 6.1.1.A:** Alcaino et al. panel mechanical properties

According to the range values reported in the **table 6.1.1.A** the fracture energies have been computed and shown in the following:

Compressive fracture energy Gfc - N/mm			
		Brick	Mortar
1 <sup>st</sup> range value	$0,5 \cdot \frac{f_i^2}{E}$	0,045	0,05
2 <sup>nd</sup> range value	$1,0 \cdot \frac{f_i^2}{E}$	0,09	0,1
3 <sup>rd</sup> range value	$1,5 \cdot \frac{f_i^2}{E}$	0,135	0,15

**Table 6.1.1.B:** Compressive fracture energy values for both materials

With regards to the variation of brick compressive fracture energies, a comparison among the obtained results can be pointed out, considering those values. In the graph legend, the curve titles assume these meanings:

- Alcaino, as the author of the experimental tests;
- Model, are the results validated using numerical analysis;
- GfcMin, represent the 1<sup>st</sup> value as defined in the **Table 6.1**;
- GfcMed, represent the 2<sup>nd</sup> value as defined in the **Table 6.1**;
- GfcMax, represent the 3<sup>rd</sup> value as defined in the **Table 6.1**;

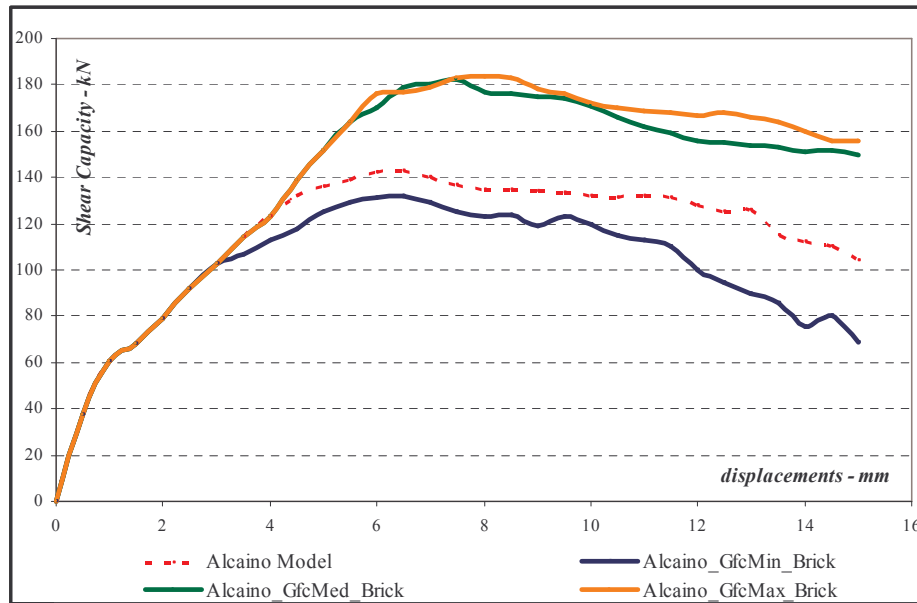


**Figure 6.1.1.A:** Brick compressive fracture energy variation

Considering the brick compressive fracture energy lower than that used to validate the numerical analyses by comparing with the experimental tests, a lower shear capacity has been reached, while the deformation associated to the maximum strength is almost the same, equal to 6 mm. Compressive fracture energy value, higher than that used for validation, have exhibited a better global behavior of the panels in terms of shear capacity and deformations, reaching an improvement of capacity about 35%. As an evidence of the outcomes after parametric analyses, the brick compressive fracture energy changes the masonry panel global response after the linear elastic branch, having no effect in terms of initial stiffness.

Model	Fracture Energy Value and formulation (N/mm)	Displacement mm	Shear Capacity kN	$\Delta$ Shear Capacity %
Alcaino_model	model definition	4	123	----
		6	142	----
		8	135	----
		10	132	----
Alcaino_GfcMin_B	$G_{fc,Brick} = \frac{f_c^2}{2E} = G_{fc,min}$	4	113	-8,1
		6	131	-7,7
		8	123	-8,9
		10	120	-9,1
Alcaino_GfcMed_B	$G_{fc,Brick} = \frac{f_c^2}{E} = G_{fc,med}$	4	123	0,0
		6	170	19,7
		8	177	31,1
		10	171	29,5
Alcaino_GfcMax_B	$G_{fc,Brick} = \frac{3f_c^2}{2E} = G_{fc,max}$	4	123	0,0
		6	176	23,9
		8	184	36,3
		10	172	30,3

**Table 6.1.1.C:** Brick compressive fracture energy variation: obtained results

With regards to the variation of mortar compressive fracture energies, a comparison among the numerical results have been reported in the following:

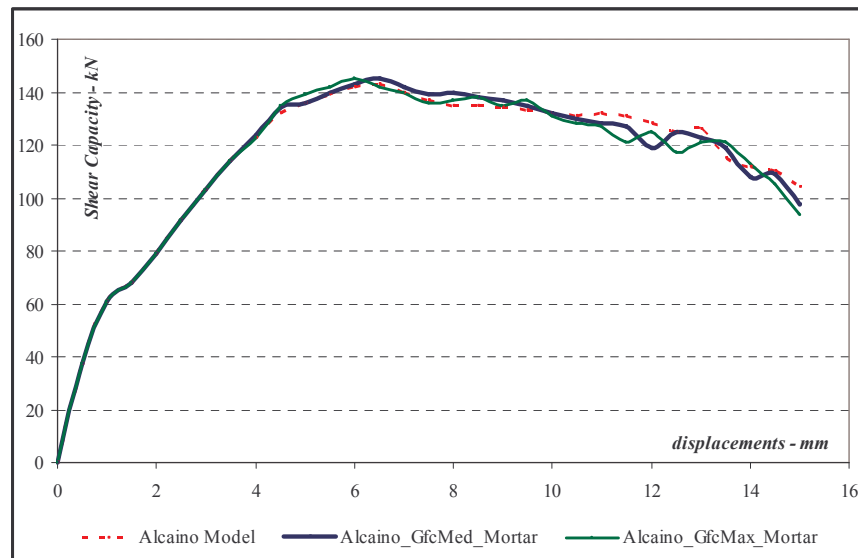


**Figure 6.1.1.B:** Brick compressive fracture energy variation

The lower value of mortar compressive fracture energy is equal to the value used into the numerical analyses to validate them, thus only two curves related to the average and maximum  $G_{fc}$  values have been introduced in the graphs. As an evidence of the outcomes after the parametric analyses, the mortar compressive fracture energy did not change the masonry panel global response neither in terms of initial stiffness, nor maximum shear capacity and associated deformations.

<i>Model</i>	<i>Fracture Energy Value and formulation (N/mm)</i>	<i>Displacement mm</i>	<i>Shear Capacity kN</i>	<i>Δ Shear Capacity %</i>
<b>Alcaino_model</b>	<i>model definition</i>	4	123	----
		6	142	----
		8	135	----
		10	132	----
<b>Alcaino_GfcMin_M</b>	$G_{fc,Mort} = \frac{f_c^2}{2E} = G_{fc,min}$	4	123	0,0
		6	142	0,0
		8	135	0,0
		10	132	0,0
<b>Alcaino_GfcMed_M</b>	$G_{fc,mort} = \frac{f_c^2}{E} = G_{fc,med}$	4	124	0,8
		6	143	0,7
		8	140	3,7
		10	132	0,0
<b>Alcaino_GfcMax_M</b>	$G_{fc,Mort} = \frac{3f_c^2}{2E} = G_{fc,max}$	4	123	0,0
		6	145	2,1
		8	137	1,5
		10	131	-0,8

**Table 6.1.1.D:** Mortar compressive fracture energy variation: obtained results

### 6.1.2. Tensile Fracture Energies for both materials

As in the previous paragraph provisions in which the parametric analyses were implemented by changing the compressive fracture energies of both bricks and mortar, in this section the results obtained from parametric numerical simulation considering different tensile fracture energies of both materials have been described.

The tensile fracture energies of both materials have been reported in the following table:

Tensile fracture energy Gft - N/mm			
		Brick	Mortar
1 <sup>st</sup> value	$0,5 \cdot \frac{f_i^2}{E}$	0,000032	0,000045
2 <sup>nd</sup> value	$1,0 \cdot \frac{f_i^2}{E}$	0,000064	0,00009
3 <sup>rd</sup> value	$1,5 \cdot \frac{f_i^2}{E}$	0,000096	0,000135

**Table 6.1.2.A:** Tensile fracture energy values for both materials

The first values of tensile fracture energy for both materials were used as a numerical simulation input data. For that reason the comparison between the validated model and the parametric analyses has been performed by considering only the average and the maximum fracture energy values.

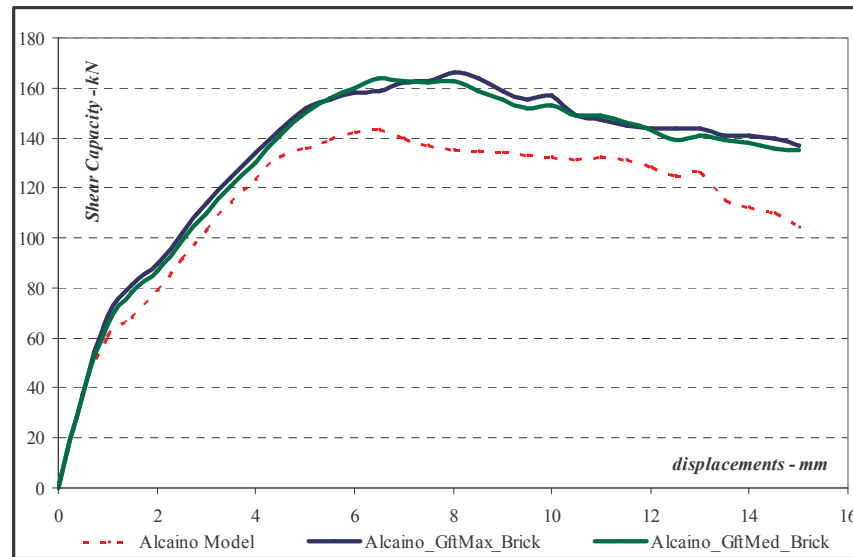


**Figure 6.1.2.A:** Brick tensile fracture energy variation

The brick tensile fracture energies change the global response of the masonry panels in terms of shear capacity and associated deformations. The shear capacity improvements are about 25% while the associated deformations pass from 6 mm to 8 mm, reaching a difference in percentage equal to 33%. The curve initial stiffness is the

same as in the graphs reported previously, while the softening branch follows the same slope as the validated model.

<i>Model</i>	<i>Fracture Energy Value and formulation (N/mm)</i>	<i>Displacement mm</i>	<i>Shear Capacity kN</i>	<i>Δ Shear Capacity %</i>
<b>Alcaino_model</b>	<i>model definition</i>	4	123	----
		6	142	----
		8	135	----
		10	132	----
<b>Alcaino_GftMin_B</b>	$G_{ft,Brick} = \frac{f_t^2}{2E} = G_{ft,min}$	4	123	0,0
		6	142	0,0
		8	135	0,0
		10	132	0,0
<b>Alcaino_GftMed_B</b>	$G_{ft,Brick} = \frac{f_t^2}{E} = G_{ft,med}$	4	130	5,7
		6	160	12,7
		8	163	20,7
		10	153	15,9
<b>Alcaino_GftMax_B</b>	$G_{ft,Brick} = \frac{3f_t^2}{2E} = G_{ft,max}$	4	134	8,9
		6	158	11,3
		8	166	23,0
		10	157	18,9

**Table 6.1.2.B:** Brick tensile fracture energy variation: obtained results

The variation of mortar tensile fracture energy have produced the same results of those obtained by changing the mortar compressive fracture energy. After the parametric numerical simulations, there is no variation of the brickwork global response and a comparison among the results have been reported in the following.



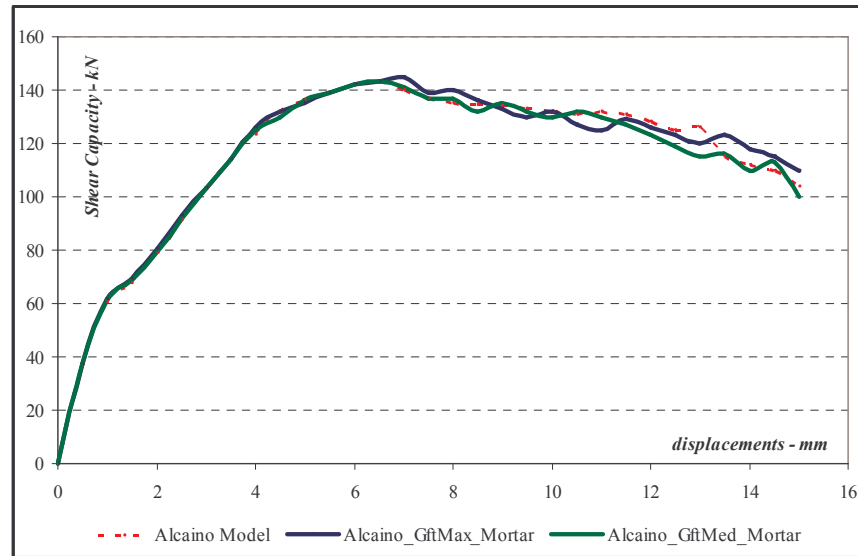


Figure 6.1.2.B: Mortar compressive fracture energy variation

Model	Fracture Energy Value and formulation (N/mm)	Displacmen mm	Shear Capa kN	$\Delta$ Shear Capacity %
Alcaino_model	model definition	4	123	----
		6	142	----
		8	135	----
		10	132	----
Alcaino_GftMin_M	$G_{ft,Mort} = \frac{f_t^2}{2E} = G_{ft,min}$	4	123	0,0
		6	142	0,0
		8	135	0,0
		10	132	0,0
Alcaino_GftMed_M	$G_{ft,Mort} = \frac{f_t^2}{E} = G_{ft,med}$	4	125	1,6
		6	142	0,0
		8	140	3,7
		10	130	-1,5
Alcaino_GftMax_M	$G_{ft,Mort} = \frac{3f_t^2}{2E} = G_{ft,max}$	4	126	2,4
		6	142	0,0
		8	140	3,7
		10	132	0,0

Table 6.1.2.C: Mortar tensile fracture energy variation: obtained results

## 6.2. Pascale et al. panels [2]

### 6.2.1. Compressive Fracture Energies for both materials

Pascale et al. experimental tests were performed on masonry panels realized by clay bricks and premixed cementious mortar. They were implemented into the numerical simulations by means of Rankine – Von Mises criteria as shown in the previous chapter and the mechanical properties to describe the linear elastic and post elastic non linear behavior were reported in the following:

		Brick	Mortar
linear elastic	$E$	15800 N/mm <sup>2</sup>	320 N/mm <sup>2</sup>
	$\nu$	0,13	0,2
post elastic non linear	$f_c$	62 N/mm <sup>2</sup>	11 N/mm <sup>2</sup>
	$f_t$	8,9 N/mm <sup>2</sup>	1,1 N/mm <sup>2</sup>
	$G_{fc}$	0,122 N/mm	0,19 N/mm
	$G_{ft}$	0,0025 N/mm	0,0019 N/mm

**Table 6.2.1.A:** Pascale et al. panel mechanical properties

According to the range values reported in the **table 6.1**, the fracture energies have been computed and shown in the following:

Compressive fracture energy $G_{fc}$ - N/mm			
		Brick	Mortar
1 <sup>st</sup> value	$0,5 \cdot \frac{f_i^2}{E}$	0,12	0,19
2 <sup>nd</sup> value	$1,0 \cdot \frac{f_i^2}{E}$	0,24	0,38
3 <sup>rd</sup> value	$1,5 \cdot \frac{f_i^2}{E}$	0,37	0,57

**Table 6.2.1.B:** Compressive fracture energy values for both materials

The lower values of both mortar and bricks compressive fracture energies are equal to the values used into the numerical analyses to validate the experimental tests; thus only two curves related to the average and maximum  $G_{fc}$  values have been introduced

in the following graphs. As shown on both capacity curves and tables, in which the obtained results have been reported for both materials, the variation of brick and mortar compressive fracture energies did not produce any different panel global response in terms of stiffness, shear capacity and associated deformations.

As an example, only the brick compressive fracture energies variation has been reported in the following representations.

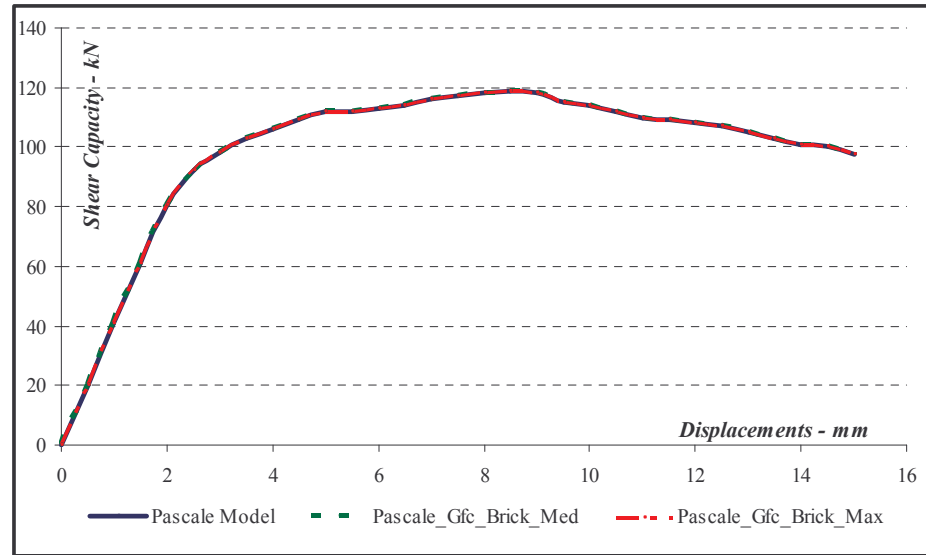


**Figure 6.2.1.A:** Brick compressive fracture energy variation

<i>Model</i>	<i>Fracture Energy Value and formulation (N/mm)</i>	<i>Displacement mm</i>	<i>Shear Capacity kN</i>	<i>Δ Shear Capacity %</i>
<b>Pascale model</b>	<i>model definition</i>	4	106	----
		6	113	----
		8	118	----
		10	114	----
<b>Pascale_GfcMin_B</b>	$G_{fc,Brick} = \frac{f_c^2}{2E} = G_{fc,min}$	4	106	0,0
		6	113	0,0
		8	118	0,0
		10	114	0,0
<b>Pascale_GfcMed_B</b>	$G_{fc,Brick} = \frac{f_c^2}{E} = G_{fc,med}$	4	106	0,0
		6	113	0,0
		8	118	0,0
		10	114	0,0
<b>Pascale_GfcMax_B</b>	$G_{fc,Brick} = \frac{3f_c^2}{2E} = G_{fc,max}$	4	106	0,0
		6	113	0,0
		8	118	0,0
		10	114	0,0

Table 6.2.1.C: Brick compressive fracture energy variation: obtained results

<i>Model</i>	<i>Fracture Energy Value and formulation (N/mm)</i>	<i>Displacement mm</i>	<i>Shear Capacity kN</i>	<i>Δ Shear Capacity %</i>
<b>Pascale model</b>	<i>model definition</i>	4	106	----
		6	113	----
		8	118	----
		10	114	----
<b>Pascale_GfcMin_M</b>	$G_{fc,Mort} = \frac{f_c^2}{2E} = G_{fc,min}$	4	106	0,0
		6	113	0,0
		8	118	0,0
		10	114	0,0
<b>Pascale_GfcMed_M</b>	$G_{fc,mort} = \frac{f_c^2}{E} = G_{fc,med}$	4	106	0,0
		6	113	0,0
		8	118	0,0
		10	114	0,0
<b>Pascale_GfcMax_M</b>	$G_{fc,Mort} = \frac{3f_c^2}{2E} = G_{fc,max}$	4	106	0,0
		6	113	0,0
		8	118	0,0
		10	114	0,0

Table 6.2.1.D: Mortar compressive fracture energy variation: obtained results

### 6.2.2. Tensile Fracture Energies for both materials

In this paragraph the results obtained from parametric numerical simulation considering different tensile fracture energy for both materials have been described. Using the formula reported in the **Table 6.1**, the following input data were used into the simulations and compared to the validated model results.

The tensile fracture energies of both materials have been reported in the following table:

Tensile fracture energy Gft - N/mm			
		Brick	Mortar
1 <sup>st</sup> value	$0,5 \cdot \frac{f_i^2}{E}$	0,0025	0,0019
2 <sup>nd</sup> value	$1,0 \cdot \frac{f_i^2}{E}$	0,005	0,0038
3 <sup>rd</sup> value	$1,5 \cdot \frac{f_i^2}{E}$	0,0075	0,0057

**Table 6.2.2.A:** Tensile fracture energy values for both materials

The first values of tensile fracture energy for both materials were used as numerical simulation input data. For that reason the comparison between the validated model and the parametric analyses has been performed by considering only the average and the maximum fracture energy values (2<sup>nd</sup> and 3<sup>rd</sup> values as cited in the table).

As obtained by changing the compressive fracture energies of both materials, also in this case the analyses show close outcomes for both bricks and mortar variations.

The capacity curves obtained by varying the brick tensile fracture energy are very similar to those obtained when the brick compressive fracture energy have been changed, without having differences in terms of shear capacity, associated deformation and initial stiffness.

In the following **Figure 6.2.2.A**, the capacity curves changing the mortar tensile fracture energy have been reported in order to show the global response of the masonry panels.

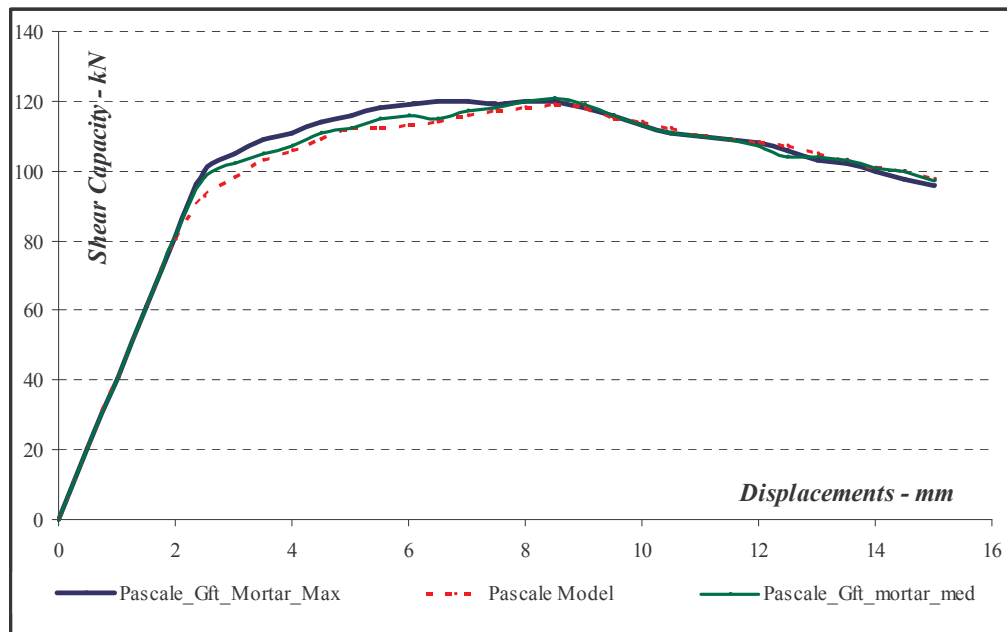


**Figure 6.2.2.A:** Mortar tensile fracture energy variation

The initial stiffness is the same for the validated model and the outcomes obtained by changing the tensile fracture energy values; moreover the softening branches have been described by means of the same overlapped curves. The maximum shear capacity also maintained the same value as well as the associated deformations, while it is noticed a small difference between the elastic and post peak non linear behaviour.

Analysing this circumstances, considering 4 mm and 6 mm deformations, the associated shear capacity values diverge with respect to the validated model of about 5 % in both cases.

<i>Model</i>	<i>Fracture Energy Value and formulation (N/mm)</i>	<i>Displacement mm</i>	<i>Shear Capacity kN</i>	<i>Δ Shear Capacity %</i>
<b>Pascale model</b>	<i>model definition</i>	4	106	----
		6	113	----
		8	118	----
		10	114	----
<b>Pascale_GftMin_B</b>	$G_{ft,Brick} = \frac{f_t^2}{2E} = G_{ft,min}$	4	106	0,0
		6	113	0,0
		8	118	0,0
		10	114	0,0
<b>Pascale_GftMed_B</b>	$G_{ft,Brick} = \frac{f_t^2}{E} = G_{ft,med}$	4	106	0,0
		6	113	0,0
		8	118	0,0
		10	114	0,0
<b>Pascale_GftMax_B</b>	$G_{ft,Brick} = \frac{3f_t^2}{2E} = G_{ft,max}$	4	106	0,0
		6	113	0,0
		8	118	0,0
		10	114	0,0

<i>Model</i>	<i>Fracture Energy Value and formulation (N/mm)</i>	<i>Displacement mm</i>	<i>Shear Capacity kN</i>	<i>Δ Shear Capacity %</i>
<b>Pascale model</b>	<i>model definition</i>	4	106	----
		6	113	----
		8	118	----
		10	114	----
<b>Pascale_GftMin_M</b>	$G_{ft,Mort} = \frac{f_t^2}{2E} = G_{ft,min}$	4	105	-0,9
		6	113	0,0
		8	118	0,0
		10	116	1,8
<b>Pascale_GftMed_M</b>	$G_{ft,Mort} = \frac{f_t^2}{E} = G_{ft,med}$	4	107	0,9
		6	116	2,7
		8	120	1,7
		10	113	-0,9
<b>Pascale_GftMax_M</b>	$G_{ft,Mort} = \frac{3f_t^2}{2E} = G_{ft,max}$	4	111	4,7
		6	119	5,3
		8	120	1,7
		10	113	-0,9

Table 6.2.2.C: Results obtained by changing the bricks and mortar tensile fracture energy

### 6.3. Manfredi et al. panels [3]

#### 6.3.1. Compressive Fracture Energies for both materials

Manferdi et al experimental tests were performed on masonry panels made of tuff blocks and premixed cementious mortar. The validation was described in the previous chapter, providing the mechanical properties reported in the following table, where linear elastic and post elastic behavior have been assessed with respect to Rankine – Von Mises criterion. Also in this case, linear elastic behavior of both bricks and mortar have been computed by means of Young's modulus and poisson's coefficient; post elastic non linear behavior of both materials have been described by using compressive and tensile strength and compressive and tensile fracture energies.

		Brick	Mortar
linear elastic	$E$	500 N/mm <sup>2</sup>	250 N/mm <sup>2</sup>
	$\nu$	0,2	0,2
post elastic non linear	$f_c$	3,5 N/mm <sup>2</sup>	2 N/mm <sup>2</sup>
	$f_t$	0,25 N/mm <sup>2</sup>	0,1 N/mm <sup>2</sup>
	$G_{fc}$	0,012 N/mm	0,008 N/mm
	$G_{ft}$	0,000063 N/mm	0,00002 N/mm

**Table 6.3.1.A:** Manfredi et al. panel mechanical properties

The compressive fracture energies of both materials have been computed according to the formula reported in the **table 6.1** and shown in the following:

Compressive fracture energy $G_{fc}$ - N/mm			
		Brick	Mortar
1 <sup>st</sup> value	$0,5 \cdot \frac{f_i^2}{E}$	0,012	0,008
2 <sup>nd</sup> value	$1,0 \cdot \frac{f_i^2}{E}$	0,025	0,016
3 <sup>rd</sup> value	$1,5 \cdot \frac{f_i^2}{E}$	0,037	0,024

**Table 6.3.1.B:** Compressive fracture energy values of both materials



By using the brick compressive fracture energy variation, parametric analyses were performed and the main results were depicted in the following **Figure 6.3.1.A**. The lower value of brick compressive fracture energy is equivalent to the compressive fracture energy value used into the validation of the analyses. For that reason, only the second and third values were implemented and were compared to the validated model.

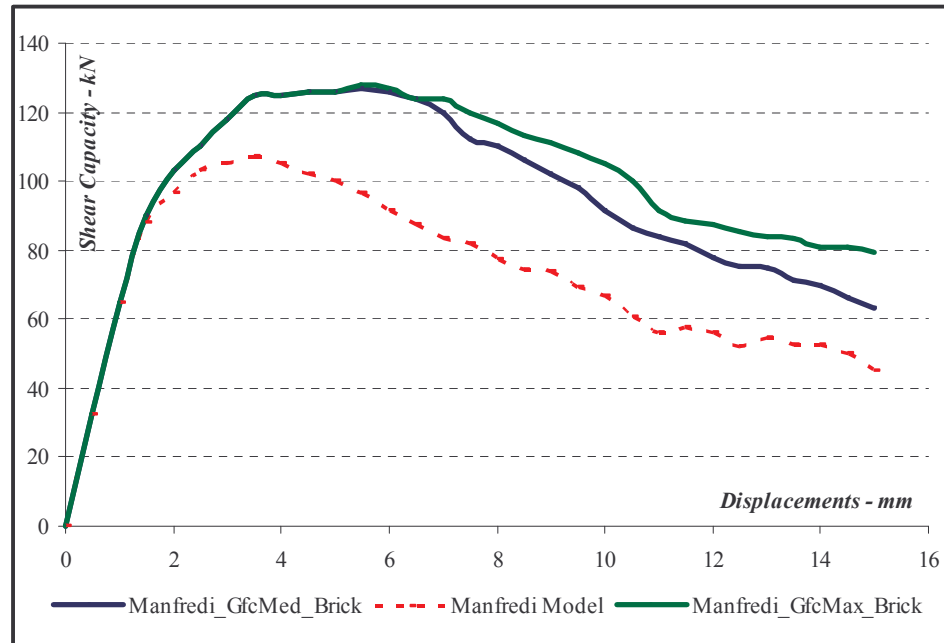


**Figure 6.3.1.A:** Brick compressive fracture energy variation

With respect to the validated model, the variation of brick compressive fracture energy using both values of the range shows a capacity strength increment and an improvement of the associated deformation values, too. In fact, the shear capacity improves about 20 % and the associated deformation passes from 4 mm to 6 mm. The initial stiffness of the curve did not change and maintained the same slope up to the non linear elastic behaviour, just before the maximum shear capacity. After reaching the peak shear capacity, the third value, corresponding to the maximum brick compressive fracture energy defined, provides a smooth softening branch compared to that related to the average brick compressive fracture energy value (second value).

<i>Model</i>	<i>Fracture Energy Value and formulation (N/mm)</i>	<i>Displacement mm</i>	<i>Shear Capacity kN</i>	<i>Δ Shear Capacity %</i>
<b>Manfredi mode</b>	<i>model definition</i>	4	105	----
		6	91,4	----
		8	77,2	----
		10	66,8	----
<b>Manfredi_GfcMin_B</b>	$G_{fc,Brick} = \frac{f_c^2}{2E} = G_{fc,min}$	4	105	0,0
		6	91,4	0,0
		8	77,2	0,0
		10	66,8	0,0
<b>Manfredi_GfcMed_B</b>	$G_{fc,Brick} = \frac{f_c^2}{E} = G_{fc,med}$	4	125	19,0
		6	126	37,9
		8	110	42,5
		10	91,5	37,0
<b>Manfredi_GfcMax_B</b>	$G_{fc,Brick} = \frac{3f_c^2}{2E} = G_{fc,max}$	4	125	19,0
		6	127	38,9
		8	117	51,6
		10	105	57,2

**Table 6.3.1.C:** Results obtained by changing the brick compressive fracture energy

With regard to the variation of mortar compressive fracture energy, a comparison among the results have been depicted in the following **Figure 6.3.1.B**, considering that the mortar compressive fracture energy used into the validated model is equal to the first value defined in the **Table 6.3.1.B**:

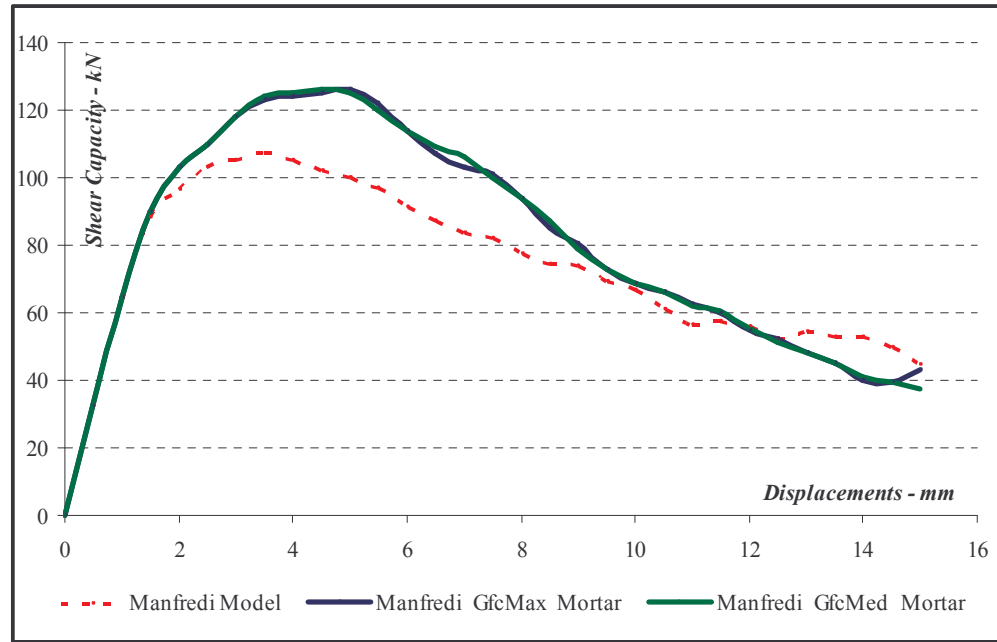


**Figure 6.3.1.B:** Mortar compressive fracture energy variation

Thus only two capacity curves related to the average and maximum  $G_{fc}$  values have been introduced in the graphs.

As an evidence of the outcomes obtained by using parametric analyses, the mortar compressive fracture energy did not change the masonry panel global response in terms of initial stiffness, maintaining the same slope. The shear capacity, on the contrary, improves about 20%, equal to the increasing percentage related to the brick compressive fracture energy variations and, moreover, the associated deformation passes from 4 mm to 5 mm.

The softening branch smoothness become more marked compared to the post peak non linear behaviour described by changing the brick compressive fracture energies.

<i>Model</i>	<i>Fracture Energy Value and formulation (N/mm)</i>	<i>Displacement mm</i>	<i>Shear Capacity kN</i>	<i>Δ Shear Capacity %</i>
<b>Manfredi_GfcMed_M</b>	$G_{fc,mort} = \frac{f_c^2}{E} = G_{fc,med}$	4	125	19,0
		6	114	24,7
		8	93,7	21,4
		10	68,5	2,5
<b>Manfredi_GfcMax_M</b>	$G_{fc,Mort} = \frac{3f_c^2}{2E} = G_{fc,max}$	4	124	18,1
		6	114	24,7
		8	93,7	21,4
		10	68,6	2,7

**Table 6.1.1.D:** Results obtained by changing the mortar compressive fracture energy

### 6.3.2. Tensile Fracture Energies for both materials

Based on the results highlighted in the previous paragraph, in which the parametric analyses were implemented by changing the compressive fracture energies for both materials, in this section the results obtained from parametric numerical simulations considering different tensile fracture energies for both bricks and mortar have been shown.

The following input data in terms of tensile fracture energies were used into the simulations and compared to the validated model outcomes:

Tensile fracture energy Gft - N/mm			
		<i>Brick</i>	<i>Mortar</i>
<i>1<sup>st</sup> value</i>	$0,5 \cdot \frac{f_i^2}{E}$	0,000063	0,00002
<i>2<sup>nd</sup> value</i>	$1,0 \cdot \frac{f_i^2}{E}$	0,000125	0,00004
<i>3<sup>rd</sup> value</i>	$1,5 \cdot \frac{f_i^2}{E}$	0,000188	0,00006

**Table 6.3.2.A:** Tensile fracture energy values for both materials

The first values of tensile fracture energy for both materials were used as numerical simulation input data. For that reason the comparisons between the validated model

and the parametric analyses have been performed by considering the average and the maximum fracture energy values only.

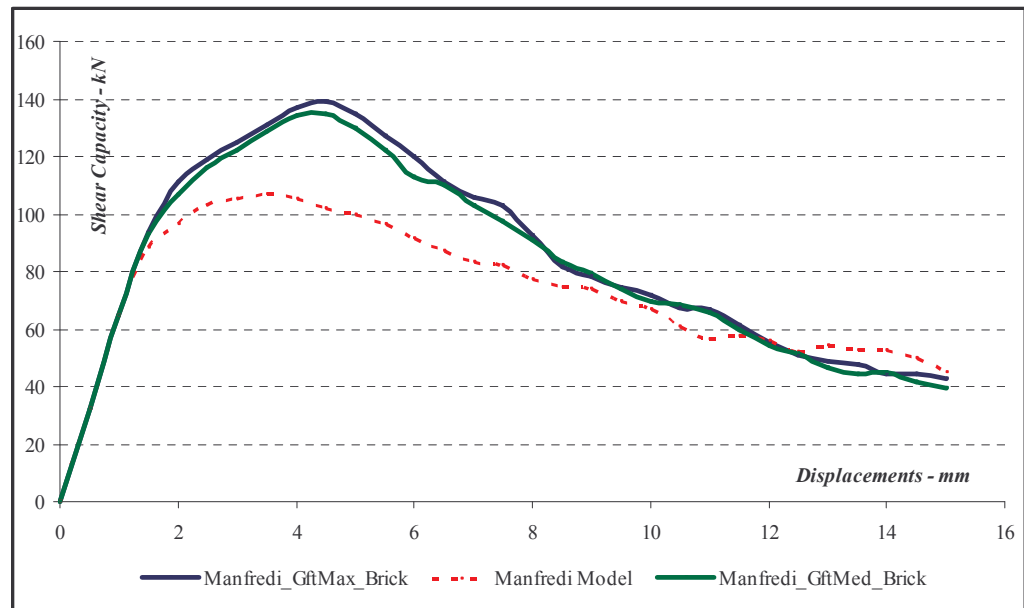


**Figure 6.3.2.A:** Brick tensile fracture energy variation

The brick tensile fracture energies change the global response of the masonry panels in terms of shear capacity and associated deformations. The shear capacity improvements is computed of about 30% while the associated deformation pass from 4 mm to approximately to 5 mm. The capacity curve initial stiffness is the same, while the softening branch comes down quickly compared to the validated model.

<i>Model</i>	<i>Fracture Energy Value and formulation (N/mm)</i>	<i>Displacement mm</i>	<i>Shear Capacity kN</i>	<i>Δ Shear Capacity %</i>
<b>Manfredi mode</b>	<i>model definition</i>	4	105	----
		6	91,4	----
		8	77,2	----
		10	66,8	----
<b>Manfredi_GftMin_B</b>	$G_{ft,Brick} = \frac{f_t^2}{2E} = G_{ft,min}$	4	105	0,0
		6	91,4	0,0
		8	77,2	0,0
		10	66,8	0,0
<b>Manfredi_GftMed_B</b>	$G_{ft,Brick} = \frac{f_t^2}{E} = G_{ft,med}$	4	134	27,6
		6	113	23,6
		8	91	17,9
		10	69,8	4,5
<b>Manfredi_GftMax_B</b>	$G_{ft,Brick} = \frac{3f_t^2}{2E} = G_{ft,max}$	4	137	30,5
		6	120	31,3
		8	92,8	20,2
		10	71,6	7,2

**Table 6.3.2.B:** Results obtained by changing the brick tensile fracture energy

The brickworks global response varies in terms of shear capacity, associated deformation and softening behavior depending on the values associated to the mechanical parameters; the comparison among the results have been reported in the following:

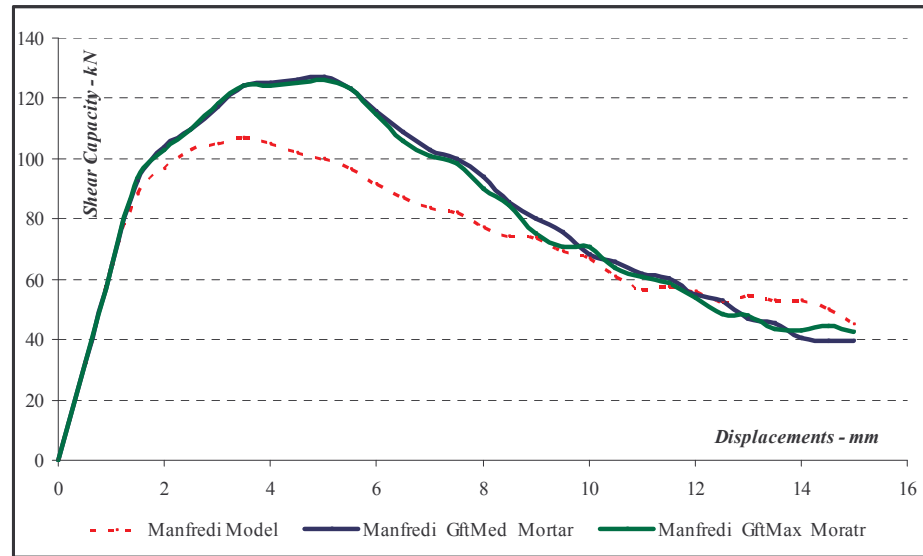


**Figure 6.3.2.B:** Mortar tensile fracture energy variation

The shear capacity improvement is around 20 % and it is also noticed an associated deformations increase from about 4 mm to 5 mm.

There is no difference between the results obtained comparing the masonry panels global response performed with various mortar tensile fracture energy values.

Model	Fracture Energy Value and formulation (N/mm)	Displacement mm	Shear Capacity kN	$\Delta$ Shear Capacity %
Manfredi_GftMed_M	$G_{ft,Mort} = \frac{f_t^2}{E} = G_{ft,med}$	4	125	19,0
		6	116	26,9
		8	93,8	21,5
		10	68,2	2,1
Manfredi_GftMax_M	$G_{ft,Mort} = \frac{3f_t^2}{2E} = G_{ft,max}$	4	124	18,1
		6	115	25,8
		8	90,1	16,7
		10	70,7	5,8

**Table 6.3.2.C:** Results obtained by changing the mortar tensile fracture energy

## 6.4. Final Remarks

This chapter has focused the attention on the influence of different constituents material fracture energies on the global behavior of the masonry panels.

The fracture energy in fact is not an easily determined parameter by means of mechanical tests or implicitly known by the choice of materials, but it can be calculated through the mathematical relationships present in the literature relating those energies with other material mechanical properties.

The fracture energy plays a crucial role to obtain the final results, of non-linear numerical analyses.

For this reason, a feasible range of energies for both constituent materials were considered and three typical values were adopted to perform the parametric analyses changing the fracture energies only. In this way it was possible to determine the actual variability of the panel global response as a function of both compression and tension fracture energy variability.

### *6.4.1. Conclusion about Alcaïno et al. experimental tests [1]*

The variation of the brick compression fracture energy causes a panel global response changing in the post peak nonlinear behaviour in terms of maximum shear capacity and associated displacement.

A similar result was achieved by varying the tensile fracture energy of the brick material, obtaining different panel global performances compared with those previously defined. Instead, the variation of both mortar fracture energies did not induce any changing.

For instance the graph reported below shows the capacity curves obtained considering the parametric analyses conducted by introducing into the model the maximum brick compression and tensile fracture energies taken from a feasible range.



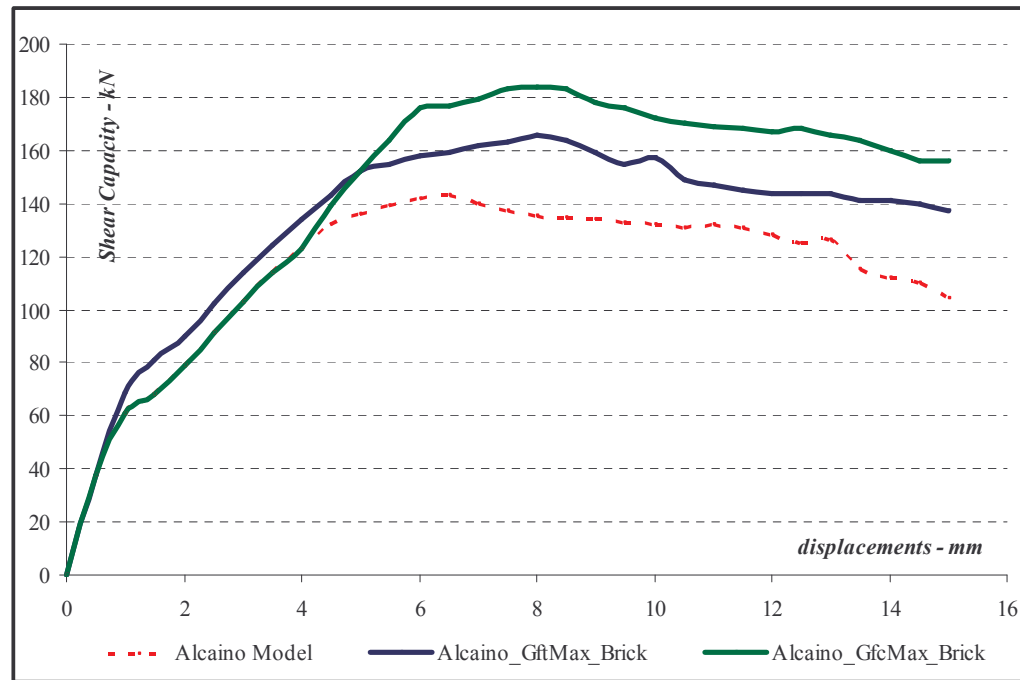


**Figure 6.4.1.A:** Maximum brick compressive and tensile fracture energy values

The maximum value of the brick compression fracture energy determines a shear capacity variation shortly close to the peak strength, while there is no clear change in the elastic and post elastic branch.

Same result was achieved when the tensile fracture energy has been changed, producing a sudden change in the elastic branch up to a maximum shear strength lower than that achieved in other simulations.

#### 6.4.2. Conclusion about Manfredi et al. experimental tests [3]

The global behaviour of the panel tested by Manfredi et al. by changing the compression and tensile fracture energies did not produce variation of the initial stiffness and of the linear elastic performances.

On the non-linear elastic branch and just before reaching the maximum shear capacity, a global response variation has been noticed and continued throughout the non linear post-peak branch changing the softening branch.

For instance, the comparison between the masonry panel behaviour using the maximum compressive and tensile fracture energies values is depicted in the graph reported in the following **Figure 6.4.2.A**:

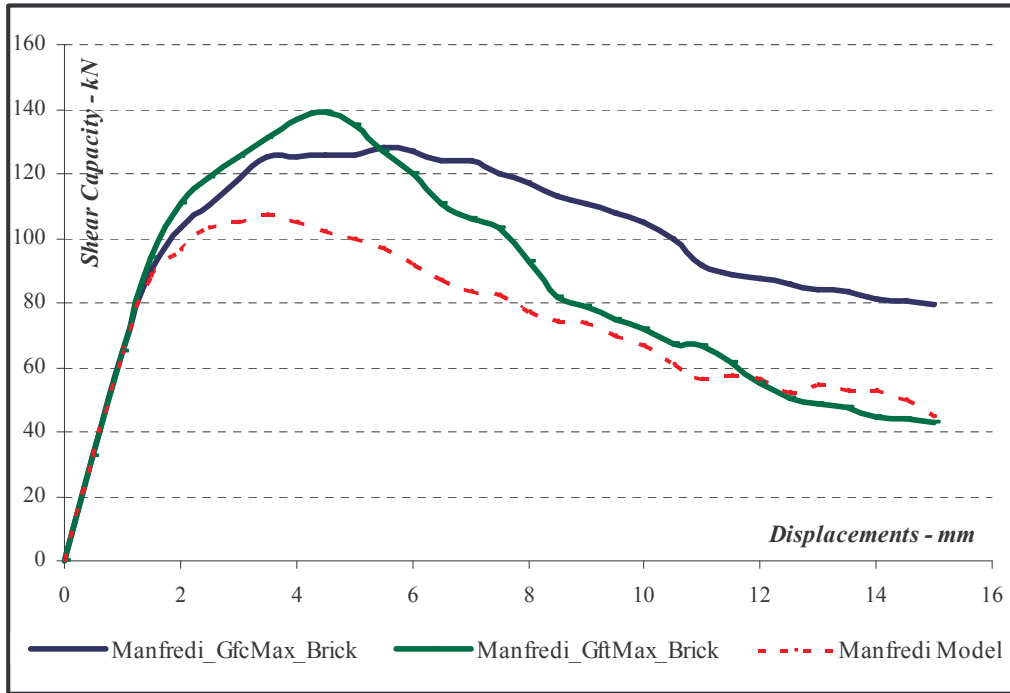


**Figure 6.4.2.A:** Maximum brick compressive and tensile fracture energy values

As shown, the variation of both compressive and tensile fracture energies of the brick have induced a post elastic branch variation, maintaining the same initial stiffness value.

The compressive fracture energy variation shows a smoother trend on softening branch in contrast to that obtained by considering the maximum tensile fracture energy.

### 6.4.3. Final remarks about ductility

The fracture energy variations of both materials lead to change the masonry panels global behavior, in terms of shear capacity and ductility.

The paragraphs described before show a variation of the masonry panel global behavior in terms of shear capacity in the post-elastic branch, while the specimens elastic behavior seems unchanged; In fact, a variation of the initial stiffness does not appear.

Starting from these observations, the global performances due to the fracture energy variation on the post-elastic behavior in terms of ductility were analysed. The model has been studied by means of nonlinear static analyses and thus, the ductility was calculated in terms of displacement, by using the following formula:

$$\mu = \delta_u / \delta_y \quad (1)$$

where  $\delta_u$  is the displacement associated to the ultimate shear capacity, assumed equal to the 90% maximum shear capacity;  $\delta_y$  is the displacement associated to the yielding shear capacity.

The yielding shear capacity and the associated displacement were evaluated by using bi-linear capacity curves, obtained by means of area compensation theory. The bilinear capacity curve was assumed with the same initial stiffness of the original ones.

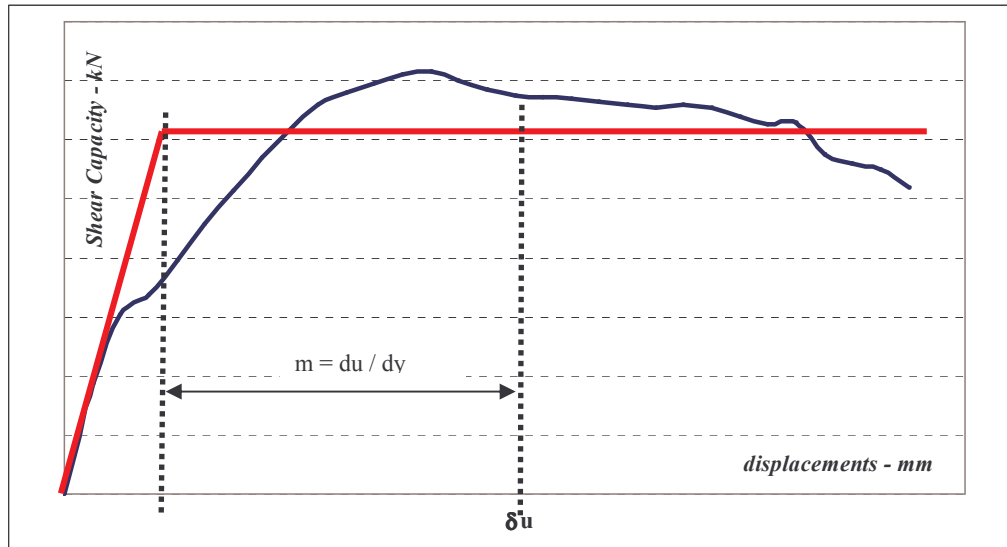


Fig. 6.4.3.1: Bilinear capacity curve

The FEM results obtained for all the masonry panels by changing both fracture energies of the materials have been summarized in the table reported in the following:

<i>ALCAINO</i>	$V_{\max}$	$V_{90\% \max}$	$\delta_y$	$\delta_u$	$\mu$
<i>Bricks</i>	<i>kN</i>	<i>kN</i>	<i>mm</i>	<i>mm</i>	
$G_{fc,1}$	132.0	119.0	2.1	9.0	4.3
$G_{fc,2}$	182.0	163.8		11.0	5.2
$G_{fc,3}$	184.0	165.6		13.3	6.3
$G_{ft,1}$	1433.0	128.0		12.0	5.7
$G_{ft,2}$	164.0	147.6		11.3	5.4
$G_{ft,3}$	166.0	149.4		10.5	5.0

Table 6.4.3.1: Brick fracture energies variation – Alcaino panels

<b>ALCAINO</b>	<b>V<sub>max</sub></b>	<b>V<sub>90%max</sub></b>	<b>δ<sub>y</sub></b>	<b>δ<sub>u</sub></b>	<b>μ</b>
<i>Mortar</i>	<i>kN</i>	<i>kN</i>	<i>mm</i>	<i>mm</i>	
G <sub>fc,1</sub>	143.0	128.7	2.1	12.0	5.7
G <sub>fc,2</sub>	145.0	130.5		10.5	5.0
G <sub>fc,3</sub>	145.0	130.5		9.8	4.6
G <sub>ft,1</sub>	143.0	128.7		12.0	5.7
G <sub>ft,2</sub>	143.0	128.7		11.3	5.4
G <sub>ft,3</sub>	145.0	130.5		9.5	4.5

**Table 6.4.3.2:** Mortar fracture energies variation – Alcaino panels

<b>PASCALE</b>	<b>V<sub>max</sub></b>	<b>V<sub>90%max</sub></b>	<b>δ<sub>y</sub></b>	<b>δ<sub>u</sub></b>	<b>μ</b>
<i>Bricks</i>	<i>kN</i>	<i>kN</i>	<i>mm</i>	<i>mm</i>	
G <sub>fc,1</sub>	119.0	107.0	3.0	12.5	4.2
G <sub>fc,2</sub>	119.0	107.0		12.5	4.2
G <sub>fc,3</sub>	119.0	107.0		12.5	4.2
G <sub>ft,1</sub>	119.0	107.0		12.5	4.2
G <sub>ft,2</sub>	119.0	107.0		12.5	4.2
G <sub>ft,3</sub>	119.0	107.0		12.5	4.2

**Table 6.4.3.3:** Brick fracture energies variation – Pascale panels

<b>PASCALE</b>	<b>V<sub>max</sub></b>	<b>V<sub>90%max</sub></b>	<b>δ<sub>y</sub></b>	<b>δ<sub>u</sub></b>	<b>μ</b>
<i>Mortar</i>	<i>kN</i>	<i>kN</i>	<i>mm</i>	<i>mm</i>	
G <sub>fc,1</sub>	119.0	107.0	3.0	12.5	4.2
G <sub>fc,2</sub>	119.0	107.0		12.5	4.2
G <sub>fc,3</sub>	119.0	107.0		12.5	4.2
G <sub>ft,1</sub>	119.0	107.1		12.5	4.2
G <sub>ft,2</sub>	121.0	108.9		12.3	4.1
G <sub>ft,3</sub>	120.0	108.0		12.0	4.0

**Table 6.4.3.4:** Mortar fracture energies variation – Pascale panel

<b>MANFREDI</b>	<b>V<sub>max</sub></b>	<b>V<sub>90%max</sub></b>	<b>δ<sub>y</sub></b>	<b>δ<sub>u</sub></b>	<b>μ</b>
<i>Bricks</i>	<i>kN</i>	<i>kN</i>	<i>mm</i>	<i>mm</i>	
G <sub>fc,1</sub>	107.0	96.0	1.5	6.2	4.1
G <sub>fc,2</sub>	127.0	114.0		7.3	4.8
G <sub>fc,3</sub>	128.0	115.0		8.3	5.5
G <sub>ft,1</sub>	107.0	96.0		6.2	3.7
G <sub>ft,2</sub>	135.0	122.0		6.2	4.1
G <sub>ft,3</sub>	139.0	125.0		6.2	4.1

Table 6.4.3.5: Brick fracture energies variation – Manfredi panels

<b>MANFREDI</b>	<b>V<sub>max</sub></b>	<b>V<sub>90%max</sub></b>	<b>δ<sub>y</sub></b>	<b>δ<sub>u</sub></b>	<b>μ</b>
<i>Mortar</i>	<i>kN</i>	<i>kN</i>	<i>mm</i>	<i>mm</i>	
G <sub>fc,1</sub>	107.0	96.0	1.5	6.2	4.1
G <sub>fc,2</sub>	126.0	113.4		6.2	4.1
G <sub>fc,3</sub>	126.0	113.4		6.3	4.1
G <sub>ft,1</sub>	107.0	96.0		6.2	4.1
G <sub>ft,2</sub>	127.0	114.3		6.3	4.1
G <sub>ft,3</sub>	126.0	114.3		6.3	4.1

Table 6.4.3.6: Mortar fracture energies variation – Manfredi panels

The panels adopted in experimental tests made by Alcaïno et al. [1] and Manfredi et al. [3] show an increase of ductility by increasing the value of the brick compression fracture energy. Furthermore, increasing the brick tensile fracture energy and both mortar energies it is possible to notice the reduction or the same values of the ductility reached by validated masonry panels. The Pascale et al. [2] masonry tests, however, did not produce changing of ductility by varying the compression fracture of both materials and the tensile fracture energy of the brick. However, a decrease of the ductility has been noticed by increasing the mortar tensile fracture energy. Analyzing the summary of mechanical properties of the different specimens it can be established:

ALCAINO	E - Mpa	fc - Mpa	ft - Mpa	$E_b/E_m$	$f_{cb}/f_{cm}$	$f_{tb}/f_{tm}$
Bricks (b)	2500	15	0.4	2.5	1.5	1.4
Mortar (m)	1000	10	0.3			

**Table 6.4.3.7:** Brick fracture energies variation – Alcaino et al. [1]

PASCALE	E - Mpa	fc - Mpa	ft - Mpa	$E_b/E_m$	$f_{cb}/f_{cm}$	$f_{tb}/f_{tm}$
Bricks (b)	15800	62.0	8.9	49.4	5.6	29.7
Mortar (m)	320	11.0	0.3			

**Table 6.4.3.8:** Brick fracture energies variation – Pascale et al. [2]

MANFRED I	E - Mpa	fc - Mpa	ft - Mpa	$E_b/E_m$	$f_{cb}/f_{cm}$	$f_{tb}/f_{tm}$
Bricks (b)	500	3.5	0.25	2.0	1.8	2.5
Mortar (m)	250	2.0	0.1			

**Table 6.4.3.9:** Brick fracture energies variation – Manfredi et al. [3]

- For low ratios between the Young's modules, tensile and compression strength of the two materials, increasing the brick compressive fracture energy leads to panel ductility increment; increasing the brick tensile fracture energy a panel ductility decrease has been reached. The variation of both mortar fracture energy generates a small decrement of ductility.
- For high ratios between the Young's modulus, compressive and tensile strength of both materials, a variation of panel global behavior in terms of ductility is given by the mortar tensile fracture energy only (ductility decrease).

### References

- [1] Alcaino P., Santa Maria H., 2008. “*Experimental response of externally retrofitted masonry walls subjected to shear loading*”. ASCE Journal of Composites for Construction, Vol. 12, issue 5, Pages 489-498.
- [2] T.Stratford, G.Pascale, O.Manfroni and B.Bonfiglioli, 2004. “*Shear strengthening masonry panels with sheet GFRP*”. ASCE Journal of Composites for Construction, Vol. 8(5).
- [3] G.Faella, G.Manfredi, R.Realfonzo, 1991. “*Comportamento sperimentale di pannelli in muratura di tufo sottoposti ad azioni orizzontali di tipo ciclico*” . V Italian Congress - L’Ingegneria Sismica in Italia 1991- Palermo.



## **7. MASONRY PANELS REINFORCED BY USING FRP SUBJECTED TO IN-PLAN ACTIONS**

Recent seismic events registered in Italy, highlighted the importance of proper structural design to withstand adequately the horizontal actions.

With regard to masonry constructions, structural damages caused by different seismic event have been found and cataloged as out-of-plan and in-plan mechanisms.

The buildings built before the '60s have been characterized by strong limits of the global behavior under horizontal actions and, in many cases, the structural seismic strengthening should be realized by means of traditional techniques and by using innovative constructions materials.

Traditional techniques cause permanent changes on the global behavior, without possibility to modify the intervention because of its non-reversibility.

The interventions by using innovative materials, however, guarantee the reversibility of the design solution, without increasing the stresses and improving the global behavior.

As explicitly defined in the Italian guidelines CNR DT 200/2004 [1], the expressions proposed to check the FRP masonry strengthening systems may not be exhaustive and should be supplemented with additional controls. The design code defines two masonry element reinforcement configurations in order to improve the in the plan shear behaviour, providing diagonal or horizontal fibers layout.

In the following, these geometric reinforcement arrangements have been analyzed, highlighting the pros and cons of both. The finite element method was adopted to model the panels of the experimental programs, selected and described in previous chapters.

The material mechanical properties were adopted to describe the unreinforced and reinforced specimens behavior exhaustively by comparing experimental results with data obtained from FEM analyses in terms of capacity, strength, associated displacements, post peak behaviour and crack patterns.

### 7.1. Modeling

The masonry panels were tested at the micro-scale model, defining the mortar and bricks separately.

The FRP strips were modeled by supposing the complete adhesion with the substrate by using GRID reinforcement elements, available in DIANA software [2].

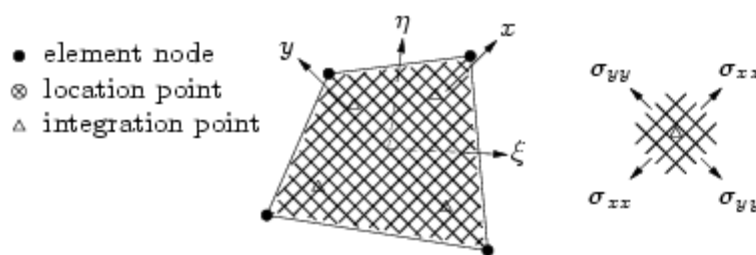


**Fig. 7.1.1:** Reinforcement grid; a) particular 2D – b) stresses

The total area of the grid is considered to be divided in several particles. Each particle contributes to the stiffness of the element that embeds it. The definition of a particle depends on the dimensionality of the embedding structural element.

Two-dimensional elements are completely covered by a particle of grid reinforcement. Therefore the location of a grid particle in a two-dimensional element is fully determined by the edges of the embedding element.

DIANA performs numerical integration of each particle of a reinforcement grid separately, the isoparametric  $\xi$  and  $\eta$  axes are indicated in **Fig. 7.1.1 a**. In this figure, integration points are marked with a small triangle  $\Delta$ . The variables for a grid reinforcement are the strains  $\epsilon_{xx}$  and  $\epsilon_{yy}$  and the stresses  $\sigma_{xx}$  and  $\sigma_{yy}$  oriented in the user-specified  $x$  and  $y$  directions of the grid **Fig.7.1.1 b**. The strains and stresses are coupled to the degrees of freedom of the embedding element.

The following example specifies a grid reinforcement with one section (see Fig.7.1.2). The nodes of the section are input with node numbers.

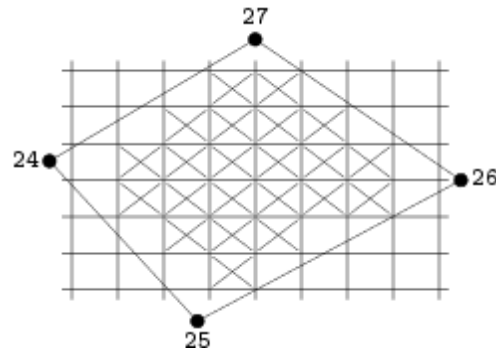


Fig. 7.1.2: GRID section in plane stress elements (example)

The grid is embedded in a mesh of plane stress elements. DIANA automatically determines which elements are covered completely by the grid (those marked with a cross).

Numerical simulations have been performed by applying the gravity load on the top surface of the panels; moreover the horizontal actions were modeled by means of controlled displacements induced by an hydraulic jack placed in a reference point on the panel. The FRP geometric characteristics, both diagonal and horizontal, were changed adopting values calculated according to the panel size.

Considering the horizontal strengthening system, the reinforcement width minimum size,  $b_f$ , was assumed equal to 100 mm, while the maximum size has been assumed equal to 300 mm; the reinforcement was spaced according to the strip width dimension ( $b_f$ ). Thus, three measures were used equal to  $b_f$ , twice ( $2b_f$ ) and three times ( $3b_f$ ) the strip width. The diagonal configuration strengthening was modeled by providing a strip width ( $b_f$ ) ranging from 100mm to 400mm.

The masonry panels structural behavior has been investigated to determine the influence of the reinforcement geometric characteristics variability, as found during the experimental tests. The experimental and FEM results were also compared with the theoretical results by applying the design code formulations.

## 7.2. Alcaino et al Panel [3]

### 7.2.1. Diagonal reinforcement layouts

The masonry panels tested by Alcaino et al. were made by using hollow clay bricks and premixed cement mortar; at the ends of the panel, two steel bars 25 mm diameter were placed to ensure the in-plan shear mechanisms. The gravitational load equal to 98 kN was applied on the top surface of the panel and the horizontal actions were applied by means of controlled displacements made by an hydraulic jack. After the model validation, already presented in Chapter 5 of the present work, different reinforcement configurations have been studied by varying the geometry to test the influence on the global panel performances. The unreinforced panels have provided a maximum shear capacity equal to 140.5 kN; the crack pattern have shown a clear large diagonal crack and a microcracks network extends on the lateral surface of the panel.

The numerical simulations were performed by considering the CFRP diagonal arrangement varying the strip width from 100 mm to 400 mm. Another reinforcement configuration was also investigated by covering both lateral surfaces by using CFRP grids embedded in a premixed cement mortar.

The results have been summarized in the following, specifying the maximum shear strength capacity, its increment by comparing the unreinforced masonry panel shear capacity and the crack pattern shown on the reinforced masonry panels.

<i>Panel</i>	<i>Reinforcement layout</i>	<i>Shear Capacity FEM</i>	<i><math>\Delta</math> Shear capacity</i>
	UR panel Shear Capacity 140.5 kN	<i>kN</i>	<i>%</i>
<i>D_100</i>	Diagonal Reinforcement	185	32,2%
<i>D_200</i>		215	53,6%
<i>D_300</i>		256	82,9%
<i>D_400</i>		268	91,5%
<i>RINF.</i>	Fully covered panel	322	130%

**Table 7.2.1.1:** FEM Analyses results

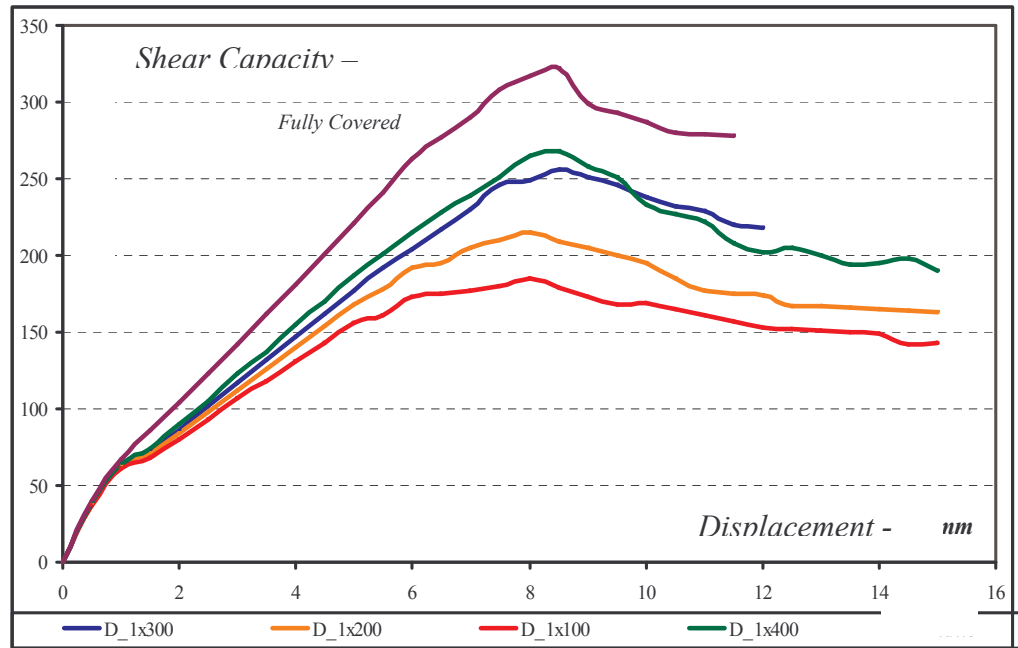


Fig. 7.2.1.2: FEM Analyses capacity curves

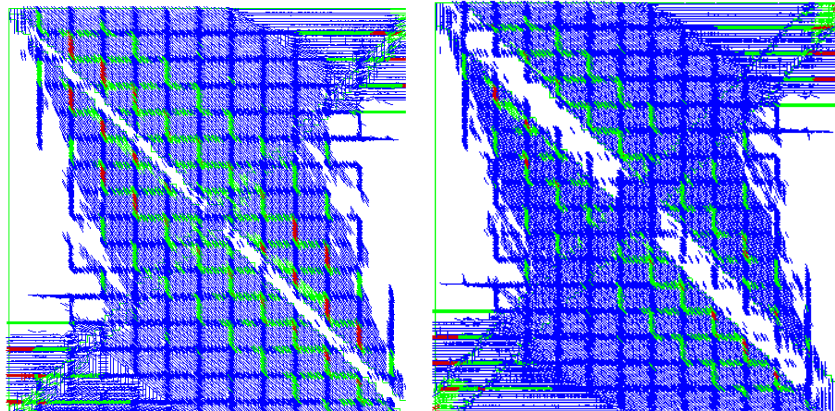
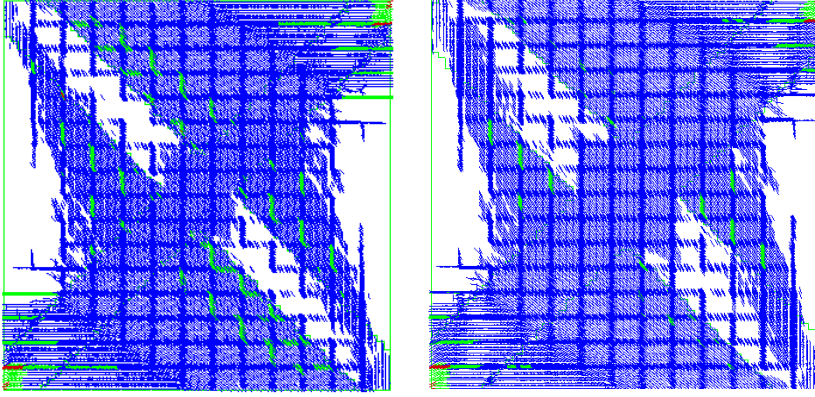


Fig. 7.2.1.3: FEM Analyses crack pattern; a) diagonal strip 100 mm wide; b) diagonal strip 200 mm wide



**Fig. 7.2.1.4:** FEM Analyses crack pattern; a) diagonal strip 300 mm wide; b) diagonal strip 400 mm wide

The CFRP strip width increment produces a progressive maximum shear capacity increment; in fact the maximum shear capacity increment obtained by analysing the D\_100 panel (CFRP strip 100 mm wide) compared to the unreinforced panel shear strength is equal to 32.2 %, rising to 91.5% considering the masonry panels reinforced with strips 400 mm wide.

The crack patterns of reinforced panels show a greater spread of the microcracks on the lateral surface of the panels. Again, the largest strip width leads to a greater microcracks spreading and to a better stress distribution.

Furthermore, the FEM results were compared with the shear capacity of the reinforced panels computed by using the formula introduced in the literature (Prota et al [4]); it was evaluated equal to the sum of the unreinforced panel shear capacity contribution ( $V_{rd,ur}$ ) and the CFRP shear increment ( $V_{rd,f}$ ):

$$\begin{aligned} V_{rd,tot} &= V_{rd,ur} + V_{rd,f} \\ V_{rd,f} &= \varepsilon_{fd} \cdot E_f \cdot A_{fd} \cdot \cos \alpha \end{aligned} \quad (1)$$

where  $\varepsilon_{fd}$  is the CFRP design strain computed by using the design code provisions [CNR DT 200/2004],  $E_f$  is the CFRP Young's modulus,  $A_{fd}$  is the CFRP cross section area and  $\alpha$  is the CFRP fiber angle.

The results show a satisfactory approximation always below 10%. In particular, the maximum percentage variation (equal to 7,8%) has been obtained for the panel reinforced with strips 400 mm wide.

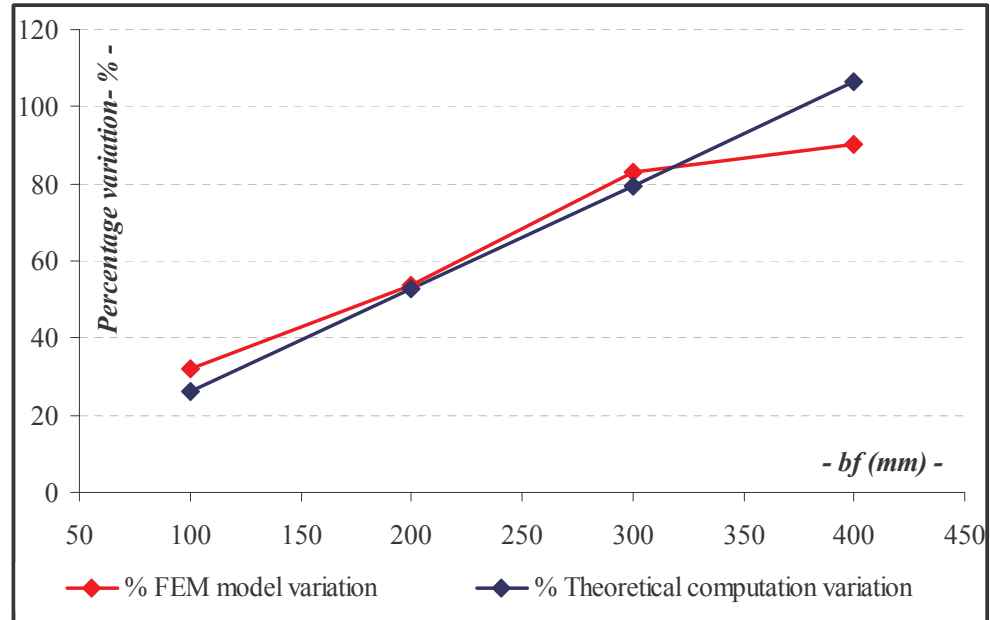


Fig. 7.2.1.5: Comparison between Theoretical and FEM obtained results

The FEM analyses performed on panels reinforced by using diagonal strips have been completed studying other reinforcement layouts, testing their influence on the panel global performances.

In fact, the same reinforcement area was taken into account applying a second CFRP strip on the existing one, as shown below:

<i>Diagonal layouts</i>	<i>description</i>	<i>Area – mm<sup>2</sup></i>
D_100_2str	2 layers 100 mm wide applied	26,00
D_200	1 layer 200 mm wide applied	26,00
D_200_2str	2 layers 200 mm wide applied	52,00
D_400	1 layer 400 mm wide applied	52,00

Table 7.2.1.2: Comparison between different CFRP layouts

The FEM results show a better behavior of the masonry panel reinforced by using one layer of diagonal strips (characterized by a greater CFRP strip width) compared to the performance of the masonry panel reinforced by using two CFRP layers (characterized by smaller CFRP strip width dimension) in terms of shear capacity, shear stresses distribution and crack patterns.

In fact, the D\_100\_2str model (two layers of CFRP strips, 100 mm wide) has performed a maximum shear capacity about 10% lower compared to the results obtained for D\_200 model (one layer of CFRP strip, 200 mm wide).

The percentage variation decreases to 7% by comparing the D\_200\_2str model (two layer of CFRP strips 200 mm wide) and the model D\_400 model (one layer of CFRP strip 400 mm wide).

Panels	Description	$A_{fw} - \text{mm}^2$	Vmax - kN	$\Delta V_{\text{max}} - \%$
URP	Unreinforced panel	----	140.50	----
D_100_2str	2 layers 100 mm wide	26.00	197.00	40.00%
D_200	1 layers 200 mm wide	26.00	215.00	53.00%
D_200_2str	2 layers 200 mm wide	52.00	251.00	79.00%
D_400	1 layers 400 mm wide	52.00	268.00	91.00%

**Table 7.2.1.3:** Comparison between different CFRP layouts

Panels	Description	Vmax - kN	$\Delta V_{\text{max}} - \%$
D_100_2str	2 layers 100 mm wide	197.00	----
D_200	1 layers 200 mm wide	215.00	9.00%
D_200_2str	2 layers 200 mm wide	251.00	----
D_400	1 layers 400 mm wide	268.00	7.00%

**Table 7.2.1.4:** Comparison between different CFRP layouts



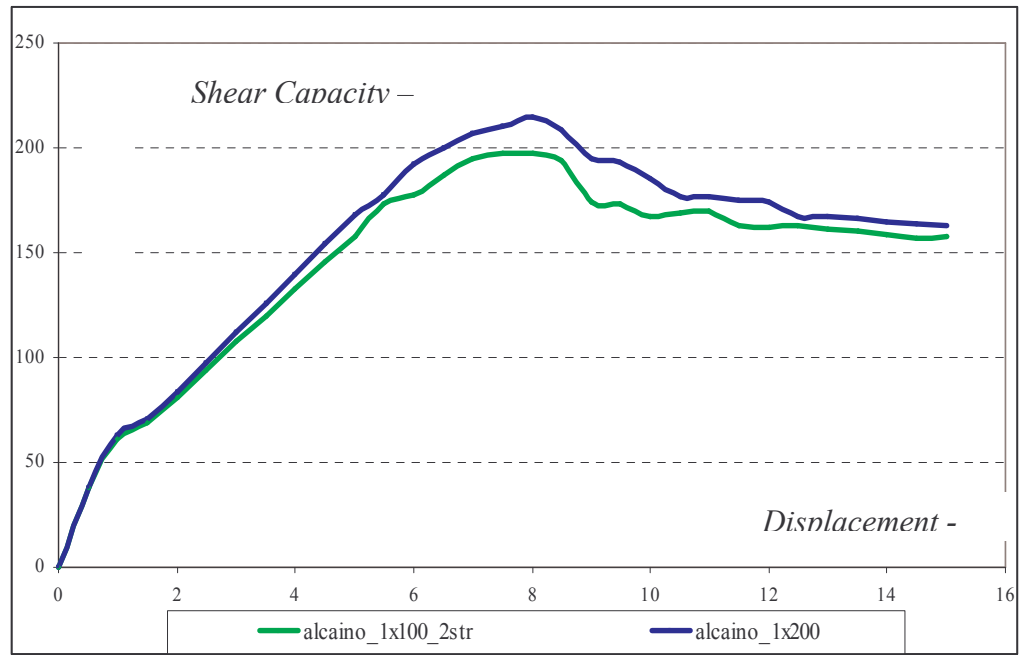


**Fig. 7.2.1.6:** Comparison between D\_100\_2str and D\_200 capacity curves

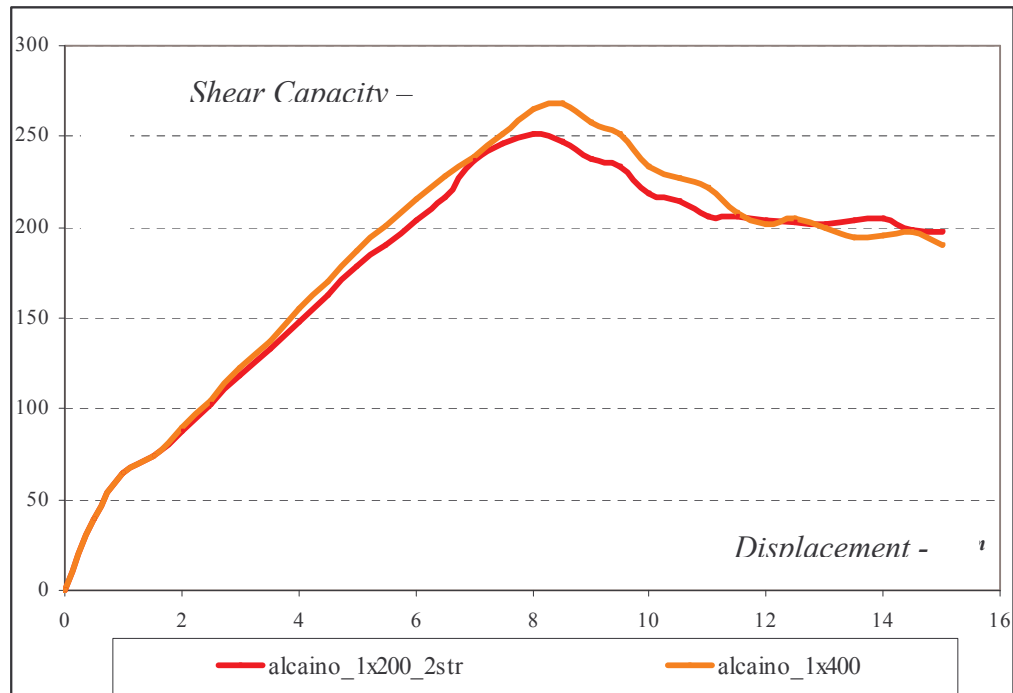


Fig. 7.2.1.7: Comparison between D\_1200\_2str and D\_400 capacity curves

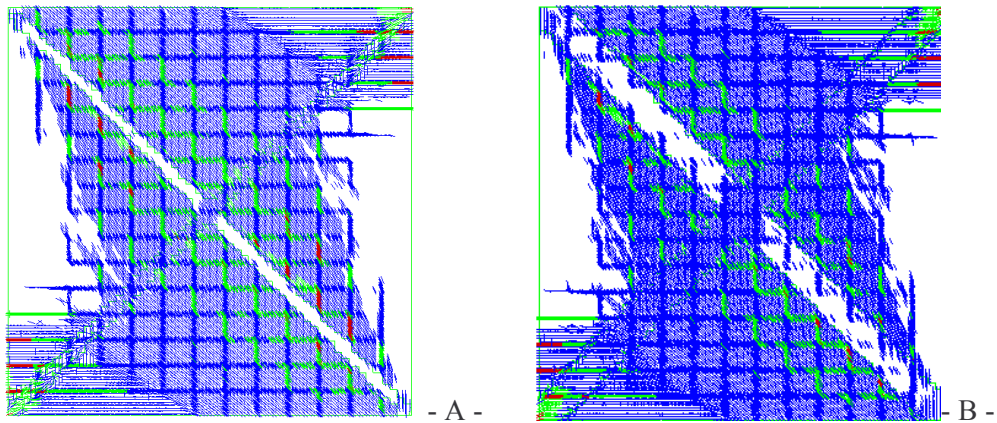
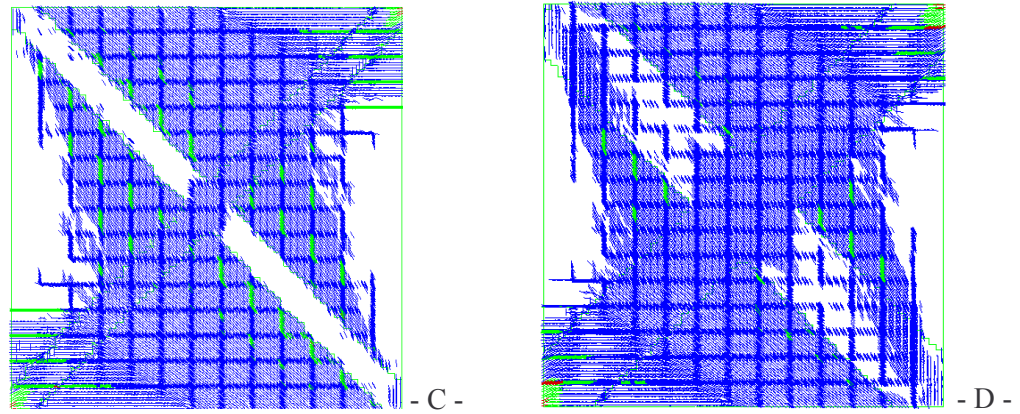


Fig. 7.2.1.8: Crack patterns: A) D\_100\_2str; B) D\_200



**Fig. 7.2.1.8:** Crack patterns: C) D\_200\_2str; D) D\_400

### 7.2.2. Horizontal reinforcement layouts

The second reinforcement configuration has been characterized by CFRP horizontal strips, varying the strips width ( $b_f$ ) and the spacing between them ( $p_f$ ).

The CFRP strips width was changed between 100 mm and 300 mm, while the spacing was chosen equal to 455mm, 555mm and 655mm, according to the panel geometry.

<i>Panels</i>	<i>Layouts</i>	<i>b<sub>f</sub> - mm</i>	<i>p<sub>f</sub> - mm</i>
<i>H_100_1</i>	3 horizontal layers	100	455
<i>H_100_2</i>			555
<i>H_100_3</i>			655
<i>H_150_1</i>		150	455
<i>H_150_2</i>			555
<i>H_150_3</i>			655
<i>H_200_1</i>		200	455
<i>H_200_2</i>			555
<i>H_200_3</i>			655
<i>H_300_1</i>		300	455
<i>H_300_2</i>			555
<i>H_300_3</i>			655

**Table 7.2.2.1:** Shear capacity and displacements

The unreinforced and reinforced masonry panel results in terms of maximum shear capacity obtained by using numerical simulation were reported in the following:

<i>Panels</i>	<i>Shear Capacity FEM</i>	<i><math>\Delta</math>Shear Capacity</i>
	<i>kN</i>	<i>%</i>
<i>URP</i>	140.5	-----
<i>H_100_1</i>	206.0	47.0
<i>H_100_2</i>	204.0	45.7
<i>H_100_3</i>	203.0	45.0
<i>H_150_1</i>	216.0	53.6
<i>H_150_2</i>	210.0	50.0
<i>H_150_3</i>	207.0	47.9
<i>H_200_1</i>	223.0	59.3
<i>H_200_2</i>	215.0	53.6
<i>H_200_3</i>	213.0	52.1
<i>H_300_1</i>	238.0	70.0
<i>H_300_2</i>	232.0	65.7
<i>H_300_3</i>	227.0	62.1

**Table 7.2.2.2:** Shear Capacity and displacements

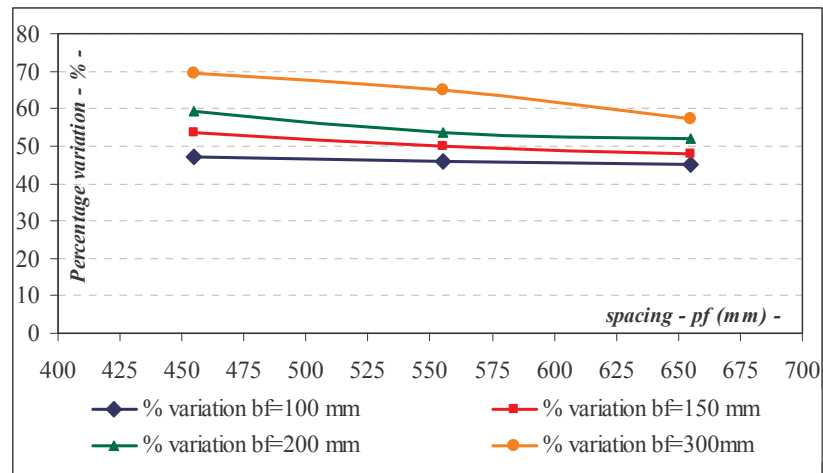


**Fig. 7.2.2.1:** Percentage variation by changing the spacing ( $p_f$ )

In the **Table 2**, the FEM results obtained considering the reinforced panel show that greater CFRP strip width leads to shear capacity increment. At constant strips width, however, the shear capacity decreases by considering the increment of the spacing ( $p_f$ ) between strips. Comparing the FEM models reinforced by using CFRP strips characterized by different widths ( $b_f$ ), but equally spaced ( $p_f$ ), a global behaviour improvement has been highlighted passing from CFRP strips 100 mm wide to 300 mm wide.

<i>Panels</i>	<i>Shear Capacity FEM</i>	<i><math>\Delta</math>Shear Capacity</i>
	<i>kN</i>	<i>%</i>
<i>H_100_1</i>	206	47,0%
<i>H_150_1</i>	216	53,6%
<i>H_200_1</i>	223	59,3%
<i>H_300_1</i>	238	70,0%
<i>H_100_2</i>	204	45,7%
<i>H_150_2</i>	210	50,0%
<i>H_200_2</i>	215	53,6%
<i>H_300_2</i>	232	65,7%
<i>H_100_3</i>	203	45,0%
<i>H_150_3</i>	207	47,9%
<i>H_200_3</i>	213	52,1%
<i>H_300_3</i>	227	62,1%

**Table 7.2.2.3:** Shear capacity and displacements

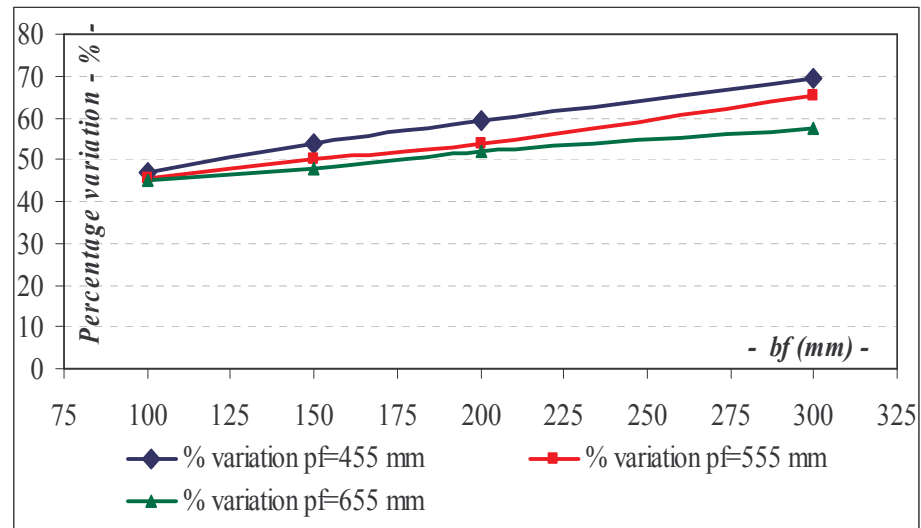


**Fig. 7.2.2.2:** Percentage variation by changing the strips wide ( $b_f$ )

For instance, in the following graph, the comparison among the FEM capacity curves of the masonry panels reinforced by using 200 mm wide strips and different spacing, was reported.

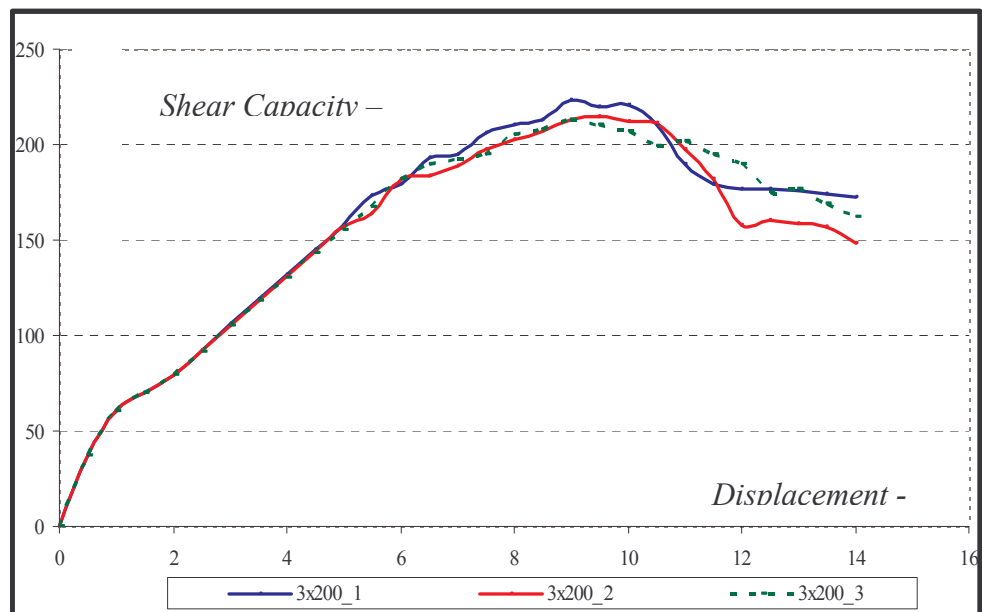


**Fig. 7.2.2.3:** Reinforced masonry panel capacity curves ( $b_f=200$ mm and changing the spacing )

The crack pattern of the masonry panels reinforced by using wider CFRP strips, creates a better microcracks network diffusion on the specimens surface; thus, the cracks width is reduced, and the reinforced masonry panel global behavior improves significantly.

For instance, the crack patterns of the specimens reinforced by using different widths of CFRP strips and equally spaced are depicted in the following.

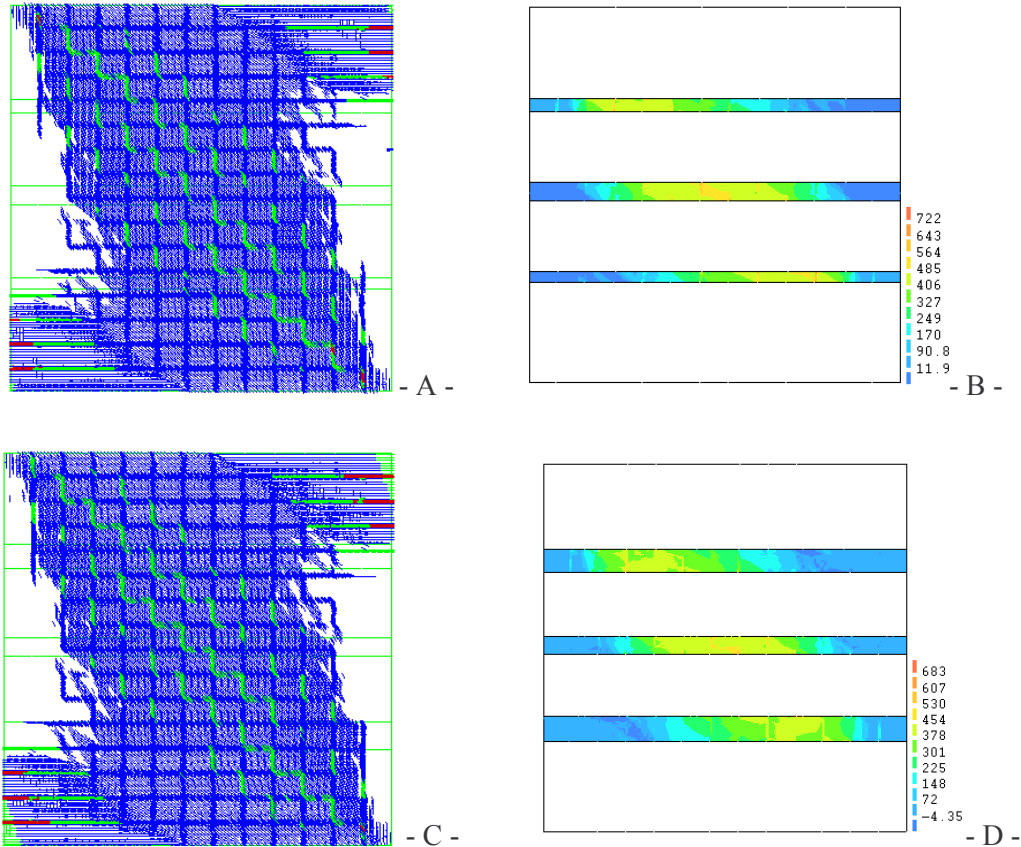


**Fig.7.2.2.4-A:** A) crack pattern H\_100\_1; B) FRP stresses on H\_100\_1; C) crack pattern H\_150\_1; D) FRP stresses on H\_150\_1



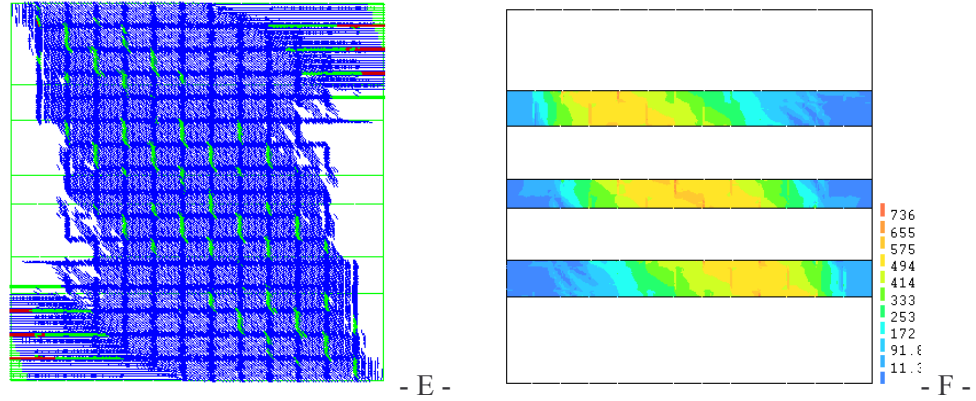


**Fig.7.2.2.4-A:** E) crack pattern H\_200\_1; F) FRP stresses on H\_200\_1.

The reinforcement configuration made by using horizontal strips allows the maximum stresses in the middle of the specimens to be reached, while at the extreme parts of the CFRP the stresses are very low.

Consequently there is a band of horizontal strips, assessed according to the width  $B$  of the masonry panel, which is not being loaded; that band was computed to be lower than 10% of the panel width ( $B$ ).

Furthermore, the results obtained by implementing FEM analyses were compared with the results using the design code expressions.

$$V_{rd,tot} = V_{rd,ur} + V_{rd,f}$$

$$V_{rd,f} = \frac{1}{\gamma_{rd}} \frac{0,6 \cdot d \cdot A_{fw} \cdot f_{fd}}{p_f} \quad (2)$$

where  $d$  is the distance between the centre of the panel and the surface subjected to compression,  $A_{fw}$  is the FRP cross-section area,  $f_{fd}$  is the FRP design strength and  $p_f$  is the FRP strips spacing.

The comparison between the results obtained by performing FEM analyses and applying the theoretical expressions proposed by the design provisions, have led to an average percentage variation about 6.7%.

<i>Panels</i>	<i>Shear Capacity FEM</i>	<i>Shear Capacity Theoretical</i>	<i><math>\Delta</math> Shear Capacity</i>
	<i>kN</i>	<i>kN</i>	<i>%</i>
<i>URP</i>	140.5	-----	-----
<i>H_100_1</i>	206.0	187.9	8.8
<i>H_100_2</i>	204.0	178.8	12.3
<i>H_100_3</i>	203.0	172.9	14.8
<i>H_150_1</i>	216.0	210.5	2.5
<i>H_150_2</i>	210.0	197.4	6.0
<i>H_150_3</i>	207.0	189.2	8.6
<i>H_200_1</i>	223.0	218.4	2.1
<i>H_200_2</i>	215.0	204.3	4.9
<i>H_200_3</i>	213.0	194.6	8.6
<i>H_300_1</i>	238.0	257.2	-8.1
<i>H_300_2</i>	232.0	236.2	-1.8
<i>H_300_3</i>	227.0	221.6	2.4

**Table 7.2.2.4:** Comparison between FEM and Theoretical results

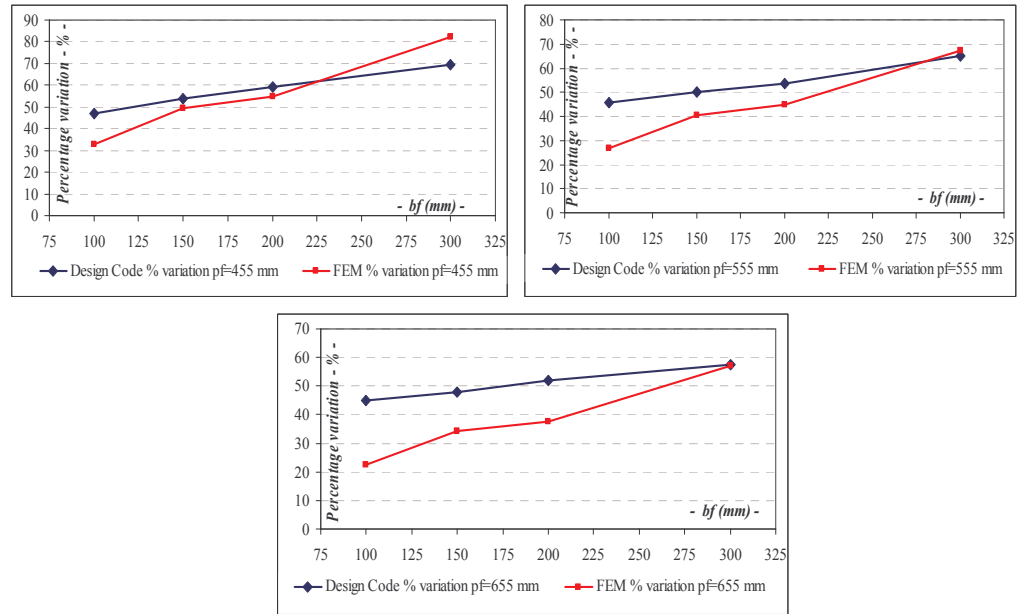


**Fig.7.2.2.5:** Comparison between FEM and Theoretical results

### 7.3. Pascale et al. Panel [5]

#### 7.3.1. Diagonal reinforcement layouts

The masonry panels of the Pascale et al. experimental tests were made by using clay bricks and premixed cement mortar.

The gravitational loads were applied on the specimen top section by means of two forces both equal to 50 kN and 600 mm spaced each other; the horizontal actions were applied by means of controlled displacements realized by using an hydraulic jack.

Once the masonry panels validation was done, as described in the previous chapter, different CFRP reinforcement configurations have been studied by varying the geometry, to check the influence on the global response of the panel.

The unreinforced masonry panels exhibit a shear capacity equal to 109 kN; the crack pattern showed a clear sliding shear mechanism on the top and on the bottom

section of the specimens and a micro-cracks network on the lateral surface. Different CFRP reinforcement geometric solutions were taken into account during the numerical simulations by means of diagonal arrangements; the CFRP applied on the specimens is characterized by strips 100 mm wide to 400 mm wide. The results have been summarized in the following, specifying the maximum shear capacity, the increment compared to unreinforced masonry panel shear capacity and the crack patterns developed on reinforced panels.

<i>Panel</i>	<i>Reinforcement layout</i>	<i>Shear Capacity FEM</i>	<i><math>\Delta</math> Shear capacity</i>
	UR panel Shear Capacity = 112 kN	<i>kN</i>	<i>%</i>
<i>D_100</i>	Diagonal Reinforcement	174	51.3%
<i>D_200</i>		237	106.0%
<i>D_300</i>		272	136.5%
<i>D_400</i>		307	167.0%

**Table 7.3.1.1:** FEM Analyses results

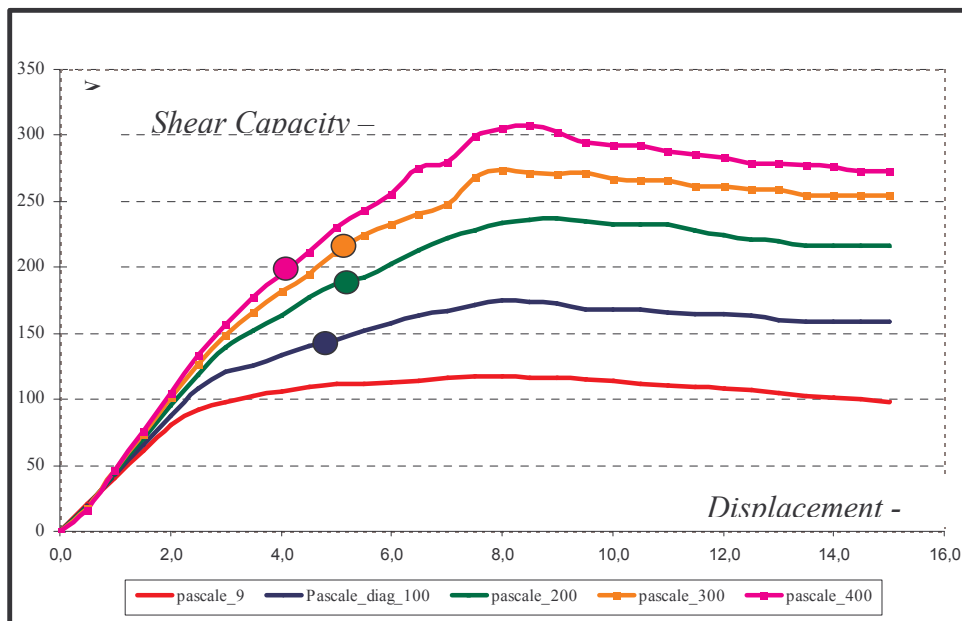


**Fig. 7.3.1.1:** FEM Analyses capacity curves

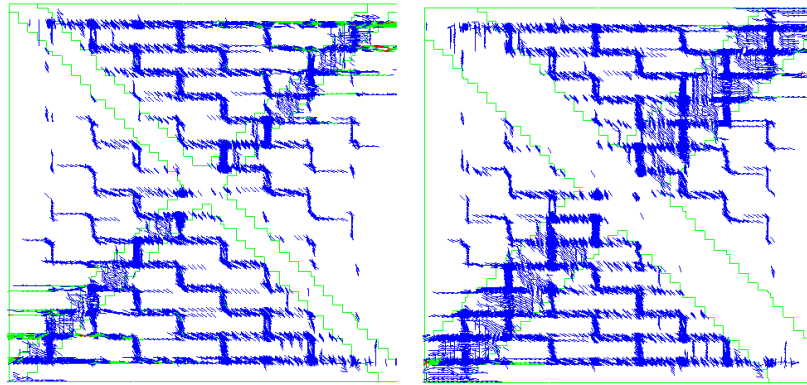


**Fig. 7.3.1.2:** FEM Analyses crack pattern; a) diagonal strip 100 mm wide; b) diagonal strip 200 mm wide

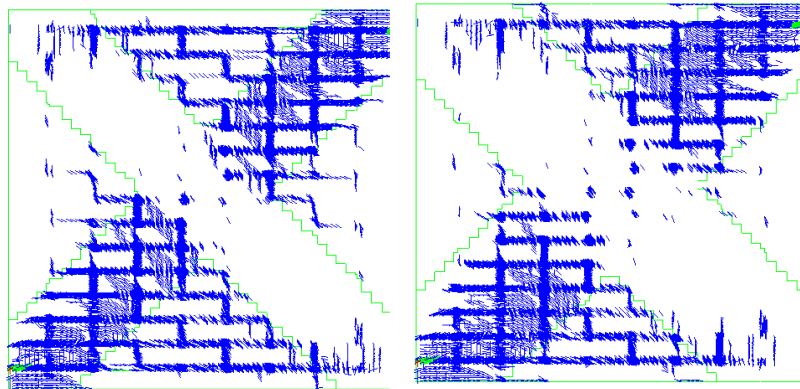


**Fig. 7.3.1.3:** FEM Analyses crack pattern; a) diagonal strip 300 mm wide; b) diagonal strip 400 mm wide

The CFRP strips width increment leads to a progressive shear capacity growth; in fact the maximum shear capacity increment obtained by analysing the D\_100 panel (CFRP strip 100 mm wide) is equal to 51.3% compared with the unreinforced panel, while an increase of about 167.0% has been reached for masonry panel reinforced with strips 400 mm wide.

The reinforced panel crack patterns show a greater spread of the microcracks network on the panel surfaces. Again, the largest width of the stripes leads to a greater spread of microcracks and a better stresses distribution.

Furthermore, the FEM results were compared with the reinforced panel shear capacity evaluated by using the expression (1) introduced in literature (*Prota et al., 2006*).

The comparison shows a satisfactory agreement between the FEM and theoretical results, reaching a variation always below 10%. In particular, the maximum percentage variation (equal to 8.9% in absolute value) has been achieved by considering the panels reinforced with strips 200 mm wide.

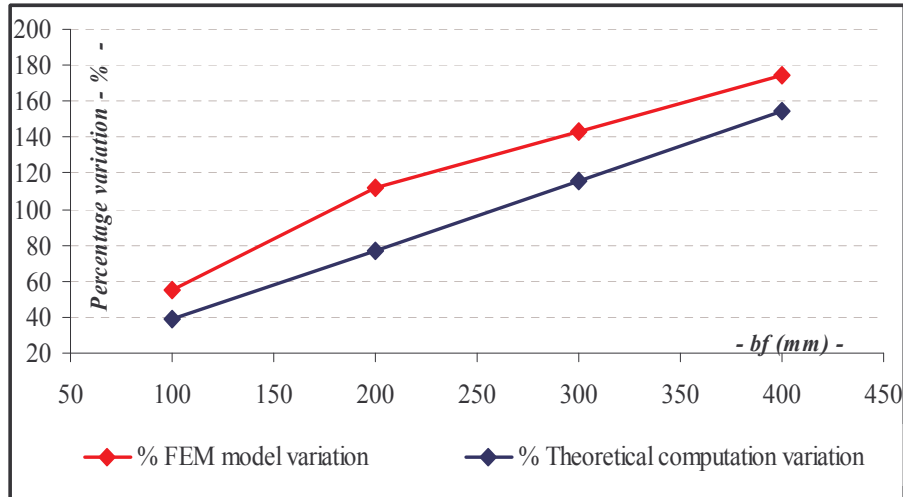


**Fig. 7.3.1.4:** Comparison between Theoretical and FEM obtained results

The FEM analyses performed on panels reinforced with diagonal stripes have been completed by studying other reinforcement layouts.

In fact, a second CFRP reinforcement strip was applied on the existing one, reducing the width, as shown below:

<i>Diagonal layouts</i>	<i>description</i>	<i>Area – mm<sup>2</sup></i>
D_100_2str	2 layers 100 mm wide applied	26,00
D_200	1 layer 200 mm wide applied	26,00
D_200_2str	2 layers 200 mm wide applied	52,00
D_400	1 layer 400 mm wide applied	52,00

**Table 7.3.1.2:** Comparison between different CFRP layouts

The results obtained by implementing FEM analyses show a better behavior in terms of shear capacity and stresses distribution considering the specimen reinforced with one layer of CFRP characterized by a greater width. Indeed, the D\_100\_2str panel (two layers of CFRP 100 mm wide) shows a maximum shear capacity about 30% lower than the shear capacity obtained by considering D\_200 panels (one layer of CFRP 200 mm wide). The percentage variation drops to 19% by comparing the D\_200\_2str panels (two layers of CFRP 200 mm wide) and the D\_400 panels (one layer of CFRP 400 mm wide).

<b>Panels</b>	<b>Description</b>	<b>A<sub>fw</sub> – mm<sup>2</sup></b>	<b>V<sub>max</sub> - kN</b>	<b>Δ V<sub>max</sub> - %</b>
URP_FEM	Unreinforced panel	----	112	----
D_100_2str	2 layers 100 mm wide	26.00	183.0	55.0%
D_200	1 layers 200 mm wide	26.00	237.0	101.0%
D_200_2str	2 layers 200 mm wide	52.00	257.0	118.0%
D_400	1 layers 400 mm wide	52.00	307.0	160.0%

<b>Panels</b>	<b>Description</b>	<b>V<sub>max</sub> - kN</b>	<b>Δ V<sub>max</sub> - %</b>
D_100_2str	2 layers 100 mm wide	183.0	----
D_200	1 layers 200 mm wide	237.0	30.0%
D_200_2str	2 layers 200 mm wide	257.0	----
D_400	1 layers 400 mm wide	307.0	19.0%

**Table 7.3.1.3:** Comparison between different CFRP layouts

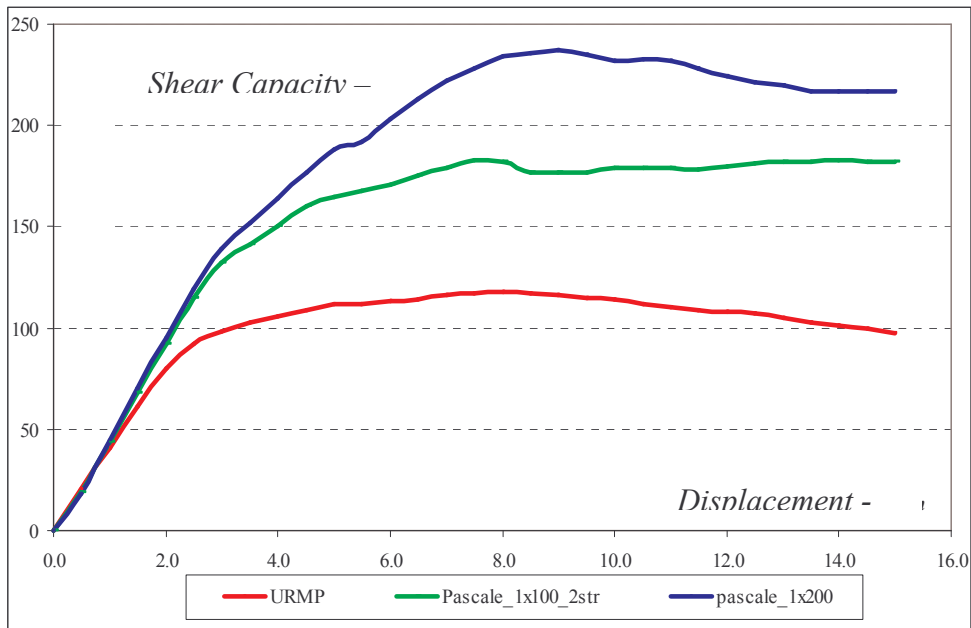


Fig. 7.3.1.5: Comparison between D\_100\_2str and D\_200 capacity curves

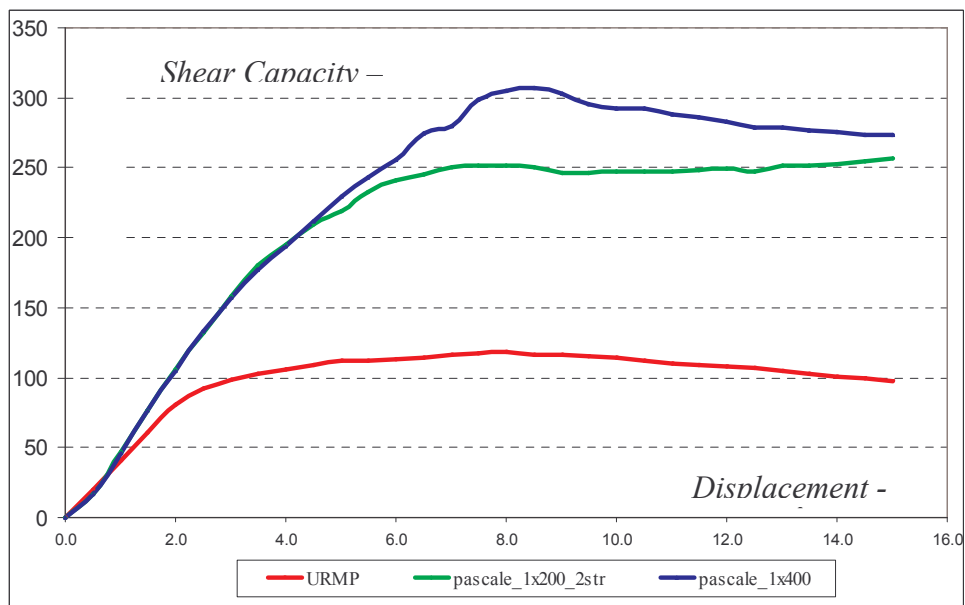
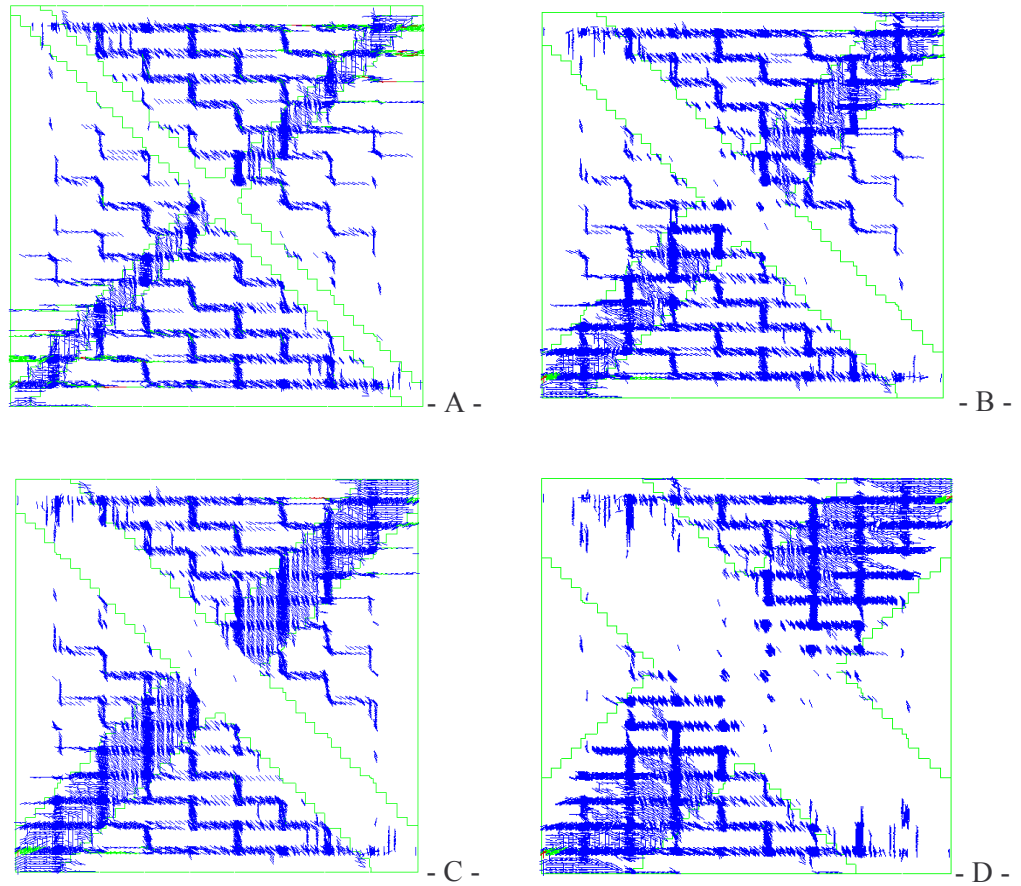


Fig. 7.3.1.6: Comparison between D\_1200\_2str and D\_400 capacity curves





**Fig. 7.3.1.7:** Crack patterns: A) D\_100\_2str; B) D\_200; C) D\_200\_2str; D) D\_400

### 7.3.2. Horizontal reinforcement layouts

The horizontal reinforcement configurations were analyzed by varying the strip width ( $b_f$ ) and the spacing between them ( $p_f$ ).

The CFRP strips width ( $b_f$ ) was assumed equal to 100 mm, 200 mm and 300 mm, spaced at  $b_f$ , twice  $b_f$  ( $2 b_f$ ) and three times  $b_f$  ( $3 b_f$ ), respectively.

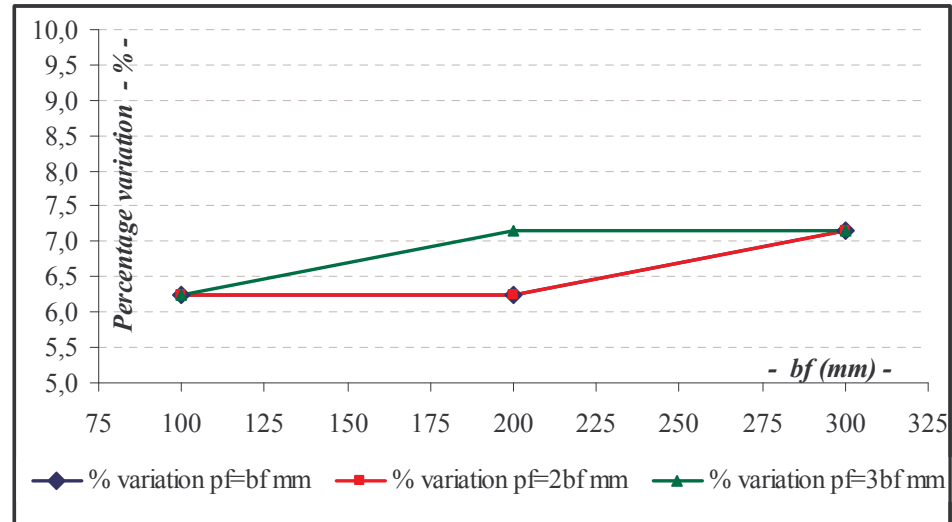
<i>Panels</i>	<i>Layouts</i>	<i>b<sub>f</sub> - mm</i>	<i>p<sub>f</sub> - mm</i>
<i>H_100_1</i>	3 horizontal layers	100	bf = 100 mm
<i>H_100_2</i>			2bf = 200 mm
<i>H_100_3</i>			3bf = 300 mm
<i>H_200_1</i>		200	bf = 200 mm
<i>H_200_2</i>			2bf = 400 mm
<i>H_200_3</i>			3bf = 300 mm
<i>H_300_1</i>		300	bf = 300 mm
<i>H_300_2</i>			2bf = 600 mm
<i>H_300_3</i>			3bf = 900 mm

Table 7.3.2.1: Shear capacity and displacements

The numerical simulation results of reinforced panels in terms of maximum shear capacity and a comparison with the maximum shear capacity of unreinforced panels are reported in the following table:

<i>Panels</i>	<i>Shear Capacity FEM</i>	<i>Δ Shear Capacity</i>
	<i>kN</i>	<i>%</i>
<i>URP</i>	112.0	-----
<i>H_100_1</i>	119.0	6.3%
<i>H_100_2</i>	120.0	7.1%
<i>H_100_3</i>	120.0	7.1%
<i>H_200_1</i>	119.0	6.3%
<i>H_200_2</i>	120.0	7.1%
<i>H_200_3</i>	120.0	7.1%
<i>H_300_1</i>	119.0	6.3%
<i>H_300_2</i>	119.0	6.3%
<i>H_300_3</i>	120.0	7.1%

Table 7.3.2.2: Shear capacity and displacements



**Fig. 7.3.2.1:** Percentage variation by changing the spacing ( $p_f$ )

The horizontal reinforcement configuration does not induce increments in terms of shear capacity; the maximum percentage increased is equal to 7.1%. The results are related to the sliding-shear collapse mechanism of the panel, which makes it not effectively reinforced by using horizontal strips. This theory has been demonstrated by studying the same panel reinforced with horizontal strips connected at the ends by applying vertical strips 40 mm wide. In fact, implementing the parametric finite element analysis, it is:

- At constant strips width and varying the spacing between them, the reinforced panel shear capacity is the same;
- Comparing the experimental results by varying the strips width and the spacing between them, the shear capacity did not reach noticeable variations (the shear capacity increment is about 51.8% for all the reinforcement typologies).

For instance, in the following graph, the comparison among the FEM analyses capacity curves of the masonry panels reinforced by using 200 mm wide strips and different spacing, connected by using vertical strips 40 mm wide at the horizontal strips ends, were reported.

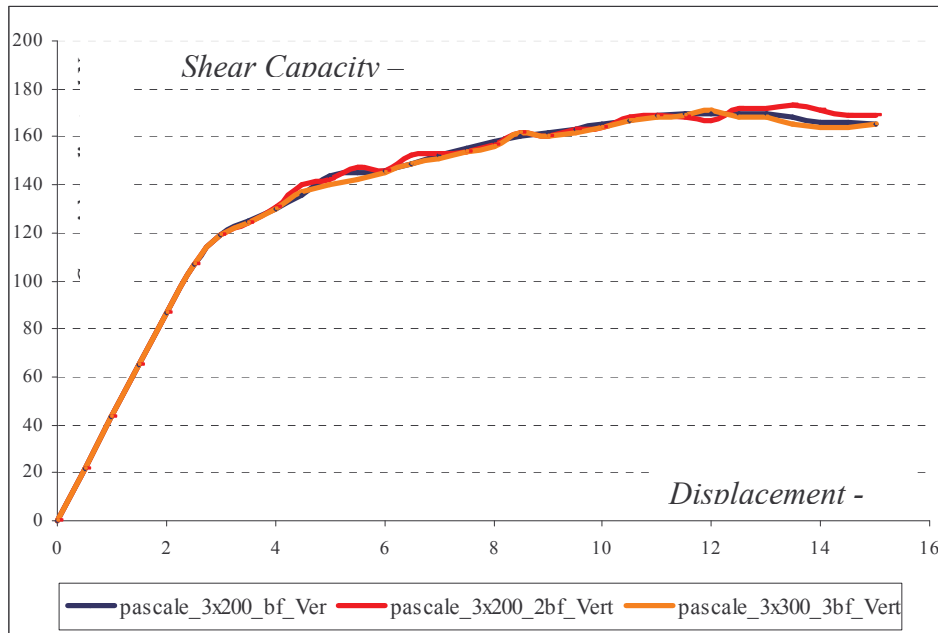


**Fig. 7.3.2.2:** Reinforced masonry panel capacity curves ( $b_f=200\text{mm}$  and changing the spacing  $p_f$ )

Comparing the crack patterns of the masonry specimens reinforced with horizontal strips connected or not by using vertical strips 40 mm wide, a better micro-cracks diffusion has been detected on the lateral surface; thus, the global behavior improves significantly applying the vertical strips.

For instance, the crack patterns of the masonry panels reinforced by using horizontal strips 200 mm wide, with and without connection made by using vertical strips 40 mm wide have been reported:

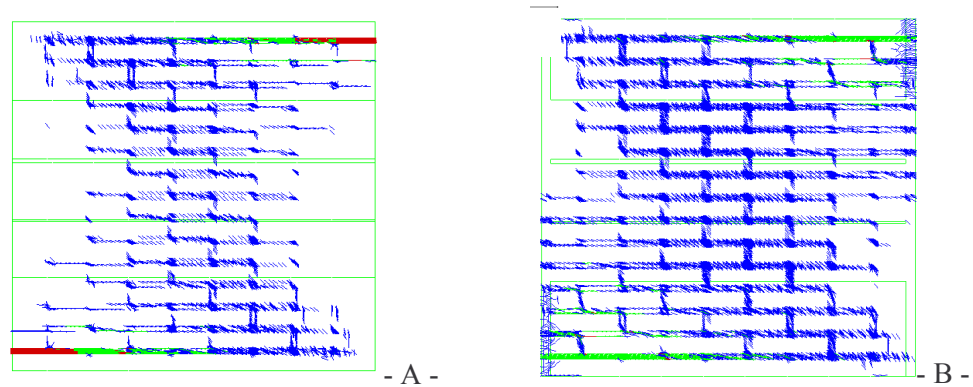


**Fig.7.3.2.3:** Crack patterns. A) H\_200\_1; B) H\_200\_1 with vertical strips

The comparison between the results obtained by performing FEM analyses on masonry panels reinforced by using horizontal and vertical strips, and applying the theoretical expressions proposed by the design provisions, have led to an average percentage variation about 9.8%.

Analyzing the results obtained comparing the FEM analyses on masonry panels reinforced by using horizontal strips only, the average percentage variation has been computed about 52%.

In the following the percentage variations obtained by implementing both masonry panels reinforced by using horizontal strips, connected or not to the vertical strips, have been reported:

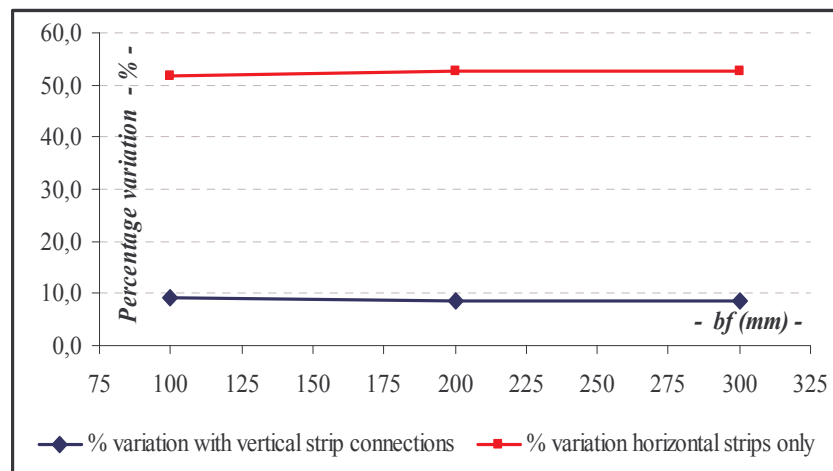


**Fig.7.3.2.4:** Comparison between FEM and Theoretical results

## 7.4. Manfredi et al. Panel [6]

### 7.4.1. Diagonal reinforcement layouts

The masonry panels tested by Manfred et al. experimental tests were made by using tuff blocks and premixed cement mortar.

Two types of gravitational loads were applied on the top surface of the panel equal to 130 kN and 325 kN, respectively. The horizontal actions were applied by means of controlled displacements by using an hydraulic jack.

The model has been validated and different reinforcement configurations have been studied by varying the geometries to test their influence on the global response of the panel.

The unreinforced masonry panels loaded by 130 kN have shown a shear capacity about 102 kN and the crack pattern showed three large diagonal cracks with a micro-cracks network extended on the lateral surface of the panel. The numerical simulations have shown the masonry specimens global behaviour by using CFRP diagonal reinforcement, considering the strip width ranging from 100 mm to 400 mm. The results have been summarized in the following, specifying the maximum shear capacity and the crack pattern developed for reinforced panels and the shear capacity increment compared to unreinforced masonry panel.

<i>Panel</i>	<i>Reinforcement layout</i>	<i>Shear Capacity FEM</i>	<i>Δ Shear capacity</i>
	UR panel Shear Capacity = 102 kN	<i>kN</i>	<i>%</i>
<i>D_100</i>	Diagonal Reinforcement	119	17.0%
<i>D_200</i>		129	26.0%
<i>D_300</i>		146	43.0%
<i>D_400</i>		160	57.0%

**Table 7.4.1.1:** FEM Analyses results

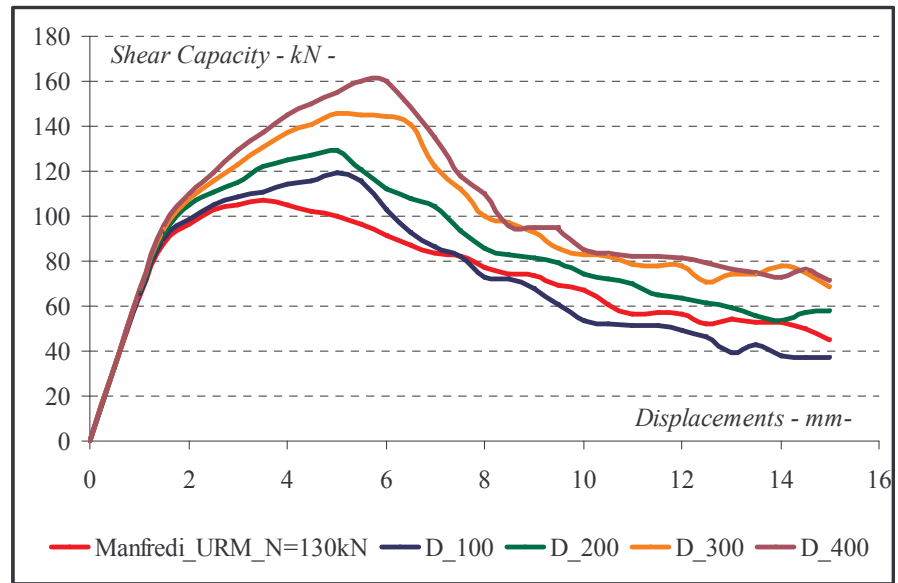
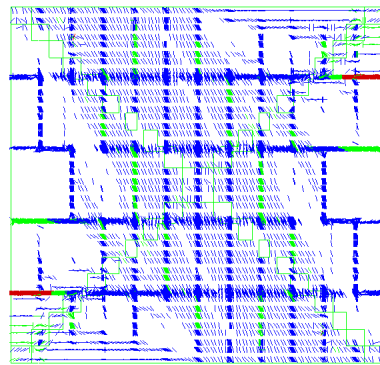
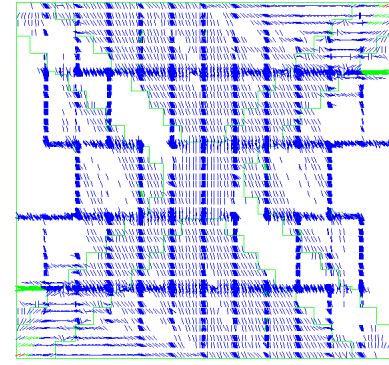


Fig. 7.4.1.1: FEM Analyses capacity curves



- A -



- B -

Fig. 7.4.1.2: FEM Analyses crack pattern; a) diagonal strip 100 mm wide; b) diagonal strip 200 mm wide

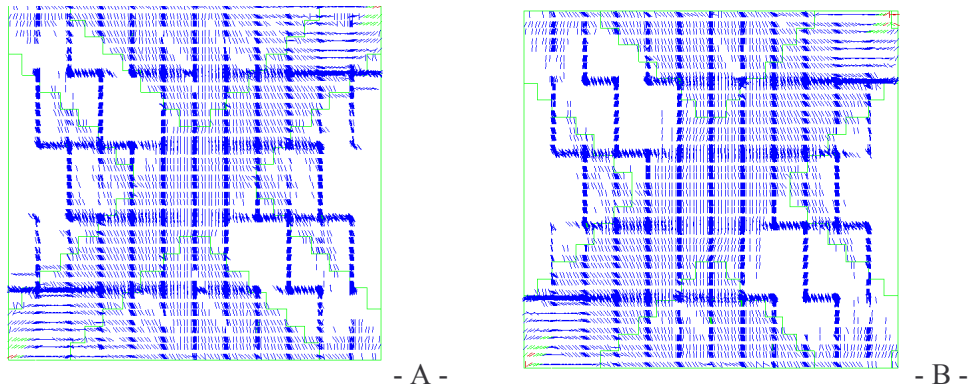


**Fig. 7.4.1.3:** FEM Analyses crack pattern; a) diagonal strip 300 mm wide; b) diagonal strip 400 mm wide

The CFRP strips width increment produces a progressive increase of the maximum shear capacity; in fact the shear capacity obtained by evaluating the D\_100 panels (CFRP strip 100 mm wide) is 17.0% more than the unreinforced panel shear capacity, passing to about 57.0% for the panel reinforced by using strips 400 mm wide. The reinforced specimens crack patterns show a greater spread of the micro-cracks network on the lateral surface of the panels and thus, a better stresses distribution.

Furthermore, the numerical and theoretical (obtained by using the expression [1]) shear capacity were compared and the results have been reported in the next. The results show a satisfactory agreement characterized by a percentage variation always below 3%. In particular, the maximum difference in percentage (equal to 2.85%) is obtained by considering the panel reinforced with strips 200 mm wide.



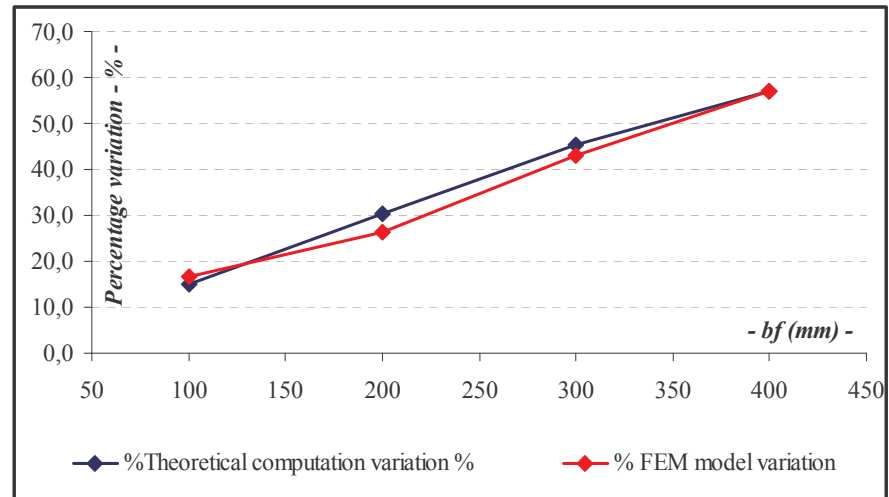


**Fig. 7.4.1.4:** Comparison between Theoretical and FEM obtained results

The numerical simulations of masonry panels reinforced by using diagonal arrangements have been completed taking into account different configurations characterized by the same area, but different CFRP strips number, as reported below:

<i>Diagonal layouts</i>	<i>description</i>	<i>Area – mm<sup>2</sup></i>
D_100_2str	2 layers 100 mm wide applied	26.00
D_200	1 layer 200 mm wide applied	26.00
D_200_2str	2 layers 200 mm wide applied	52.00
D_400	1 layer 400 mm wide applied	52.00

**Table 7.4.1.2:** Comparison between different CFRP layouts

The numerical results show a better behavior in terms of shear capacity and stresses distribution of the panels reinforced by using one layer of CFRP characterized by a greater strip width.

Indeed, for the D\_100\_2str panel (two layers of CFRP strip 100 mm wide) the maximum shear capacity was about 9.0% lower than the maximum shear capacity obtained considering D\_200 panel (one layer of CFRP strip 100 mm wide). The percentage variation is about 10% comparing the D\_200\_2str panel (two layers of

CFRP strip 200 mm wide) and the D\_400 panel (one layer of CFRP strip 400 mm wide).

Panels	Description	$A_{fw} - \text{mm}^2$	Vmax - kN	$\Delta V_{\text{max}} - \%$
URP	Unreinforced panel	----	102.0	----
D_100_2str	2 layers 100 mm wide	26.00	119.0	17.0%
D_200	1 layers 200 mm wide	26.00	129.0	26.0%
D_200_2str	2 layers 200 mm wide	52.00	145.6	43.0%
D_400	1 layers 400 mm wide	52.00	160.0	57.0%

Panels	Description	Vmax - kN	$\Delta V_{\text{max}} - \%$
D_100_2str	2 layers 100 mm wide	119.0	----
D_200	1 layers 200 mm wide	129.0	8.4%
D_200_2str	2 layers 200 mm wide	145.6	----
D_400	1 layers 400 mm wide	160.0	9.9%

**Table 7.4.1.3:** Comparison between different CFRP layouts

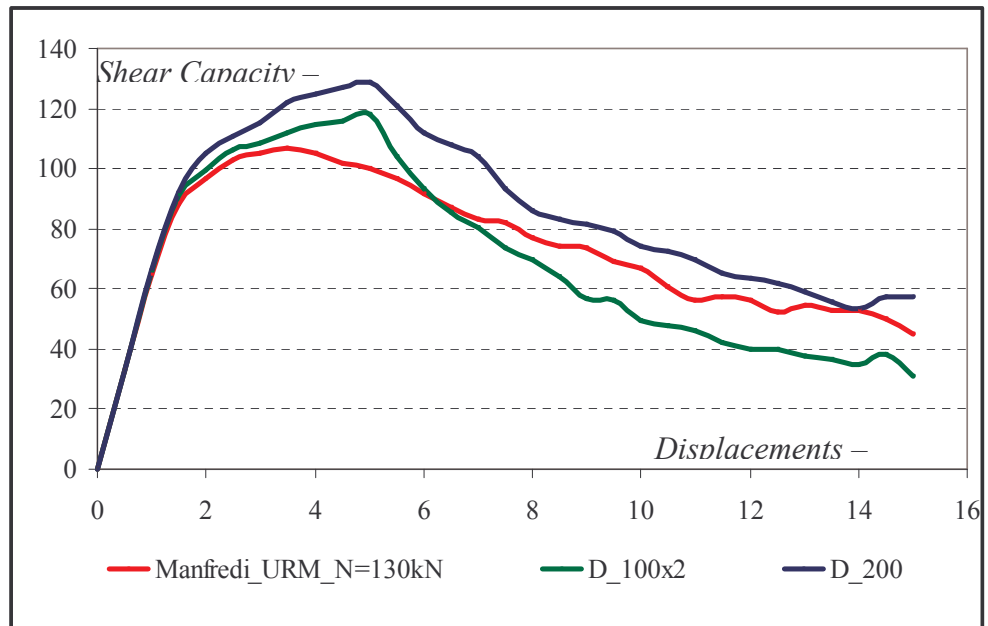
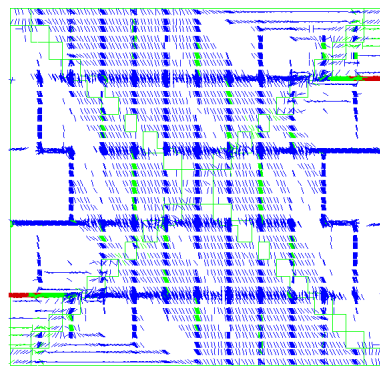
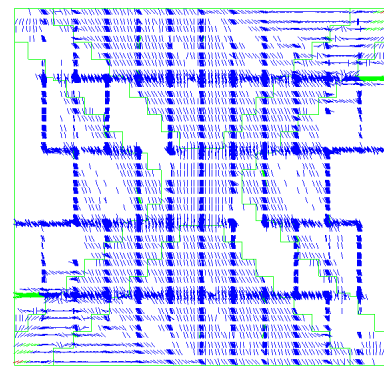


Fig. 7.4.1.5: Comparison between D\_100\_2str and D\_200 capacity curves



- A -



- B -

Fig. 7.4.1.6: A) D\_100x2 crack pattern; B) D\_200 crack pattern

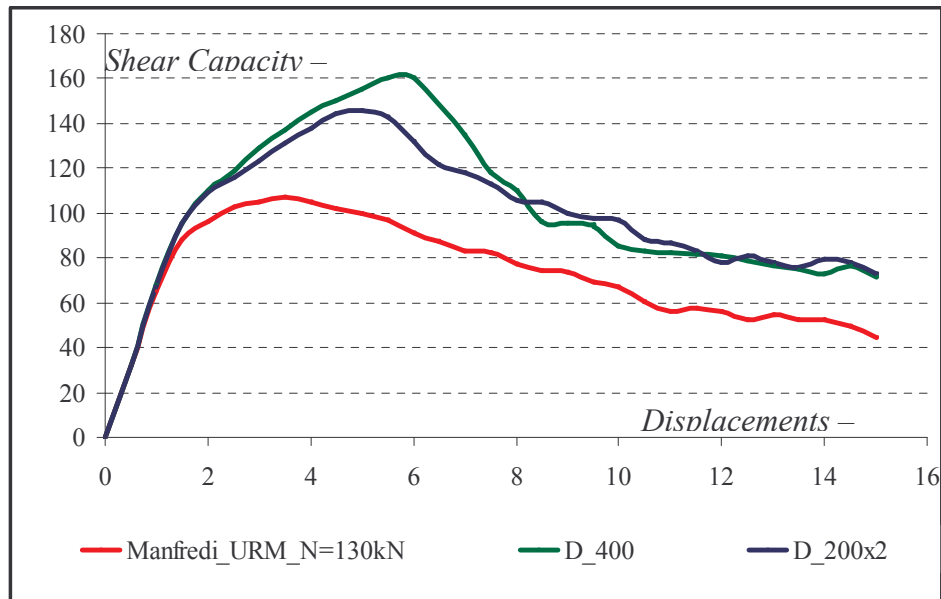


Fig. 7.4.1.7: Comparison between D\_100\_2str and D\_200 capacity curves

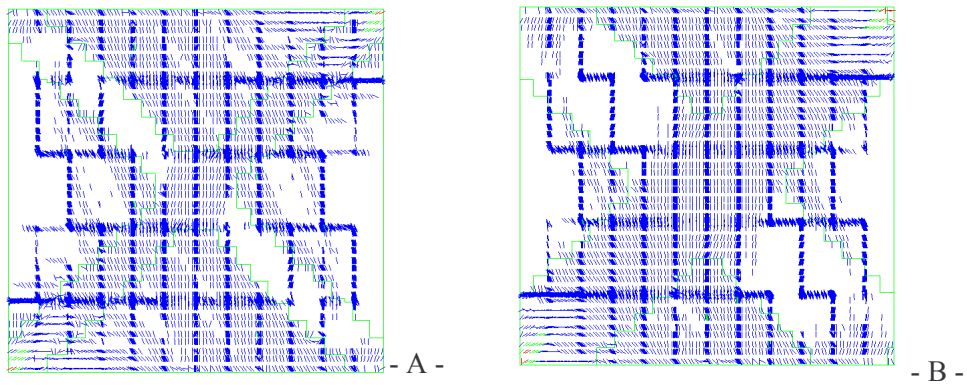


Fig. 7.4.1.8: A) D\_100x2 crack pattern; B) D\_200 crack pattern

### 7.4.2. Horizontal reinforcement layouts

The second configuration of the reinforcement considered in the parametric analysis considers the horizontal arrangement of CFRP strips. Several layouts were analyzed, varying the strips width ( $b_f$ ) and the spacing between them ( $p_f$ ). In particular, the CFRP strips width were changed between 100 mm and 300 mm, while the spacing was chosen equal to the strip width ( $b_f$ ), twice the strip width ( $2b_f$ ) and three times the strip width ( $3b_f$ ).

<i>Panels</i>	<i>Layouts</i>	<i><math>b_f</math> - mm</i>	<i><math>p_f</math> - mm</i>
<i>H_100_1</i>	3 horizontal layers	100	$b_f = 100$ mm
<i>H_100_2</i>			$2b_f = 200$ mm
<i>H_100_3</i>			$3b_f = 300$ mm
<i>H_200_1</i>		200	$b_f = 200$ mm
<i>H_200_2</i>			$2b_f = 400$ mm
<i>H_200_3</i>			$3b_f = 600$ mm
<i>H_300_1</i>		300	$b_f = 300$ mm
<i>H_300_2</i>			$2b_f = 600$ mm
<i>H_300_3</i>			$3b_f = 900$ mm

**Table 7.4.2.1:** Shear capacity and displacements

The comparison among the results obtained by implementing the numerical simulation of reinforced and unreinforced panels in terms of maximum shear capacity was reported in the following **Table 7.4.2.2**:

<i>Panels</i>	<i>Shear Capacity FEM</i>	<i><math>\Delta</math> Shear Capacity</i>
	<i>kN</i>	<i>%</i>
<i>URP</i>	102.0	-----
<i>H_100_1</i>	133.0	30.4%
<i>H_100_2</i>	132.0	29.4%
<i>H_100_3</i>	131.0	28.4%
<i>H_200_1</i>	133.0	30.4%
<i>H_200_2</i>	132.0	29.4%
<i>H_200_3</i>	129.0	26.5%
<i>H_300_1</i>	134.0	31.0%
<i>H_300_2</i>	131.0	28.0%
<i>H_300_3</i>	----	-----

**Table 7.4.2.2:** shear capacity and displacements

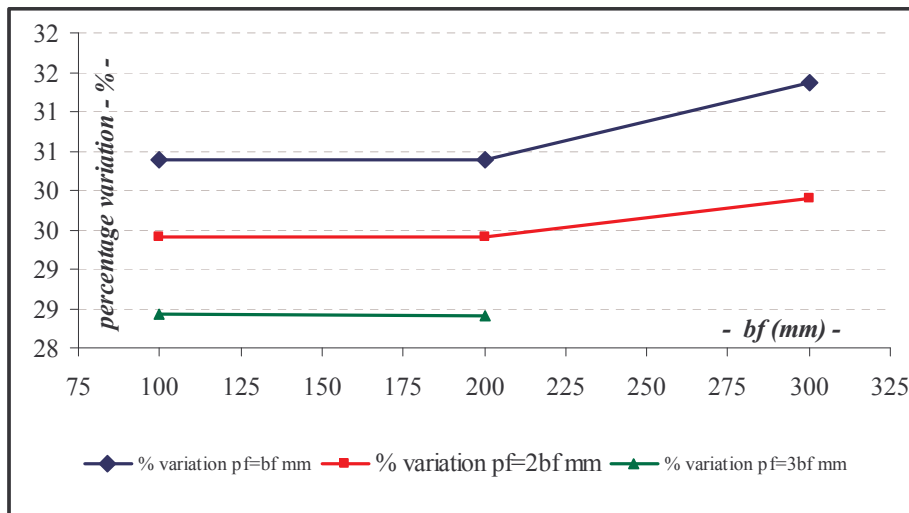


**Fig. 7.4.2.1:** Percentage variation by changing the spacing ( $p_f$ )

Regardless of the strips width (bf) and spacing (pf), the percentage variation of the reinforced panels shear capacity compared to the unreinforced panels shear capacity is almost equal to 30%.

For instance, in the following graph, the comparison among the FEM analysis capacity curves of the masonry panels reinforced by using 200 mm wide strips and different spacing, was reported.

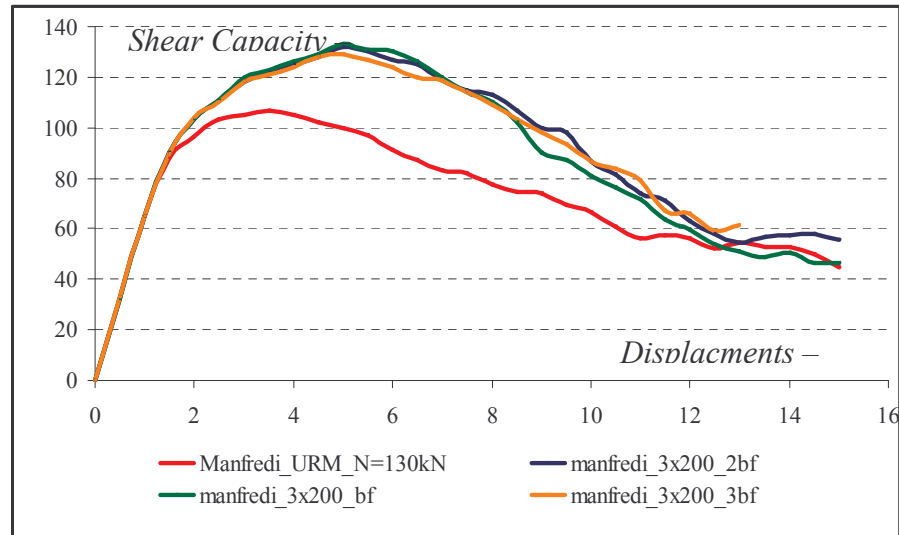


**Fig. 7.4.2.2:** Reinforced masonry panel capacity curves ( $b_f=200\text{mm}$  and changing the spacing)

The masonry panels reinforced by using larger strips define a better stresses distribution and widespread micro-cracks on the surfaces of the specimens. The main directions of the three major diagonal cracks have been preserved.

For instance, the crack patterns of masonry panels reinforced by using horizontal strips characterized by different widths (100 mm , 200 mm and 300 mm) and equally spaced ( $pf = 2 bf$ ), were depicted in the following.

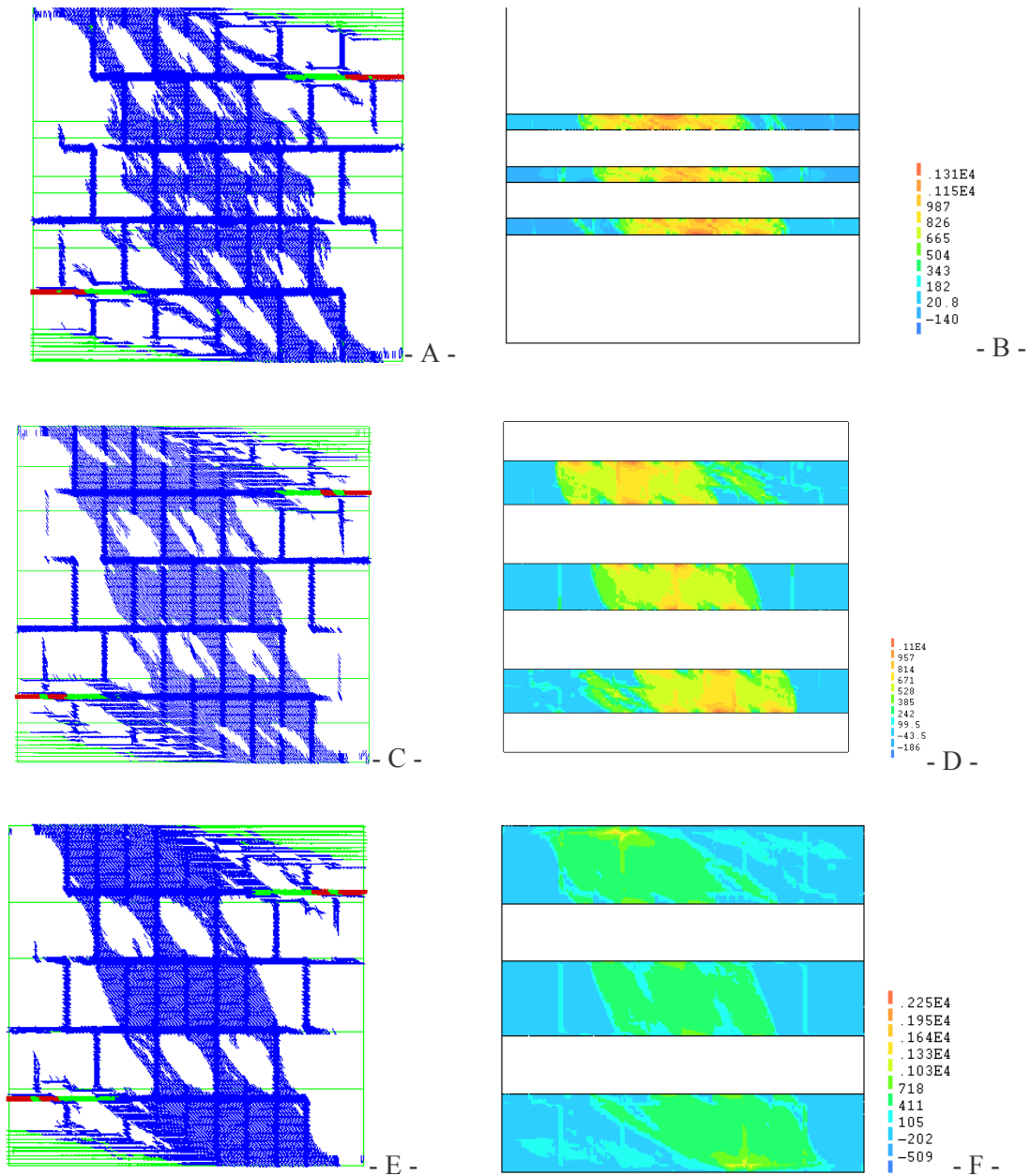


**Fig.7.4.2.3:** A) crack pattern H\_100\_2; B) FRP stresses on H\_100\_2; C) crack pattern H\_200\_2; D) FRP stresses on H\_200\_2; E) crack pattern H\_300\_2; F) FRP stresses on H\_300\_2



The strengthening system made by using horizontal strips allows to reach the maximum stresses in the middle of the reinforcement, while at the ends of the CFRP strips, the stress level is lower.

Consequently a band of horizontal strip ends, assessed according to the width  $B$  of the panel, is not being loaded by the actions. These band have been measured not exceeding an average 9% of the width of the panel. Furthermore, the numerical and theoretical results (computed according to the expression [2]) obtained by considering the horizontal strengthening arrangement were analysed. The comparison between the results obtained by performing FEM analyses and applying the theoretical expression proposed by the design provisions, led to an average percentage variation about 8.8%.

### 7.5. Final Remarks

The application of the masonry structures reinforcement by using innovative building materials, provides different geometric configurations; in this case, two strengthening layouts by means of diagonal and horizontal strips were studied and analyzed.

Three different experimental tests, described in previous chapters, have been examined.

In particular, the panels studied by Alcaïno et al. [3] and Manfredi et al.[6] reach the in-plan collapse mechanism, achieving the diagonal cracks on the specimens surfaces, while the numerical simulations of Pascale et al. [5] masonry panels lead to sliding shear mechanisms characterized by horizontal cracks on the top and on the bottom of the specimens.

Based on these observations, the first models (Alcaïno et al. [3] and Manfredi et al. [6]) implemented into the numerical simulations by using finite element modelling, determine a shear capacity increase of the reinforced panels considering both strengthening arrangements, by using diagonal and horizontal strips; moreover a better stresses distribution and a crack width reduction have been highlighted.

The latter masonry panels (Pascale et al. [5] experimental tests) provide a global behaviour improvement in terms of shear capacity by applying the diagonal strips layouts only. Even in this case, the strengthening system performs a better stresses

distribution and reduce the cracks width. The reinforcement made by horizontal strips is not effective.

An improvement of the panels performances in terms of maximum shear capacity and crack patterns is provided by applying CFRP strips 40 mm wide (minimum size introduced in the market) at the ends of the horizontal strips, in order to ensure their collaboration.

Applying the reinforcement strips characterized by a larger width, the outcomes show a good response of the masonry panel global behavior due to the better stresses distribution.

In terms of strength, the masonry panels behavior is almost identical reaching a maximum variation about 10% for both diagonal and horizontal strengthening systems.

Regarding the horizontal reinforcement, increasing the spacing between the CFRP strips, a decrease of the maximum shear capacity has been detected. The percentage variation was estimated about 10% passing from the spacing equal to the strip width ( $b_f$ ) to the spacing equal to three times the strip width ( $3b_f$ ).

## References

- [1] CNR DT 200/2004, 2004. *“Guide for the design and construction of externally bonded FRP systems for strengthening existing structures”*. Rome – CNR Institute.
- [2] TNO DIANA rel. 9.2. *“International Software Company for FEA applications in civil and geotechnical engineering”*.
- [3] Alcaino P., Santa Maria H., 2008. *“Experimental response of externally retrofitted masonry walls subjected to shear loading”*. ASCE Journal of Composites for Construction, Vol. 12, issue 5, Pages 489-498.
- [4] A.Prota, G.Manfredi, F.Nardone, 2008. *“Assessment of design formulas for In-plane FRP strengthening of masonry walls”*. ASCE Journal of composites for construction, Vol.12 n.6, Pages 643-649.
- [5] T.Stratford, G.Pascale, O.Manfroni and B.Bonfiglioli, 2004. *“Shear strengthening masonry panels with sheet GFRP”*. ASCE Journal of Composites for Construction, Vol. 8(5).
- [6] G.Faella, G.Manfredi, R.Realfonzo, 1991. *“Comportamento sperimentale di pannelli in muratura di tufo sottoposti ad azioni orizzontali di tipo ciclico”*. V Italian Congress - L’Ingegneria Sismica in Italia 1991- Palermo.

## CONCLUSIONS

Earthquakes occurred in Italy during the last year have highlighted the problems relating to the reinforcement of existing structures. The vast majority of these structures was designed without take into account horizontal forces; at the current state, thanks to a growing awareness of these actions and to a greater knowledge of the problems connected, detailed analyses of these structures should be done to verify the associated safety level. This affects not only the RC constructions or ordinary masonry buildings, but also the ecclesiastic structures. In this regard, a study was conducted on three important Gothic churches placed in Barcelona (Spain), to verify the global behavior under seismic actions. It should be noted that the Spanish coastal area is not considered at seismic risk, but the study has shown, however, a non optimal seismic behavior of the churches. The structures were divided into macro-elements and non linear cinematic analyses were implemented obtaining the associated capacity curves compared with the demand curves of the earthquake in order to establish the safety level. The results were compared with the structural behavior described by the historical evidences showing a correlation between the damages occurred during the times and those identified by the analysis of the mechanisms (with a safety level that could cause considerable structural damages).

As described by the Italian design provisions and by numerous papers about the cinematic analysis method, the influence of the macro element vibration modes is not taken into account into the calculations. For instance, considering the upper part of the principal façade of the structure, the capacity curve could be obtained assuming the influence of the whole macro element (façade). Thus, the out-of-plane collapse

mechanisms were studied with both approaches, the traditional method and the experimental one by considering the first three macro-element vibration modes. The results obtained by implementing the traditional methods are more conservative. In fact, the multiplier coefficient of unitary horizontal force (and thus the capacity curves), generating out-of-plane mechanisms is smaller applying the traditional method. As for the ecclesiastical structures, even on the ordinary masonry structures subjected to horizontal actions out-of-plane and in-plane collapse mechanisms should be produced.

For ecclesiastical structures, based on the realized studies and historical evidences, in-plane collapse mechanisms are not common because of the massive geometric characteristics of the structural elements. In ordinary masonry buildings in-plan mechanisms play an important role on the global structural behaviour. Thus, three masonry panels tested by three different groups were described and analysed.

The first series was made by using hollow clay bricks, the second by using solid clay bricks and the latter by using tuff blocks; premixed cement mortar was used for all the masonry specimens. A numerical simulation program was planned, modeling the panels by using Finite Element code, TNO DIANA rel. 9.2. The panel components were modeled separately describing the mechanical properties of both materials, mortar and brick, by considering the Rankine-Von Mises theory, assuming a linear softening behavior. Several mechanical parameters, not available from experimental tests, but crucial to implement the nonlinear static analyses of masonry panels by using finite element model, were calibrated starting from design expressions or were related to the available data.

The FEM and experimental tests results of “as built” masonry panels were compared obtaining a good agreement, and thus validating the model.

As aforementioned, some mechanical properties were not provided during the material characterization of experimental tests, but were required to model the specimens properly; the fracture energies of both materials should be considered. Numerical parametric analyses were realized identifying a plausible range within selecting the values of fracture energy for both materials, mortar and brick.

For hollow clay brick panels, the brick compressive fracture energy variation leads to shear capacity improvement after the elastic branch, leaving unchanged the initial stiffness.

The brick tensile fracture energy variation provide shear capacity increment less than that produced by compressive fracture energy changing.

Appreciable change have not been noticed by choosing different values of both mortar fracture energies.

Similar result have been obtained by studying tuff blocks panels varying the brick compressive and tensile fracture energies.

The biggest difference is related to the softening branch of capacity curve; by varying the compressive fracture energy the softening branch is less sloping.

The variation of fracture energies of both materials can be related to the panel global behavior in terms of ductility.

Two possible conditions can be defined according to low and high ratios among the mechanical properties of both materials, respectively:

- increasing the brick compressive fracture energy leads to panel ductility increment; increasing the brick tensile fracture energy, a ductility decrease has been found. The variation of both mortar fracture energies generates a small decrement of ductility.
- the variation of panel global behavior in terms of ductility is generated by the mortar tensile fracture energy only (ductility decrease).

Once the materials mechanical properties and their influence on the masonry panel global behavior were defined, a series of parametric simulations were planned on masonry specimens reinforced by using CFRP strips.

The numerical simulations were performed on panels validated models and two different reinforcement configurations were assumed (diagonal and horizontal arrangements of the strips on both sides of panel).

Diagonal reinforcement arrangement provides the shear capacity improvement and a better stresses distribution independently from the collapse mechanism.

Horizontal reinforcement arrangement appears to be strongly related to the failure modes.

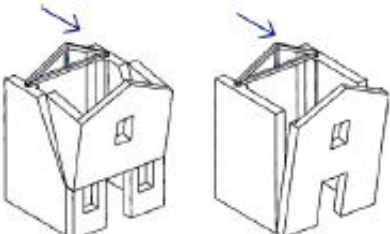
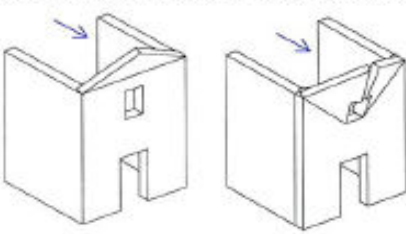
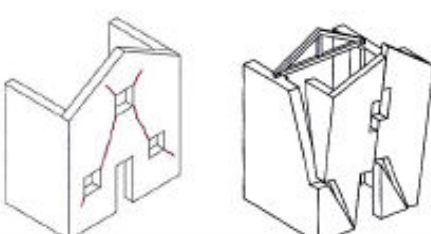
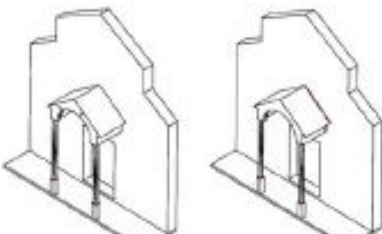
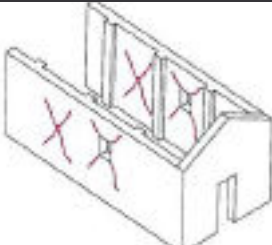
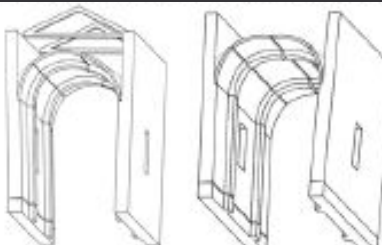
Indeed, for the diagonal shear mechanisms, reinforcement made by using horizontal stripes clearly improves the global behavior; the sliding shear mechanism makes ineffective the application of horizontal reinforcement.

In fact, the collaboration between different horizontal CFRP strips obtained by applying the vertical strips at the extreme sections of the panel has been considered necessary to improve the panel global behavior.

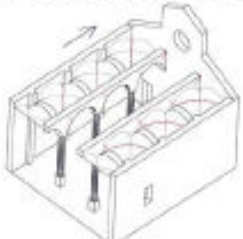
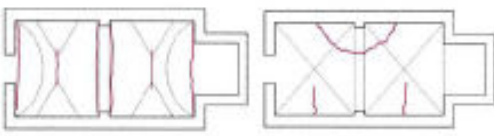
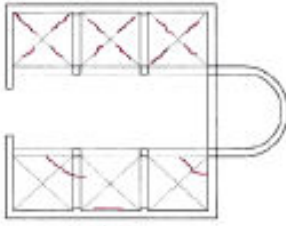
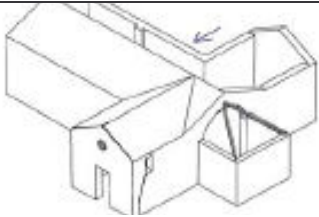
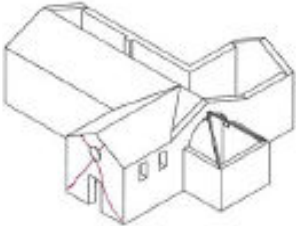
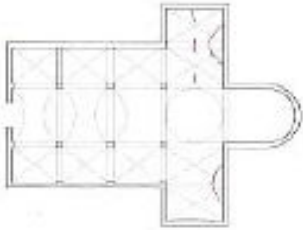
Taking into account the horizontal reinforcement, the spacing increase among the horizontal strips produces a shear capacity reduction, about 10-20%.

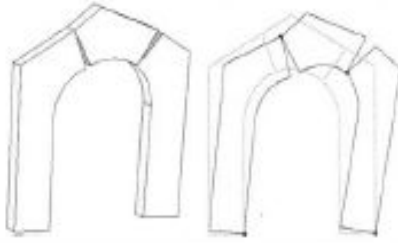
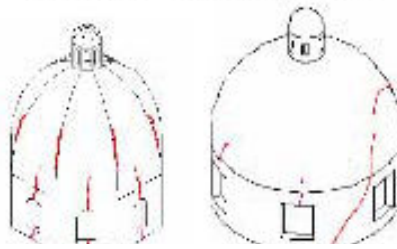
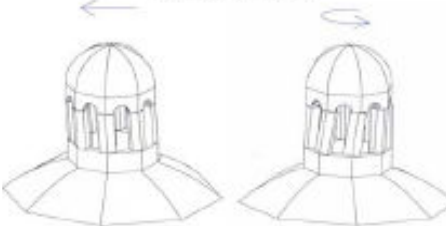
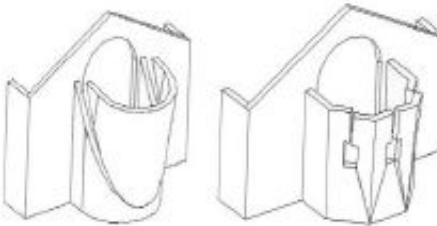
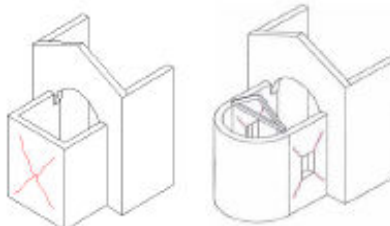
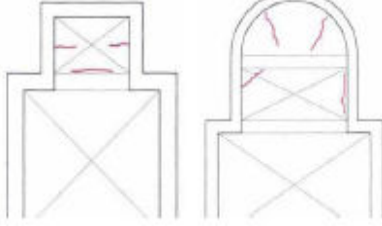
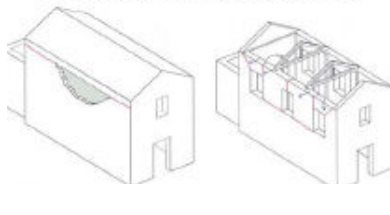

The stress levels were also computed on reinforcement, reaching high values in the middle of the strips. At the ends a lower stresses value was reached, avoiding the extreme debonding. This band was measured equal to about 10% of the masonry panel width.

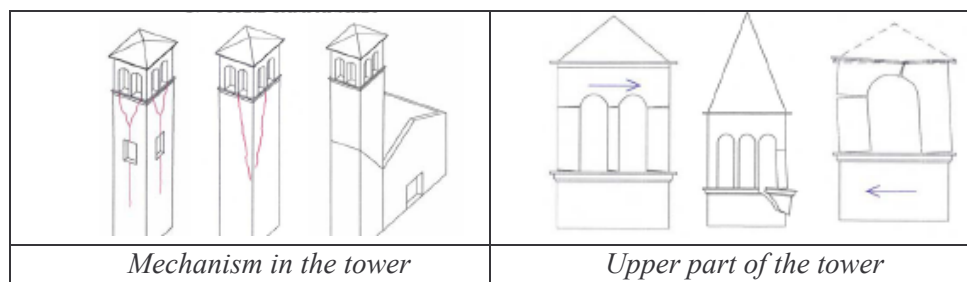
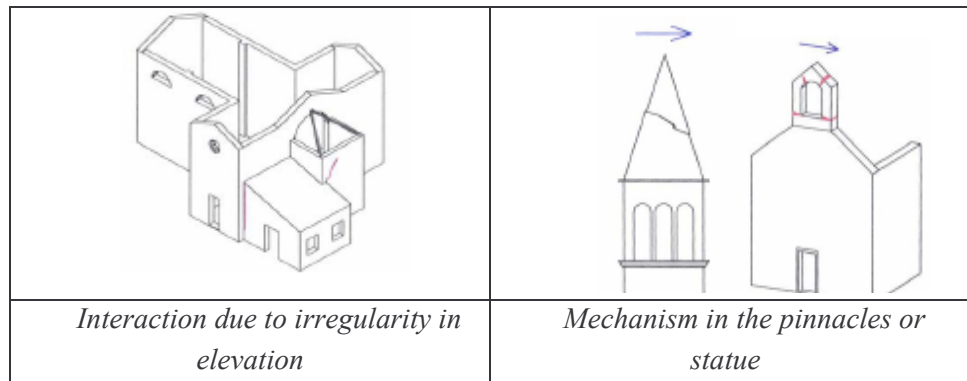
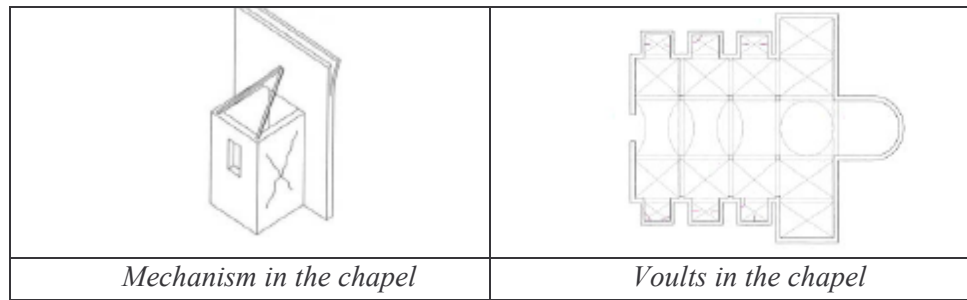
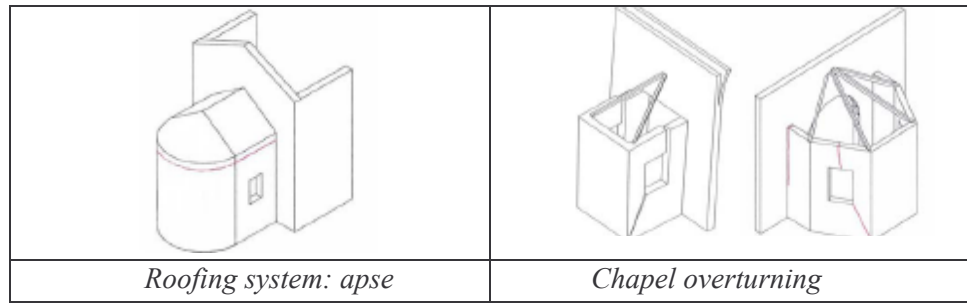
**ANNEX A: COLLAPSE MECHANISMS OF THE CHURCHES –  
(Italian guide line for evaluation and reduction of the seismic risk of the  
cultural heritage - 2006)**

	
<p><i>Façade over turning</i></p>	<p><i>Overturning of the upper part of the façade</i></p>
	
<p><i>Façade: In plane mechanism</i></p>	<p><i>Principal façade: mechanisms</i></p>
	
<p><i>Transversal response of the lateral façade</i></p>	<p><i>Shear mechanism cause of longitudinal actions</i></p>



	
<p><i>Longitudinal response on the columned</i></p>	<p><i>Dome of the central nave</i></p>
	
<p><i>Dome of the central nave</i></p>	<p><i>Overturning of the extreme façade</i></p>
	
<p><i>Shear mechanism in the extreme façade</i></p>	<p><i>Mechanism in the transept</i></p>

	
<p><i>Triumphal arches</i></p>	<p><i>Dome and dome cladding</i></p>
	
<p><i>Upper part of the tower</i></p>	<p><i>Apse over turning</i></p>
	
<p><i>Shear mechanism in the apse</i></p>	<p><i>Dome of the apse</i></p>
	
<p><i>Roofing system</i></p>	<p><i>Roofing system: transept</i></p>



## ANNEX B

### Whole CSM calculation procedure applied on the Santa Maria del Pi church for the mechanism 5

Santa Maria del Pi church is divided in eleven different macro-elements and for each of these sub-structures, the C.S.M. has been applied.

The main point of this procedure is to compare the demand curve with the capacity curve and for that reason it is possible to start from the study of the fore mentioned graphs. Santa Maria del Pi church is located in the Catalonia region and using detailed study carried out on the Barcelona soil, it is possible to know its mechanical properties and identify the said soil based on the classification used in the EuroCode 8, and namely as typology B.

The European design rule divide the soil in three different typologies, already introduced in the previous chapters, and in the following table reported.

	S	$\beta_o$	$K_1$	$K_2$	$T_B$	$T_C$	$T_D$	$a_g = a * g$
A	1	2.5	1	2	0.1	0.4	3	0.3924
B	1	2.5	1	2	0.15	0.6	3	0.3924
C	0.9	2.5	1	2	0.2	0.8	3	0.3924

**Table B-1:** Value introduced by the E.C.8 in order to draw the response spectrum graph

Using the parameters located in the table above, the elastic response spectrum can be depicted and is reported in the next (**Figure B-1**).

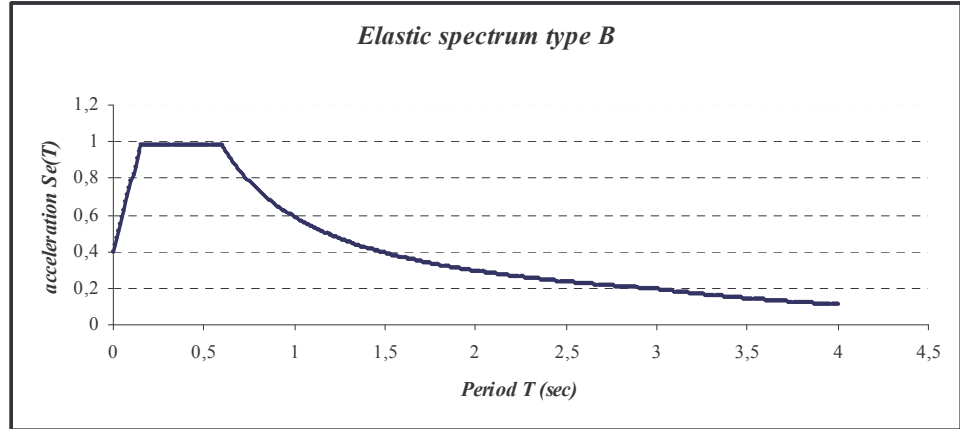


**Figure B-1:** Elastic response spectrum for soil B

It is required to relate the spectral acceleration to the spectral displacement using the following formulation in order to obtain the Acceleration Displacement Response Spectrum (ADRS), depicted in the **Figure B-2**.

$$S_d = \frac{T^2}{4 \cdot \pi^2} \cdot S_a$$

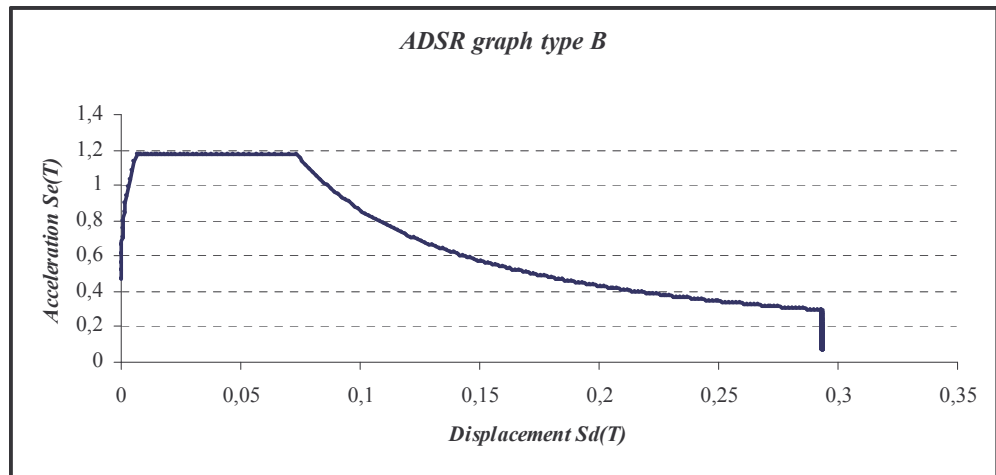


**Figure B-2:** ADSR for soil B

After evaluating the ADSR graph, it is necessary to compute the capacity curve related to the selected macro-element for a given mechanism. In the following, as an example, all the calculations of the principal façade (one of the possible selected macro-elements on the structure) subjected to out of plane mechanism (mechanism 5) will be described. The selected part is reported in the next picture and the mechanism which can occur for seismic action applied on longitudinal direction is shown.

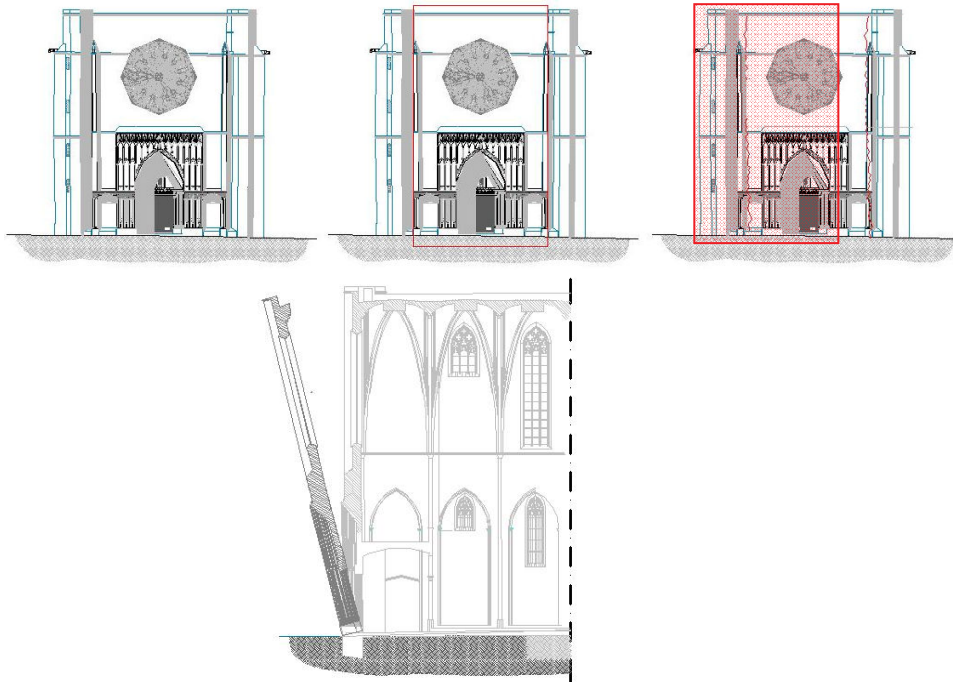


**Figure B-3:** Out of plane mechanism of principal façade of the Church

The limit analysis procedure can be applied when the geometrical properties of the structure are well-known because it is a principal of virtual works application. Thus, the following step is to describe the sub-structure in terms of its geometry, establishing the rotation point when the mechanism is activated and describe all the forces applied on the macro-element, due to the structural system or due to the mass of the structure object of the study. In the next **Figure B-4** the geometrical properties of the principal façade are reported considering this element divided in two different blocks, named *block 1* and *block 2*.

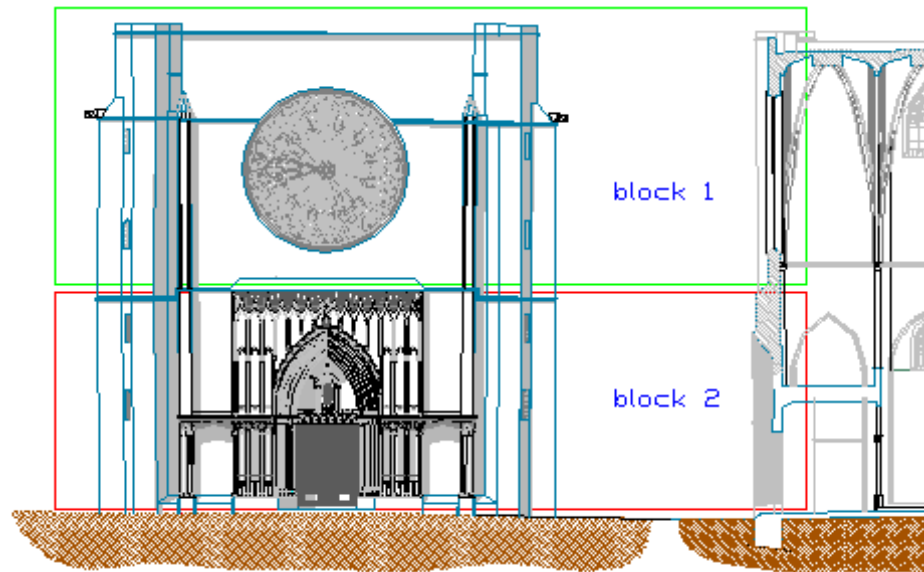


**Figure B-4:** Different parts of the same macro-element.

<i>block 1</i> <i>geometrical and mechanical prop.</i>			<i>block 2</i> <i>geometrical and mechanical prop.</i>		
<i>thickness</i>	0.75	m	<i>thickness</i>	1.4	m
<i>height</i>	14.95	m	<i>height</i>	13.5	m
<i>length</i>	17.6	m	<i>length</i>	17.6	m
<i>volume</i>	138.465	m <sup>3</sup>	<i>volume</i>	236.629	m <sup>3</sup>
<i>density</i>	2.3	ton/m <sup>3</sup>	<i>density</i>	2.3	ton/m <sup>3</sup>
<i>weight P<sub>1</sub></i>	318.5	ton	<i>weight P<sub>1</sub></i>	544.2	ton

**Table B-2:** Geometrical properties of the selected macro-element.

Using the measures above reported it is possible to apply the principle of virtual works, in order to know the multiplier  $\alpha_0$ . This coefficient represents the relation between the vertical and horizontal forces acting on the macro-element that activate this mechanism.

In order to evaluate  $\alpha_0$ , it is possible to consider the following formulation:

$$M_{st} = M_{des}$$

$$P_1 \cdot l_1 + P_2 \cdot l_2 = \alpha_o \cdot (P_1 \cdot h_1 + P_2 \cdot h_2)$$

$$\alpha_o = \frac{P_1 \cdot l_1 + P_2 \cdot l_2}{P_1 \cdot h_1 + P_2 \cdot h_2}$$

The geometrical measures and the value of the forces involved in the formulation above mentioned are reported in the next table and lead to following value for the multiplier coefficient:

$$\alpha_o = 0.0683 \Rightarrow M_{st} = M_{des} = 707.4 \text{ ton} \cdot \text{m}$$

Force (ton)		distance (m)	
P <sub>1</sub>	318.5	L <sub>1</sub>	1.025
P <sub>2</sub>	544.2	L <sub>2</sub>	0.7

Force (ton)		distance (m)	
P <sub>1</sub>	318.5	h <sub>1</sub>	20.975
P <sub>2</sub>	544.2	h <sub>2</sub>	6.75

**Table B-3:** Values used in order to find the multiplier coefficient.

Knowing only the  $\alpha_o$  value is not enough to have a global idea about the behaviour of the macro-element for a given mechanism.

In fact, the multiplier coefficient gives an information of the first step of the motion, but on the other hand, to understand the total movement until the collapse of the sub-structure is also important.

In the literature, it is possible to find the formulation that allows to know the reference point displacement value obtained when the multiplier  $\alpha_o$  is equal to zero.

The reference point has been chosen on the top of the sub structure as shown in the following picture:



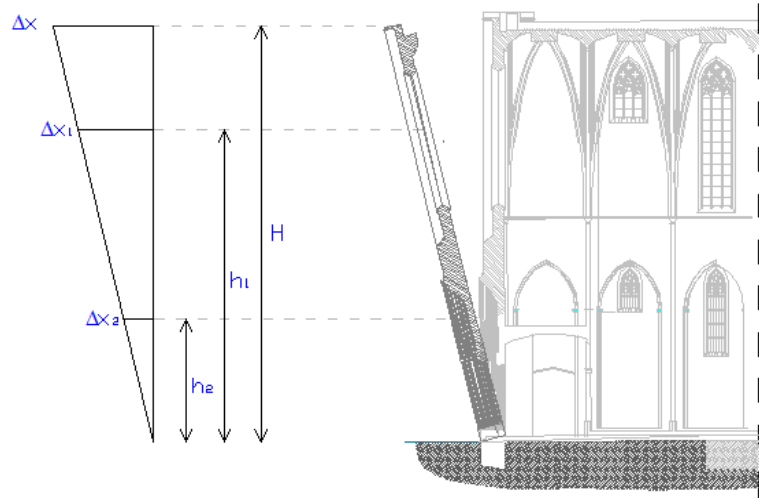


**Figure B-5:** Mechanism of the principal façade.

$$P_1 \cdot L_1 + P_2 \cdot L_2 = P_1 \cdot \frac{h_1}{H} \cdot \Delta x + P_2 \cdot \frac{h_2}{H} \cdot \Delta x$$

$$\Delta x = \frac{P_1 \cdot L_1 + P_2 \cdot L_2}{P_1 \cdot \left( \frac{h_1}{H} \right) + P_2 \cdot \left( \frac{h_2}{H} \right)} = d_{k,o} = 1.94m$$

Adopting the above formulation is possible to know the reference point displacement when the multiplier coefficient is equal to zero. This condition describes the impossibility to find an equilibrium configuration between the destabilizing moment and stabilizing moment and thus the collapse can occur.

Using the following formulation is possible to depict the total capacity curve, in which the horizontal forces are represented by means of multiplier coefficients and located on the vertical axis, while the displacements are situated on the horizontal axis.

$$\alpha = \alpha_o \cdot \left( 1 - \frac{d_h}{d_{k,o}} \right)$$

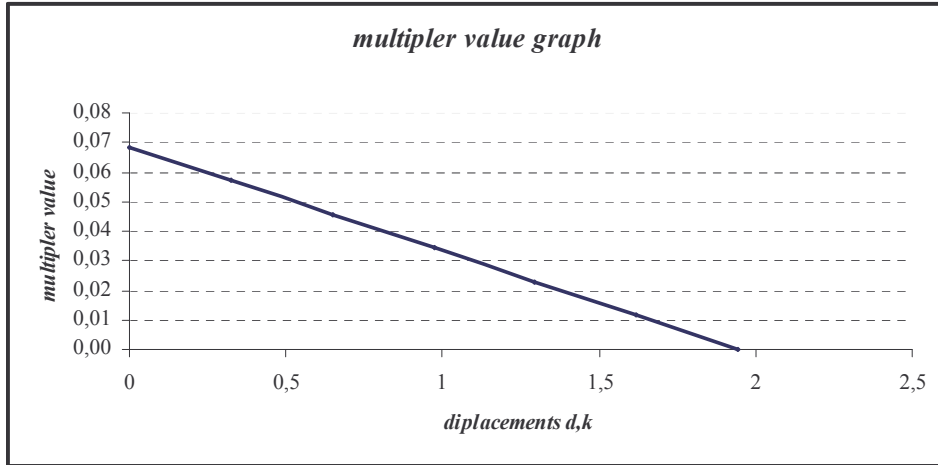


**Figure B-6:** Capacity curve for the selected macro-element and given mechanism.

In order to compare the structural capacity and the seismic demand, the above graph has to be modified to obtain the spectral accelerations and the spectral displacement on the vertical and horizontal axes, respectively.

To do it, some value must be known using the formulations listed in the following and described in the chapters of the work.

- 1) Participation mass:

$$M^* = \frac{\left( \sum_{i=1}^{n+m} P \cdot \delta_{x,i} \right)^2}{\left( \sum_{i=1}^{n+m} P \cdot \delta_{x,i}^2 \right)}$$

- 2) Fraction of the participation mass in the mechanism:

$$e^* = \frac{g \cdot M^*}{\sum_{i=1}^{n+m} P_i}$$

- 3) Spectral acceleration of the activation of the mechanism:

$$a_o^* = \frac{\alpha_o \cdot \sum_{i=1}^{n+m} P_i}{M^*} = \frac{\alpha_o \cdot g}{e^*}$$

Even the spectral displacement of the reference point, related to the spectral acceleration equal to zero, can be obtained using the following relations:

$$d^* = d_{k,0} \cdot \frac{\sum_{i=1}^{n+m} P_i \cdot \delta_{x,i}}{\delta_{x,k} \cdot \sum_{i=1}^{n+m} P_i} \rightarrow d^* = \varphi \cdot d_k \rightarrow \varphi = \frac{\sum_{i=1}^{n+m} P_i \cdot \delta_{x,i}}{\delta_{x,k} \cdot \sum_{i=1}^{n+m} P_i}$$

$$a^* = a_o^* \cdot \left( 1 - \frac{d_k^*}{d_{k,0}^*} \right)$$

At the end, the spectral capacity curve can be depicted as shown below:

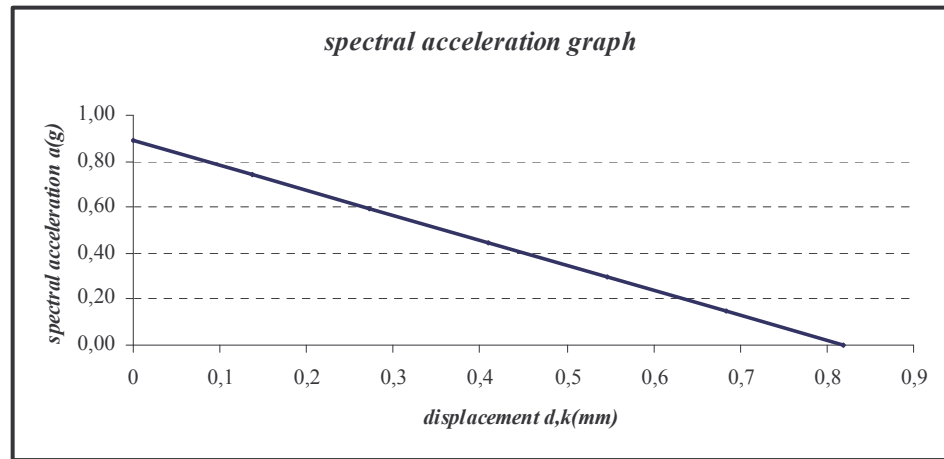


**Figure B-7:** Spectral capacity curve of the principal façade for a given mechanism.

The elastic branch of the capacity curve must be determined. It is necessary to know the displacement and the acceleration values in the limit elastic condition.

The displacement in the limit elastic condition can be evaluated given the following assumption:

$$d_s^* = 0.4 \cdot d_u^* \rightarrow d_u^* = 0.4 \cdot d_{k,o}^*$$

After knowing the displacement value it is possible to know the spectral acceleration value in the limit elastic condition ( $a_s^*$ ) using the inverse of the following formulation:

$$a^* = a_o^* \cdot \left( 1 - \frac{d_k^*}{d_{k,o}^*} \right)$$

The secant period of the elastic branch can be obtained using the following equation:

$$T_s^* = 2\pi \cdot \sqrt{\frac{d_s^*}{a_s^*}}$$

The values obtained have been listed in the following table:

$d_u^*$ (m)	$d_s^*$ (m)	$a_s^*$ (m/sec <sup>2</sup> )	$T_s^*$ (sec)
0.328	0.131	0.747	2.631

**Table B-4:** Values used to obtain the elastic branch of the capacity curve.

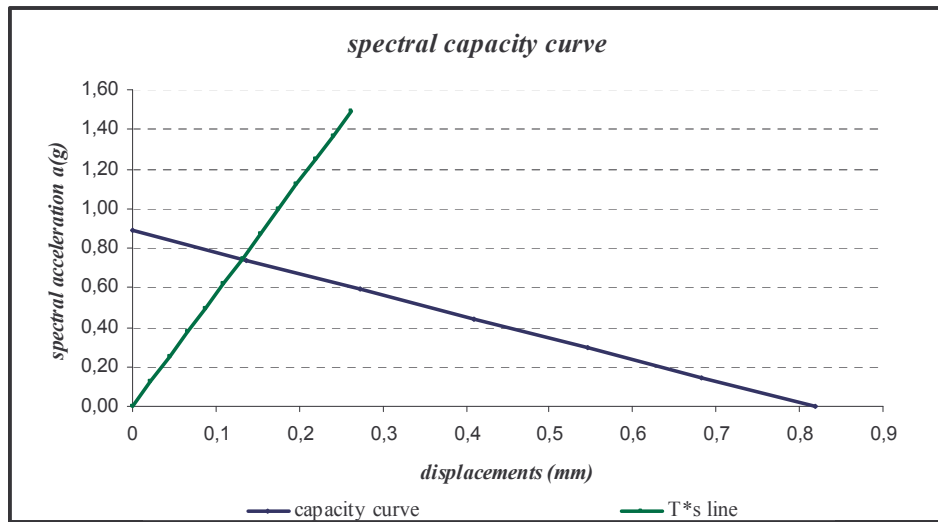


**Figure B-8:** Spectral capacity curve of the principal façade for a given mechanism with elastic branch.

The last step consists of putting in the same graph the demand curve and the spectral capacity curve, as shown in the following picture:

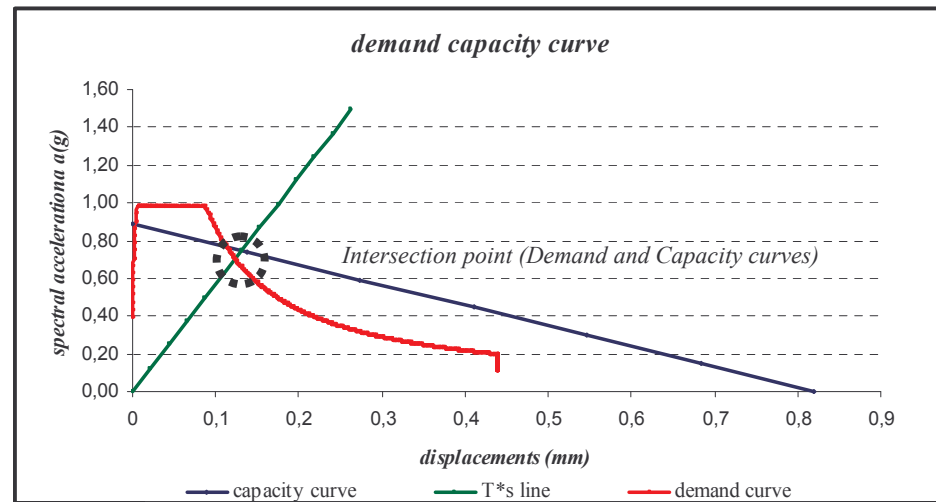


**Figure B-9:** Comparison between the capacity curve and demand curve.

The intersection point occurs in the elastic branch of the spectral capacity curve. Actually, the computation of the hysteretic energy dissipation is avoided. The evaluation of the demand displacement  $d_d^*$  has been conducted using the formulation introduced in the paragraph 3.5 of the present work.

For that reason the comparison between the ultimate capacity displacement and demand displacement can be evaluated without doing more complex calculations. The demand displacement is equal to the horizontal coordinate of the intersection point. In the following table the demand displacement, the ultimate displacement and the safety factor are reported. The safety factor has been obtained by means of the ratio between the displacement fore mentioned; safety factor more than unit value allows the technician to state the safety of the structures under seismic load condition, while safety factor less than the unit value establishes a dangerous situation for the building object of study.

$d_d^*(m)$	$d_u^*(m)$	safety coefficient	
0.129	0.328	$S.c. = \frac{d_u^*}{d_d^*}$	2.54

**Table B-5:** displacement values and safety coefficient

The level of the damages that can occur on the macro-element considering seismic actions on the structure can be evaluated according to Lagomarsino's assumption (described in chapter 3) as in the following shown:

$Sd =$	0.13	$m$
$0.7 Sdy =$	0.09	$m$
$Sdy =$	0.13	$m$
$0.25 Sdu =$	0.20	$m$
$0.5 Sdu =$	0.41	$m$
$Sdu =$	0.82	$m$

<i>label</i>	<i>Analyses results</i>	
<b>D0</b>	FALSE	<i>moderate damage</i>
<b>D1</b>	TRUE	
<b>D2</b>	FALSE	
<b>D3</b>	FALSE	
<b>D4</b>	FALSE	

**Table B-6:** Level of damage according to Lagomarsino's assumption

Taking into account the fore reported values, it is possible to state that the macro-element of the structure shows a safety coefficient equal to 2.54 and for that reason, dangerous situation is avoided. Moreover, using the Lagomarsino's classification, the maximum level of damage expected in the structure is equal to D1 (moderate damages), under seismic action.

### Whole CSM calculation procedure applied on the S.Maria del Mar church for the mechanism 8

Santa Maria del Mar church is divided in fifteen different macro-elements and for each of these sub-structures, the C.S.M. has been applied.

Santa Maria del Mar church is located in the Catalonia region and using detailed study carried out on the Barcelona soil, it is possible to know its mechanical properties and to identify that soil based on the classification used in the EuroCode 8, and namely as typology B, the same considered for Santa Maria del Pi church.

	S	$\beta_0$	$K_1$	$K_2$	$T_B$	$T_C$	$T_D$	$a_g = a * g$
A	1	2.5	1	2	0.1	0.4	3	0.3924
B	1	2.5	1	2	0.15	0.6	3	0.3924
C	0.9	2.5	1	2	0.2	0.8	3	0.3924

**Table B-7:** Values introduced by the E.C.8 in order to draw the response spectrum graph

The procedure to obtain the ADSR graph is the same already performed in the previous example of calculation, and thus, only the representation of the graph will be reported:

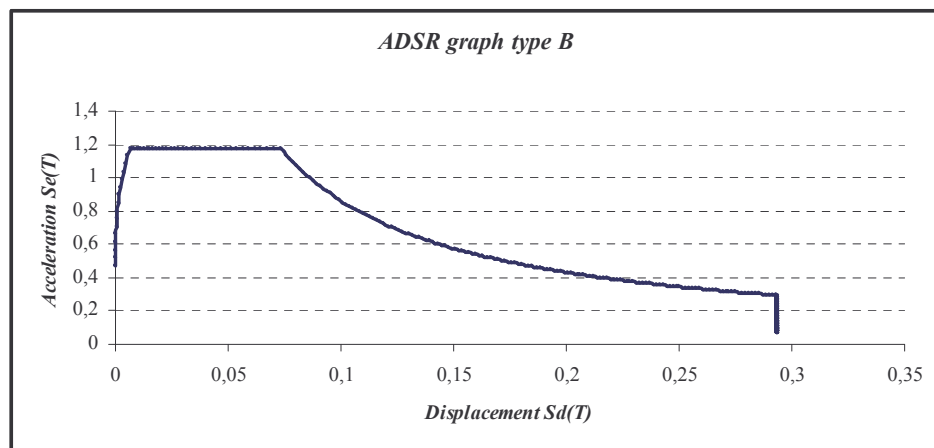


**Figure B-10:** ADSR for soil B

After evaluating the ADSR graph, it is necessary to compute the capacity curve related to the selected macro-element for a given mechanism. In the following all the

calculations of the transept (one of the possible selected macro-elements on the structure) subjected to in plane mechanism (mechanism 8) will be described.

The selected part is reported in the next picture and the mechanism that can occur for seismic action applied on transversal direction is shown.

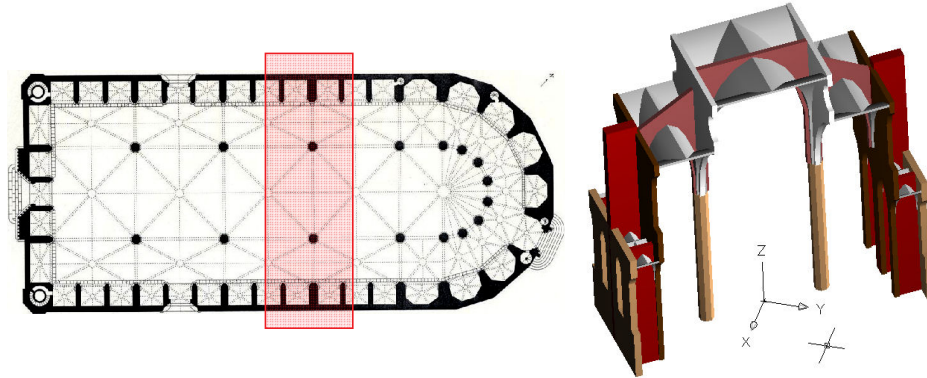


**Figure B-11:** In plane mechanism of transept

The limit analysis procedure can be applied when the geometrical properties of the structure are well-known because the main measures pass through the principal of virtual works application.

Thus, the following step is to describe the sub-structure in terms of its geometry, establishing the plastic hinges position when the mechanism is activated and to describe all the forces applied on the macro-element, due to the structural system or due to the mass of the structure. In the next **Figure B-12** the geometrical properties of the transept will be reported considering this element divided into different blocks, depending on the plastic hinges formation. These elements have been studied considering some papers in literature. In fact, in the chapter 3<sup>rd</sup>, three different plastic hinges locations have been taken into account (mechanism 8, mechanism 9 and mechanism 10). In this application only one of the total transept mechanisms will be introduced.



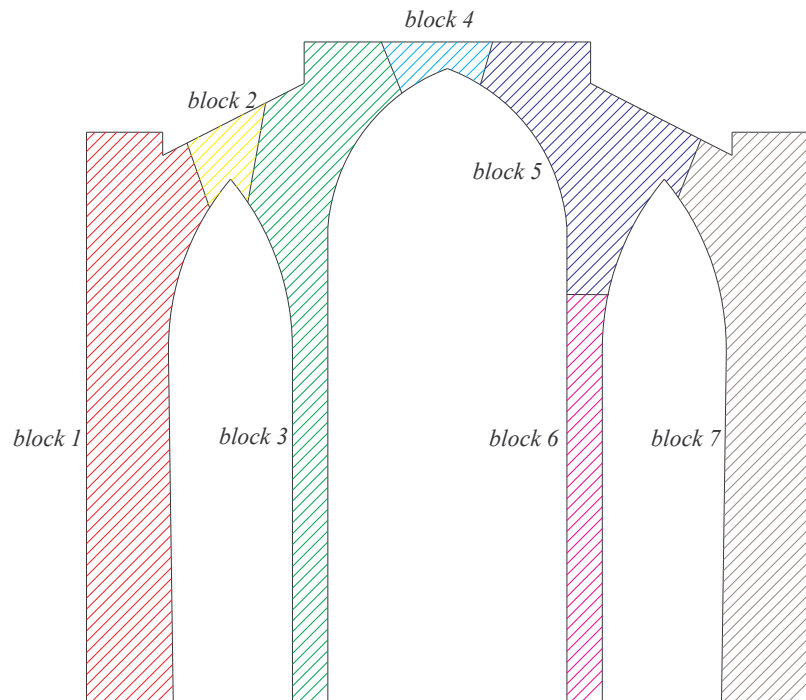


**Figure B-12:** Different parts of the same macro-element.

	<i>Area (m<sup>2</sup>)</i>	<i>thickness (m)</i>	<i>Volume m<sup>3</sup></i>
<i>block 1</i>	70.97	1.7	120.65
<i>block 2</i>	8.77	1.7	14.90
<i>block 3</i>	84.93	1.7	144.38
<i>block 4</i>	8.50942	1.7	14.47
<i>block 5</i>	60.46	1.7	102.78
<i>block 6</i>	36.03	1.7	61.26
<i>block 7</i>	121.229	1.7	206.09

	<i>Volume (m<sup>3</sup>)</i>	<i>density (t/m<sup>3</sup>)</i>	<i>Force (t)</i>
<i>block 1</i>	120.65	2.3	277.49
<i>block 2</i>	14.90	2.3	34.27
<i>block 3</i>	144.38	2.3	332.07
<i>block 4</i>	14.47	2.3	33.27
<i>block 5</i>	102.78	2.3	236.40
<i>block 6</i>	61.26	2.3	140.89
<i>block 7</i>	206.09	2.3	474.01

**Table B-8:** Geometrical properties of the selected macro-element.

Using the geometry above reported it is possible to apply the principal of virtual works, in order to know the multiplier  $\alpha_o$ . This coefficient represents the relation between the vertical and horizontal forces acting on the macro-element that activate the mechanism. In order to evaluate  $\alpha_o$ , it is possible to consider the following formulation:

$$M_{st} = M_{des}$$

$$F_{vA} \cdot l_{vA} + F_{vB} \cdot l_{vB} + F_{vC} \cdot l_{vC} + F_{oA} \cdot l_{oA} + F_{oB} \cdot l_{oB} + F_{oC} \cdot l_{oC} = 0$$

$$F_{vA} \cdot l_{vA} + F_{vB} \cdot l_{vB} + F_{vC} \cdot l_{vC} + \alpha \cdot F_{vA} \cdot l_{oA} + \alpha \cdot F_{vB} \cdot l_{oB} + \alpha \cdot F_{vC} \cdot l_{oC} = 0$$

The geometrical measures and the value of the forces involved in the formulation above mentioned are reported in the next table and lead to the following multiplier coefficient:

$$\alpha_o = 0.088$$

	<i>Force (t)</i>	<i>lvi (m)</i>	<i>loi (m)</i>
<i>A</i>	277.49	-0.9563	6.273
<i>B</i>	34.27	-1.28705	13.5632
<i>C</i>	332.07	-0.17785	13.2106
<i>D</i>	33.27	0.065523	17.5647
<i>E</i>	236.40	-1.29953	8.73011
<i>F</i>	140.89	-0.41966	4.82527
<i>G</i>	474.01	-0.70515	4.63027

**Table B-9:** Values used in order to find the multiplier coefficient.

Knowing only the  $\alpha_o$  value is not enough to have a global idea about the behaviour of the macro-element for a given mechanism. In fact, the multiplier coefficient gives an information about the first step of the motion, but on the other hand, understanding the total movement until the collapse of the sub-structure is also important. In the literature, it is possible to find the formulation that allows to know the reference point displacement value obtained when the multiplier  $\alpha_o$  is equal to zero.

In order to have a global information it is necessary to know another important geometrical parameter,  $\theta$ , by using the cinematic chains, as shown in the following

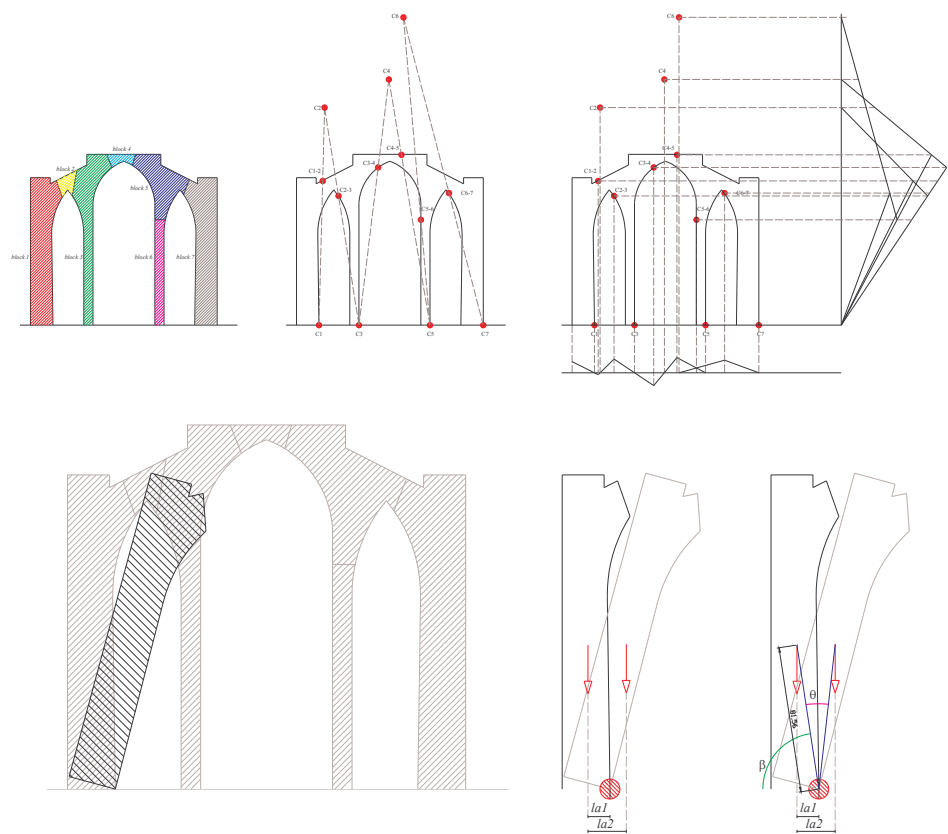
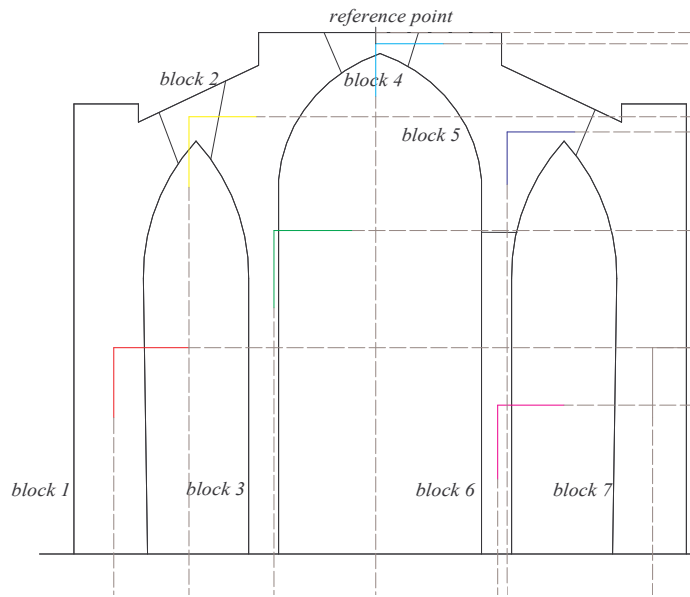


Figure B-14: Mechanism of the transept to compute  $\theta$ .

$A$	277.49	$ton$
$II$	1.81	$m$
$R$	12.72	$m$
$\beta$	1.41	$rad$
$\theta$	0.142511343	$rad$

→ 81 °  
→ 8.17 °

Using the cinematic chain, it is also possible to know the reference point displacement, chosen in the top of the transept as reported in the picture below:



Adopting the above procedure it is possible to know the reference point displacement when the multiplier coefficient is equal to zero. This condition describes the impossibility to find an equilibrium configuration between the destabilizing moment and stabilizing moment and thus the collapse can occur. In order to compare the structural capacity and the seismic demand, the capacity curve must be represented considering the acceleration on the vertical axis and the displacements on the horizontal axis, taking into account the SDOF system.

To do this, some values must be known using the formulations previously described.

1) Participation mass:

$$M^* = \frac{\left( \sum_{i=1}^{n+m} P \cdot \delta_{x,i} \right)^2}{\left( \sum_{i=1}^{n+m} P \cdot \delta_{x,i}^2 \right)}$$

2) Fraction of the participation mass in the mechanism:

$$e^* = \frac{g \cdot M^*}{\sum_{i=1}^{n+m} P_i}$$

3) Spectral acceleration of the activation of the mechanism:

$$a_o^* = \frac{\alpha_o \cdot \sum_{i=1}^{n+m} P_i}{M^*} = \frac{\alpha_o \cdot g}{e^*}$$

Even the spectral displacement of the reference point, related to the spectral acceleration equal to zero, can be obtained using the following relations:

$$d^* = d_{k,0} \cdot \frac{\sum_{i=1}^{n+m} P_i \cdot \delta_{x,i}}{\delta_{x,k} \cdot \sum_{i=1}^{n+m} P_i} \rightarrow d^* = \varphi \cdot d_k \rightarrow \varphi = \frac{\sum_{i=1}^{n+m} P_i \cdot \delta_{x,i}}{\delta_{x,k} \cdot \sum_{i=1}^{n+m} P_i}$$

At the end, the spectral capacity curve can be depicted as shown below:

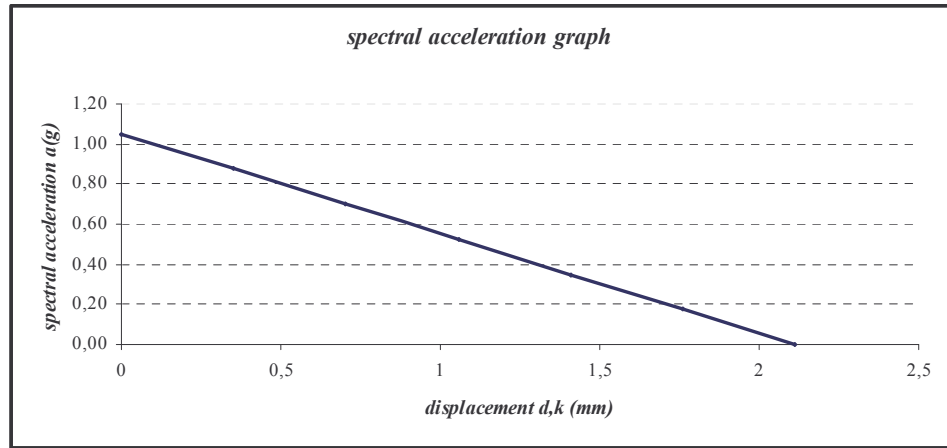


**Figure B-15:** Spectral capacity curve of the transept for a given mechanism.

The elastic branch of the capacity curve must be determined. It is necessary to know the displacement and the acceleration values in the limit elastic condition. The

displacement at the limit elastic condition can be evaluated by the following assumption:

$$d_s^* = 0.4 \cdot d_u^* \rightarrow d_u^* = 0.4 \cdot d_{k,o}^*$$

After knowing the displacement value it is possible to know the spectral acceleration value in the limit elastic condition ( $a_s^*$ ) using the inverse of the following formulation:

$$a^* = a_o^* \cdot \left( 1 - \frac{d_k^*}{d_{k,o}^*} \right)$$

The secant period of the elastic branch can be obtained using the following equation:

$$T_s^* = 2\pi \cdot \sqrt{\frac{d_s^*}{a_s^*}}$$

The values obtained can be recap in the table reported below:

$d_u^* (m)$	$d_s^* (m)$	$a_s^* (m/sec^2)$	$T_s^* (sec)$
0.846	0.338	0.883	3.886

**Table B-10:** Values used in order to obtain the elastic branch of the capacity curve.

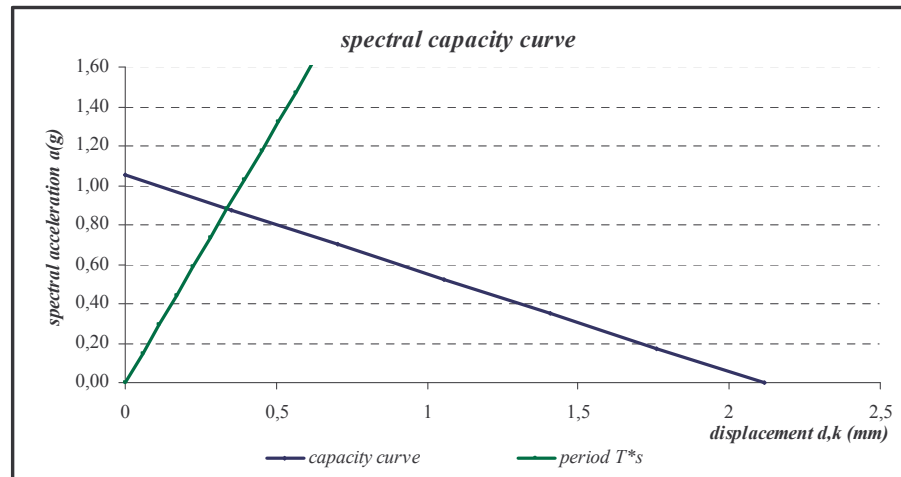


**Figure B-16:** Spectral capacity curve of the transept for a given mechanism with elastic branch.

The last step consists on putting in the same graph the demand curve and the spectral capacity curve, as shown in the following picture.

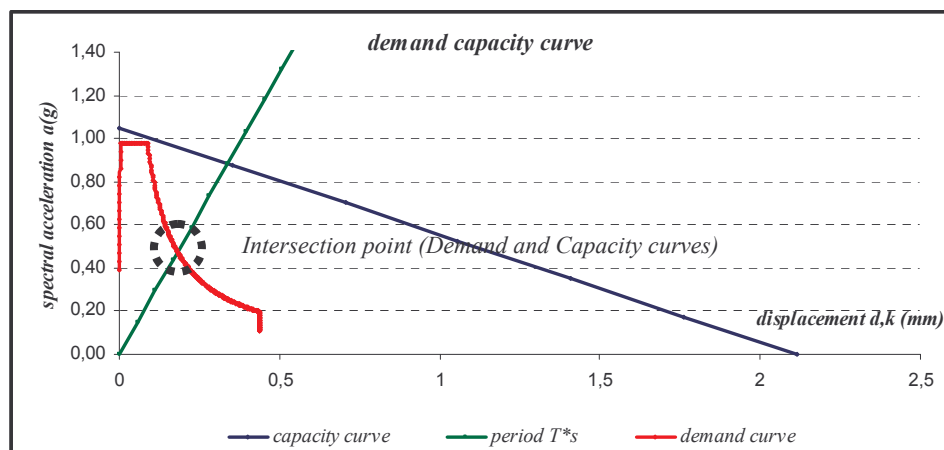


**Figure B-17:** Comparison between the capacity curve and demand curve.

The intersection point occur in the elastic branch of the spectral capacity curve. Actually, the computation of the hysteretic energy dissipation could be avoid, but the latter hypothesis has been introduced in every calculations to take into account the real

structural behaviour. The evaluation of the demand displacement  $d_d^*$  has been conducted using the formulation introduced in the paragraph 3.5 of the present work. For that reason the comparison between the ultimate capacity displacement and demand displacement can be evaluated without doing more complex calculations. The demand displacement is equal to the horizontal coordinate of the intersection point. In the following table the demand displacement, the ultimate displacement and the safety factor are reported. The safety factor has been obtained by means of the ratio between the displacement fore mentioned; safety factor more than unit value allows the technician to state the safety of the structures under seismic load condition, while safety factor less than the unit value establishes a dangerous situation for the building.

$d_d^*(m)$	$d_u^*(m)$	<i>safety coefficient</i>	
0.202	0.846	$S.c. = \frac{d_u^*}{d_d^*}$	4.19

**Table B-11:** displacements values and safety coefficient

The level of the damages that can occur on the macro-element considering seismic actions on the structure can be evaluated according to Lagomarsino's assumptions (described in the chapter 3) as in the following shown:

			<i>label</i>	<i>Analyses results</i>	
$S_d =$	0.20	$m$	<b>D0</b>	TRUE	<i>no damage</i>
$0.7 S_{dy} =$	0.24	$m$	<b>D1</b>	FALSE	
$S_{dy} =$	0.34	$m$	<b>D2</b>	FALSE	
$0.25 S_{du} =$	0.53	$m$	<b>D3</b>	FALSE	
$0.5 S_{du} =$	1.06	$m$	<b>D4</b>	FALSE	
$S_{du} =$	2.11	$m$			

**Table B-12:** Level of damage in according to Lagomarsino's hypothesis

Taking into account the fore reported values, it is possible to state that the macro-element of the structure shows a safety coefficient equal to 4.19 and for that reason, dangerous situation is avoided. Moreover, using the Lagomarsino's classification, the maximum level of damage in the structure is equal to D0 (no damages), under seismic action.



### Whole CSM calculation procedure applied on the Santa Maria del Pi church for the mechanism 3 MODE

Using the same parameters listed in the mechanism 5 calculation described before, the elastic response spectrum can be depicted and is reported in the next (**Figure B-1**).

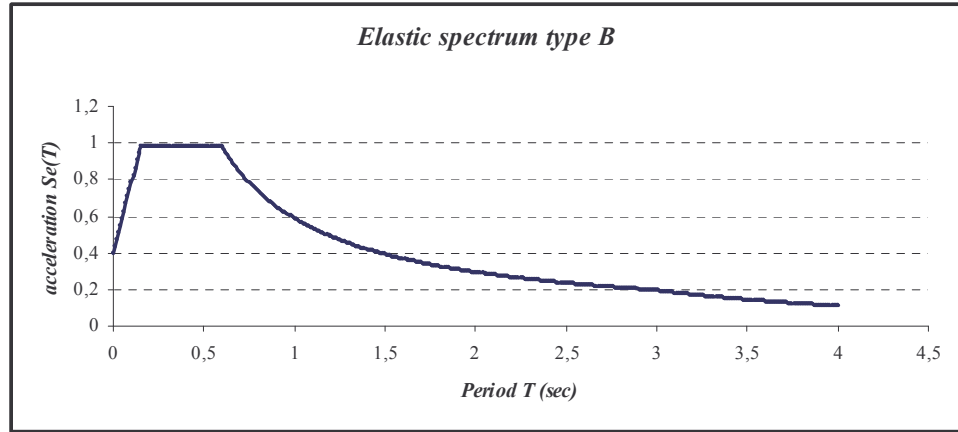


**Figure B-1:** Elastic response spectrum for soil B

It is required to relate the spectral acceleration to the spectral displacement using the following formulation in order to obtain the Acceleration Displacement Response Spectrum (ADRS), depicted in the **Figure B-2**.

$$S_d = \frac{T^2}{4 \cdot \pi^2} \cdot S_a$$

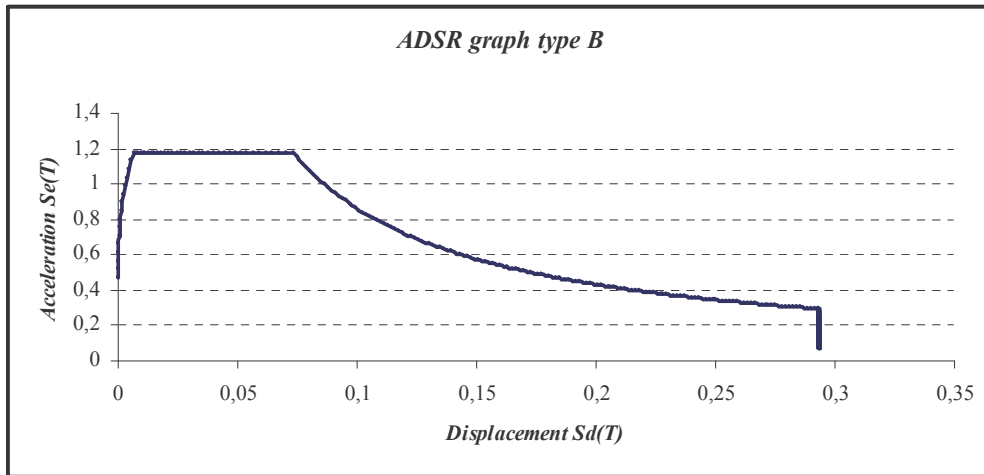


**Figure B-2:** ADSR for soil B

After evaluating the ADSR graph, it is necessary to compute the capacity curve related to the selected macro-element for a given mechanism. In the following, as an example, all the calculations of the principal façade (one of the possible selected macro-elements on the structure) subjected to out of plane mechanism (mechanism 5) will be described. The selected part is reported in the next picture and the mechanism that can occur for seismic action applied on longitudinal direction is shown.

The mechanism 3 mode is the same of the mechanism 3, but taking into account the whole principal façade that may influence the structural behaviour of the upper part. For that reason, two formulation introduced by the Spanish design rule have been used and have been reported in the follow:

$$\Phi_{ik} = \text{sen}[(2i - 1) \pi \cdot h_k / 2H]$$

$$\eta_{ik} = \Phi_{ik} \frac{\sum_{k=1}^n m_k \Phi_{ik}}{\sum_{k=1}^n m_k \Phi_{ik}^2}$$

For that reason the principal façade has been divided in different blocks as shown in the following picture reported below:

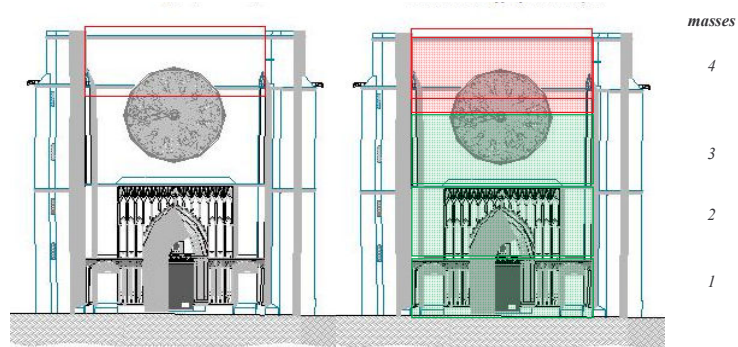


**Figure B-10:** Division into different masses

The obtained parameters are reported in the following table.

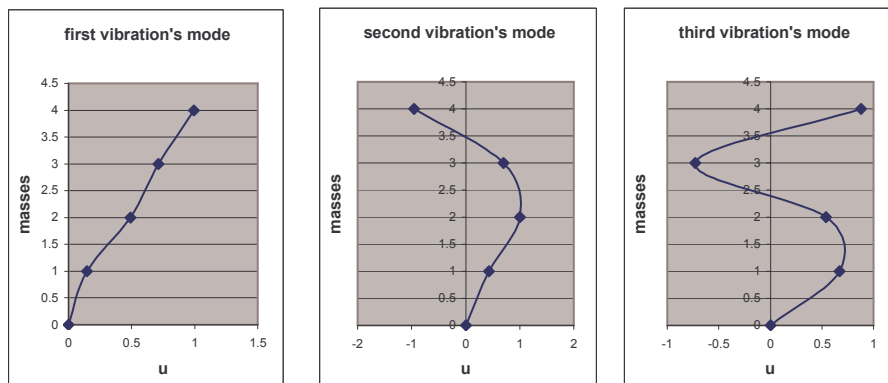
The masses were computed equal to:

element	h (m)	d (m)	thick. (m)	Volume (m <sup>3</sup> )
1	5,45	16,45	0,75	147,79
2	8,2	16,45	0,75	222,37
3	7,15	16,45	0,75	138,49
4	8,35	16,45	0,75	161,74

element	dens (t/m <sup>3</sup> )	Weight (t)	Mass (t/g)	position (m)
1	2,3	339,92	34,65	2,725
2	2,3	511,44	52,13	9,55
3	2,3	318,54	32,47	14,7
4	2,3	372,00	37,92	27,3

$$\Phi_{ik} = \text{sen}[(2i - 1) \pi \cdot h_k / 2H]$$

element	mode	mode	mode
	1	2	3
1	0,146	0,426	0,670
2	0,492	1,000	0,539
3	0,712	0,694	-0,729
4	0,995	-0,955	0,877



using the Formulation reported above, is possible to obtain the  $\eta$  coefficient that can be used in order to have a new seismic coefficient (*Evaluation of reduction parameter*).

element	coefficient $\eta$		
	mode 1	mode 2	mode 3
1	0.199	0.209	0.529
2	0.669	0.490	0.426
3	0.967	0.340	-0.576
4	1.353	-0.468	0.692

$$\eta_{tot,4} = \sqrt{\sum_{i=1}^3 \eta_{i,4}^2} = 1.59$$

$$\alpha_{\eta} = \alpha_o / \eta_{i,4}$$

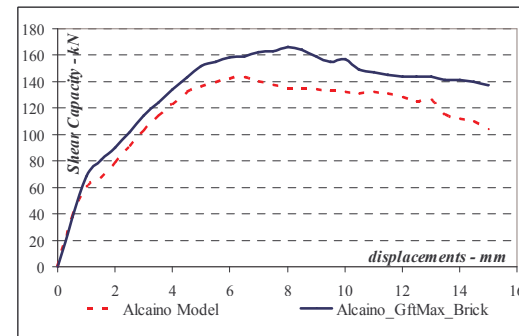
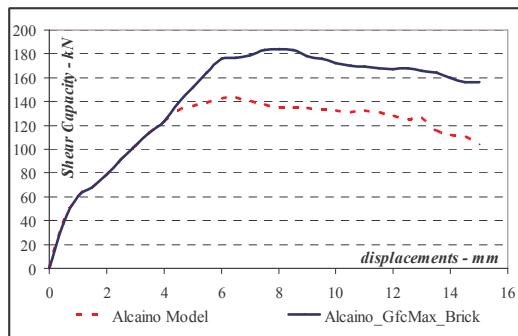
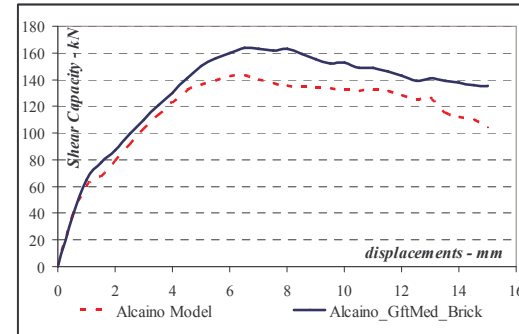
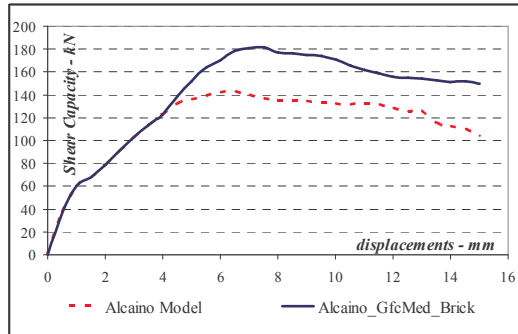
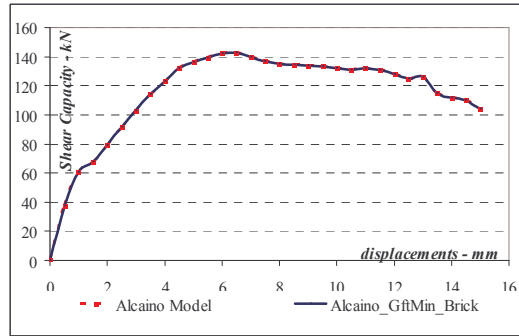
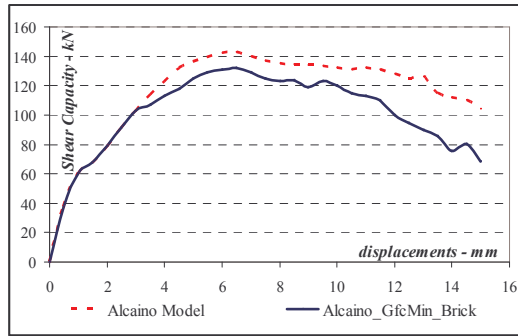
The obtained seismic coefficient  $\alpha_{\eta}$  is equal to 0.0838.

The procedure is the same of those reported in the previous example; only the capacity curve of the selected macro-element change, while the rest of the calculation should be considered equal.

**ANNEX C****ALCAINO et al masonry panels:****Results obtaining by changing both brick fracture energies**

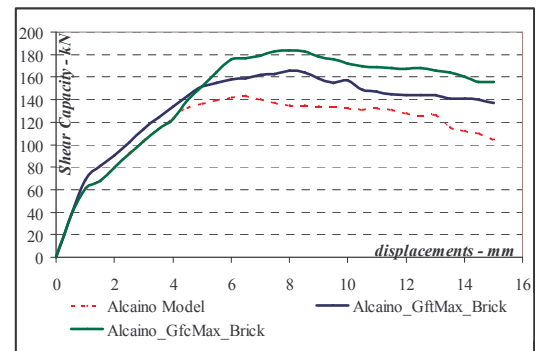
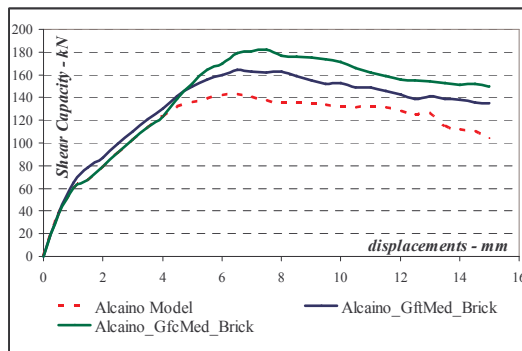
<i>Model</i>	<i>Fracture Energy Value and formulation (N/mm)</i>	<i>Displacement mm</i>	<i>Shear Capacity kN</i>	<i>Δ Shear Capacity %</i>
Alcaino_Real	<i>model definition</i>	4	123	----
		6	142	----
		8	135	----
		10	132	----
Alcaino_GfcMin_B	$G_{fc,Brick} = \frac{f_c^2}{2E} = G_{fc,min}$	4	113	-8,1
		6	131	-7,7
		8	123	-8,9
		10	120	-9,1
Alcaino_GfcMed_B	$G_{fc,Brick} = \frac{f_c^2}{E} = G_{fc,med}$	4	123	0,0
		6	170	19,7
		8	177	31,1
		10	171	29,5
Alcaino_GfcMax_B	$G_{fc,Brick} = \frac{3f_c^2}{2E} = G_{fc,max}$	4	123	0,0
		6	176	23,9
		8	184	36,3
		10	172	30,3

<i>Model</i>	<i>Fracture Energy Value and formulation (N/mm)</i>	<i>Displacement mm</i>	<i>Shear Capacity kN</i>	<i>Δ Shear Capacity %</i>
Alcaino_Real	<i>model definition</i>	4	123	----
		6	142	----
		8	135	----
		10	132	----
Alcaino_GftMin_B	$G_{ft,Brick} = \frac{f_t^2}{2E} = G_{ft,min}$	4	123	0,0
		6	142	0,0
		8	135	0,0
		10	132	0,0
Alcaino_GftMed_B	$G_{ft,Brick} = \frac{f_t^2}{E} = G_{ft,med}$	4	130	5,7
		6	160	12,7
		8	163	20,7
		10	153	15,9
Alcaino_GftMax_B	$G_{ft,Brick} = \frac{3f_t^2}{2E} = G_{ft,max}$	4	134	8,9
		6	158	11,3
		8	166	23,0
		10	157	18,9



Model	Fracture Energy Value and formulation (N/mm)	Displacement mm	Shear Capacity kN	$\Delta$ Shear Capacity %
Alcaino_GfcMed_B	$G_{fc,Brick} = \frac{f_c^2}{E} = G_{fc,med}$	4	123	0,0
		6	170	19,7
		8	177	31,1
		10	171	29,5
Alcaino_GftMed_B	$G_{ft,Brick} = \frac{f_t^2}{E} = G_{ft,med}$	4	130	5,7
		6	160	12,7
		8	163	20,7
		10	153	15,9

Model	Fracture Energy Value and formulation (N/mm)	Displacement mm	Shear Capacity kN	$\Delta$ Shear Capacity %
Alcaino_GfcMax_B	$G_{fc,Brick} = \frac{3f_c^2}{2E} = G_{fc,max}$	4	123	0,0
		6	176	23,9
		8	184	36,3
		10	172	30,3
Alcaino_GftMax_B	$G_{ft,Brick} = \frac{3f_t^2}{2E} = G_{ft,max}$	4	134	8,9
		6	158	11,3
		8	166	23,0
		10	157	18,9

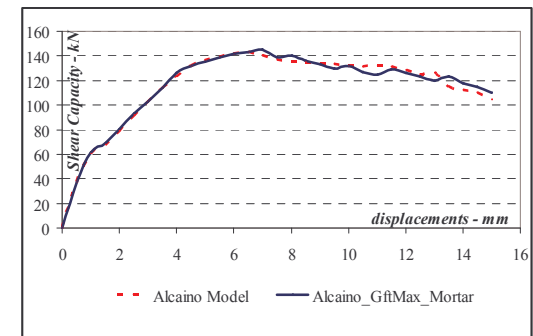
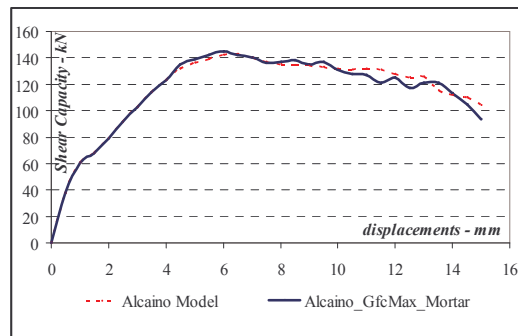
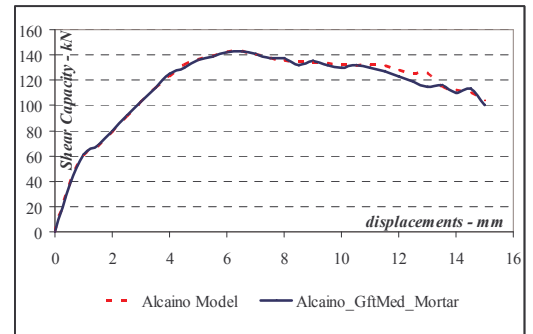
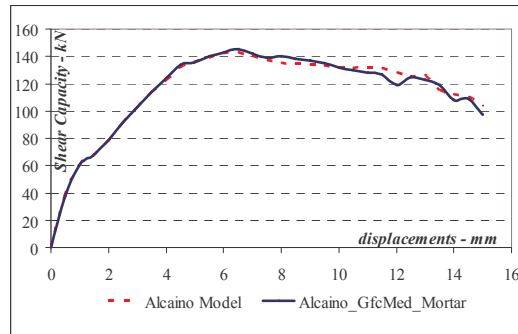
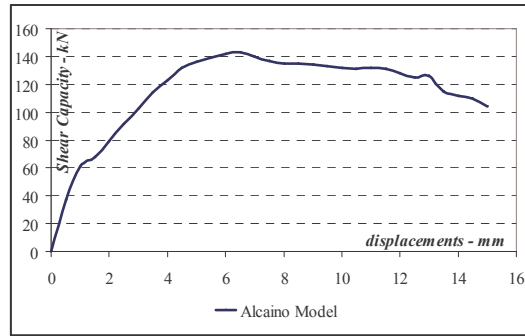


**Results obtaining by changing both mortar fracture energies**

<i>Model</i>	<i>Fracture Energy Value and formulation (N/mm)</i>	<i>Displacmen mm</i>	<i>Shear Capa kN</i>	<i>Δ Shear Capacity %</i>
Alcaino_Real	<i>model definition</i>	4	123	----
		6	142	----
		8	135	----
		10	132	----
Alcaino_GfcMin_M	$G_{fc,Mort} = \frac{f_c^2}{2E} = G_{fc,min}$	4	123	0,0
		6	142	0,0
		8	135	0,0
		10	132	0,0
Alcaino_GfcMed_M	$G_{fc,mort} = \frac{f_c^2}{E} = G_{fc,med}$	4	124	0,8
		6	143	0,7
		8	140	3,7
		10	132	0,0
Alcaino_GfcMax_M	$G_{fc,Mort} = \frac{3f_c^2}{2E} = G_{fc,max}$	4	123	0,0
		6	145	2,1
		8	137	1,5
		10	131	-0,8

<i>Model</i>	<i>Fracture Energy Value and formulation (N/mm)</i>	<i>Displacmen mm</i>	<i>Shear Capa kN</i>	<i>Δ Shear Capacity %</i>
Alcaino_Real	<i>model definition</i>	4	123	----
		6	142	----
		8	135	----
		10	132	----
Alcaino_GftMin_M	$G_{ft,Mort} = \frac{f_t^2}{2E} = G_{ft,min}$	4	123	0,0
		6	142	0,0
		8	135	0,0
		10	132	0,0
Alcaino_GftMed_M	$G_{ft,Mort} = \frac{f_t^2}{E} = G_{ft,med}$	4	125	1,6
		6	142	0,0
		8	140	3,7
		10	130	-1,5
Alcaino_GftMax_M	$G_{ft,Mort} = \frac{3f_t^2}{2E} = G_{ft,max}$	4	126	2,4
		6	142	0,0
		8	140	3,7
		10	132	0,0

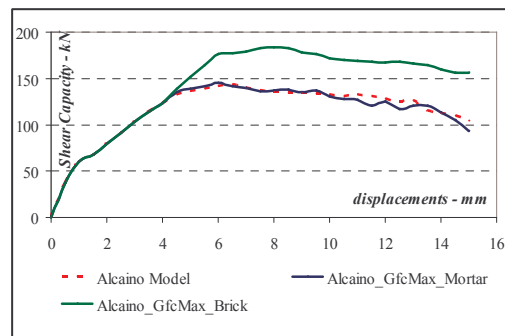
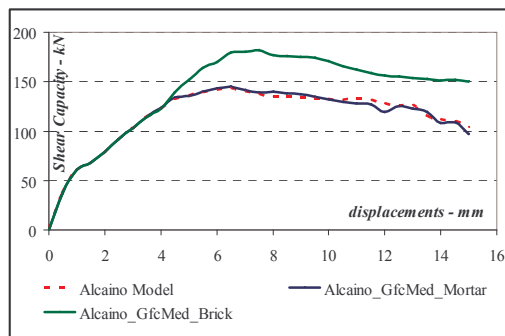




**Comparison between compressive fracture energy of both materials**

Model	Fracture Energy Value and formulation (N/mm)	Displacement mm	Shear Capacity kN	$\Delta$ Shear Capacity %
Alcaino_GfcMed_B	$G_{fc,Brick} = \frac{f_c^2}{E} = G_{fc,med}$	4	123	0,0
		6	170	19,7
		8	177	31,1
		10	171	29,5
Alcaino_GfcMed_M	$G_{fc,mort} = \frac{f_c^2}{E} = G_{fc,med}$	4	124	0,8
		6	143	0,7
		8	140	3,7
		10	132	0,0

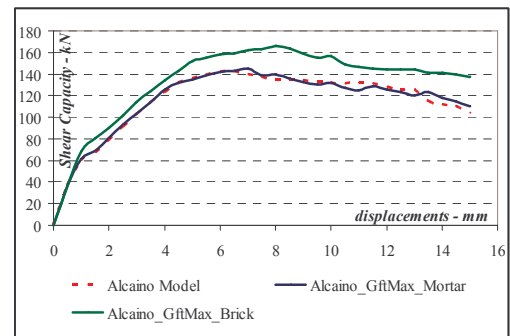
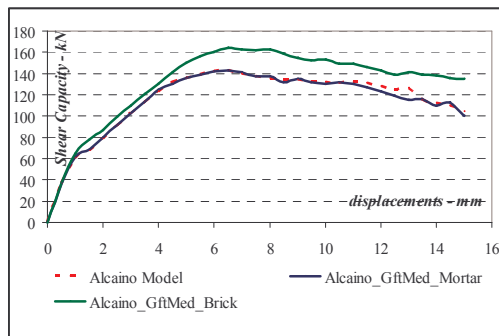
Model	Fracture Energy Value and formulation (N/mm)	Displacement mm	Shear Capacity kN	$\Delta$ Shear Capacity %
Alcaino_GfcMax_B	$G_{fc,Brick} = \frac{3f_c^2}{2E} = G_{fc,max}$	4	123	0,0
		6	176	23,9
		8	184	36,3
		10	172	30,3
Alcaino_GfcMax_M	$G_{fc,Mort} = \frac{3f_c^2}{2E} = G_{fc,max}$	4	123	0,0
		6	145	2,1
		8	137	1,5
		10	131	-0,8



**Comparison between tensile fracture energy of both materials**

Model	Fracture Energy Value and formulation (N/mm)	Displacement mm	Shear Capacity kN	$\Delta$ Shear Capacity %
Alcaino_GftMed_B	$G_{ft,Brick} = \frac{f_t^2}{E} = G_{ft,med}$	4	130	5,7
		6	160	12,7
		8	163	20,7
		10	153	15,9
Alcaino_GftMed_M	$G_{ft,Mort} = \frac{f_t^2}{E} = G_{ft,med}$	4	125	1,6
		6	142	0,0
		8	140	3,7
		10	130	-1,5

Model	Fracture Energy Value and formulation (N/mm)	Displacement mm	Shear Capacity kN	$\Delta$ Shear Capacity %
Alcaino_GftMax_B	$G_{ft,Brick} = \frac{3f_t^2}{2E} = G_{ft,max}$	4	134	8,9
		6	158	11,3
		8	166	23,0
		10	157	18,9
Alcaino_GftMax_M	$G_{ft,Mort} = \frac{3f_t^2}{2E} = G_{ft,max}$	4	126	2,4
		6	142	0,0
		8	140	3,7
		10	132	0,0



**PASCALE et al masonry panels:****Results obtaining by changing both brick fracture energies**

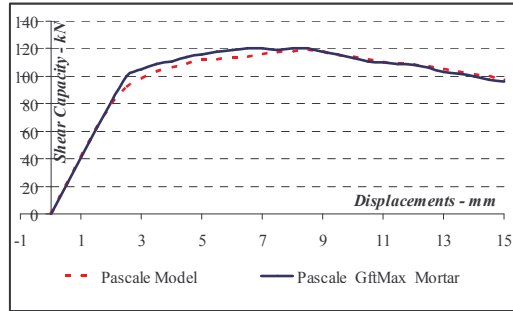
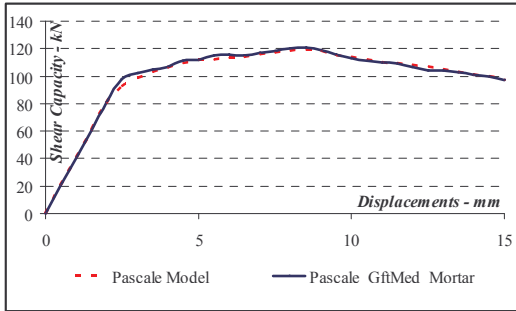
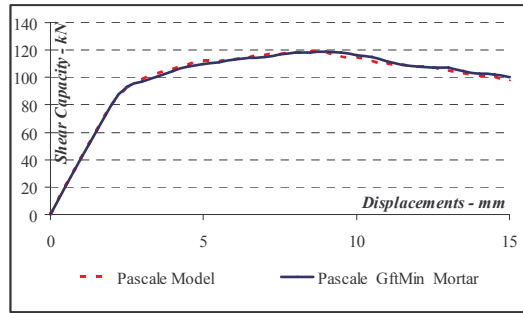
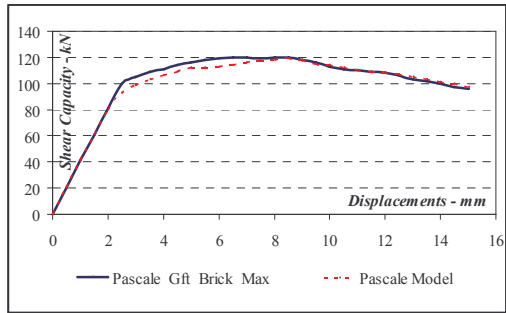
<i>Model</i>	<i>Fracture Energy Value and formulation (N/mm)</i>	<i>Displacement mm</i>	<i>Shear Capacity kN</i>	<i>Δ Shear Capacity %</i>
<b>Pascale_Real</b>	<i>model definition</i>	4	106	----
		6	113	----
		8	118	----
		10	114	----
<b>Pascale_GfcMin_B</b>	$G_{fc,Brick} = \frac{f_c^2}{2E} = G_{fc,min}$	4	106	0,0
		6	113	0,0
		8	118	0,0
		10	114	0,0
<b>Pascale_GfcMed_B</b>	$G_{fc,Brick} = \frac{f_c^2}{E} = G_{fc,med}$	4	106	0,0
		6	113	0,0
		8	118	0,0
		10	114	0,0
<b>Pascale_GfcMax_B</b>	$G_{fc,Brick} = \frac{3f_c^2}{2E} = G_{fc,max}$	4	106	0,0
		6	113	0,0
		8	118	0,0
		10	114	0,0

<i>Model</i>	<i>Fracture Energy Value and formulation (N/mm)</i>	<i>Displacement mm</i>	<i>Shear Capacity kN</i>	<i>Δ Shear Capacity %</i>
<b>Pascale_Real</b>	<i>model definition</i>	4	106	----
		6	113	----
		8	118	----
		10	114	----
<b>Pascale_GftMin_B</b>	$G_{ft,Brick} = \frac{f_t^2}{2E} = G_{ft,min}$	4	106	0,0
		6	113	0,0
		8	118	0,0
		10	114	0,0
<b>Pascale_GftMed_B</b>	$G_{ft,Brick} = \frac{f_t^2}{E} = G_{ft,med}$	4	106	0,0
		6	113	0,0
		8	118	0,0
		10	114	0,0
<b>Pascale_GftMax_B</b>	$G_{ft,Brick} = \frac{3f_t^2}{2E} = G_{ft,max}$	4	106	0,0
		6	113	0,0
		8	118	0,0
		10	114	0,0

**Results obtaining by changing both mortar fracture energies**

<i>Model</i>	<i>Fracture Energy Value and formulation (N/mm)</i>	<i>Displacement mm</i>	<i>Shear Capacity kN</i>	<i>Δ Shear Capacity %</i>
<b>Pascale_Real</b>	<i>model definition</i>	4	106	----
		6	113	----
		8	118	----
		10	114	----
<b>Pascale_GfcMin_M</b>	$G_{fc,Mort} = \frac{f_c^2}{2E} = G_{fc,min}$	4	106	0,0
		6	113	0,0
		8	118	0,0
		10	114	0,0
<b>Pascale_GfcMed_M</b>	$G_{fc,mort} = \frac{f_c^2}{E} = G_{fc,med}$	4	106	0,0
		6	113	0,0
		8	118	0,0
		10	114	0,0
<b>Pascale_GfcMax_M</b>	$G_{fc,Mort} = \frac{3f_c^2}{2E} = G_{fc,max}$	4	106	0,0
		6	113	0,0
		8	118	0,0
		10	114	0,0

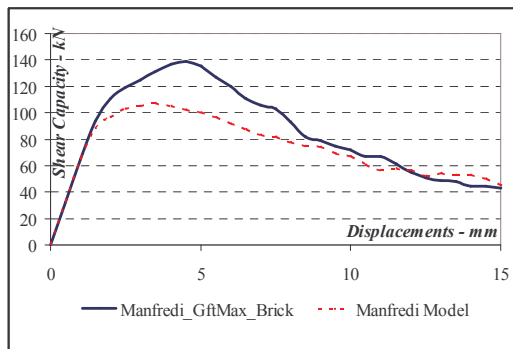
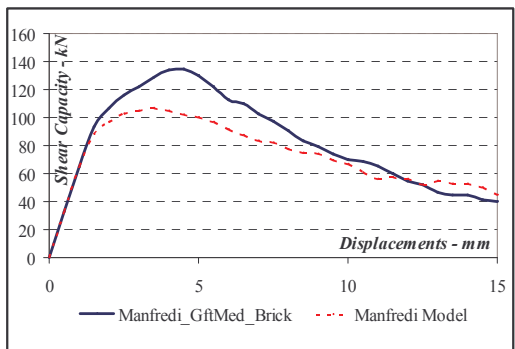
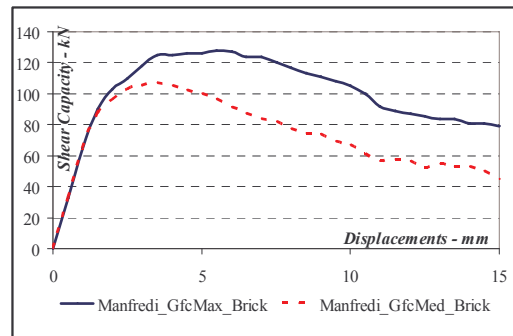
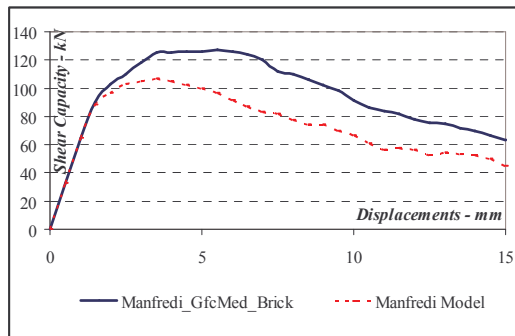
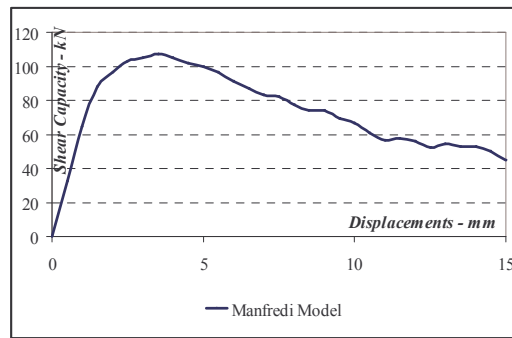
<i>Model</i>	<i>Fracture Energy Value and formulation (N/mm)</i>	<i>Displacement mm</i>	<i>Shear Capacity kN</i>	<i>Δ Shear Capacity %</i>
<b>Pascale_Real</b>	<i>model definition</i>	4	106	----
		6	113	----
		8	118	----
		10	114	----
<b>Pascale_GftMin_M</b>	$G_{ft,Mort} = \frac{f_t^2}{2E} = G_{ft,min}$	4	105	-0,9
		6	113	0,0
		8	118	0,0
		10	116	1,8
<b>Pascale_GftMed_M</b>	$G_{ft,Mort} = \frac{f_t^2}{E} = G_{ft,med}$	4	107	0,9
		6	116	2,7
		8	120	1,7
		10	113	-0,9
<b>Pascale_GftMax_M</b>	$G_{ft,Mort} = \frac{3f_t^2}{2E} = G_{ft,max}$	4	111	4,7
		6	119	5,3
		8	120	1,7
		10	113	-0,9



**MANFREDI et al masonry panels:****Results obtaining by changing both brick fracture energies**

<i>Model</i>	<i>Fracture Energy Value and formulation (N/mm)</i>	<i>Displacement mm</i>	<i>Shear Capacity kN</i>	<i>Δ Shear Capacity %</i>
<b>Manfredi_Real</b>	<i>model definition</i>	4	105	----
		6	91,4	----
		8	77,2	----
		10	66,8	----
<b>Manfredi_GfcMin_B</b>	$G_{fc,Brick} = \frac{f_c^2}{2E} = G_{fc,min}$	4	105	0,0
		6	91,4	0,0
		8	77,2	0,0
		10	66,8	0,0
<b>Manfredi_GfcMed_B</b>	$G_{fc,Brick} = \frac{f_c^2}{E} = G_{fc,med}$	4	125	19,0
		6	126	37,9
		8	110	42,5
		10	91,5	37,0
<b>Manfredi_GfcMax_B</b>	$G_{fc,Brick} = \frac{3f_c^2}{2E} = G_{fc,max}$	4	125	19,0
		6	127	38,9
		8	117	51,6
		10	105	57,2

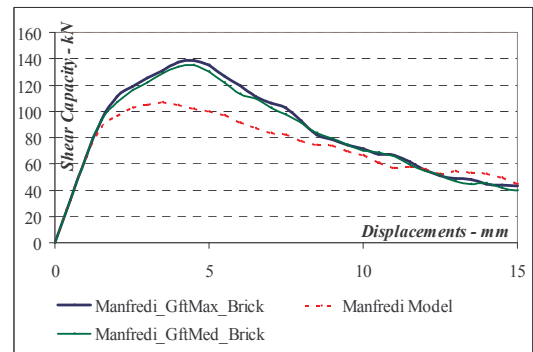
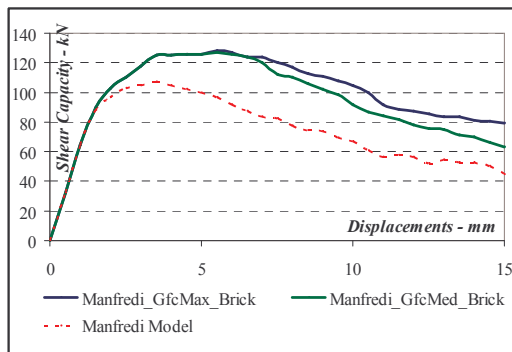
<i>Model</i>	<i>Fracture Energy Value and formulation (N/mm)</i>	<i>Displacement mm</i>	<i>Shear Capacity kN</i>	<i>Δ Shear Capacity %</i>
<b>Manfredi_Real</b>	<i>model definition</i>	4	105	----
		6	91,4	----
		8	77,2	----
		10	66,8	----
<b>Manfredi_GftMin_B</b>	$G_{ft,Brick} = \frac{f_t^2}{2E} = G_{ft,min}$	4	105	0,0
		6	91,4	0,0
		8	77,2	0,0
		10	66,8	0,0
<b>Manfredi_GftMed_B</b>	$G_{ft,Brick} = \frac{f_t^2}{E} = G_{ft,med}$	4	134	27,6
		6	113	23,6
		8	91	17,9
		10	69,8	4,5
<b>Manfredi_GftMax_B</b>	$G_{ft,Brick} = \frac{3f_t^2}{2E} = G_{ft,max}$	4	137	30,5
		6	120	31,3
		8	92,8	20,2
		10	71,6	7,2





Model	Fracture Energy Value and formulation (N/mm)	Displacmen mm	Shear Capacity kN	$\Delta$ Shear Capacity %
Manfredi_GfcMed_B	$G_{fc,Brick} = \frac{f_c^2}{E} = G_{fc,med}$	4	125	19,0
		6	126	37,9
		8	110	42,5
		10	91,5	37,0
Manfredi_GfcMax_B	$G_{fc,Brick} = \frac{3f_c^2}{2E} = G_{fc,max}$	4	125	19,0
		6	127	38,9
		8	117	51,6
		10	105	57,2

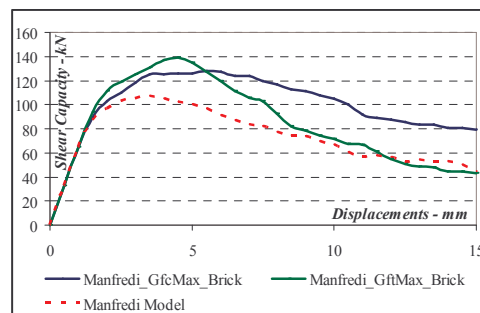
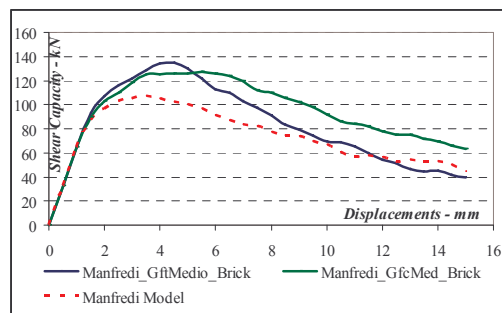
Model	Fracture Energy Value and formulation (N/mm)	Displacmen mm	Shear Capacity kN	$\Delta$ Shear Capacity %
Manfredi_GftMed_B	$G_{ft,Brick} = \frac{f_t^2}{E} = G_{ft,med}$	4	134	27,6
		6	113	23,6
		8	91	17,9
		10	69,8	4,5
Manfredi_GftMax_B	$G_{ft,Brick} = \frac{3f_t^2}{2E} = G_{ft,max}$	4	137	30,5
		6	120	31,3
		8	92,8	20,2
		10	71,6	7,2



**Results obtaining by changing brick compressive and tensile fracture energies**

Model	Fracture Energy Value and formulation (N/mm)	Displacement mm	Shear Capacity kN	$\Delta$ Shear Capacity %
Manfredi_GfcMed_B	$G_{fc,Brick} = \frac{f_c^2}{E} = G_{fc,med}$	4	125	19,0
		6	126	37,9
		8	110	42,5
		10	91,5	37,0
Manfredi_GftMed_B	$G_{ft,Brick} = \frac{f_t^2}{E} = G_{ft,med}$	4	134	27,6
		6	113	23,6
		8	91	17,9
		10	69,8	4,5

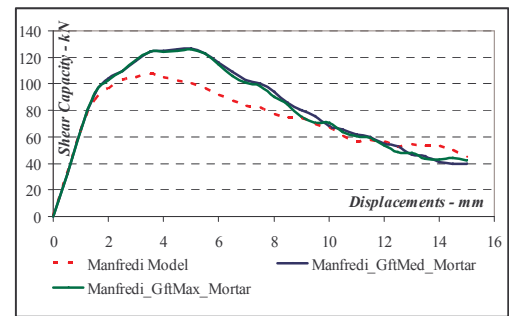
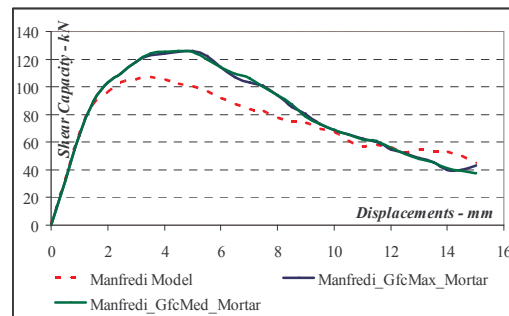
Model	Fracture Energy Value and formulation (N/mm)	Displacement mm	Shear Capacity kN	$\Delta$ Shear Capacity %
Manfredi_GfcMax_B	$G_{fc,Brick} = \frac{3 f_c^2}{2 E} = G_{fc,max}$	4	125	19,0
		6	127	38,9
		8	117	51,6
		10	105	57,2
Manfredi_GftMax_B	$G_{ft,Brick} = \frac{3 f_t^2}{2 E} = G_{ft,max}$	4	137	30,5
		6	120	31,3
		8	92,8	20,2
		10	71,6	7,2



**Results obtaining by changing mortar compressive and tensile fracture energies**

Model	Fracture Energy Value and formulation (N/mm)	Displacmen mm	Shear Capacity kN	Δ Shear Capacity %
Manfredi_GfcMed_M	$G_{fc,mort} = \frac{f_c^2}{E} = G_{fc,med}$	4	125	19,0
		6	114	24,7
		8	93,7	21,4
		10	68,5	2,5
Manfredi_GfcMax_M	$G_{fc,Mort} = \frac{3f_c^2}{2E} = G_{fc,max}$	4	124	18,1
		6	114	24,7
		8	93,7	21,4
		10	68,6	2,7

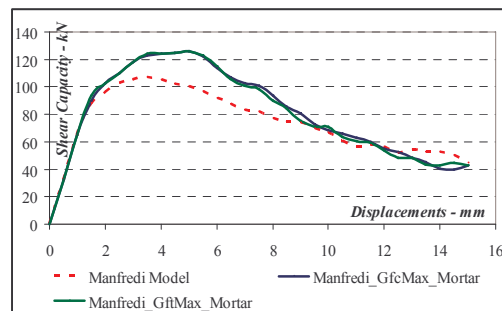
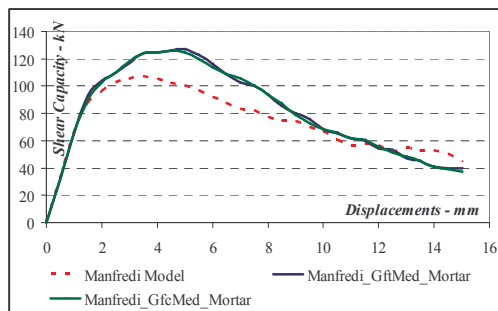
Model	Fracture Energy Value and formulation (N/mm)	Displacmen mm	Shear Capacity kN	Δ Shear Capacity %
Manfredi_GftMed_M	$G_{ft,Mort} = \frac{f_t^2}{E} = G_{ft,med}$	4	125	19,0
		6	116	26,9
		8	93,8	21,5
		10	68,2	2,1
Manfredi_GftMax_M	$G_{ft,Mort} = \frac{3f_t^2}{2E} = G_{ft,max}$	4	124	18,1
		6	115	25,8
		8	90,1	16,7
		10	70,7	5,8



**Results obtaining by changing mortar compressive and tensile fracture energies**

Model	Fracture Energy Value and formulation (N/mm)	Displacement mm	Shear Capacity kN	$\Delta$ Shear Capacity %
Manfredi_GfcMed_M	$G_{fc,mort} = \frac{f_c^2}{E} = G_{fc,med}$	4	125	19,0
		6	114	24,7
		8	93,7	21,4
		10	68,5	2,5
Manfredi_GftMed_M	$G_{ft,Mort} = \frac{f_t^2}{E} = G_{ft,med}$	4	125	19,0
		6	116	26,9
		8	93,8	21,5
		10	68,2	2,1

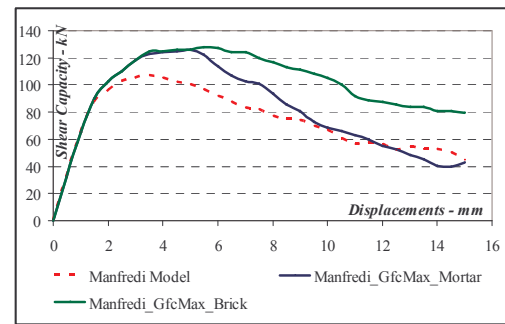
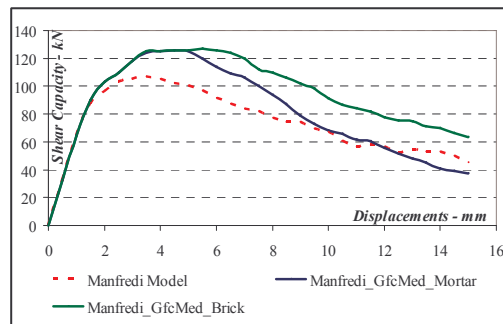
Model	Fracture Energy Value and formulation (N/mm)	Displacement mm	Shear Capacity kN	$\Delta$ Shear Capacity %
Manfredi_GfcMax_M	$G_{fc,Mort} = \frac{3f_c^2}{2E} = G_{fc,max}$	4	124	18,1
		6	114	24,7
		8	93,7	21,4
		10	68,6	2,7
Manfredi_GftMax_M	$G_{ft,Mort} = \frac{3f_t^2}{2E} = G_{ft,max}$	4	124	18,1
		6	115	25,8
		8	90,1	16,7
		10	70,7	5,8



**Results obtaining by comparing mortar and brick compressive and tensile fracture energies**

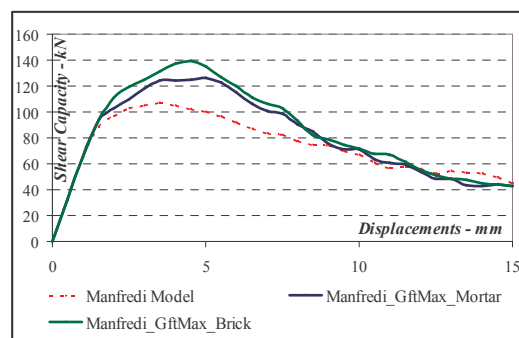
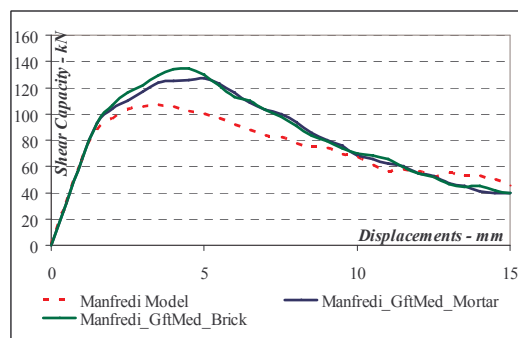
Model	Fracture Energy Value and formulation (N/mm)	Displacement mm	Shear Capacity kN	$\Delta$ Shear Capacity %
Manfredi_GfcMed_M	$G_{fc,mort} = \frac{f_c^2}{E} = G_{fc,med}$	4	125	19,0
		6	114	26,9
		8	93,7	21,5
		10	68,5	2,1
Manfredi_GfcMed_B	$G_{fc,Brick} = \frac{f_c^2}{E} = G_{fc,med}$	4	125	19,0
		6	126	37,9
		8	110	42,5
		10	91,5	37,0

Model	Fracture Energy Value and formulation (N/mm)	Displacement mm	Shear Capacity kN	$\Delta$ Shear Capacity %
Manfredi_GfcMax_M	$G_{fc,Mort} = \frac{3f_c^2}{2E} = G_{fc,max}$	4	124	18,1
		6	114	24,7
		8	93,7	21,4
		10	68,6	2,7
Manfredi_GfcMax_B	$G_{fc,Brick} = \frac{3f_c^2}{2E} = G_{fc,max}$	4	125	19,0
		6	127	38,9
		8	117	51,6
		10	105	57,2



Model	Fracture Energy Value and formulation (N/mm)	Displacement mm	Shear Capacity kN	$\Delta$ Shear Capacity %
Manfredi_GftMed_M	$G_{f_t, Mort} = \frac{f_t^2}{E} = G_{f_t, med}$	4	125	19,0
		6	116	26,9
		8	93,8	21,5
		10	68,2	2,1
Manfredi_GftMed_B	$G_{f_t, Brick} = \frac{f_t^2}{E} = G_{f_t, med}$	4	134	27,6
		6	113	23,6
		8	91	17,9
		10	69,8	4,5

Model	Fracture Energy Value and formulation (N/mm)	Displacement mm	Shear Capacity kN	$\Delta$ Shear Capacity %
Manfredi_GftMax_M	$G_{f_t, Mort} = \frac{3f_t^2}{2E} = G_{f_t, max}$	4	124	18,1
		6	115	25,8
		8	90,1	16,7
		10	70,7	5,8
Manfredi_GftMax_B	$G_{f_t, Brick} = \frac{3f_t^2}{2E} = G_{f_t, max}$	4	137	30,5
		6	120	31,3
		8	92,8	20,2
		10	71,6	7,2



## ANNEX D

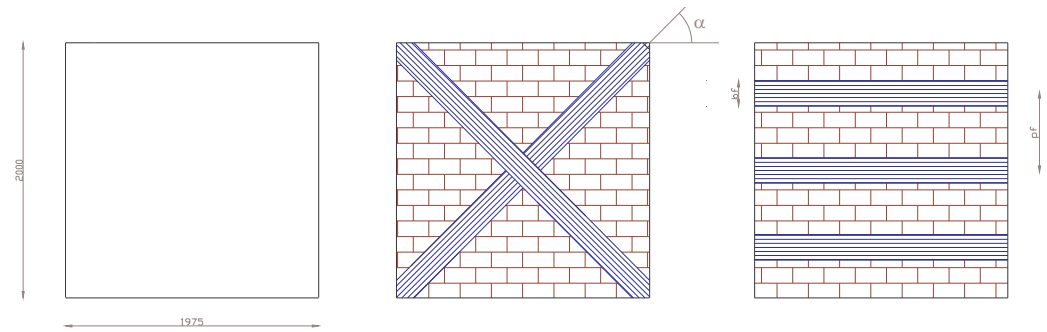
ALCAINO MASONRY PANELS

Fig. D - 1: Reinforcement layouts

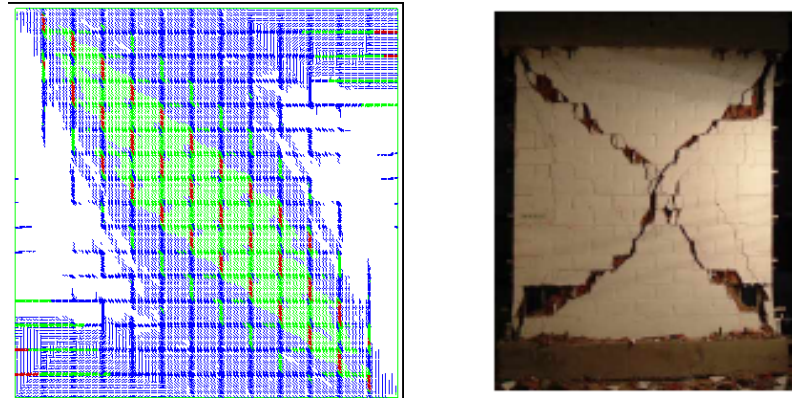


Fig.D - 2: Numerical simulation/Experimental results

<i>panels</i>	<i>Reinforcement layout</i>	<i>width <math>b_f</math>- mm</i>	<i>Spaced <math>p_f</math>- mm</i>
<i>H_100_1</i>	Three horizontal strips	100	455
<i>H_100_2</i>			555
<i>H_100_3</i>			655
<i>H_150_1</i>		150	455
<i>H_150_2</i>			555
<i>H_150_3</i>			655
<i>H_200_1</i>		200	455
<i>H_200_2</i>			555
<i>H_200_3</i>			655
<i>H_100</i>	One horizontal strips	100	-----
<i>H_200</i>		200	
<i>H_300</i>		300	
<i>D_100</i>	Two diagonal strips	100	-----
<i>D_200</i>		200	
<i>D_300</i>		300	

**Table D - 1:** reinforcement geometric characteristics



**Alcaino model – Horizontal reinforcement****Comparison between panel reinforced by using equal width differently spaced**

<b>panels</b>	<b>Reinforcement layouts</b>	<b>Shear capacity FEM</b>	<b><math>\Delta</math> shear capacity</b>
		<b>kN</b>	<b>%</b>
<i>H_100_1</i>	Three horizontal strips	206	47,0
<i>H_100_2</i>		204	45,7
<i>H_100_3</i>		203	45,0
<i>H_150_1</i>	Three horizontal strips	216	53,6
<i>H_150_2</i>		210	50,0
<i>H_150_3</i>		207	47,9
<i>H_200_1</i>	Three horizontal strips	223	59,3
<i>H_200_2</i>		215	53,6
<i>H_200_3</i>		213	52,1
<i>H_300_1</i>	Three horizontal strips	238	70,0
<i>H_300_2</i>		232	65,7
<i>H_300_3</i>		227	62,1

**Table D-2:** Shear capacity values

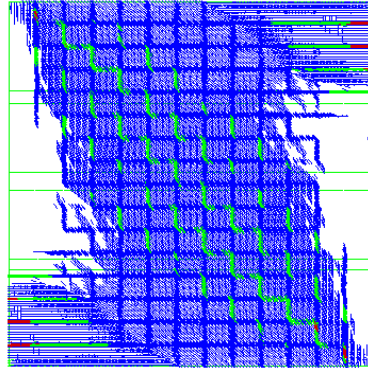
***Alcaino model – Horizontal reinforcement******Comparison between panel reinforced by using different width equally spaced***

<b><i>Pannello</i></b>	<b><i>Configurazione rinforzo</i></b>	<b><i>Taglio Sperimentale FEM</i></b>	<b><i><math>\Delta</math> Taglio Sperimentale</i></b>
		<b><i>kN</i></b>	<b><i>%</i></b>
<i>H_100_1</i>	Three horizontal strips	206	47,0%
<i>H_150_1</i>		216	53,6%
<i>H_200_1</i>		223	59,3%
<i>H_300_1</i>		238	70,0%
<i>H_100_2</i>	Three horizontal strips	204	45,7%
<i>H_150_2</i>		210	50,0%
<i>H_200_2</i>		215	53,6%
<i>H_300_2</i>		232	65,7%
<i>H_100_3</i>	Three horizontal strips	203	45,0%
<i>H_150_3</i>		207	47,9%
<i>H_200_3</i>		213	52,1%
<i>H_300_3</i>		227	62,1%

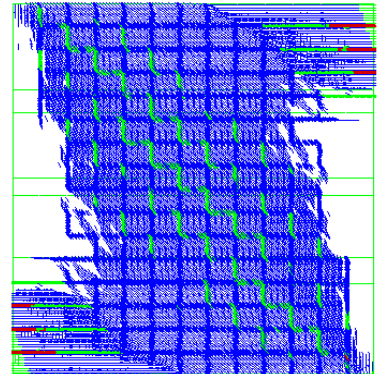
**Table D-3:** Shear capacity values

*Alcaino model – Horizontal reinforcement*

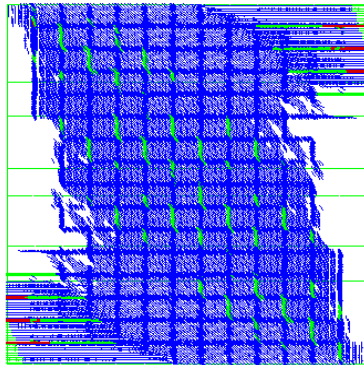
*Comparison between panel reinforced by using equal width differently spaced*



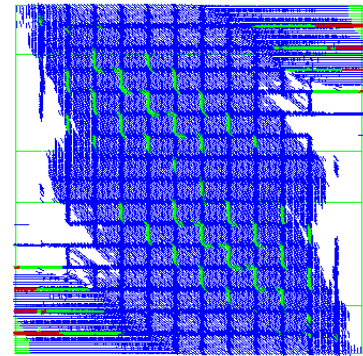
H\_100\_1



H\_150\_1



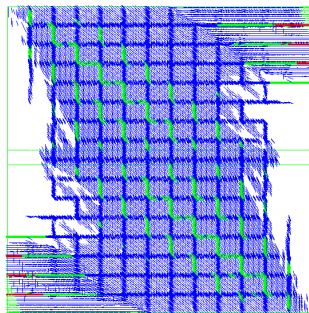
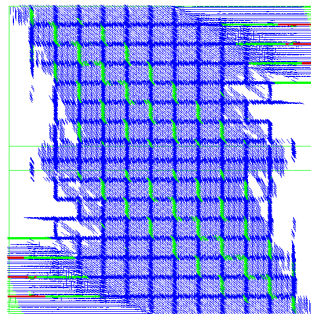
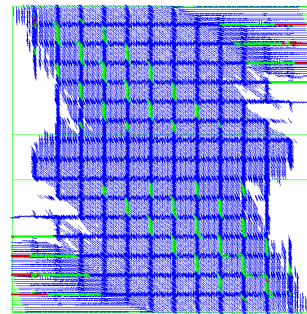
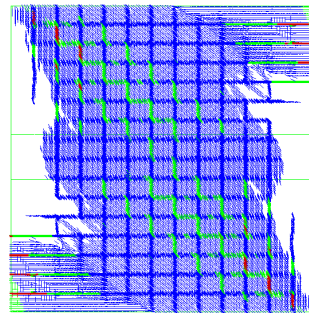
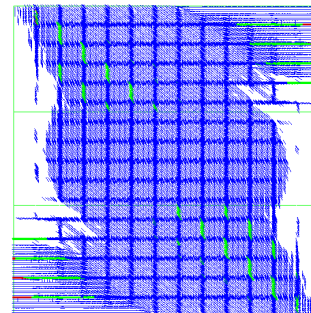
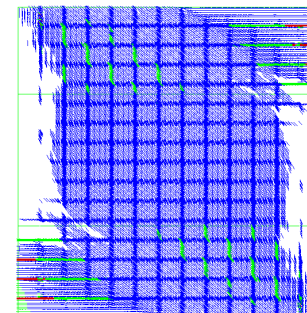
H\_200\_1



H\_300\_1

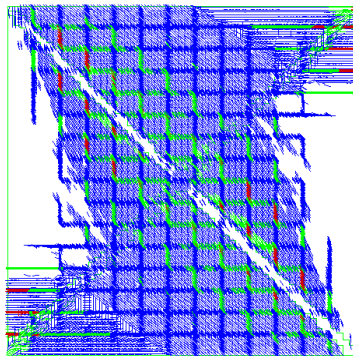
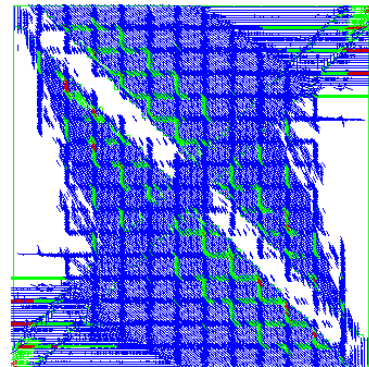
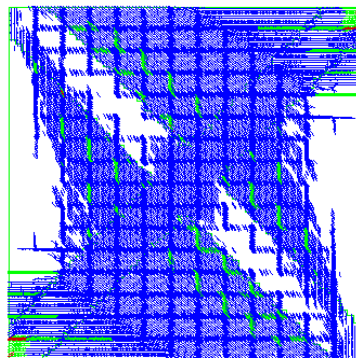
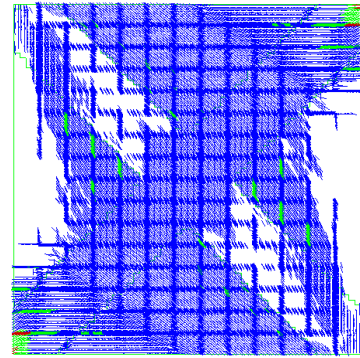
**Alcaino Model – Horizontal reinforcement****Comparison between reinforcement characterized by the same area**

<i>panels</i>	<i>Reinforcement layouts</i>	<i>Shear capacity FEM</i>	<i><math>\Delta</math> shear capacity</i>
		<i>kN</i>	<i>%</i>
<i>1x100_3str</i>	Three layer of strips	198.0	41.0%
<i>1x200_3str</i>		207.0	47.0%
<i>1x300_3str</i>		217.0	54.0%
<i>1x300</i>	One layer of strips	197.0	40.0%
<i>1x600</i>		210.0	49.0%
<i>1x900</i>		220.0	57.0%

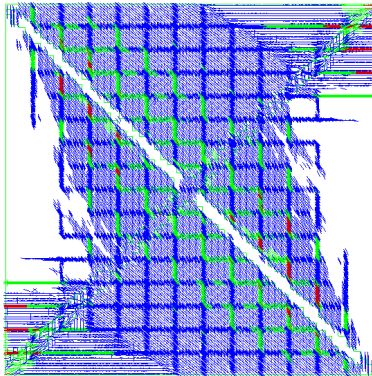
**Alcaino\_1x100\_3str****Alcaino\_1x200\_3str****Alcaino\_1x300\_3str****Alcaino\_1x300****Alcaino\_1x600****Alcaino\_1x900**

**Alcaino Model – Diagonal reinforcement****Comparison between different diagonal reinforcement**

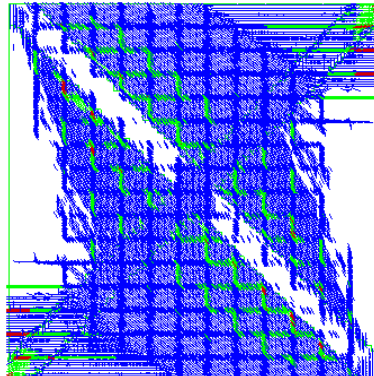
<i>panels</i>	<i>Reinforcement layouts</i>	<i>Shear Capacity FEM</i>	<i><math>\Delta</math> shear capacity</i>
		<i>kN</i>	<i>%</i>
<i>D_100</i>	Diagonal reinforcement	185	32,2%
<i>D_200</i>		215	53,6%
<i>D_300</i>		256	82,9%
<i>D_400</i>		268	91,5%
<i>RINF.</i>	Fully covered	322	130%

**Table D-4:** Shear capacity values**D\_100****D\_200****D\_300****D\_400**

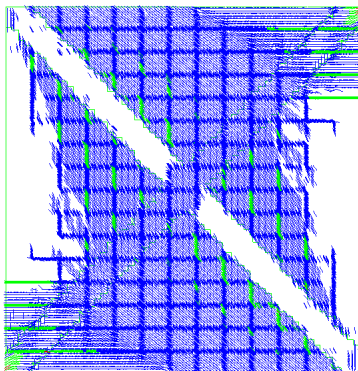
<i>panels</i>	<i>Reinforcement layouts</i>	<i>Shear Caapcity FEM</i>	<i><math>\Delta</math> shear capacity</i>
<i>URM</i>	140.5 kN	<i>kN</i>	<i>%</i>
<i>D_100_2str</i>	Diagonal reinforcement	197.0	40.0%
<i>D_200</i>		215.0	53.0%
<i>D_200_2str</i>		251.0	79.0%
<i>D_400</i>		268.0	91.0%



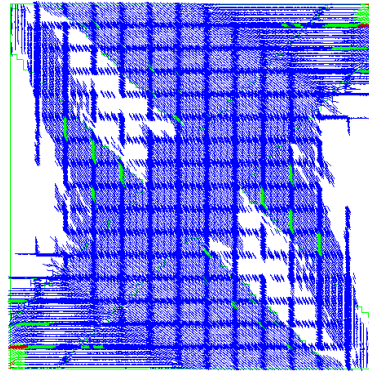
D\_100\_2str



D\_200

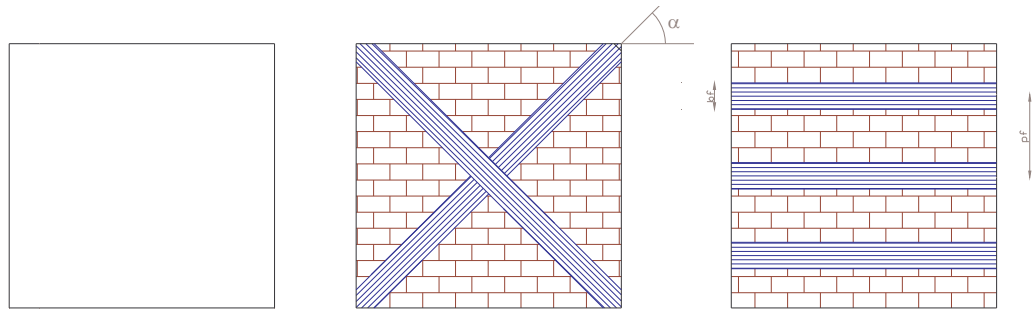
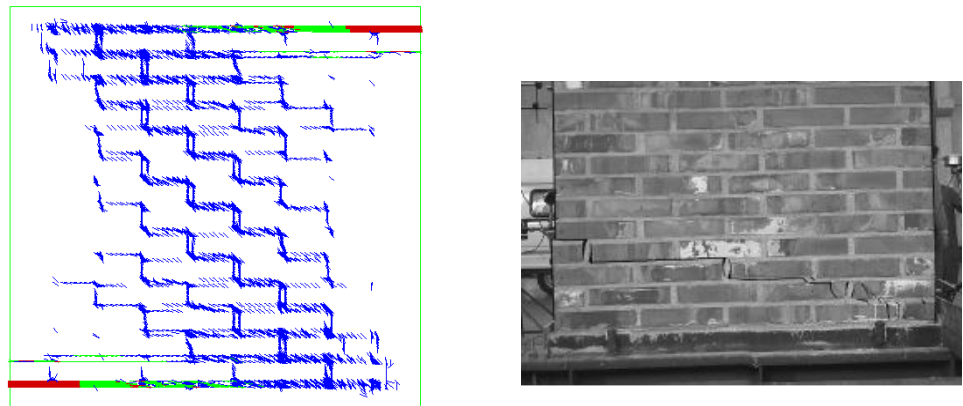


D\_200\_2str



D\_400



**PASCALE MODEL****Fig.D-13: Reinforcement layouts****Fig.D-14 Numerical simulation/experimental tests**

<i>panels</i>	<i>Reinforcement layouts</i>	<i>Width <math>b_f</math>-mm</i>	<i>Spaced <math>p_f</math>-mm</i>
<i>H_100_1</i>	Three horizontal strips	100	$p_f=b_f=100$
<i>H_100_2</i>			$p_f=2b_f=200$
<i>H_100_3</i>			$p_f=3b_f=300$
<i>H_200_1</i>		200	$p_f=b_f=200$
<i>H_200_2</i>			$p_f=2b_f=400$
<i>H_200_3</i>			$p_f=3b_f=600$
<i>H_300_1</i>		300	$p_f=b_f=300$
<i>H_300_2</i>			$p_f=2b_f=600$
<i>H_300_3</i>			$p_f=3b_f=900$
<i>D_100</i>	Two diagonal strips	100	-----
<i>D_200</i>		200	
<i>D_300</i>		300	
<i>D_400</i>		400	
<i>RINF.</i>			

**Table D-5:** Reinforcement geometric characteristic

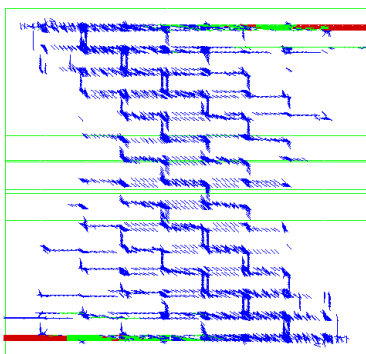


**Pascale model – Horizontal reinforcement****Comparison between reinforced masonry panel by using equal width strips differently spaced**

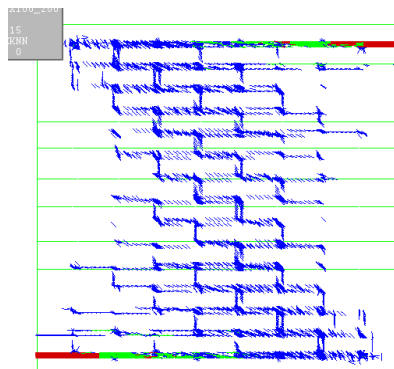
<i>Panels</i>	<i>Layouts</i>	<i>b<sub>f</sub> - mm</i>	<i>p<sub>f</sub> - mm</i>
<i>H_100_1</i>	3 horizontal layers	100	bf = 100 mm
<i>H_100_2</i>			2bf = 200 mm
<i>H_100_3</i>			3bf = 300 mm
<i>H_200_1</i>		200	bf = 200 mm
<i>H_200_2</i>			2bf = 400 mm
<i>H_200_3</i>			3bf = 300 mm
<i>H_300_1</i>		300	bf = 300 mm
<i>H_300_2</i>			2bf = 600 mm
<i>H_300_3</i>			3bf = 900 mm

**Table D-6:** Horizontal reinforcement layouts

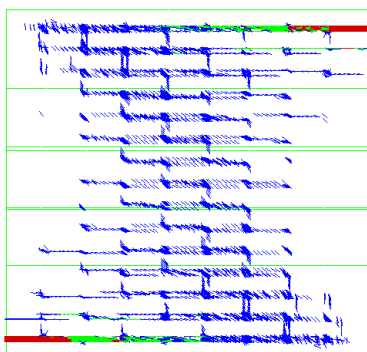
<i>Panels</i>	<i>Shear Capacity FEM</i>	<i>Δ Shear Capacity</i>
	<i>kN</i>	<i>%</i>
<i>URP</i>	112.0	-----
<i>H_100_1</i>	119.0	6.3%
<i>H_100_2</i>	120.0	7.1%
<i>H_100_3</i>	120.0	7.1%
<i>H_200_1</i>	119.0	6.3%
<i>H_200_2</i>	120.0	7.1%
<i>H_200_3</i>	120.0	7.1%
<i>H_300_1</i>	119.0	6.3%
<i>H_300_2</i>	119.0	6.3%
<i>H_300_3</i>	120.0	7.1%



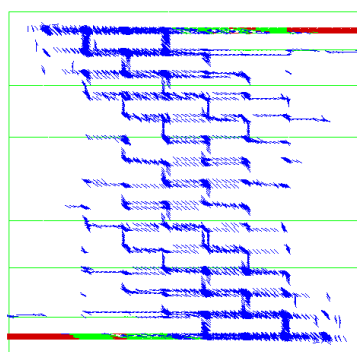
H\_100\_1



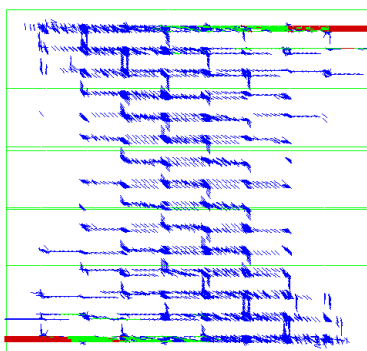
H\_100\_2



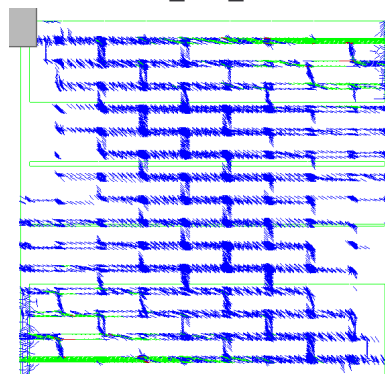
H\_200\_1



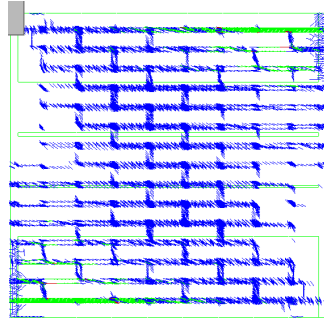
H\_300\_1



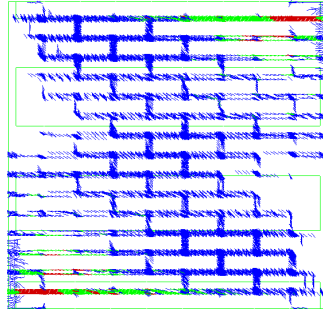
H\_200\_1



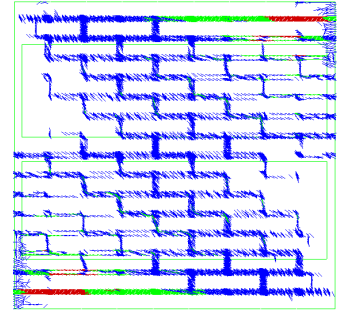
H\_200\_1\_vert



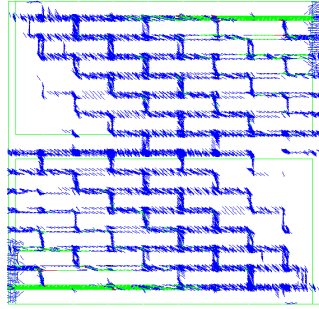
H\_200\_1\_vert



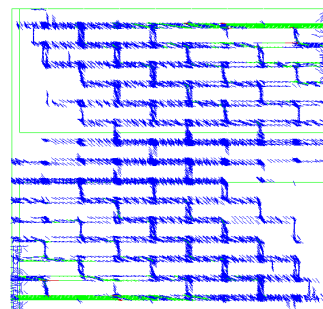
H\_200\_2\_vert



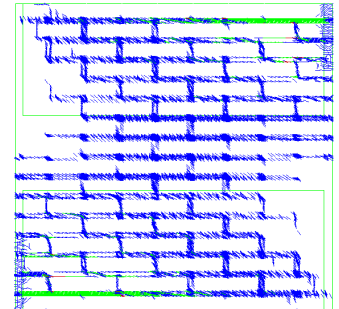
H\_200\_3\_vert



H\_1x100\_3str\_vert



H\_1x200\_3str\_vert

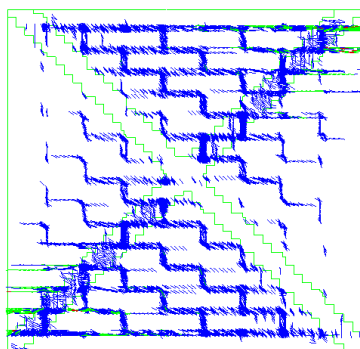


H\_1x300\_3str\_vert

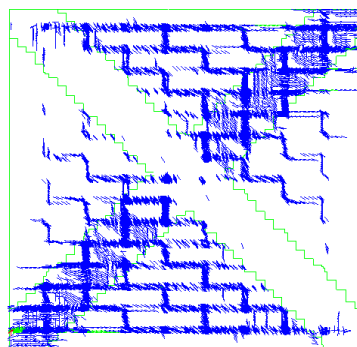
Modello Pascale – Rinforzo diagonaleConfronto tra pannelli rinforzati con strisce diagonali

<i>Panel</i>	<i>Reinforcement layout</i>	<i>Shear Capacity FEM</i>	<i><math>\Delta</math> Shear capacity</i>
	UR panel Shear Capacity = 112 kN	<i>kN</i>	<i>%</i>
<i>D 100</i>	Diagonal Reinforcement	174	51.3%
<i>D 200</i>		237	106.0%
<i>D 300</i>		272	136.5%
<i>D 400</i>		307	167.0%

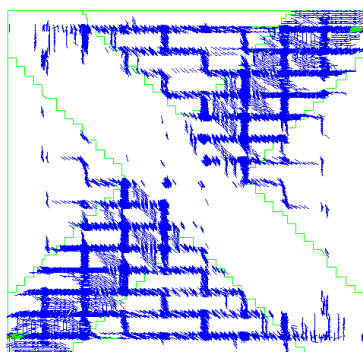
Table D-7: Shear capacity values



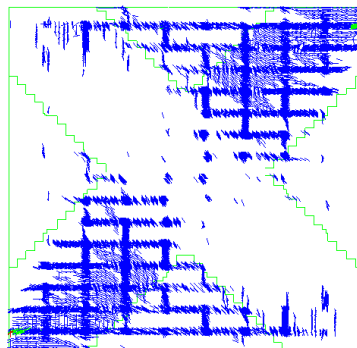
D\_100



D\_200

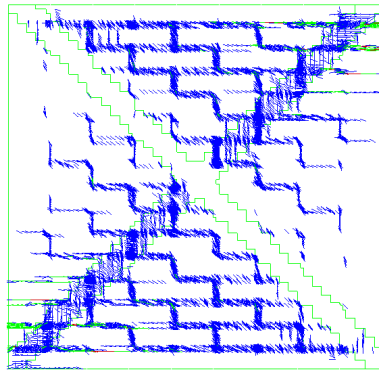
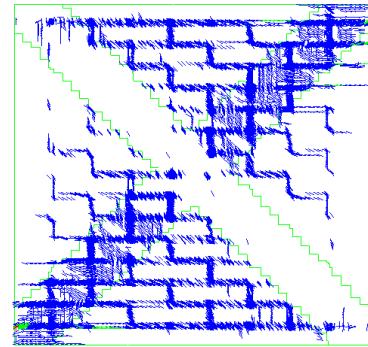
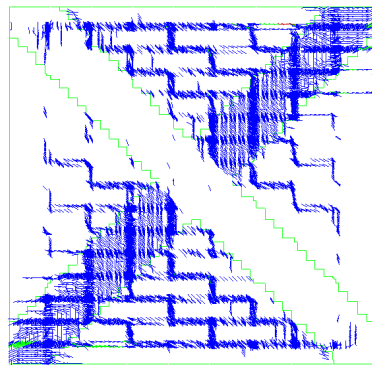
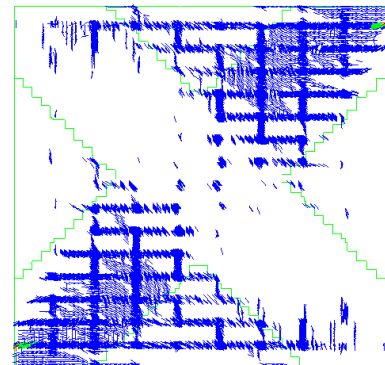


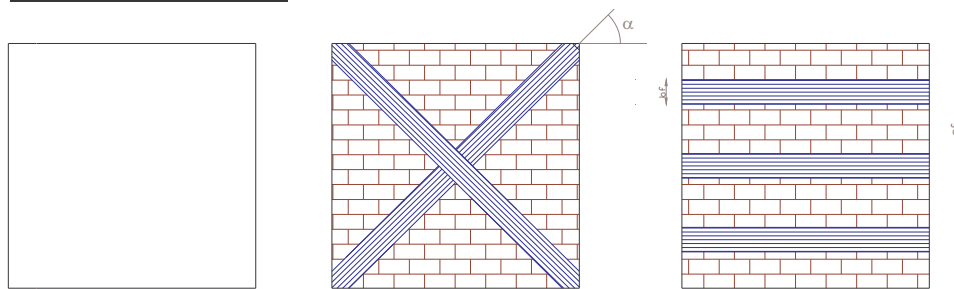
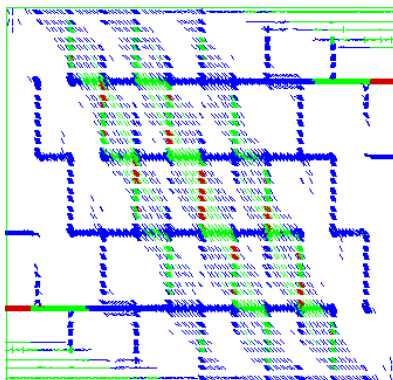
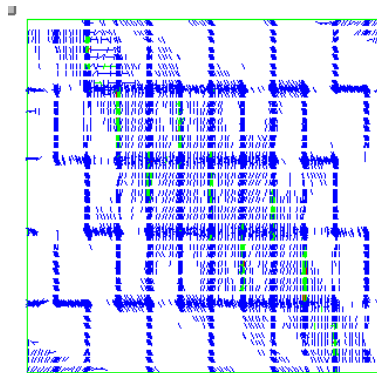
D\_300



D\_400

Panels	Description	$A_{fw} - \text{mm}^2$	Vmax - kN	$\Delta V_{\text{max}} - \%$
URP_FEM	Unreinforced panel	----	112	----
D_100_2str	2 layers 100 mm wide	26.00	183.0	55.0%
D_200	1 layers 200 mm wide	26.00	237.0	101.0%
D_200_2str	2 layers 200 mm wide	52.00	257.0	118.0%
D_400	1 layers 400 mm wide	52.00	307.0	160.0%

**D\_100\_2str****D\_200****D\_200\_2str****D\_400**

**MANFREDI PANELS****Fig.D-14: Reinforcement layouts****Load applied N=130 kN****Load applied N=325 kN****Fig.D-15: Numerical simulation/experimental tests**

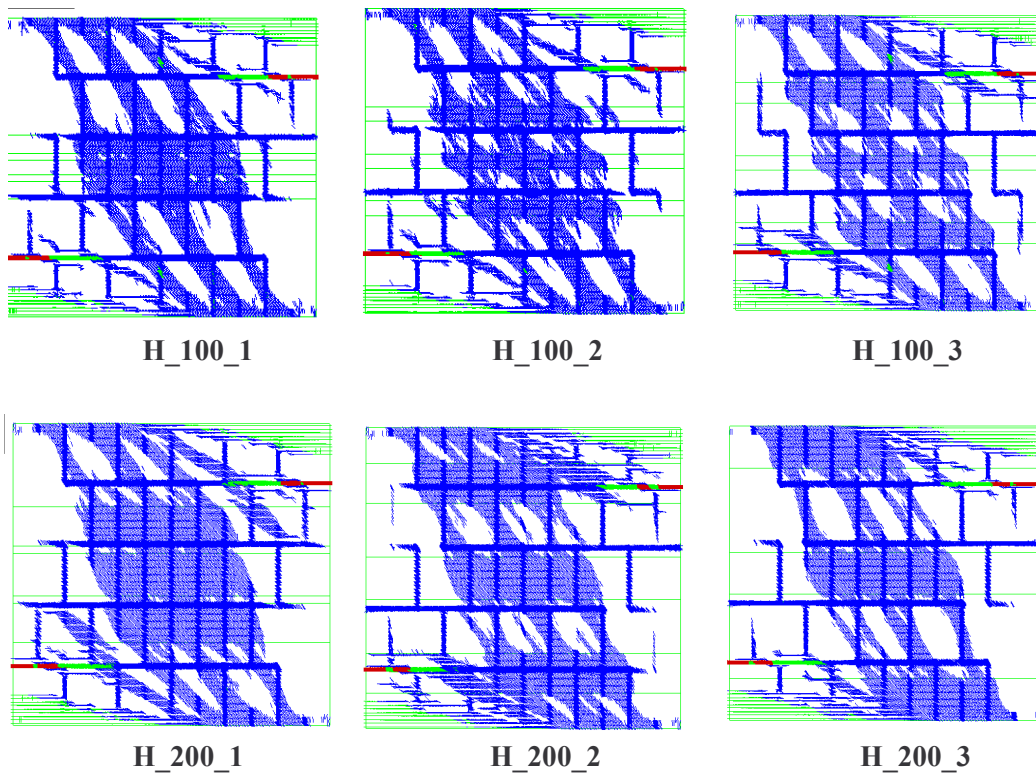
<i>Panels</i>	<i>Layouts</i>	<i>b<sub>f</sub> - mm</i>	<i>p<sub>f</sub> - mm</i>
<i>H_100_1</i>	3 horizontal layers	100	bf = 100 mm
<i>H_100_2</i>			2bf = 200 mm
<i>H_100_3</i>			3bf = 300 mm
<i>H_200_1</i>		200	bf = 200 mm
<i>H_200_2</i>			2bf = 400 mm
<i>H_200_3</i>			3bf = 600 mm
<i>H_300_1</i>		300	bf = 300 mm
<i>H_300_2</i>			2bf = 600 mm
<i>H_300_3</i>			3bf = 900 mm

**Table D-8:** Reinforcement geometric characteristic**Manfredi panels – Horizontal reinforcement**

**Comparison between masonry panel reinforced by using same width strips, differently spaced**

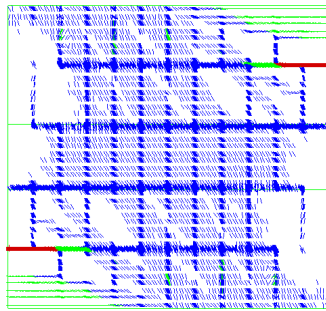
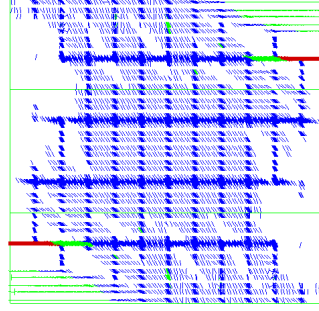
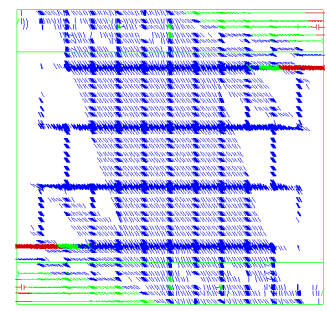
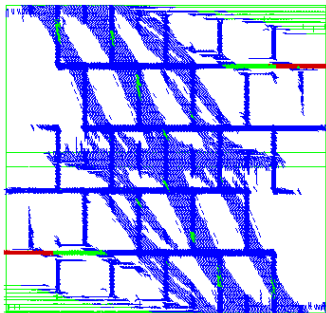
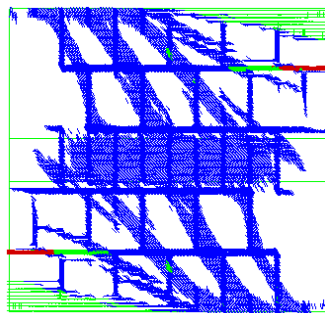
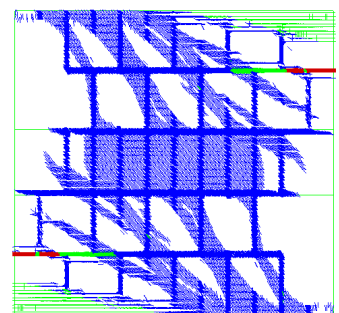
<i>Panels</i>	<i>Shear Capacity FEM</i>	<i>Δ Shear Capacity</i>
	<i>kN</i>	<i>%</i>
<i>URP</i>	102.0	-----
<i>H_100_1</i>	133.0	30.4%
<i>H_100_2</i>	132.0	29.4%
<i>H_100_3</i>	131.0	28.4%
<i>H_200_1</i>	133.0	30.4%
<i>H_200_2</i>	132.0	29.4%
<i>H_200_3</i>	129.0	26.5%
<i>H_300_1</i>	134.0	31.0%
<i>H_300_2</i>	131.0	28.0%
<i>H_300_3</i>	----	-----

**Table D-9:** Shear capacity values



<i>Panels</i>	<i>Shear Capacity FEM</i>	<i>ΔShear Capacity</i>
	<i>kN</i>	<i>%</i>
<i>URP</i>	102.0	-----
<i>H_1x100x3 str</i>	128.0	25.0%
<i>H_1x200x3 str</i>	132.0	29.0%
<i>H_1x300x3 str</i>	137.0	34.0%
<i>H_1x300</i>	132.0	29.0%
<i>H_1x600</i>	134.0	31.0%
<i>H_1x900</i>	134.0	31.0%

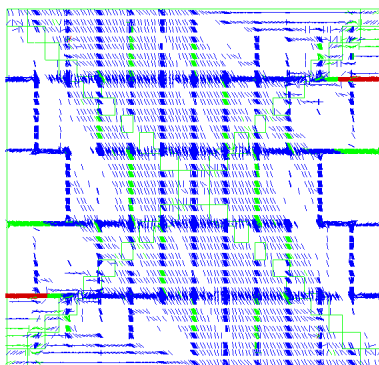
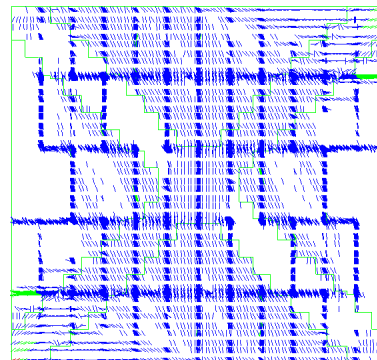


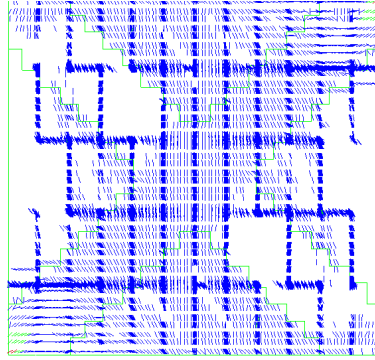
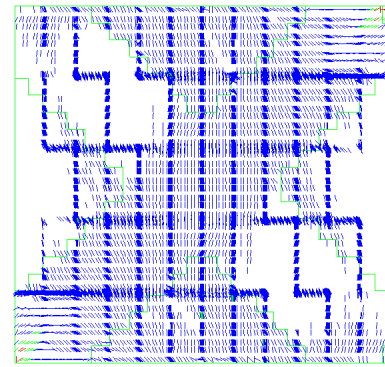
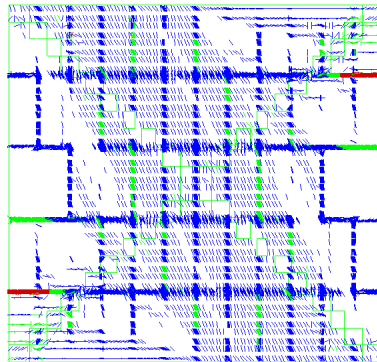
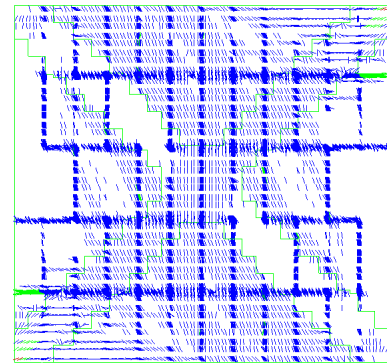
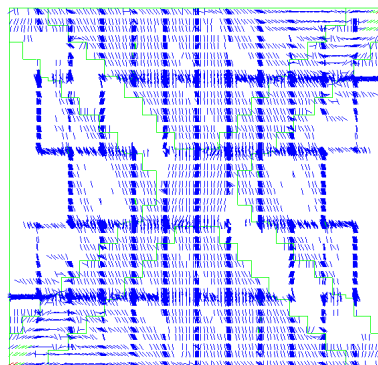
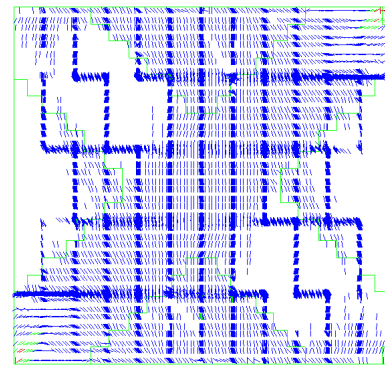
**H\_1x300****H\_1x600****H\_1x900****H\_1x100\_3str****H\_1x200\_3str****H\_1x300\_3str**

**Manfredi Model – Diagonal reinforcement****Comparison between panels reinforced by using diagonal strips**

<i>Panel</i>	<i>Reinforcement layout</i>	<i>Shear Capacity FEM</i>	<i><math>\Delta</math> Shear capacity</i>
	UR panel Shear Capacity = 102 kN	<i>kN</i>	<i>%</i>
<i>D_100</i>	Diagonal Reinforcement	119	17.0%
<i>D_200</i>		129	26.0%
<i>D_300</i>		146	43.0%
<i>D_400</i>		160	57.0%

<b>Panels</b>	<b>Description</b>	<b><math>A_{fw} - \text{mm}^2</math></b>	<b>Vmax - kN</b>	<b><math>\Delta</math> Vmax - %</b>
URP	Unreinforced panel	----	102.0	----
D_100_2str	2 layers 100 mm wide	26.00	119.0	17.0%
D_200	1 layers 200 mm wide	26.00	129.0	26.0%
D_200_2str	2 layers 200 mm wide	52.00	145.6	43.0%
D_400	1 layers 400 mm wide	52.00	160.0	57.0%

**Table D-10:** shear capacity values**D\_100****D\_200**

**D\_300****D\_400****D\_100\_2 str****D\_200****D\_200\_2str****D\_400**

